

REPORT DOCUMENTATION PAGE			Form Approved OMB No. 0704-0188	
Public reporting burden for this collection of information is estimated to average 1 hour per response, including the time for reviewing instructions, searching existing data sources, gathering and maintaining the data needed, and completing and reviewing the collection of information. Send comments regarding this burden estimate or any other aspect of this collection of information, including suggestions for reducing this burden, to Washington Headquarters Services, Directorate for Information Operations and Reports, 1215 Jefferson Davis Highway, Suite 1204, Arlington, VA 22202-4302, and to the Office of Management and Budget, Paperwork Reduction Project (0704-0188), Washington, DC 20503.				
1. AGENCY USE ONLY (Leave blank)		2. REPORT DATE 9 Sep 97		3. REPORT TYPE AND DATES COVERED
4. TITLE AND SUBTITLE SYNTHETIC IMAGE GENERATION OF FACTORY STACK AND WATER COOLING TOWER PLUMES			5. FUNDING NUMBERS	
6. AUTHOR(S) S. Didi Kuo				
7. PERFORMING ORGANIZATION NAME(S) AND ADDRESS(ES) Rochester Institute of Technology			8. PERFORMING ORGANIZATION REPORT NUMBER 97-022D	
9. SPONSORING/MONITORING AGENCY NAME(S) AND ADDRESS(ES) THE DEPARTMENT OF THE AIR FORCE AFIT/CIA 2950 P STREET WPAFB OH 45433			10. SPONSORING/MONITORING AGENCY REPORT NUMBER	
11. SUPPLEMENTARY NOTES				
12a. DISTRIBUTION AVAILABILITY STATEMENT <div style="border: 1px solid black; padding: 5px; text-align: center;"> DISTRIBUTION STATEMENT A Approved for public release Distribution Unlimited </div>			12b. DISTRIBUTION CODE	
13. ABSTRACT (Maximum 200 words) <div style="text-align: center; font-size: 2em; font-family: cursive;"> 19970919 080 </div> <div style="text-align: center; font-weight: bold; margin-top: 20px;"> DTIC QUALITY INSPECTED 4 </div>				
14. SUBJECT TERMS			15. NUMBER OF PAGES 164	
			16. PRICE CODE	
17. SECURITY CLASSIFICATION OF REPORT	18. SECURITY CLASSIFICATION OF THIS PAGE	19. SECURITY CLASSIFICATION OF ABSTRACT	20. LIMITATION OF ABSTRACT	

SYNTHETIC IMAGE GENERATION OF FACTORY STACK AND WATER COOLING TOWER PLUMES

by

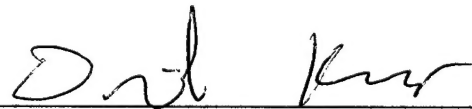
S. Didi Kuo
Captain, USAF

B.S. United States Air Force Academy (1988)

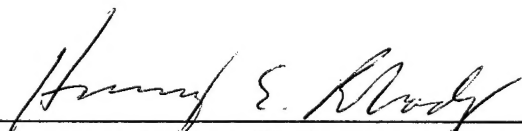
A dissertation submitted in partial fulfillment
of the requirements for the degree of Ph.D.
in the Chester F. Carlson Center for Imaging
Science in the College of Science of the
Rochester Institute of Technology

August 1997

Signature of the Author



Accepted by



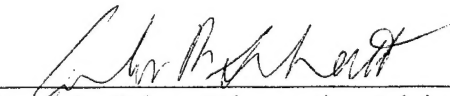
Coordinator, Ph.D. Degree Program

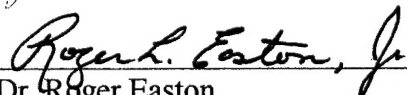
**CHESTER F. CARLSON
CENTER FOR IMAGING SCIENCE
COLLEGE OF SCIENCE
ROCHESTER INSTITUTE OF TECHNOLOGY
ROCHESTER, NEW YORK**

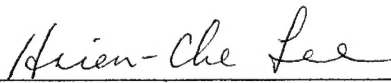
CERTIFICATE OF APPROVAL

Ph.D. DEGREE DISSERTATION

The Ph.D. Degree Dissertation of S. Didi Kuo
has been examined and approved by the
dissertation committee as satisfactory for the
dissertation requirement for the
Ph.D. degree in Imaging Science


Dr. John Schott, Dissertation Advisor


Dr. Roger Easton


Dr. Hsien Lee


Dr. Michael Kotlarchyk

29 August 1997

**DISSERTATION RELEASE PERMISSION
ROCHESTER INSTITUTE OF TECHNOLOGY
COLLEGE OF SCIENCE**

Title of Thesis: Synthetic Image Generation of Factory Stack and Water Cooling Tower Plumes

I, S. Didi Kuo, hereby grant permission to the Wallace Memorial Library of R.I.T. to reproduce my thesis in whole or in part. Any reproduction will not be for commercial use or profit.

Signature:

Dilben

Date: 29 August 1997

SYNTHETIC IMAGE GENERATION OF FACTORY STACK AND WATER COOLING TOWER PLUMES

by S. Didi Kuo

Submitted to the Center for Imaging Science
in the College of Science
in partial fulfillment of the requirements
for the Ph.D. Degree
at the Rochester Institute of Technology

ABSTRACT

Remote sensing of cooling tower and factory stack plumes may provide unique information on the constituents of the plume. Potential information of the power generated by the plant or the chemical composition of the factory products may be gathered from thermal emission and absorption in the infrared band, or from scattering of light in the visible band.

A new model for generating synthetic images of plumes has been developed using DIRSIG, a radiometrically based ray-tracing code. Existing models that determine the characteristics of the plume (constituents, concentration, particulate sizing, and temperature) are used to construct the plume in DIRSIG. The effects of scattered light using Mie theory and radiative transfer, as well as thermal self-emission and absorption from within the plume, are modeled for different regions of the plume. Both single and multiple scattering methods are available. The ray-tracing accounts for radiance from the plume, atmosphere, and background.

Synthetic generated images of a cooling tower plume, composed of water droplets, and a factory stack plume, composed of methyl chloride, are produced for visible, MWIR, and LWIR bands. Images of the plume from different sensor platforms are also produced. Observations are made on the interaction between the plume and its background and possible effects for remote sensing. Images of gas plumes using a hyperspectral sensor are illustrated. Several sensitivity studies are done to demonstrate the effects of changes in plume characteristics on the resulting image. Inverse algorithms that determine the plume effluent concentration are tested on the plume images.

A validation is done on the gas plume model using experimental data collected on a SF₆ plume. Results show the integrated plume model to be in good agreement with the actual data from five to one hundred meters from the stack exit. The scattering models are tested against MODTRAN. The validity and limitations of these models are discussed as a result of these tests. Finally two atmospheric scattering phenomena are illustrated to demonstrate qualitatively the scattering models.

Acknowledgments

I wish to thank my advisor, John Schott, for his help and guidance. His suggestion for this research topic, and continued direction, enabled me to successfully complete my dissertation. I am also grateful to my committee: Roger Easton, Hsien Lee, and Michael Kotlarchyk. They each offered me advice from their areas of expertise that helped improve the quality of my dissertation.

I am appreciative of the support from Scott Brown and Rolando Raqueno. I could never have finished if not for their help with the countless hours of debugging code. There were also several others outside of RIT that gave assistance to me. Bill Powers, Lance O'Steen, and Jack Fansalow provided me with the necessary plume models I needed. Jim Godfrey and his organization gave me experimental data for validation of my work. Thanks also to Gus Braun for the color science advice and Wendy Abbott for the sunset pictures of Maui.

Dedication

I wish to dedicate this research to my family, especially my mother and father. I could not have gotten this far without the encouragement from my parents in the pursuit of knowledge. I also want to thank the friends I've made over the three years while here in Rochester. The friendship they provided gave me a welcome break from the long stretches of studying and doing research, and made life enjoyable up here in the northern tundra. Most of all I want to thank God for His grace which enabled me to complete my work. Only He can make the real rainbows and sunsets that awe and inspire us. They surely are a sign of His handiwork and His promise to us - Genesis 9:16.

TABLE OF CONTENTS

LIST OF FIGURES.....	X
LIST OF TABLES.....	XIV
1. INTRODUCTION	1
2. THEORY	3
2.1 CONSIDERATION FOR REMOTE SENSING OF PLUMES.....	3
2.1.1 Factory Stack Plumes.....	3
2.1.2 Cooling Tower Plumes.....	5
2.2 PLUME MODELING	6
2.2.1 JPL Plume Model.....	6
2.2.2 LANL Plume Model.....	7
2.3 INTERACTION OF LIGHT WITH THE PLUME	8
2.3.1 Gas Absorption	8
2.3.2 Scattering.....	10
2.3.3 Extinction.....	14
2.3.4 Thermal Self-Emission.....	15
2.3.5 Radiative Transfer.....	16
2.4 GOVERNING EQUATIONS FOR REMOTE SENSING OF PLUMES	20
2.4.1 Solar and Self-emissive Radiation Incident on the Plume	21
2.4.2 Radiation from the Plume	23
2.4.3 Upward Looking Sensor.....	25
2.4.4 Downward Looking Sensor.....	26
3. MODELING AND ALGORITHM DEVELOPMENT	28
3.1 INTRODUCTION.....	28
3.2 LANL PLUME MODEL.....	28
3.2.1 Running the LANL Plume Model	29
3.2.2 Building the LANL ACAD Model.....	30
3.3 JPL PLUME MODEL	32
3.3.1 Running the JPL Plume Model	32
3.3.2 Building the JPL ACAD Model.....	34

3.4 PLUME MODEL TRANSLATOR.....	38
3.5 DIRSIG	42
3.5.1 <i>Initializing DIRSIG</i>	42
3.5.2 <i>Ray-tracing through Plume Regions</i>	44
3.5.3 <i>Multiple Scattering</i>	45
3.5.4 <i>Integrated JPL Plume Model</i>	47
3.5.5 <i>Other Special Cases</i>	48
4. RESULTS	49
4.1 GAS PLUMES.....	49
4.1.1 <i>JPL ACAD Model</i>	49
4.1.2 <i>Integrated JPL Model</i>	54
4.2 SCATTERING PLUMES.....	62
4.2.1 <i>Homogenous (Water Droplet) Plume</i>	62
4.2.2 <i>LANL Cooling Tower Plume</i>	78
5. VALIDATION	82
5.1 VALIDATION OF GAS PLUME MODEL.....	82
5.1.1 <i>Experimental Description</i>	82
5.1.2 <i>Creation of the DIRSIG Background Scene</i>	84
5.1.3 <i>Validation of ACAD JPL Model</i>	86
5.1.4 <i>Validation of Integrated JPL Model</i>	91
5.2 SCATTERING VALIDATION WITH MODTRAN	98
5.2.1 <i>MODTRAN</i>	99
5.2.2 <i>Results</i>	100
5.3 THE RAINBOW	104
5.3.1 <i>Theory</i>	104
5.3.2 <i>Procedure</i>	106
5.3.3 <i>Results</i>	108
5.4 SUNSET WITH RED CLOUDS	113
6. CONCLUSIONS AND RECOMMENDATIONS	119
6.1 SUMMARY	119
6.2 CONCLUSIONS.....	119
6.3 RECOMMENDATIONS.....	121

APPENDIX A: MIE SCATTERING THEORY.....	124
APPENDIX B: IMPORTANCE OF MULTIPLE SCATTERING IN PLUMES ..	130
APPENDIX C: PARTICLE SIZE DISTRIBUTION	135
APPENDIX D: TWO-STREAM APPROXIMATION FOR RADIATIVE TRANSFER IN WATER CLOUDS	140
APPENDIX E : TESTING INVERSE ALGORITHMS ON PLUME IMAGES	144
APPENDIX F: CREATING A COLOR IMAGE IN DIRSIG	150
APPENDIX G: ADDING ADDITIONAL GASES TO THE GAS DATABASE ...	151
APPENDIX H: DIRSIG PLUME FILE FORMATS	152
APPENDIX I: NTS VALIDATION FILES	158
REFERENCES.....	161

LIST OF FIGURES

Figure 2-1. Angular Scattering Distribution for a Water droplet in the Visible	
Wavelength	13
Figure 2-2. Angular Scattering Distribution for a Water Droplet in the MWIR.....	13
Figure 2-3. Source Terms for Radiative Transfer	18
Figure 2-4. Flux Streams for Two-Stream Approximation.....	18
Figure 2-5. Atmospheric Transmission, Solar Irradiance, and Thermal Self Emission.....	21
Figure 2-6. Sources of Radiation onto the Plume	22
Figure 2-7. Scattering within the Plume	23
Figure 2-8. Upward Looking Sensor.....	26
Figure 2-9. Downward Looking Sensor.....	27
Figure 3-1. Process Flow in Building Plume Scene.....	28
Figure 3-2. I/O Flow for Build_LANL.....	31
Figure 3-3. ACAD LANL Plume Model.....	31
Figure 3-4. Scene Coordinates for JPL Plume Model.....	34
Figure 3-5. I/O Flow for Build_JPL.....	35
Figure 3-6. Side View of Single Slice in ACAD Model.....	36
Figure 3-7. ACAD JPL Plume Model with Three Regions	37
Figure 3-8. ACAD JPL "Wander" Plume Model.....	37
Figure 3-9. Flowchart for PMT Code.....	39
Figure 3-10. Ray Tracing Through Rectangular Plume Model.....	44
Figure 3-11. Multiple Scattering Sources for Downward Looking Sensor.....	46
Figure 3-12. Multiple Scattering Sources for Upward Looking Sensor.....	47
Figure 4-1. Hyperspectral images of CH ₃ Cl plume from an airborne sensor at 3.33 μ m (a) and 10 μ m (b) and a ground based sensor at 3.33 μ m (c) and 10 μ m (d).....	50
Figure 4-2. JPL "wander" plume filled with water droplets (left, visible band) and methyl chloride (right, 3.33 μ m)	52
Figure 4-3. 10 μ m Images of CH ₃ Cl with Variable Concentration.....	53
Figure 4-4. 10 μ m Images of CH ₃ Cl with Variable Temperature	53
Figure 4-5. 3.33 μ m Images of CH ₃ Cl with Variable Concentration.....	53
Figure 4-6. 3.33 μ m Images of CH ₃ Cl with Variable Temperature	53
Figure 4-7. Contrast Ratios for Change in Plume Temperature and VMR.....	54

Figure 4-8. Integrated JPL model images from an airborne sensor at 3.33 μm (a) and 10 μm (b) and a ground based sensor at 3.33 μm (c) and 10 μm (d)	55
Figure 4-9. Downwind Characteristics of Integrated Plume Model	56
Figure 4-10. Reduced Gas Release Rate Images at 3.33 μm (a) and 10 μm (b) and Contrast Ratio (c).....	57
Figure 4-11. Decreased Plume Temperature Images at 3.33 μm (a) and 10 μm (b) and Contrast Ratio (c) 58	
Figure 4-12. Lowered Atmospheric Stability Images at 3.33 μm (a) and 10 μm (b) and Contrast Ratio (c)59	
Figure 4-13. Absorbance Curves for Methyl Chloride (CH_3Cl) in MWIR (a) and LWIR (b)	60
Figure 4-14. Plume Images at Designated Spectral Bands.....	61
Figure 4-15. Integrated JPL Model with Time Varying Meteorological Conditions	62
Figure 4-16. Maximum Optical Depth for Four Plume Number Densities	63
Figure 4-17. Visible Images of Plume at Noon with Varying Number Density	64
Figure 4-18. Optical and Radiometric Properties for Noon Plumes	65
Figure 4-19. Visible Images of Plume at Noon Using Single Scattering Model	66
Figure 4-20. Optical and Radiometric Properties for Noon Plumes Using Single Scattering Model	67
Figure 4-21. Visible Images of Plume at 8:00 A.M.	68
Figure 4-22. Optical and Radiometric Properties for 8:00 A.M. Plumes.....	69
Figure 4-23. Visible Images of Plume at 8:00 A.M. Using Single Scattering Model.....	70
Figure 4-24. Optical and Radiometric Properties for 8:00 A.M. Plumes Using Single Scattering Model	71
Figure 4-25. Visible Images of Plume at 11:00 A.M. for Upward Looking Sensor	72
Figure 4-26. Optical and Radiometric Properties for 11:00 A.M. Plumes for Upward Looking Sensor.....	73
Figure 4-27. Visible Images of Plume at 11:00 A.M. for Upward Looking Sensor Using Single Scattering Model	74
Figure 4-28. Optical and Radiometric Properties for 11:00 A.M. Plumes for Upward Looking Sensor Using Single Scattering Model	74
Figure 4-29. Visible Images of Plume at 8:00 A.M. for Upward Looking Sensor	75
Figure 4-30. Optical and Radiometric Properties for 8:00 A.M. Plumes for Upward Looking Sensor.....	76
Figure 4-31. Visible Images of Plume at 11:00 A.M. for Upward Looking Sensor Using Single Scattering Model	77
Figure 4-32. Optical and Radiometric Properties for 8:00 A.M. Plumes for Upward Looking Sensor Using Single Scattering Model	77
Figure 4-33. LANL Plume Properties	79
Figure 4-34. Visible, MWIR, and LWIR Images of the LANL plume model	80
Figure 4-35. Optical Properties of LANL Plume	80
Figure 5-1. Absorbance Curve for SF_6 at 10 ppm-m.....	83
Figure 5-2. Sensor Response of Band 1 (left) and Band 2 (right) of the TI IRLS-RS18c Sensor.....	83

Figure 5-3. SF ₆ Plume Images from Band 1 (left) and 2 (right) of TI ILRS-RS18c	84
Figure 5-4. DIRSIG Scene of NTS Background	85
Figure 5-5. Overhead and Side View of ACAD Plume Model (Band 1).....	87
Figure 5-6. ACAD Plume Model in Band 1 (left) and Band 2 (right) using NTS Look Angles	87
Figure 5-7. Downwind Radiance Profile in Band 1	88
Figure 5-8. Downwind Radiance Profile in Band 2	88
Figure 5-9. Cross-sectional Radiance Profile of Plume 7 Meters Downwind in Band 1.....	89
Figure 5-10. Cross-sectional Radiance Profile of Plume 7 Meters Downwind in Band 2.....	89
Figure 5-11. Cross-sectional Radiance Profile of Plume 100 Meters Downwind in Band 1.....	90
Figure 5-12. Cross-sectional Radiance Profile of Plume 100 Meters Downwind in Band 2.....	90
Figure 5-13. Overhead and Side View of Integrated JPL Plume Model.....	91
Figure 5-14. Measured Plume Temperature Downwind from Stack	92
Figure 5-15. DIRSIG Plume Temperature	92
Figure 5-16. DIRSIG Column Density Downwind from Stack	93
Figure 5-17. Column Density Profile at 100 Meters Downwind of Stack	94
Figure 5-18. Integrated Plume Model in Band 1 (left) and Band 2 (right) using NTS Look Angles.....	94
Figure 5-19. Downwind Radiance Profile in Band 1	95
Figure 5-20. Downwind Radiance Profile in Band 2	95
Figure 5-21. Cross-sectional Radiance Profile of Plume 7 Meters Downwind in Band 1.....	96
Figure 5-22. Cross-sectional Radiance Profile of Plume 7 Meters Downwind in Band 2.....	96
Figure 5-23. Cross-sectional Radiance Profile of Plume 100 Meters Downwind in Band 1.....	97
Figure 5-24. Cross-sectional Radiance Profile of Plume 100 Meters Downwind in Band 2.....	97
Figure 5-25. Geometries used for Scattering Validation.....	100
Figure 5-26. DIRSIG-MODTRAN Contrast for Downward-looking Noon Case	101
Figure 5-27. DIRSIG-MODTRAN Contrast for Downward-looking 8:00 A.M. Case.....	102
Figure 5-28. DIRSIG-MODTRAN Contrast for Upward-looking Noon Case	103
Figure 5-29. DIRSIG-MODTRAN Contrast for Upward-looking 8:00 A.M. Case	103
Figure 5-30. Angular Scattering Coefficient for a Water Droplet at 450 nm	106
Figure 5-31. Geometry Used to Create Rainbow Scene	107
Figure 5-32. Rainbow with 20 μ m mean droplet size and associated size distribution and angular scattering coefficient charts.....	109
Figure 5-33. Rainbow with 100 μ m mean droplet size and associated size distribution and angular scattering coefficient charts.....	110
Figure 5-34. Rainbow with 200 μ m mean droplet size and associated size distribution and angular scattering coefficient charts.....	111

Figure 5-35. Full DIRSIG Rainbow.....	112
Figure 5-36. Actual and DIRSIG (1815) Sunset Images.....	114
Figure 5-37. Actual and DIRSIG (1830) Sunset Images.....	115
Figure 5-38. DIRSIG (1840) Sunset Image.....	116
Figure 5-39. Solar Irradiance on Clouds at Three Sunset Times	117
Figure 5-40. Radiance from Center and Fringe of Cloud.....	118
Figure A-1. Geometry of Incident and Scattered Fields.....	124
Figure B-1. Plume Layer Model Constructed for MODTRAN3	131
Figure B-2. Average Spectral Single Scattering Albedo of Plume	132
Figure B-3. Spectral Transmission for Different Plume Models	133
Figure B-4. Spectral Ratio of Multiple to Single Scattering for Plume Models	134
Figure B-5. Spectral Ratio of Scattered to Total Radiance for Plume Models	134
Figure C-1. LANL Modified Gamma Size Distribution	136
Figure C-2. MODTRAN Modified Gamma Size Distribution	136
Figure C-3. MODTRAN Lognormal Size Distribution	137
Figure C-4. Effects of Variance in Size Distribution on Extinction Efficiency.....	139
Figure D-1. Two-Stream Approximation using Plane Parallel Layer.....	140
Figure E-1. Estimating Plume Depth	145
Figure E-2. LWIR and MWIR Images of Single Region JPL ACAD Plume	146
Figure E-3. Estimated VMR Image and Values of Plume in LWIR (a) and MWIR (b).....	147
Figure E-4. Estimated VMR Image and Values of Plume in LWIR (a) and MWIR (b) for Plume at Ambient Temperature	148
Figure E-5. LWIR and MWIR Images of Single Region JPL ACAD Plume	148
Figure E-6. Estimated VMR Image and Values of Plume in LWIR (a) and MWIR (b) from an Airborne Sensor.....	149
Figure F-1. RGB Color Matching Functions	150

LIST OF TABLES

Table 3-1. Input Parameters for LANL Plume Model	29
Table 3-2. Input Parameters for JPL Plume Model.....	33
Table 3-3. Plume Debug Images for ACAD Models	43
Table 3-4. Plume Debug Images for Integrated JPL Model.....	44
Table 4-1. Methyl Chloride Plume Properties	50
Table 4-2. Radiometric Values Plume Images.....	51
Table 4-3. Initial Plume Characteristics.....	55
Table 4-4. Optical Properties of Homogenous Plume	63
Table 4-5. Properties of LANL Plume	78
Table 4-6. Optical Properties of 6 μ m Water Droplet.....	79
Table 5-1. Emissivity and Radiance Values for NTS Scene.....	85
Table 5-2. Region Description of ACAD Plume Model.....	86
Table 5-3. Primary and Secondary Rainbow Angles Using Geometrical Optics.....	105
Table 5-4. Primary and Secondary Rainbow Angles Using Mie Scattering Theory.....	106
Table 5-5. Cloud Characteristics.....	113
Table B-1. Characteristics of Each Plume Layer	131

1. Introduction

Remote sensing of factory stack and cooling tower plumes has the potential to reveal information about the constituents of the plumes. The intelligence community, nuclear proliferation monitors, the Environmental Protection Agency (EPA), and the Department of Energy (DOE) have looked at gathering information from observations of plumes. In the case of factory stacks, determination of the species and concentration of the plume can help reveal the chemical components of the factory products. For plumes from cooling towers, the temperature and water droplet characteristics may indicate the output power of the station. Ideally, observation of the plume should be done by a sensor located next to the factory or power station; however, this is not always possible. Airborne and satellite remote sensing would provide coverage not only of inaccessible areas, but over wide areas at regular intervals. Both passive and active remote sensing of plumes are currently being investigated. While active methods (i.e., laser remote sensing) can provide more accurate determination of the concentration of effluents in the plume, they can only provide information at certain wavelengths. In addition, active platforms have limited coverage and are expensive to produce and maintain. Passive sensors on existing platforms can provide information on plumes over a wide spectral band, and multispectral image fusion can be used to yield additional information. Coverage also would be more widespread and reliable.

Synthetic image generation (SIG) will aid in the investigation of plume phenomenology and in the understanding of remote sensing of plumes. SIG is the process of using first principles from radiometry to simulate an image as seen by a particular sensor. SIG provides the ability to model images under a variety of conditions (wavelength, sensor platform, scene conditions, etc.). These synthetic images can then be used to predict sensor performance under various conditions, and provide a way to test remote sensing algorithms. Synthetic plume imagery can reveal not only how a plume will look to a sensor, but also how it will interact with the background and surrounding atmosphere. A variety of plume images can be generated using different sources, meteorological conditions, viewing conditions, and wavelengths. Algorithms designed to determine effluent concentration can be tested on these images to determine their accuracy and robustness.

The radiance reaching the sensor from the plume originates from several sources. Direct sunlight and diffuse skylight are scattered from the plume. The type of scattering (Mie or Rayleigh) depends on the spectral band and particulate size. The intensity of scattering depends on the concentrations and particle size distribution. Multiple scattering will occur within the plume if the optical depth is large. Thermal self emission and absorption by the plume will be apparent in the MWIR (3-5 μm) and LWIR (8-12 μm) regions. The amount of self-emission depends on the emissivity and temperature of the plume. The transmission of the plume will be dependent on the spectral absorbance of the particulate.

The generation of synthetic images of plumes must account for all of these factors to produce a radiometrically accurate image. The Digital Imaging and Remote Sensing Image Generation code (DIRSIG)

has this ability (Schott, 1993). It is currently employed by the Center for Imaging Science at the Rochester Institute of Technology for simulating images for various remote sensing platforms. DIRSIG is a ray-tracing code that incorporates MODTRAN to produce a radiometrically accurate image at the sensor of a scene built by the user.

The objective of this research is to develop a radiometrically accurate method for producing synthetic images of plumes. This method needs to account for the main interactions of the plume with its environment. Existing models for cooling tower and factory stack plumes are used to provide the plume geometry and characteristics (constituents, concentration, particulate sizing, and temperature). The plumes are represented either externally by AutoCAD (ACAD) models or internally within DIRSIG. The effects of scattering, self-emission, and absorption from the plume are incorporated in DIRSIG on a pixel-by-pixel basis. Atmospheric radiative transfer theory is used to account for multiple scattering within the plume. Different spectral gas databases are included in order to model a variety of gas plumes.

A secondary objective of this research is to demonstrate how this methodology can be used to understand remote sensing of plumes. SIG scenes of plumes are generated for both ground-based and airborne sensors at a variety of wavelengths. Special emphasis is given to the use of hyperspectral sensors in the detection of gas plumes. Sensitivity studies are done on the plume-background contrast based on changes in the plume characteristics. Finally, a brief demonstration is shown in the appendix of how inverse algorithms that determine plume concentrations are used with DIRSIG plumes.

The final objective is to validate the models developed in this research. This is done with actual experimental data where available, or against other validated computer models. A validation of the DIRSIG gas plume model used experimental data collected of a SF₆ plume at the Nevada Test Site. The scattering plume model is compared to results obtained from MODTRAN. Two atmospheric scattering effects simulated by DIRSIG are also presented as a result of this research.

This dissertation is divided into six chapters and nine appendices. Chapter 2 covers the theory needed for modeling plumes in DIRSIG. This includes the physics and radiometry of plumes and the governing equations for remote sensing. Chapter 3 describes the algorithms used to create the plume models and how they are implemented in DIRSIG. It is intended to be a user's manual for future users of the DIRSIG plume code. Chapter 4 gives various results and examples of plume images. Both gas and scattering plumes are shown using different sensor platforms and plume parameters. Chapter 5 presents the validation results against the NTS plumes and MODTRAN code. Also the DIRSIG images of atmospheric scattering are shown in this chapter as a qualitative validation of the code. Conclusions and recommendations of this research are given Chapter 6. The appendices give additional theoretical background on Mie scattering, radiative transfer, particle size distribution, and inverse algorithms. Code and file descriptions are also covered in the appendices.

2. Theory

This chapter discusses the theory behind modeling plumes in DIRSIG. It covers the basic physics and radiometry of how the plume interacts with its environment. The interaction of light and matter in the form of scattering, absorption, and radiative transfer is emphasized. While there is a brief discussion of how plumes are modeled, this chapter does not cover the dynamics of their plumes evolution. Other research has been done in this area and references are given to them. The governing equations for remote sensing of the plume are covered for both ground-based and airborne sensors.

2.1 Consideration for Remote Sensing of Plumes

2.1.1 Factory Stack Plumes

Release of various chemical effluents by a factory into the atmosphere can reveal materials that are being used or produced by the factory. Common emissions from power plants include CO, CO₂, NO, NO₂, N₂O, SO₂, HCl, CH₄, NH₃, H₂O, and NCHO. Sulfur hexafluoride (SF₆) is commonly used as a plume tracer gas due to its large absorbance cross-section. These particulates typically have diameters under 0.1 μm (Blumenthal, 1981). The exception is NO₂ (White, 1981) which can have diameters around 0.6 μm and is the dominant absorber in the visible region. The local humidity level can cause an increase in particulate size due to condensation of water vapor onto the nuclei (Hänel, 1972). Normally, there is very little scattering unless flyash and sulfates are present in large amounts (which may occur in modern fossil fuel power plants not under emission control). Typical temperatures at the stack exit of an oil burning plant are around 495 K° (Selby, 1978). A comprehensive study of factory stack emissions, including computer code to simulate them, was done by the EPA between 1979 and 1981 (Seigneur, 1985). The plumes of two coal-burning power plants and a copper smelter were measured by four teleradiometers at downwind distances from 17 to 34 km. The data was compared to the PLUEVUEII code which used radiative transfer equations with angular multi-scattering terms to find the radiance reaching the sensor when looking at a plume (Seigneur, 1984). In the visible region (400-650 nm), the program predicted the plume/sky radiance ratio over a range of viewing angles. The data collected from these experiments may be useful for validation, but most of the measurements are taken too far downwind from the stack exit.

A series of chemical gases were released under controlled conditions at the Nevada Test Site (NTS) in 1994 (Westberg, 1996). These plumes were monitored over the first 500 m by several instruments including a multi-spectral sensor. The images produced were calibrated radiometrically using objects with known emissivities and temperatures. One of the chemicals released was SF₆ which has a very visible plume in an image taken in the 10.4-11.0 μm region. This data set will be used in validating the plume imagery developed by this research.

The chemistry within the plume can be very complex. Some gases that emerge from the stack are converted to particulates as they interact with the atmosphere. For example sulfur dioxide will change into sulfate, and nitrogen dioxide to nitrate. The rate of conversion depends strongly on the atmospheric conditions. The temperature of the plume also drops as the cooler ambient air is entrained into it. The rate of entrainment depends on the turbulence and location of the boundary layer of the lower atmosphere. All of these effects increase the difficulty of accurately modeling the mixture of gases and particulates and their concentration downstream of the stack.

From an imaging perspective, the amount of sunlight scattered from a factory plume towards the sensor will depend on the type of particulate, its concentration, and its size distribution function. Most gas plumes scatter weakly due to the small particulate size. The type of scattering will generally be of the Rayleigh type. If a sufficient concentration of water droplets are present in the plume they will be the dominant source of scattering. An exception is when sulfates and flyash are present in the plume. These particles have diameters of 0.5 μm and larger and cause Mie scattering of visible light (White, 1981).

The detection and quantification of gases in the plume by remote sensing presents some unique problems. Many variables are involved in the formation of the plume that make the inverse problem of characterization difficult. Both active (LIDAR) and passive techniques have been investigated and developed. One of the most successful methods uses Fourier Transform Infrared Spectroscopy (FTIR). Much work has been done in this area of detection and quantification of molecules in plumes (Haus, 1994). Signal processing techniques are used to match the spectrum with known gas signatures that may exist in the plume. A plume analysis code was written for FTIR sensors and used to determine contrast SNR for a sensor on a satellite and airborne platform against different temperature plumes (Hilgeman, 1996). The types of gases, and their mixing ratios, can then be used to determine the products of the factory. While FTIR can provide spectral data, it does not provide any spatial data. However with the new generation of hyperspectral imaging sensors, the potential now exists to extract both spectral and spatial information from remotely sensed images of the plume. Spatial information would help give the physical dimension of the plume as well as provide mixing ratios of the gases as a function of position within the plume. In addition simultaneous measurements of background signature can be used to improve the SNR of the plume signature. Work is currently being done with the Thermal Infrared Imaging Spectrometer (TIRIS) for plume detection (Gat, 1997). This is a pushbroom system which operates from 7.5 - 14.0 μm in 64 spectral bands. Spectral resolution is 10 cm^{-1} at 10 μm .

The amount of gas released by a factory stack is usually measured as a release rate (lbs/hour or gms/sec) for each species. It is fairly straightforward to find the molar density from:

$$\text{molar density [moles/m}^3] = \frac{\text{release rate [gms/sec]}}{(\text{stack area [m}^2] \cdot \text{stack velocity [m/s]} \cdot \text{molecular weight [gms/mole]})} \quad (2-1)$$

The volume mixing ratio (VMR measured in parts per million) of the species is found by dividing the molar density by the normal volume of a perfect gas adjusted for the ambient temperature and pressure (.00224 m³/mole at STP). Once the molar density for each species is found, the molar ratio of the different species is defined as

$$\text{molar ratio}_{A/B} = \text{molar density of A} / \text{molar density of B.} \quad (2-2)$$

A hyperspectral image has the potential to yield the VMR of each species (and hence the molar mixing ratio) on a pixel-by-pixel basis (see Appendix E).

2.1.2 Cooling Tower Plumes

There is considerable interest in monitoring the power generated by both nuclear and fossil-fuel power plants. In the former case, non-proliferation treaties require detection of the possible production of material for nuclear weapons. The power generated is related to the waste heat released as a thermal plume from the cooling tower which contains heated ambient air as well as vaporized cooling water. The radiative properties of the plume may be detected and measured by remote sensors. The plume temperature and water droplet content will determine the amount of emitted thermal radiation. Studies of cooling tower plumes have been done by Argonnes National Lab (Carhart, 1981), DOE (O'Steen, 1995), and Los Alamos National Lab (Powers, 1995).

There are two main sources of water droplets in cooling tower plumes (Sauvageot, 1989). The circulation water of the condensers is cooled by evaporation and thermic transfer to the air and carried away by the natural or mechanical draft of the tower. When this water vapor mixes with the colder ambient air, recondensation occurs on small atmospheric nuclei present and water droplets are formed. This first type of droplet is called "recondensation" droplets and generally have diameters smaller than 20 μm. The exhaust emerging from the tower also contains small amounts of salts used to prevent algae growth on the side of the tower. These salts form larger nuclei for condensation and the resulting water droplets have sizes from 20 to 100 μm. This second type of droplets are called drift droplets. It was found that the number of recondensation droplets were ten times greater than the drift droplets. Thus, while the size distribution of the cooling tower plume is bimodal, the effects of the larger drift droplets can be ignored due to their relatively small number.

Typical plume temperatures are in the neighborhood of 300 K° (Carhart, 1991). From Planck's blackbody radiation model, the wavelength of peak emission is 9.66 μm. Thus in the MWIR and LWIR

bands, radiance from the plume will be dominated by thermal self emission. However, scattering from water droplets will also be considered. At visible wavelengths, scattering from water droplets and other plume constituents is the main source of radiance detected at the sensor. The emissivity of the plume depends on the liquid water content, which in turn depends on the size distribution of the water droplets. Droplet size distribution will also affect the scattering, absorption, and thermal self-emission from the plume.

2.2 Plume Modeling

Modeling plumes is a very complex process that involves hydrodynamic and turbulence flow theory. Since the aim of this research is to model the images of plumes and not the plumes themselves, only a brief description of plume modeling will be given. The two plume models described will be those used in DIRSIG.

2.2.1 JPL Plume Model

The first plume model is designed to model gas plumes released from a factory stack. It was originally developed by the EPA (Haugan, 1975), and has been modified by Kaman Corp and the Jet Propulsion Lab (henceforth called the JPL model). It is currently being maintained by RSA Systems. The JPL model is a Gaussian plume model based on the Brigg's equation for plume dynamics (Bennett, 1992, Halitsky, 1989). For a neutral atmosphere, the Brigg equation is commonly used to give the plume centerline height. It assumes a buoyant rise of the plume. The plume entrains ambient air at a rate proportional to its velocity and cross-sectional area relative to the surrounding area. For a neutrally buoyant effluent, the plume height is:

$$h = h_o + 3 \left(\frac{r_o m^2}{m + 3} \right)^{2/3} x^{1/3}, \quad (2-3)$$

where h_o is the stack height, r_o is the stack radius, x the downwind distance, and m the emission velocity ratio, defined as the vertical emission velocity divided by the wind velocity. A Gaussian distribution of the concentration of gases or aerosols from the plume centerline is assumed of the form:

$$C = \frac{Q}{2\pi\sigma_y\sigma_z\mu} \exp\left(-\frac{y^2}{2\sigma_y^2}\right) \left[\exp\left(-\frac{(z-h)^2}{2\sigma_z^2}\right) + \exp\left(-\frac{(z+h)^2}{2\sigma_z^2}\right) \right], \quad (2-4)$$

where x is the downwind distance, y is the lateral distance from the centerline, z is the vertical distance from the ground, Q is the source intensity (mass released per unit time), μ is the mean wind speed, h the plume centerline (from the Briggs equation), and σ_y (or σ_z) is the lateral (or vertical) coefficient of dispersion. The values for σ_y or σ_z must often be derived by fitting curves to empirical measurements.

The dilution factor at a particular position within the plume can be found by dividing the original stack concentration $C_o = Q/\pi r_o^2 w$ by C :

$$D = \frac{Q}{C\pi r_o^2 w} = \frac{2\sigma_y\sigma_z}{r_o^2 m} \exp\left(-\frac{y^2}{2\sigma_y^2}\right) \left[\exp\left(-\frac{(z-h)^2}{2\sigma_z^2}\right) + \exp\left(-\frac{(z+h)^2}{2\sigma_z^2}\right) \right], \quad (2-5)$$

where w is the vertical emission velocity and $m = w/\mu$. It should be noted that the Gaussian model in the lateral direction holds for all stability conditions, while the vertical distribution only holds for stable and neutral atmospheric conditions.

The JPL model calculates the initial conditions at the stack exit for several parameters including plume temperature and VMR. The dilution factor is then calculated downwind at any point within the plume using eqn. 2-5. The parameters of the plume at that point are then determined by multiplying the dilution factors with the initial parameters at the stack exit. The JPL model is designed for factory stack plumes containing multiple species. Inputs to the code include gas type and release rate, stack geometry, and meteorological conditions (including time-varying conditions). The outputs are downwind location, plume centerline height, and plume characteristics (dilution, temperature, and volume mixing ratio (VMR)). Chapter 3 gives a detailed description of the JPL code and its outputs.

2.2.2 LANL Plume Model

The second plume model used in DIRSIG was originally developed by Argonnes National Lab and University of Illinois (ANL/UI) and modified by Los Alamos National Labs (henceforth to be referred to as the LANL model). It is designed to simulate cooling tower plumes and uses an integral approach in which dispersion and plume rise take place simultaneously. A set of coupled ordinary non linear differential equations are solved to yield plume trajectory and properties. The model conserves fluxes of physical plume properties, while representing the dilution of the plume by entrainment of the surrounding ambient air. The differential equations are represented by the conservation of mass, horizontal and vertical momentum, enthalpy, and total water. This model treats the cross section of the plume as a whole and solves the governing equations using the local values for the wind speed, direction, and temperature gradient. Thus the plume is cylindrical in shape and its properties are uniform along a cross-section perpendicular to the plume axis. Also the increase in water droplet size due to condensation is tracked using classic cloud models (Liou, 1992). The initial plume temperature and droplet number density is specified by the user. The initial number density is determined as

$$N_o = \frac{\rho_a w_l}{\frac{4}{3}\pi\rho_l r^3}, \quad (2-6)$$

where ρ_a is the density of water in ambient air, w_l is the mass liquid water mixing ratio, ρ_l is the density of liquid water, and r is the initial droplet radius. w_l describes the amount of initial liquid water in the plume. The droplet radius will have a size distribution as described in appendix C. The outputs of the code are plume radius, temperature, water droplet size, and number density as a function of distance downwind from the tower. The number density downwind is determined as:

$$N = N_o \left(\frac{\Delta T}{\Delta T_o} \right) \quad (2-7)$$

where N_o and ΔT_o are the initial (stack) number density and temperature contrast, and ΔT is the temperature contrast at the downwind point. This determination of the number density is a change added by the author based on the dilution factor used in the JPL plume model. It was not part of the original code which did not expressly account for dilution effects. A detailed description of the LANL model is found in Carhart (1991) and Powers (1995).

2.3 Interaction of Light with the Plume

This section describes aspects of scattering, absorption, and emission theory as they pertain to modeling synthetic imagery of plumes. Multiple libraries have been written on these subjects. For the area of scattering theory, the classic is by Van de Hulst (1959). However, a more readable and updated form can be found in Bohren (1980). The same holds true for radiative transfer, where Chandrasekhar (1960) is the classic, but Liou (1980) and Goody (1989) present an updated version. Detailed derivations for Mie scattering and radiative transfer are included in Appendices A and D.

2.3.1 Gas Absorption

The different species in a gas plume absorb light at various wavelengths, depending on the electronic, vibrational, and rotational bands. The field of spectroscopy specifically considers how gases can be identified by their absorption "fingerprints." Since modeling of gas plumes requires knowledge of the absorption spectrum, this section will briefly touch on this process. For a more complete coverage of this topic and how it relates to remote sensing the reader is referred to texts by Stephens (1994), Goody (1989) and the Handbook of Geophysics and the Space Environment (1985).

There are three main properties that describe absorption by gas molecules: the central position of the line in the spectrum, the strength of the line, and the shape or profile of the line. In the visible region electronic transitions in individual atoms and molecules absorb the impinging electromagnetic wave. These electronic transitions are relatively quick (10^{-15} seconds). At longer infrared wavelengths, absorption is due mainly to transitions in the vibrational states of the molecules. These transitions have longer lifetimes

(10^{-12} seconds) and thus smaller transition energies. In the far infrared ($>20 \mu\text{m}$) and microwave region, rotational transitions are the dominant absorption processes. Vibrational transitions occur in polar molecules and the transition states are governed by quantum mechanics. Rotational transitions depend on the geometrical configuration of the molecules and orientation of the moment of inertia. Gases found in plumes can be characterized as linear (such as CO_2 , N_2O), symmetric top (NH_3 , CH_3Cl), spherical symmetric top (CH_4), and asymmetric top (water vapor). The type of configuration determines the location of the absorption spectra.

The actual absorption line shape is determined by several factors. The first is natural broadening which results in a band of transition levels due to quantum mechanical effects. This is a minor factor in gas plumes since frequent collisions between molecules shorten the natural lifetime in the excited state. These collisions contribute to pressure broadening of the line shape. The resulting shape is described by a Lorentzian function and the half-width is determined by the atmospheric pressure and temperature. The Doppler effect also broadens the absorption line. This profile is described by a Maxwellian distribution and again depends on atmospheric pressure and temperature. The importance of pressure vs. Doppler broadening is expressed as a ratio,

$$\frac{\alpha_D}{\alpha_L} \approx 10^{-12} \frac{\nu_o}{p} \quad (2-8)$$

where α_D and α_L are the half-widths of the Doppler and Lorentzian profiles, ν_o is the center frequency (in Hz), and p is the pressure in mbars. In the LWIR at $10 \mu\text{m}$ at a pressure of 1000 mbars, this ratio is 0.03 indicating that pressure broadening is the main factor in determining line shape.

The absorption coefficient $k_{\text{abs}}(\nu)$ is defined as,

$$k_{\text{abs}}(\nu) = S \cdot f(\nu - \nu_o) \text{ [m}^{-1}\text{]} \quad (2-9)$$

where S is the strength factor of the absorbing line (based on the transition probability) and f is the line shape function centered on ν_o . The transmission through a gas plume is found using the Beer-Lambert law (also known as the Bouguer law)

$$dE = k_{\text{ext}} E dz \quad [\text{W/m}^2], \quad (2-10)$$

where E is the irradiance, k_{ext} is the extinction coefficient, and dz a unit path length (the implicit dependence on wavelength has been omitted). When scattering is negligible (as in the case of gas plumes), then the extinction and scattering coefficient are the same. The exponential form for a homogeneous medium is

$$E = E_o e^{-k_{\text{ext}} z} \quad [\text{W/m}^2]. \quad (2-11)$$

The term $k_{ext} z$ is referred to as the optical thickness or optical depth, τ' . The transmission is the ratio of irradiance out to irradiance in:

$$\tau = \frac{E}{E_o} = \exp(-k_{ext} z) = \exp(-\tau'). \quad (2-12)$$

Databases for gases often measure transmittance in terms of absorbance

$$A = -\log_{10} \tau. \quad (2-13)$$

The absorbance is measured for a gas at a particular temperature and column density. The column density is the VMR of the gas multiplied by the path length of the gas and is expressed as ppm-m.

For a plume with a known VMR and temperature, k_{abs} is derived from the absorbance of a given database through

$$k_{abs} = \frac{A_{DB} \cdot VMR_p \cdot T_p}{\log_{10}(e) \cdot CD_{DB} \cdot T_{DB}}, \quad (2-14)$$

where A_{DB} , CD_{DB} , and T_{DB} are the absorbance, column density, and temperature from the gas database. VMR_p and T_p are the volume mixing ratio and temperature of the particular gas species in the plume. If there are multiple gas species, then the total absorption coefficient of the plume is the sum of the individual coefficients. If the column density of the plume is given, then the optical depth of the plume can be found from:

$$\tau' = \frac{CD_p \cdot T_p \cdot A_{DB}}{\log_{10}(e) \cdot CD_{DB} \cdot T_{DB}} \quad (2-15)$$

where CD_p is the column density of the plume.

2.3.2 Scattering

A plume scatters both sunlight and skylight. The amount and direction of scattering depends on the type of particle, its number density, and the size distribution. Since no active sources are considered, the incoming light is assumed to be broad band and unpolarized. Mie theory rigorously describes scattering of electromagnetic radiation from spherical particles (and several other shapes). Rayleigh scattering can be treated as an approximation of Mie scattering for particles that are small compared to the wavelength of light. Implicit in the scattering considered here is the assumption that the wavelength is not changed by the scattering: no Raman or non linear effects are considered. Also, the scattered light is incoherent, that is, there are no phase effects between the light scattered from multiple particles. Multiple scattering can have an important effect and approaches to its computation are addressed in section 2.3.5. Only particles that are homogenous and spherical are modeled in this research. It may be desirable in the future to model a coated

sphere, which may be the case if large aerosol nuclei undergo condensation and has an outer shell composed of water. Also, scattering from ice crystals in cirrus clouds can be modeled using cylindrical particles. Algorithms for Mie scattering from coated spheres and cylinders are found in Appendix B and C in Bohren (1983).

The general formulation is to start from Maxwell's equations with a spherical scatterer that has a different index of refraction from the surrounding medium. An electromagnetic field is generated inside the sphere and a scattered field will be induced outside the sphere. Boundary conditions are imposed so that the tangential components of the electric and magnetic fields are continuous across the interface between media. A scattering matrix in terms of the Stokes parameters for the incident and scattered light is expressed as:

$$\begin{pmatrix} I_s \\ Q_s \\ U_s \\ V_s \end{pmatrix} = \frac{1}{k^2 r^2} \begin{pmatrix} S_{11} & S_{12} & S_{13} & S_{14} \\ S_{21} & S_{22} & S_{23} & S_{24} \\ S_{31} & S_{32} & S_{33} & S_{34} \\ S_{41} & S_{42} & S_{43} & S_{44} \end{pmatrix} \begin{pmatrix} I_i \\ Q_i \\ U_i \\ V_i \end{pmatrix} \quad (2-16)$$

where I, Q, U, and V are the Stokes parameters, k the wavevector, and r the distance to the detector. The elements of the amplitude scattering (S_{11}, S_{12}, \dots) depend on the scattering angle. This scattering matrix is also known as a Mueller matrix. For a spherical particle, only the diagonal terms and S_{12}, S_{21}, S_{34} , and S_{43} are not zero due to the symmetry. Since the Stokes parameters of light scattered by a collection of randomly separated particles is the sum of the Stokes parameters of the individual particles, the scattering matrix for a collection of these particles is the sum of the individual scattering matrices. This assumes that the scattering is independent among the particles with no phase relationship between them. For unpolarized sunlight, the relationships for the Stokes parameters reduce to

$$E_s = \frac{1}{k^2 r^2} S_{11} E_i \quad Q_s = \frac{1}{k^2 r^2} S_{12} E_i \quad U_s = V_s = 0 \quad (2-17)$$

Note the notation for irradiance has been changed from I to E [W/m^2] for consistency with the DIRSIG notation.

Several terms encountered in scattering theory are relevant to scattering in a plume. The first is the particle size parameter:

$$x = ka = \frac{2\pi n_o a}{\lambda}, \quad (2-18)$$

where a is the radius of the particle and n_o is the medium index of refraction. For small values of x , the Rayleigh scattering approximation can be used. For larger values of x , geometrical optics approximations can be used (such as the case of the rainbow, see Chapter 5).

The scattering cross section C_{sca} is defined as the amount of energy scattered across the surface area of the particle by the incident irradiance. For a sphere, this is expressed as

$$C_{sca} = \frac{2\pi}{k^2} \sum_{n=1}^{\infty} (2n+1) (|a_n|^2 + |b_n|^2) \quad [\text{m}^2], \quad (2-19)$$

where a_n and b_n are scattering coefficients that depend on the relative index of refraction ratio of the sphere to the surrounding medium expressed through the Riccati-Bessel and Hankel functions. The convergence of the series is roughly proportional to the size parameter. Thus for larger particles, lengthy computation (and longer computer run-times) will be needed to find the cross-section. The extinction cross-section is similarly determined as:

$$C_{ext} = \frac{2\pi}{k^2} \sum_{n=1}^{\infty} (2n+1) \text{Re}\{a_n + b_n\} \quad [\text{m}^2], \quad (2-20)$$

The differential scattering cross section $dC_{sca}/d\Omega$ is the energy scattered per unit time into a unit solid angle about the scattering angle θ and azimuthal angle ϕ . The irradiance of the scattered light is related to the incident irradiance through the differential scattering cross section:

$$E_s = \frac{dC_{sca}}{d\Omega r^2} E_i \quad [\text{W}/\text{m}^2], \quad (2-21)$$

where r is the distance to the detector. For unpolarized light, the differential scattering cross section is expressed as:

$$\frac{dC_{sca}}{d\Omega} = \frac{S_{11}}{k^2} \quad [\text{m}^2/\text{sr}], \quad (2-22)$$

The angular scattering coefficient $\beta(\theta)$ is the amount of light scattered into the direction θ per unit solid angle per unit length of the scattering medium. It is defined as

$$\beta(\theta) = N \frac{dC_{sca}}{d\Omega} \quad [\text{m}^{-1}\text{sr}^{-1}], \quad (2-23)$$

where N is the number density of the medium.

The phase function is often used to describe the angular distribution of the scattered energy:

$$p = \frac{1}{C_{sca}} \frac{dC_{sca}}{d\Omega} \quad (2-24)$$

The asymmetry parameter g is the average cosine of the scattering angle and is defined as

$$g = \langle \cos \theta \rangle = \int_{4\pi} p \cos \theta d\Omega \quad (2-25)$$

When the scattering is isotropic, g is zero. If scattering is in the forward direction g is positive (with g equal to one for total forward scattering). Backscatter causes g to be negative, with $g = -1$ for total back scattering.

The scattering efficiency is the scattering cross section divided by the particle cross-sectional area. For a sphere this is

$$Q_{sca} = \frac{C_{sca}}{G} = \frac{C_{sca}}{\pi a^2} \quad (2-26)$$

The scattering diagrams for a spherical water droplet as a function of the incident wavelength are shown in Figure 2-1 and Figure 2-2. The plot was generated by a Mie scattering code described in Appendix A. Notice that when the size of the particle and wavelength of incident light are approximately equal, almost all of the scattering is in the forward direction, which is considered Mie scattering.

Particle Type: Water Droplet

Index of refraction: 1.33

Incident wavelength: .6328 microns

Droplet radius: .525 microns

Asymmetry parameter (g) = 0.828



Figure 2-1. Angular Scattering Distribution for a Water droplet in the Visible Wavelength

Particle Type: Water Droplet

Incident wavelength: 5.0 microns

Index of refraction: $1.321 + .0126i$

Droplet radius: .525 microns

Asymmetry parameter (g) = 0.0789

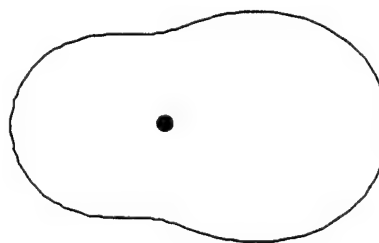


Figure 2-2. Angular Scattering Distribution for a Water Droplet in the MWIR

Scattered light can be highly polarized, especially at a scattering angle of 90°. However, current sensors modeled in DIRSIG are not differentially sensitive to polarized light, thus the polarization state of scattered light is not recorded (even though Mie scattering calculates the degree of polarization, see Appendix A). In addition, multiple scattering is dominant in plumes, in which case any effects due to polarization are averaged out.

2.3.3 Extinction

Closely related to the scattering parameters are the extinction parameters. Extinction is the rate of removal of electromagnetic energy along a path within the medium. Extinction is accounted by absorption (which transforms the electromagnetic energy into other forms) and scattering. In the case for gas plumes where scattering is negligible, then the extinction coefficient is equal to the absorption coefficient. When scattering is present, the extinction cross-section is defined as

$$C_{ext} = C_{abs} + C_{sca} \quad [m^2], \quad (2-27)$$

where the absorption cross section is defined as the rate of energy absorbed by the particle divided by the incident irradiance. The absorption and extinction efficiencies are defined similarly to the scattering efficiency

$$Q_{abs} = \frac{C_{abs}}{G} \quad Q_{ext} = \frac{C_{ext}}{G}, \quad (2-28)$$

where $G = \pi a^2$ for a sphere. For a small particle size parameter (Rayleigh conditions),

$$Q_{abs} = 4x \operatorname{Im} \left\{ \frac{m^2 - 1}{m^2 + 2} \right\}, \quad (2-29)$$

where m is the ratio of the index of refraction of particle to the surrounding medium.

The extinction, absorption, and scattering coefficients can be defined as the respective cross section multiplied by the particle density in the medium

$$k = N \cdot C \quad [m^{-1}] \quad (2-30)$$

$$k_{ext} = k_{abs} + k_{sca}.$$

For a distribution of particle size, k must be derived through

$$k = N \int C(a)n(a)da \quad (2-31)$$

where $n(a)$ is the normalized size distribution function. The water droplets in cooling tower plumes are found to follow a modified Gamma distribution (Sauvageot, 1989). Appendix C gives a detailed description on the particle size distributions used for this research.

The Beer-Lambert law (eqn. 2-12) is then used to determine the transmission. For a plume with multiple constituents, the transmission is expressed as

$$\tau = \exp\left(-\sum_i k_{\text{ext},i} z\right), \quad (2-32)$$

where the individual extinction coefficients for each constituents are now summed together.

2.3.4 Thermal Self-Emission

For a perfect Lambertian blackbody, the spectral radiance is described by Planck's equation

$$L_{\lambda BB}(T) = \frac{2hc^2}{\lambda^5 (e^{-hc/K\lambda T} - 1)} \quad [\text{W m}^{-2} \mu\text{m}^{-1}] \quad (2-33)$$

where h , c , K , and T are Planck's constant, the speed of light, Boltzmann's constant, and the temperature in degrees Kelvin, respectively. The emissivity of an object is a measure of how well it radiates compared to a perfect blackbody:

$$\varepsilon(\lambda) = \frac{L_{\lambda}(T)}{L_{\lambda BB}(T)} \quad (2-34)$$

Following Kirchoff's law (that a perfect particle emits all it absorbs), the emissivity can be defined as

$$\varepsilon = \alpha = 1 - e^{-K_{\text{abs}} z} \quad (2-35)$$

where α is the absorption of the medium. The assumption here is that the particle is in local thermodynamic equilibrium. The model for plume self-emission is based on Kirchoff's law and thus the self-emitted radiance depends on the absorption coefficient. This means that the plume strongly absorbs (low transmission) at the same wavelengths where it strongly emits. If all transmission losses are due to scattering, then there is no self-emission.

2.3.5 Radiative Transfer

Radiative transfer theory is often used to calculate the transport of solar flux and self-emission through the atmosphere. It is the basis for atmospheric transport codes such as MODTRAN. While it is out of the scope of this chapter to cover radiative transfer theory in detail, the applications for plume modeling will be touched upon briefly. Radiative transfer is applied to cloud models in calculating reflectance and

transmission values based on several cloud parameters. The main drawback in using radiative transfer is that it becomes mathematically difficult to solve unless simple geometries are assumed. That is why the plane-parallel atmosphere is often used. Unfortunately plume geometries do not readily lend themselves to this assumption. However radiative transfer can be used as an approximation at the expense of accuracy (and added complexity) if certain assumptions are made. This will be the case in DIRSIG when multiple scattering is present in the plume.

The single scattering albedo is defined as

$$\omega_o = \frac{C_{sca}}{C_{ext}}. \quad (2-36)$$

For cooling tower plumes in visible wavelengths, the single scattering albedo is unity, which indicates that extinction through the plume is due solely to scattering. When the droplet number density, and hence the optical depth, is high, then significant multiple scattering will occur. This means that the Beer-Lambert law may not be applicable for large optical depths if significant scattering is present. The suggested condition (Van de Hulst, 1957) for multiple scattering to occur is $\tau' > 0.3$. For $\tau' < 0.1$, single scattering prevails, while for $0.1 < \tau' < 0.3$ double scattering must be considered. Another estimate to see if multiple scattering is the dominant effect is to approximate the number of scatterings undergone by a photon in the plume before exiting. This is estimated using

$$\Delta = \frac{[\omega_o(1 - \tau)]^{n+1}}{[1 - \omega_o(1 - \tau)]}, \quad (2-37)$$

where Δ is the difference between the scattered radiance calculated with n-orders of scattering and all orders of scattering. For $\Delta = 1\%$, $\omega_o = 1$, and $\tau = 0.05$ (typical values for a cooling tower plume in visible light), $n = 130$. Thus the average photon will scatter 130 times in a dense cooling tower plume.

A study by the author was done to determine the importance of multiple scattering in the radiance reaching the sensor from a plume (see Appendix C for details). This was done by simulating a plume (using multiple layers) in MODTRAN and comparing the radiance reaching the sensor for single scattering and multiple scattering models. The results indicate that for an optical depth of three ($\tau = 0.05$), multiple scattered radiance is twenty times greater than single scattered radiance. The study also showed that for $\lambda > 2.5 \mu\text{m}$, scattered radiance becomes negligible compared to self-emissive radiance. This is due to the drop in solar irradiance in the IR bands. Thus multiple scattering needs to be considered for cooling tower plumes in the visible wavelengths.

There are several approaches to modeling multiple scattering. The first uses 3-D Monte Carlo methods. Here a large number of photons are followed through a cubic cloud as they undergo scattering from multiple particles (McKee, 1974). A more recent and realistic technique is the independent pixel

approximation (IPA). Fractal models are used to represent clouds. The radiation properties of each pixel is approximated by plane-parallel radiative transfer. The albedo of each pixel is based only on that particular pixel's optical depth, and is independent of the neighboring pixel. This way a full 3-D radiation calculation is replaced by an ensemble of plane-parallel calculations.

Another method developed from a computer graphics standpoint (Nishita, 1995) is to subdivide a fractal cloud into volume elements (voxels). An average scattering pattern based on the phase function is calculated (in matrix form) for the cloud. A viewing ray is then traced through the cloud. At each voxel the ray passes through, the scattering pattern is applied from all the neighboring voxels to obtain the intensity at that voxel. To simulate multiple scattering, this process is repeated for each neighboring voxel. Third-order scattering has been considered using this method.

The two preceding methods for multiple scattering are more advanced than using the plane parallel radiative transfer method. However, excessive complexity causes difficulty when integrating the routines into DIRSIG, not to mention the added computer run-times. As a result, the initial modeling of multiple scattering will use the plane parallel radiative transfer approach in the form of a parameterized two-stream model. Future advances in DIRSIG and plume and cloud modeling may wish to use these more advanced techniques (see Chapter 6).

The basic radiative transfer equation in a scattering atmosphere for diffuse radiance (L) is

$$\mu \frac{dL(\tau', \mu, \phi)}{d\tau'} = -L(\tau', \mu, \phi) + J(\tau', \mu, \phi) \quad (2-38)$$

where μ is the cosine of zenith solar angle, τ' the optical depth of the layer, and ϕ the azimuthal angle. Note that without the last term, the equation is similar to the Beer-Lambert law (exponential decrease in radiance through the layer based on optical depth). J is source term from within the layer:

$$\begin{aligned} J = & \frac{\omega_o}{4\pi} \int_0^{2\pi} \int_1^1 P(\mu, \phi; \mu', \phi') L(\tau', \mu', \phi') d\mu' d\phi' \\ & + \frac{1}{4} \omega_o P(\mu, \phi; \mu', \phi') \exp(-\tau'/\mu) E_s \\ & + [1 - \omega_o] B(T) \end{aligned} \quad (2-39)$$

where $P(\mu, \phi; \mu', \phi')$ is the scattering phase function for light incident at (μ', ϕ') and scattered in the direction (μ, ϕ) , E_s is the solar irradiance at the top of the layer, $B(T)$ the Planck blackbody function at temperature T of the layer. Figure 2-3 shows these terms.

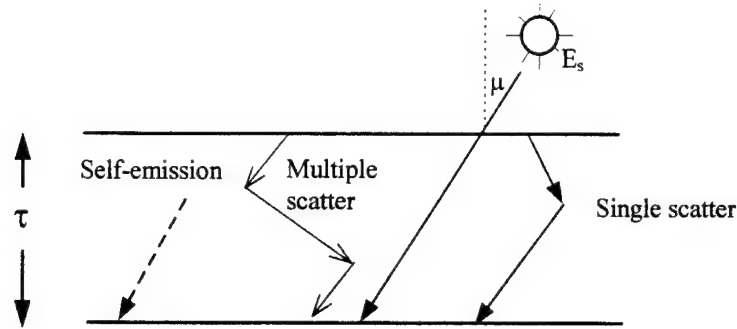


Figure 2-3. Source Terms for Radiative Transfer

The first term on the right hand side of eqn. (2-39) is the radiance contribution from multiple scattering, the second term is the contribution from single scattering, and the last term is the thermal self-emission from within the layer. For cooling tower plumes in visible wavelengths, the last term is negligible since $\omega_0 \approx 1$. The formal solution to eqn. (2-38) with multiple scattering is iterative since J is defined in terms of L . There are several techniques including the Gauss-Seidel iterative method, the layer-adding method, and the discrete ordinates method. If the primary interest is solving for the solar irradiance (calculating the reflectance and transmittance through the layers), then the two-stream approximation is used for solving the transfer equations. Since the sun will be the primary source of visible irradiance for plumes (remembering that solar irradiance, and hence multiple scattering, is negligible past the MWIR), a modified two-stream approximation will be used to account for multiple scattering in plumes.

A detail mathematical description of the parameterized two-stream approximation used in this research is shown in Appendix D. Only a brief qualitative description will be given here. Consider a flux stream (F_0) incident on a plane parallel uniform slab of cloud or plume (see Figure 2-4).

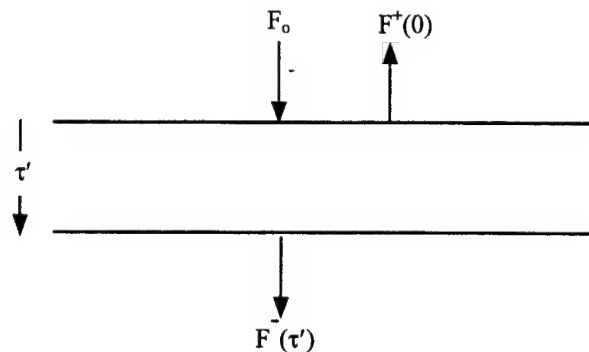


Figure 2-4. Flux Streams for Two-Stream Approximation

The flux stream emerges from the bottom of the layer after attenuation from absorption and scattering and is denoted by $F^-(\tau')$ where the $-$ indicates a downward traveling flux. There will also be an upward traveling flux stream $F^+(0)$ from the light scattered off the layer. These two streams describe the energy balance of the layer. One basic assumption made is that the flux distribution of the multiple scattering integral is fixed with increasing depth into the layer. Studies show (Twomey, 1980) that for large optical depths and single scattering albedos (as found in cooling tower plumes) the fine angular details in the scattering phase function (eqn. 2-24) are lost and the properties of the layer are controlled by several parameters. These parameters are the optical depth, single scattering albedo, and asymmetry parameter (τ' , ω_o , and g). This allows for simplifications in the solution of the resulting fluxes. Once solutions are obtained (see Appendix D), then the reflectance and transmission of the plume are defined as

$$R = \frac{F^+(0)}{F_o} \quad T = \frac{F^-(\tau')}{F_o} \quad (2-40)$$

There are several types of two-stream approximations. The main difference is how strong forward scattering is handled. The model used in this research uses the Delta-Eddington approximation designed for water clouds (Joseph, 1976 and Slingo, 1989). A Dirac delta function is used to approximate the strong forward scattering as often found in water droplet clouds ($g \approx 0.85$). The input parameters for the model are single scattering albedo, asymmetry parameter (both of which are derived from the Mie theory), and the optical depth and solar incident angle. The resulting diffuse reflectivity for direct incident (solar) radiation and diffuse incident radiation are calculated. The latter value can be used to determine the scattering of downwelled thermal and solar scattered radiance (skylight) as well as background thermal and reflected radiance. The diffuse transmission through the plume is also calculated for direct and diffuse incident radiation. These values will all be spectrally dependent since the scattering input parameters are spectrally dependent. As mentioned previously, the transmission for direct incident radiation with multiple scattering will not follow the Beer-Lambert law. Instead the transmission is calculated through

$$\tau = \exp[-(1 - \omega_o f)\tau'], \quad (2-41)$$

where f is the fraction of the scattered direct flux which emerges at angles close to the incident beam. This scattered light can be added back to the original unscattered light. In the two-stream Delta-Eddington approximation, f is expressed as

$$f = g^2. \quad (2-42)$$

If no scattering is present ($\omega_0 = 0$) or the scattering is isotropic ($f = 0$), then eqn. 2-41 is identical to the Beer-Lambert law. If the scattering is purely in the forward direction (and $\omega_0 = 0$), then there is no attenuation of the beam. This equation only holds for isotropic or forward scattering ($g \geq 0$).

One of the main drawbacks with this approach for multiple scattering is the assumption of infinite homogenous layers in the two-stream approximation, which obviously does not apply to plumes. The result will be extra scattering from the sides beyond the plume boundary, and thus the reflectivity will be overestimated. However, since forward scattering is dominant in water clouds, the leakage from the sides should be minimized. The Delta-Eddington model is most accurate for conservative scattering ($\omega_0 = 1$), large optical depths ($\tau' \geq 5$), and at small solar zenith angles ($\mu \geq 0.5$) (King, 1985). Again, cooling tower plumes generally satisfy the first two conditions, and the last one is satisfied by observing in the middle of the day. The model has been tested on marine stratocumulus and arctic clouds with the observed reflectivities differing less than 10% with the model predictions (Slingo, 1989). The comparisons were done only from 0.4 μm out to 4 μm , and thus represents another drawback to the model. However scattered radiance past this wavelength is negligible since the single scattering albedo for water droplets and the solar irradiance decreases in the IR.

2.4 Governing Equations for Remote Sensing of Plumes

As noted earlier, only passive sources will be considered when generating synthetic images of plumes. While the most dominant source is sunlight, other sources will have to be considered, particularly in the LWIR. These other sources include downwelled solar radiance (skylight), reflected radiance from the earth (earthshine) and other background objects, atmospheric thermal self-emission, and thermal self-emission from the earth. Other sources affect the radiance reaching the sensor that do not interact directly with the plume. The main component is upwelled atmospheric path radiance and sunlight scattered from the atmosphere towards the sensor. While these last two sources will not be covered here, they are considered in DIRSIG through MODTRAN calculations. The strength of each of these sources is very wavelength dependent, and this will have an important impact on the plume interactions. Figure 2-5 shows the comparison of the atmospheric transmission, solar irradiance, and thermal self emission from the earth.

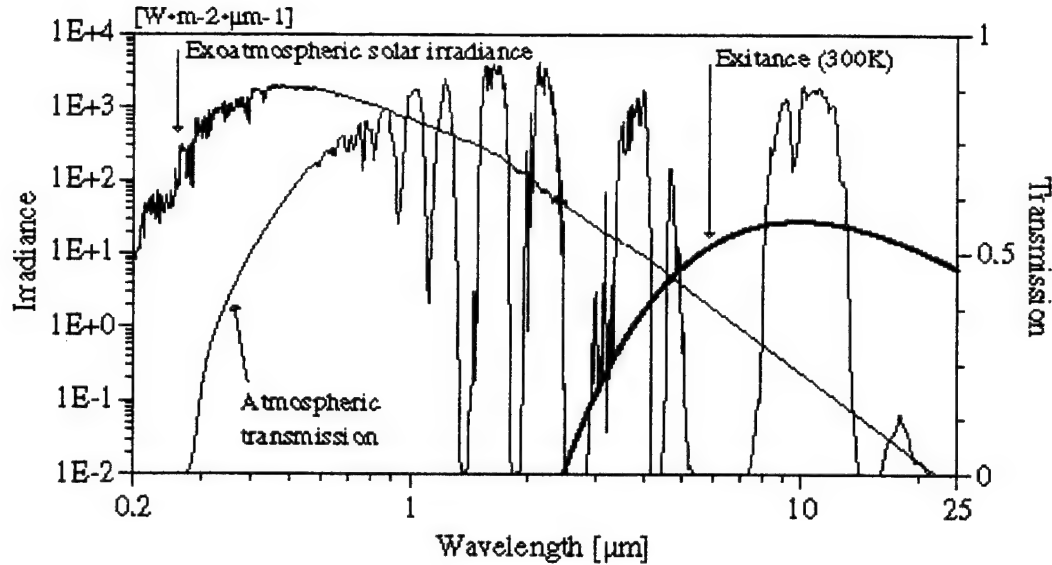


Figure 2-5. Atmospheric Transmission, Solar Irradiance, and Thermal Self Emission

In the visible and near-IR (NIR) regions, sunlight is the dominant source of photons. In the MWIR, both sunlight and self-emission are of the same order of magnitude, while in the LWIR the impact of solar irradiance is negligible.

2.4.1 Solar and Self-emissive Radiation Incident on the Plume

The solar spectral irradiance onto the plume can be expressed as

$$E_{S\lambda} = E'_{S\lambda} e^{-\tau'(\lambda) \sec \sigma} \quad [\text{W/m}^2], \quad (2-43)$$

where $E'_{S\lambda}$ is the exo-atmospheric irradiance, τ' is the optical depth of the intervening atmosphere, and σ is the solar declination (zenith) angle. This will be the only source of direct incident radiation.

The atmosphere also scatters sunlight onto the plume. This is referred to as downwelled solar scattered radiance (L_{DS}), or skylight. It is a function of both the azimuthal (ϕ) and zenith (σ) directions. MODTRAN is used to calculate the downwelled radiance at preset angular increments for ϕ (from 0° to 360°) and for σ (from 0° to 90°). Integration over the hemisphere will give the total downwelled radiance onto the plume. This will be considered a diffuse source of radiation. At low solar elevation angles, upwelled scattered sunlight from below the plume is possible. Since the atmosphere below the plume is assumed negligible, this contribution is ignored. There is also upwelled solar scattered radiance, L_{US} . This will not interact with the plume, but it will contribute to the final radiance at the sensor (usually as noise).

Direct sunlight is also diffusely reflected from the ground (earthshine):

$$L_{Er} = \frac{E_s r_E}{\pi} \quad [\text{W m}^{-2} \text{sr}^{-1}] \quad (2-44)$$

where r_E is the diffuse Lambertian reflectance of the ground. Note the wavelength dependent subscripts have been dropped for clarity. This will be another source of diffuse radiance onto the plume. While there are other solar sources such as reflected skylight from the ground, these will be ignored due to their insignificant contributions. These terms may be added in the future if there is the desire to account for all possible sources.

Thermal self-emission becomes a significant source of radiation in the MWIR and LWIR. All self-emissive sources are considered diffuse incident radiation. One such source is downwelled thermal self-emission from the atmosphere (L_{De}). Like solar downwelled radiance, it is directional in nature. MODTRAN also calculates downwelled emission at angular increments and upon integrating over the hemisphere the total atmospheric emission onto the plume is found. Upwelled emission from below the plume will be considered negligible. Upwelled self-emission from the intervening atmosphere between the plume and sensor (L_{Ue}) will contribute to radiance reaching the sensor.

There is also thermal emission from the earth and background L_{Ee} . The radiance is modeled using Planck's formula (eqn. 2-33). It is then multiplied by the emissivity of the object, usually defined as one minus the reflectivity. These values all are spectral in nature. Other minor sources such as atmospheric self-emission reflected from the earth onto the plume are considered negligible. Figure 2-6 shows the main sources of radiation onto the plume.

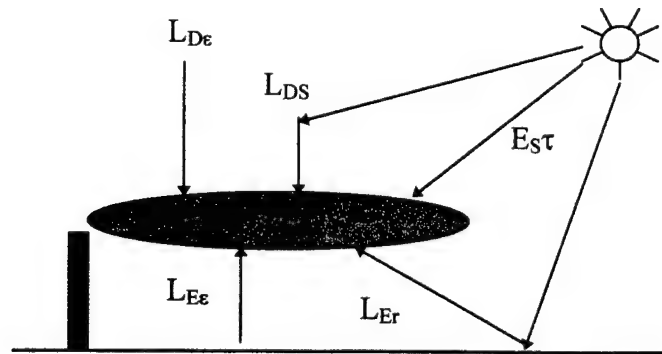


Figure 2-6. Sources of Radiation onto the Plume

2.4.2 Radiation from the Plume

There are two main sources of radiation from the plume reaching a sensor. The first is scattered radiance, which may be either single or multiple scattering. Single scattering occurs when the number

density is low, and thus there are only a few independent scattering centers (see section 2.3.5 for criteria of when single or multiple scattering occurs). Only direct solar irradiance is considered for single scattering. One reason for this is that scattering is only significant in the visible and NIR spectra where the predominant source is direct solar irradiance (see Appendix B). The other reason is that if enough scattering occurs for these other sources to make a significant contribution, then multiple scattering needs to be considered.

Each region of the plume has an associated angular scattering coefficient $\beta(\lambda, \theta)$ (eqn. 2-23). The element of scattered radiance to the sensor along the traversing sensor ray in that region is:

$$dL = E_s \beta(\theta) \tau_{p1}(l) \tau_{p2}(l) dl \quad [\text{W m}^{-2} \text{sr}^{-1}], \quad (2-45)$$

where θ is the scattering angle, τ_{p1} is the transmission along the path where the solar ray enters the plume to the point dl along the sensor ray, and τ_{p2} is the transmission along the path from dl to where the sensor ray exits the plume. Assuming that θ , τ_{p1} , τ_{p2} remain constant along the ray, the integral of eqn. 2-45 along the sensor path through the region becomes

$$L_{ps} = E_s \beta(\theta) \bar{\tau}_{p1} \bar{\tau}_{p2} l \quad [\text{W m}^{-2} \text{sr}^{-1}], \quad (2-46)$$

where $\bar{\tau}_{p1}$ is the transmission from the entrance of the solar ray to the mid-point of the sensor ray in that region and $\bar{\tau}_{p2}$ is the transmission from the mid-point to the point where the ray enters that region (see Figure 2-7).

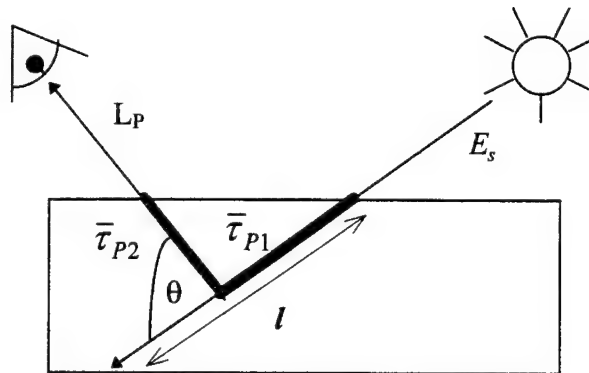


Figure 2-7. Scattering within the Plume

The assumption that the scattering angle remain constant over l can be made since the extent of the plume is small compared to the angular distance to the sensor and sun. The assumption that $\bar{\tau}_{p2}$, and $\bar{\tau}_{p1}$ remains constant over l can be made since for single scattering the optical depth must be small (< 0.3). Almost all cases of single scattering will occur only in single region plumes.

For multiple scattering, the two-stream approximation for radiative transfer will be used. As mentioned in section 2.3.5 there are several limitations to this approach, but it is a suitable first cut at modeling multiple scattering in plumes. The scattered radiance from direct solar irradiance is

$$L_{Ps} = E_S r_{dir} \pi^{-1} \text{ [W m}^{-2} \text{sr}^{-1}], \quad (2-47)$$

where r_{dir} is the diffuse reflectivity for direct incident radiation as calculated from the two-stream approximation (see Appendix D). For diffuse incident radiation, such as the integrated downwelled solar scattered or self-emission, the scattered radiance is

$$L_{Ps} = L_{dif} r_{dif} \text{ [W m}^{-2} \text{sr}^{-1}], \quad (2-48)$$

where r_{dif} is the diffuse reflectivity for diffuse incident radiation. Note that both reflectivities are dependent on the sun-plume-sensor geometry, in addition to the plume characteristics. The set-up of this geometry is described in detail in Chapter 3.

For gas absorption and single scattering plumes, the transmission is calculated using the Beer-Lambert law (eqn. 2-12). With a multiple scattering plume, the transmission from the two-stream approximation is used (eqn. 2-41). This accounts for forward scattered radiation that emerges in the same direction as the original radiation, and thus is added back in. There are three types of transmission values: the first is analogous to the Beer-Lambert law except for the forward scattering being considered. This is for direct transmission (τ_{DB}) of the direct incident solar radiation. The second is diffuse transmission (τ_{dir}) for direct incident radiation. This represents multiply scattered light emerging from the plume diffusely (i.e., not in the original direction of the incident radiation). The third is diffuse transmission (τ_{dif}) for diffuse incident radiation. This is similar to τ_{dir} except the incident radiation is diffuse. This type of transmission would be used to determine the amount of light scattered from downwelled skylight when looking up at the plume.

The plume will also radiate from thermal self-emission. The temperature of the plume determines the amount of blackbody radiation (L_{PBB}) from Planck's equation (2-33). The emissivity is determined from Kirchoff's equation (2-35). The product of the blackbody radiation and emissivity gives the amount of thermal self-emission. Note that the emissivity depends only on the absorption coefficient. If the plume's single scattering albedo is close to one, then there will be very little if any self-emission.

A term used to determine how visible the plume is against the background is the contrast ratio. This is defined as:

$$C = \frac{L_{Plume} - L_{Background}}{L_{Background}}, \quad (2-49)$$

where L_{plume} is the radiance reaching the sensor from a plume pixel, and $L_{\text{background}}$ is the radiance from a background pixel. The contrast ratio is used later on as a figure of merit when presenting the results in Chap. 4. Notice this is spatial in nature and all values are at the same wavelength. A spectral contrast ratio can be similarly defined where the background radiance is from the same pixel, but at a different wavelength.

2.4.3 Upward Looking Sensor

Consider a ground-based sensor looking up through a plume (Figure 2-8). In visible wavelengths, where scattering is the dominant process and thermal self-emission is negligible the following equation determines the radiance reaching the sensor (assuming multiple scattering and the sun is not in the field-of-view):

$$L = E_S \tau_{\text{Pdir}} \pi^{-1} + L_{\text{DS}} \tau_{\text{Pdif}} + L_{\text{DS}}(\phi, \theta) \tau_{\text{PDB}} \quad [\text{W m}^{-2} \text{sr}^{-1}]. \quad (2-50)$$

The first term is the multiply scattered light from direct solar illumination, the second is the multiply scattered light from the integrated skylight, and the final term is the angular downwelled skylight behind the plume at the azimuth and elevation at which the sensor is looking at (this may be direct sunlight if the sensor is looking up at the sun). Any effects from the atmosphere under the plume is ignored. Thus no transmission losses, scattered light, or self-emission is accounted for from this region. The second term will be omitted in DIRSIG, since it causes an overestimation of the radiance. This is because τ_{dif} becomes unity for smaller optical depths. Thus if there is no plume, all integrated downwelled radiance would be transmitted for that ray, which is not realistic. Further studies will have to be done on how to model diffusely scattered skylight through the plume. This is important since plumes are still visible on a cloudy day.

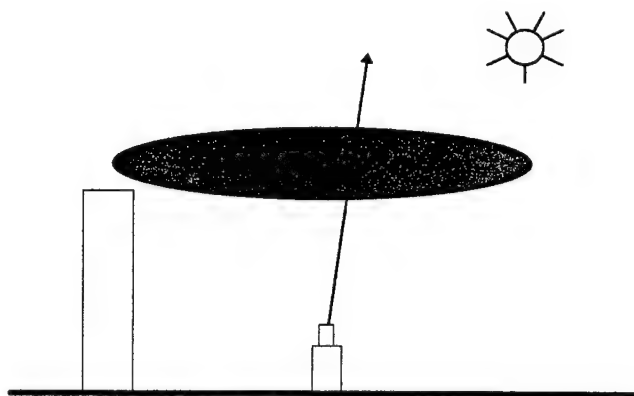


Figure 2-8. Upward Looking Sensor

In the LWIR where self-emission is dominant and scattering is negligible, the radiance reaching the sensor is:

$$L = \epsilon_p L_{PBB} + L_{DE}(\phi, \theta) \tau_p \text{ [W m}^{-2}\text{sr}^{-1}\text{]}. \quad (2-51)$$

The first term is the plume self-emission and the second term is angular downwelled atmospheric self-emission. The plume transmission is based on the Beer-Lambert Law where attenuation is due solely to absorption and $\epsilon = 1 - \tau$. In the MWIR where scattering and self-emission may both be present, the governing equation is:

$$L = E_S \tau_{Pdir} \pi^{-1} + L_{DS} \tau_{Pdif} + L_{DS}(\phi, \theta) \tau_{PDB} + \epsilon_p L_{PBB} + L_{DE}(\phi, \theta) \tau_{PDB} + L_{DE} \tau_{Pdif} \text{ [W m}^{-2}\text{sr}^{-1}\text{]}, \quad (2-52)$$

where the last term is the scattered downwelled atmospheric self-emission.

2.4.4 Downward Looking Sensor

An airborne or satellite sensor looking down will have additional radiance sources from the intervening atmosphere. Figure 2-9 shows the geometry for a downward-looking sensor.

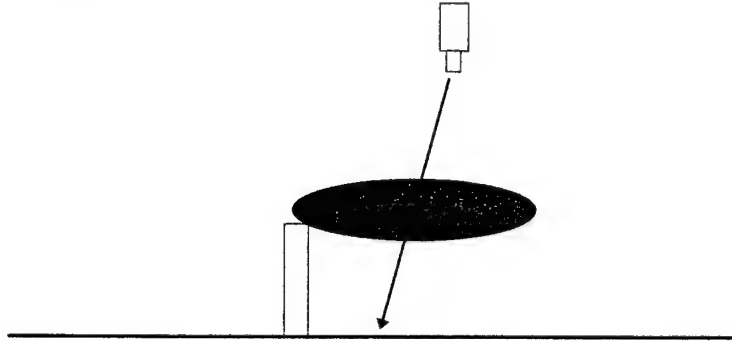


Figure 2-9. Downward Looking Sensor

In the visible region the radiance reaching the sensor is:

$$L = E_S \pi^{-1} r_E \tau_{PDB} \tau_{atm} + E_S \pi^{-1} r_{dir} \tau_{atm} + L_{DS} r_{dif} \tau_{atm} + L_{US} \text{ [W m}^{-2}\text{sr}^{-1}\text{]}, \quad (2-53)$$

where the first term is the reflected sunlight off the background pixel, the second is the scattered sunlight from the plume, the third is the scattered skylight from the plume, and the final term is the upwelled solar scattered radiance. Again the atmosphere under the plume is considered negligible. Also any reflection of the plume off the background is also considered negligible. In the LWIR, the radiance is:

$$L = (1 - r_E) L_{E\mathcal{E}} \tau_P \tau_{atm} + \epsilon_p L_{PBB} \tau_{atm} + L_{DE} r_{dif} \tau_{atm} + L_{U\mathcal{E}} \text{ [W m}^{-2}\text{sr}^{-1}\text{]}. \quad (2-54)$$

The first term is the earth's thermal self emission, the second is the plume's self-emission, the third is the scattered downwelled atmospheric self-emission, and the last term is the upwelled radiance from the atmosphere. In the MWIR the radiance is:

$$L = E_S \pi^{-1} r_E \tau_{PDB} \tau_{atm} + E_S \pi^{-1} r_{dir} \tau_{atm} + L_{DS} r_{dif} \tau_{atm} + L_{US} +$$

$$(1 - r_E) L_E \epsilon \tau_{PDB} \tau_{atm} + \epsilon_P L_{PBB} \tau_{atm} + L_D \epsilon r_{dif} \tau_{atm} + L_{UE} \quad [\text{W m}^{-2} \text{sr}^{-1}]. \quad (2-55)$$

The reflected downwelled thermal and solar scattered radiance from the background, as well as diffuse scattering from the background, are considered negligible.

3. Modeling and Algorithm Development

3.1 Introduction

This chapter describes how the various computer algorithms are used to build the plume models. A description is given for each piece of code and how it works. Examples of the input and output files used are given in Appendix H. The actual source code listings are not included due to their size (and will most likely be modified in the future).

There are several steps involved in running the plume model in DIRSIG. These vary depending on the type of model being run. For the LANL and JPL ACAD model, several pre-processing steps need to be done before actually running DIRSIG. Figure 3-1 is a block diagram which shows the procedure involved.

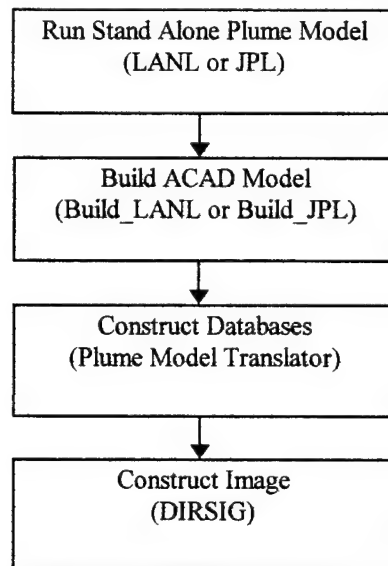


Figure 3-1. Process Flow in Building Plume Scene

Each step requires input files and also produces several output files for the next step. In the integrated JPL plume model, the first two steps are omitted and DIRSIG directly calls the plume model. Each of the following sections will describe these steps in detail and describe how to run the code. This is specifically written so a software engineer can understand the code so as to make further improvements and modifications. As such this chapter will read very much like documentation for a piece of software (the reader is forewarned).

3.2 LANL Plume Model

The LANL plume model is designed to model cooling tower plumes. As mentioned in section 2.2.2, this is an integral model that solves a set of coupled non-linear differential equations. The output of

the code is then converted into an ACAD model for use in DIRSIG. The output is also used by the Plume Model Translator to create the necessary databases. The only constituent in these plumes is water droplets. The effects of water vapor are not accounted for, although DIRSIG has the capability to handle both water droplets and water vapor in plumes. The LANL code has been modified by the author from the original code developed at LANL, which in turn is a modified version of a program written by ANL/UI. As such this is a third-generation piece of software, and it is still undergoing development. The LANL plume code is written in IDL. To build the ACAD model, a separate program called Build_LANL is run. This produces a output file for ACAD as well as the files necessary to generate the databases. This code was written by the author in the C/C++ language.

3.2.1 Running the LANL Plume Model

The LANL Plume model is an interactive code. It is run in IDL by typing "anl" at the prompt. It is composed of several different routines, with the bulk of the code contained in anl.pro. The listing of the code has been omitted due to its size and in keeping with the policy of only listing code directly written by the author. There are numerous input parameters to the code that are intended to be entered interactively, but they can be hardcoded into anl.pro if desired. The parameters can be grouped into four categories: 1) plume adjustment parameters, 2) plume characteristic parameters, 3) meteorological conditions, and 4) tower geometry. Table 3-1 shows what falls under each of these categories.

Plume adjustment	Plume characteristics	Meteorological	Tower geometry
stop time (s)	plume release temp. (K°)	wind speed (m/s)	tower height (m)
time step (s)	release velocity (m/s)	ambient temperature (K°)	tower radius(m)
data dump interval (s)	mass liquid H ₂ O mixing ratio	ambient pressure (mbar)	
	size distribution (μ and α)	relative humidity (%)	

Table 3-1. Input Parameters for LANL Plume Model

The "stop time" parameter determines how far out to model the plume. The number of seconds entered multiplied by the wind speed will give the distance of the plume. The "time step" determines the accuracy of the model, with the tradeoff that a smaller time step leads to improved accuracy but longer run times. The "data dump interval" gives the time interval for the data output. This interval, when multiplied by the wind speed, will give the length of each plume region. This parameter also determines the total number of plume regions.

The "plume characteristics" describe the cooling tower plume itself. The "mass liquid H₂O mixing ratio" describes the initial amount of liquid water in the plume. The ratio is usually given in grams of liquid water per gram of moist air. This factor will determine the initial water droplet number density in the plume according to eqn. 2-6. The size distribution of the water droplets follows a modified Gamma

distribution (see Appendix C). The mean droplet radius size (μ) and halfwidth (α) determine the shape of the distribution. The shape of the plume in terms of its radius and height are determined by the meteorological conditions. These conditions will also determine the rate of droplet growth due to condensation. Only the recondensation droplets are tracked in the current model. The tower height and radius are self-explanatory. The tower height can be set to zero and later adjusted in ACAD. Note that no wind direction is specified. The plume is always extending in the positive x direction (north). The plume can be rotated when inserted into the ACAD scene.

The code will calculate the plume parameters at every time step. At the specified data dump intervals, the following information is output to the file "anl.out":

- horizontal plume position (m)
- vertical plume position (m)
- temperature (K)
- plume radius (m)
- mean droplet radius (μm)
- droplet number density (cm^{-3})

This information is repeated at every dump interval until the stop time is reached. Each region is evenly spaced along the plume axis with the length determined by the dump interval times the wind velocity. The number of regions is determined by the stop time divided by the dump interval time. This number is printed out at the beginning of "anl.out." The spatial resolution of the plume can be increased by reducing the data dump interval (at the usual expense of computation time). Since the plume is assumed to have a uniform cross-sectional distribution, the plume properties are constant out to the specified plume radius. The droplet radius will increase due to condensation of water vapor onto the aerosol nuclei. The LANL model not only tracks the change in the droplet size, but also the half-width of the distribution (α). However α currently is assumed to be constant throughout the plume.

3.2.2 Building the LANL ACAD Model

Once the "anl.out" file is produced, the next step is to build the ACAD model and the plume description file. This is done through the Build_LANL program which creates two files. An ACAD dxf file geometrically describes the plume and is inserted into an ACAD scene. Build_LANL also creates the plume description file that give the temperature, droplet size, and number density of each region. Build_LANL is a single program written by the author and the code listing is included in Appendix J. It is run by typing "build_lanl." The only additional prompt will be to indicate what the material number will be for the first region (with following regions having sequential material numbers). The "anl.out" file is read in automatically. Figure 3-2 shows the input and output files for Build_JPL.

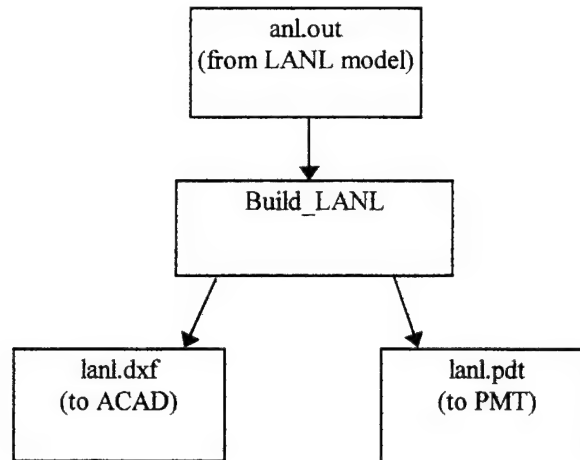


Figure 3-2. I/O Flow for Build_LANL

Once the characteristics for each plume region is read, the ACAD file is built. A plume centerline is formed by connecting the x-z points for each region in "anl.out.". The plume is composed of cylindrical regions with endpoints at each region coordinate. The radius of the cylinder is the average of the plume radius at each endpoint. The cylinders will usually be tilted at an angle since the plume centerline is generally rising. 16 evenly spaced facets form the cylindrical region. The radius of each region, along with the plume centerline, is used to determine the actual x, y, z, points for these facets. A coordinate transform is done from plume space into ACAD space. Between each region are 16 triangular facets that resembles a pizza. This is done so the DIRSIG ray tracer can recognize when it enters a different region. Once the points for all the regions are connected together the "lanl.dxf" file is written out. When imported into ACAD, a facetized model of the plume results. This is shown in Figure 3-3.

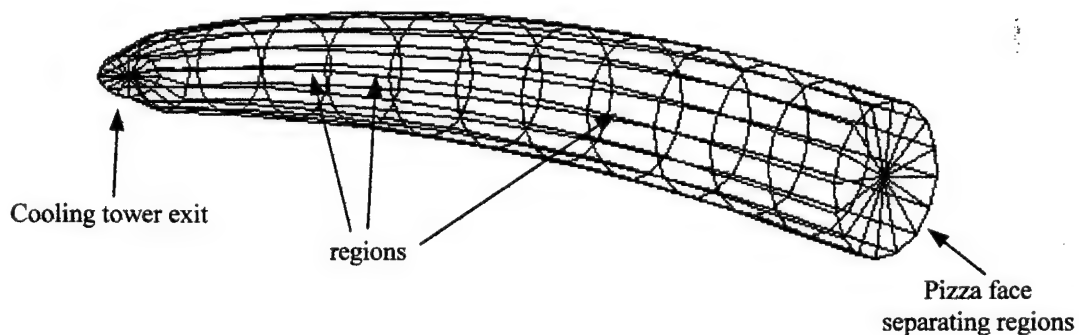


Figure 3-3. ACAD LANL Plume Model

The pizza facets between each region have been omitted for clarity. The total number of facets can be roughly determined by the number of regions multiplied by 48. The temperature of each region is automatically assigned to the facet when it is written out to the dxf file. The plume description file,

"lanl.pdt," is also written which contains the region number, temperature, droplet size, and number density. The current limits for Build_LANL are:

Maximum number of regions: 30

Number of facets on a circle: 16

These numbers are arbitrary and can be increased if necessary.

3.3 JPL Plume Model

The JPL plume model is designed to model gas plumes released from factory stacks. The effluents contained in the plume are determined by the user, and multiple effluents are possible. While not designed to model cooling tower plumes, water droplets can be specified as a plume constituent. There are several versions of the model. The first version is the stand alone model as delivered in the original form. The second version is specially modified to produce output for the "Build_JPL" program described below. The final version is designed to be directly called as a function in DIRSIG. The first two versions will be described in this section and the last will be described in the DIRSIG section below. Both the JPL plume model and Build_JPL programs are written in the C/C++ language.

3.3.1 Running the JPL Plume Model

The version received from JPL, and now being maintained by RSA Systems, originally had several bugs and produced no output. It was modified by the author and updated by RSA Systems to produce the current version. Thus like the LANL code, the JPL code is also third-generation. It is likely to be further refined in the future. It should not be difficult to modify for use with DIRSIG since most of the changes made were in the input and output functions.

The JPL plume model is run from the command prompt. It is not interactive, but rather reads in input files. The first (stand-alone) version is run by typing "jpl_model" while the second (ACAD) version is run by typing "jpl_acad_model." The integrated version is called directly by DIRSIG. All three versions use the same input file "Plume_Input."; a listing of this file is given in Appendix H. Numerous parameters can be adjusted in this file. They can also be grouped into four categories: 1) plume adjustment parameters, 2) plume characteristic parameters, 3) scene meteorological parameters, and 4) scene geometry parameters. Table 3-2 shows the parameters in each categories.

Plume adjustment	Plume initial conditions	Scene meteorological	Scene geometry
dilution minimum	species type	wind direction (deg)	stack height (m)
dilution change	release rate (lbs/hr)	wind speed (knots)	stack diameter (m)
sampling step size	plume release temp. (F°)	atm. Stability number	stack location x,y,z (m)
contrast contribution	release velocity (m/s)		target point x,y,z (m)
number planes modeled			sensor point x,y,z (m)
sampling time interval			

Table 3-2. Input Parameters for JPL Plume Model

The “plume adjustment” parameters govern the shape and characteristics of the plume. For example, decreasing the “dilution change” parameter will increase the dilution factor. Increasing the number of plume planes will increase the length of the plume downwind. The sampling step size is given as a fraction of the stack diameter. These parameters can be adjusted so as to match the plume model with any available experimental data.

The “plume initial conditions” parameters determine the initial conditions of the plumes. Multiple species type and their individual release rate can be specified. The molecular weight of each species is also needed. The release rate, release velocity, and stack diameter will impact the downwind VMR and column density.

The “scene meteorological” parameters determine the meteorological conditions at the stack. This can be described either through time-varying conditions or as a time-averaged condition. If the time-averaged parameters are used, a plume with constant shape results. If time-varying conditions are used by specifying a meteorological file, then the user must supply the parameters as they vary over time. The format for the meteorological file is given in Appendix H. This filename is specified in the “Plume_Input” file. By using time-varying parameters, the plume can be given some texture and made to “puff.” The wind speed controls how much the plume is bent over. The atmospheric stability number determines how quickly the plume disperses; the lower the number the lower the dilution downwind. The ambient temperature is not specified in the input file. but in the file “KamanStub.C.”

The scene geometry parameters determine how the plume is to be sampled. The orientation of the scene is shown in Figure 3-4.

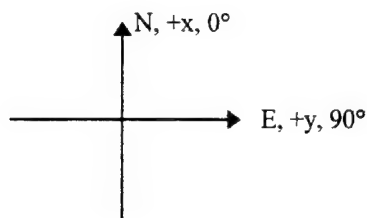


Figure 3-4. Scene Coordinates for JPL Plume Model

If the wind direction is specified as out of the north (0°), then the plume will blow in the negative-x direction. Note that the y axis is inverted with respect to the DIRSIG/ACAD orientation. In that case, east (90°) is the negative-y direction. The units can be specified as either meters or feet, but should match the DIRSIG scene units.

In the "jpl_model," a series of sensor and target (x,y,z) points are specified. A ray is traced between these two positions and the average plume temperature and column density for each species are reported. Any position can be specified, but if the ray does not intersect the plume nothing will be returned. This is essentially the same routine used when integrated into DIRSIG. In "jpl_acad_model" a preset number of points are run. Instead of specifying the sensor and target points, the user inputs the number of points to be sampled along the plume centerline and the interval of the points. At the appropriate downwind intervals, the target point is located directly beneath the centerline of the plume and the sensor point over it. Along the ray going through the plume the dilution factor, temperature contrast, and VMR at each point are recorded. The number of points determined is based on several plume adjustment parameters. Thus the plume is "sliced open" at certain downwind intervals and its characteristics recorded along the vertical axis through its center. These values are recorded in the "jpl.dat" file to build the ACAD model. The code is written so that the plume moves in the positive y-axis (i.e., the wind must blow from the west at 270°).

3.3.2 Building the JPL ACAD Model

The next step is to create the ACAD model and the plume description file. Once the "jpl.dat" file is created from the JPL plume model, the Build_JPL program is run using this file. This program creates two files: The first is an ACAD dxf file which describes the multiple plume regions and which is ready to be inserted into an ACAD scene. Build_JPL also creates the plume description file ("jpl.pdt") that gives the temperature, species type, and VMR of each region. An input file is needed to describe how each region is to be built. Build_JPL is a single program written by the author and the code listing is included in Appendix J. The command to run it is "build_jpl". All files are read and no interaction with the user is necessary. Figure 3-5 shows the I/O flow for Build_JPL.

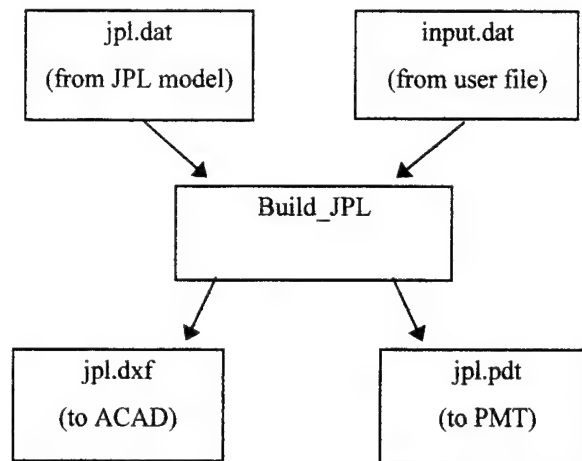


Figure 3-5. I/O Flow for Build_JPL

The first file read is called "input.dat" and describes the number of regions to be created, the maximum dilution factor to be used, the fraction of the maximum dilution each region will contain, and the material number for each region. This is created by the user and the format for this file is given in Appendix H. The number of regions is up to the user, with the tradeoff that more regions results in greater resolution in dilution steps, temperature, and VMR, and thus a more realistic plume model. However, increasing the number of regions increases the number of facets to be modeled and results in a slower run-time. Three to four regions is usually a good choice. The maximum dilution is specified by the user based on examination of the "jpl.dat" file. Usually this dilution will be the maximum dilution in the first plume slice. However, if the slice is within 5 m of the stack exit, the code may not make an accurate prediction and the dilution may be greater than one (which is physically impossible). In this case the maximum dilution of the next slice should be used. For each region, the fraction of the maximum dilution and material number must be entered. This fraction determines the maximum size of the region. Thus if the maximum dilution is unity, and the step size is 0.25, the radius of the specified region will extend to the location where the dilution is 0.25. The first region specified is the outermost region, and thus will have the lowest fraction. Succeeding regions will have progressively higher fractions with the last innermost region having the highest fraction. While the fractions can have identical step increments, this is not recommended since the plume is Gaussian and thus the dilution does not drop off linearly. The user will have to determine what the appropriate step size is depending on the conditions to be modeled. The material number assigned to each region must correspond to what is specified in the material file.

The "jpl.dat" file is read in to determine the stack radius and temperature, the ambient temperature, the number of plume slices, and the interval of the slices. Then the altitude, dilution factor, temperature

contrast, and VMR for each species in each slice is read in. Each slice may contain anywhere from 5 to 30 of these points, depending on how the JPL model was run. This represents a cross-sectional slice through the plume. The centerline of the plume is determined by connecting the location of the maximum dilution point for each slice.

For each slice the radius of each region is determined starting with the outermost. Using the fraction of the maximum dilution specified by the input file, the matching dilution along the cross-section is found. An interpolation between two points is made if necessary. The corresponding location of this point is then determined and subtracted from the centerline position to determine the radius for this slice. In addition, the temperature contrast and VMR are recorded at this position. This process is repeated for each region until the innermost region of that slice is reached. Note that the temperature contrast and VMR will be the same for each region in each slice since the same dilution fraction is used to determine the region characteristics. Also note that these characteristics are specified at the edge of each region. If the local maximum dilution in a particular slice has dropped below that specified for a region, then that region will not be created in that slice. That way all the regions will be present in a slice near the stack exit. Further downwind of the stack where the plume has been diluted, fewer regions will be needed until only a single region is used to represent the last slice of the plume. Figure 3-6 shows the side view of a slice with two regions.

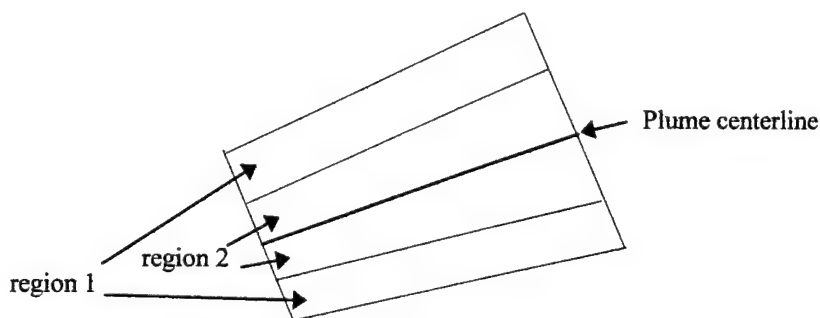


Figure 3-6. Side View of Single Slice in ACAD Model

The plume is assumed to be circular and represented by 16 evenly spaced facets. The radius of each region for each slice and the plume centerline are used to determine the actual (x, y, z) points for these facets. A coordinate transformation is performed from plume space to ACAD space. Each slice is centered about the downwind distance specified in the "jpl.dat" file. Thus if the distance is 30 m downwind, and the slice interval is 10 m, the slice will extend from 25 to 35 m. The last slice is designed so as to converge to a single point so that the plume does not abruptly end.

Once the points for all the regions and slices are connected together the "jpl_plume.dxf" file is written out. When imported into ACAD a facetized model of the plume results. This is shown in Figure 3-7.

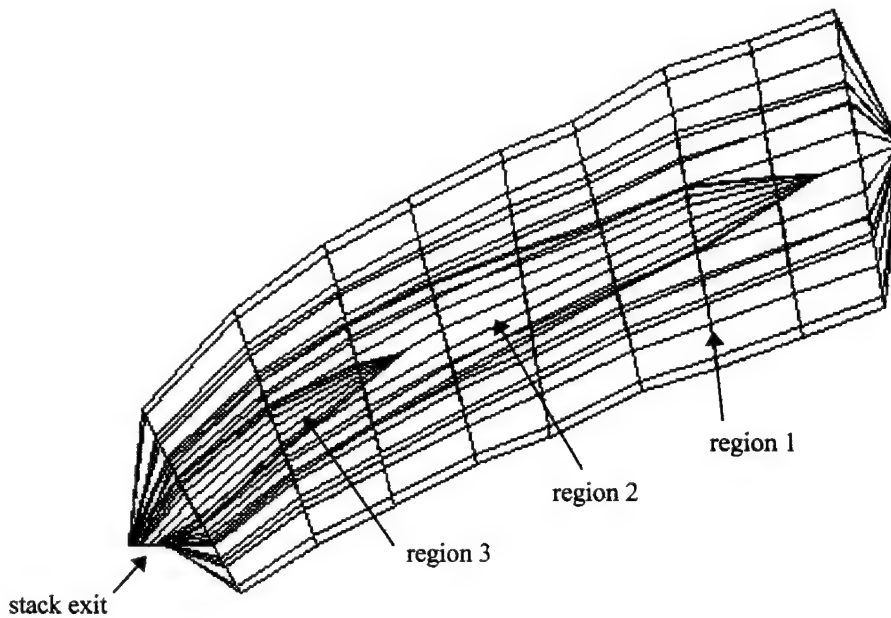


Figure 3-7. ACAD JPL Plume Model with Three Regions

The total number of facets can be determined roughly by multiplying the number of regions in each slice by 16, remembering that not all slices have the same number of regions. The temperature of each region is automatically assigned to the facet when it is written to the dxf file. The plume description file "jpl.pdt" is also written which contains the region number, temperature, species type, and VMR. If the meteorological file is used in the "Plume_Input" file, then the resulting plume will wander and have more shape and texture. Figure 3-8 shows the "wander" model.

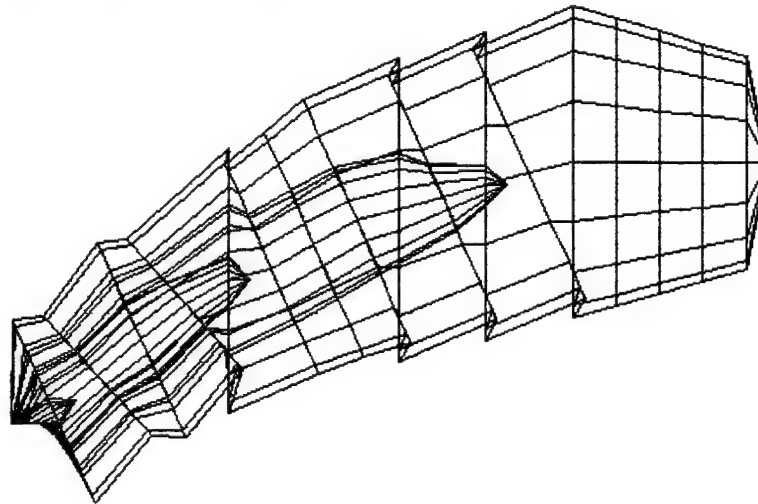


Figure 3-8. ACAD JPL "Wander" Plume Model

The current limits for Build_JPL are:

Maximum number of regions: 10

Maximum number of slices: 30

Maximum number of samples in each slice: 100

Maximum number of species: 6

Number of facets on a circle: 16

These numbers are arbitrary and can be increased if necessary. Also any region that has a radius less than 0.1 m in a particular slice is omitted.

3.4 Plume Model Translator

The plume model translator (PMT) is designed to take the PDT file generated by Build_LANL or Build_JPL and create the necessary database files needed in DIRSIG. The PMT is interactive (it prompts for user inputs) and requires several input files. Examples of all the files are given in Appendix H. Figure 3-9 on the following page shows the I/O and flow for the PMT.

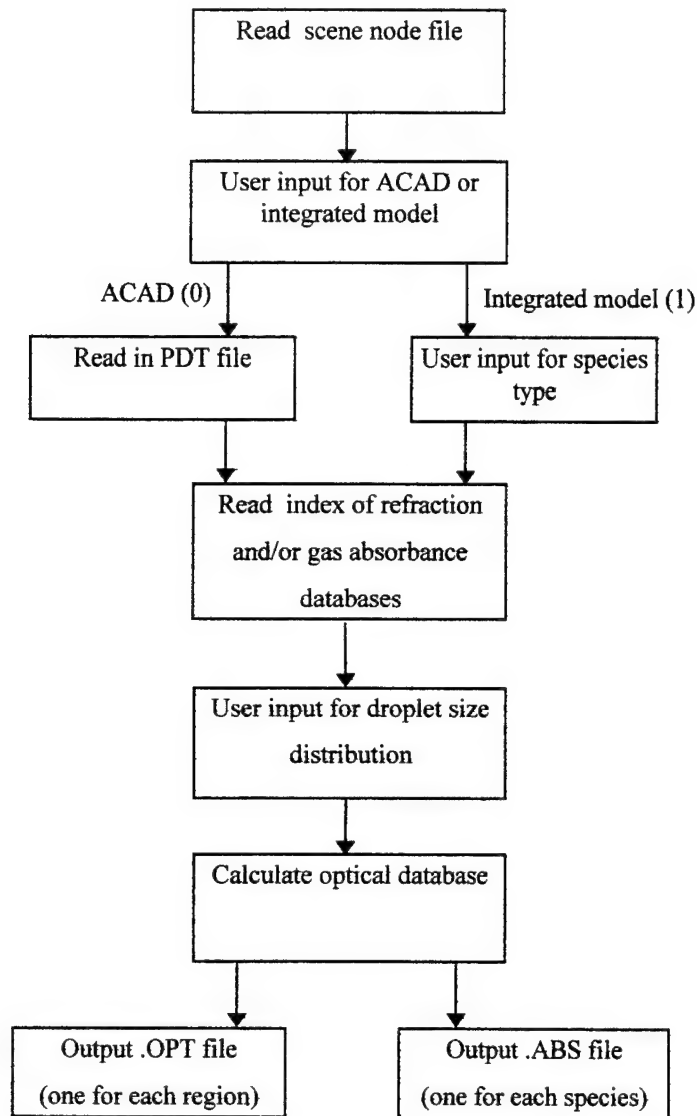


Figure 3-9. Flowchart for PMT Code

The scene node file used should be identical to that actually used in DIRSIG. This will determine the bandpasses from which the databases will be generated. The type of file produced is then determined from the user input. If the ACAD plume model is used, then the PDT file is read in. This gives the number of plume regions and the temperature, species type, number density or VMR, and particle radius (if applicable) for each region. The current database and assigned species number consists of:

water droplet = 1
 NO_2 = 2
 CH_4 = 3
 CH_3Cl = 4
 SO_2 = 5

$C_2HCl_3 = 6$

$SF_6 = 7$

water vapor = 8

Additional databases can be easily added using the procedure in Appendix G. If the integrated JPL model is used then the user specifies the species.

The next step is to read the database. The minimum and maximum frequencies of the database are checked against the requested bandpasses. If the frequencies are exceeded, the user is notified of the frequency limitations and the program terminates. Most of the gas databases have a range from 600 to 4500 cm^{-1} (2.2 - 16.6 μm). If the species type is water droplets, then the real and imaginary parts of the index of refraction are read in for the appropriate frequencies. For gases, the absorbance, column density, and temperature are read in from the database. The smeared-line model is used where an interpolation is done over the frequency interval specified in the scene node file. This assumption is valid only if the spacing between the spectral lines is less than the linewidths themselves (Penner, 1959). While this may not be the case for all gases, this assumption is used. This may result in an underestimation of the absorption if the spectral lines do not overlap. The smeared line model also holds if the concentration is weak enough so that the optical depth is less than one.

If water droplets are present, the size distribution must be determined. The user is prompted for the following choices of size distribution types:

Lognormal = 1

Modified Gamma for LANL model = 2

Modified Gamma for MODTRAN fog model = 3

None (Dirac delta function) = 4

The detailed description and illustration of these distributions are given in Appendix C. The user then enters the size distribution parameters (σ , α , etc.) depending on the distribution chosen. If the LANL plume model is used, then the modified gamma distribution should be used with the same alpha (α) as used in the plume model. Based on these parameters and the mean radius, 100 radius bin are determined. The bins are logarithmically spaced, and the probability density value is calculated for each bin radius from the distribution function. The integrated value over the probability density function must be unity. This way the size distribution function is normalized to 1 particle/ cm^3 . The minimum and maximum radius bins are determined at the point where the probability density value is .001 of the maximum value.

The PMT then determines the optical coefficients for each region at each bandpass frequency. In the case of water droplets, the Mie scattering code is called. The input parameters are the index of refraction, incident wavelength, and particle radius. Using the Mie scattering theory described in Appendix A the extinction, absorption, scattering, and differential angular scattering cross-sections, and the asymmetry parameter are returned. The angular scattering cross-sections are determined at 10° increments. If there is a size distribution indicated then the Mie scattering code is called for each radius bin. The

returned values (extinction, absorption, etc.) for each radius are multiplied by the probability density at that radius. These weighted values are then integrated over the 100 radius bins to determine the representative values for that particular size distribution. If no size distribution is chosen, then the values for the mean radius are returned. The cross-sections are then multiplied by the number density for that region to determine the corresponding coefficients. The single scattering albedo is calculated by taking the ratio of the scattering coefficient to the extinction coefficient. This entire procedure is repeated for each frequency in the bandpass.

If the species type is a gas, then the absorbance tables are used. The particular gas absorbance value for the specified frequency is read from the database. The VMR of the region is adjusted by the ratio of the region temperature to the database temperature. The absorption coefficient is then calculated based on eqn. 2-14. Since scattering is assumed to be negligible in gases, the scattering coefficient is set to zero and the extinction coefficient is set equal to the absorption coefficient. If multiple species are present (either several gases or water droplets and gases), then the individual coefficients are summed to determine the coefficient for the region.

If the user indicated that the integrated JPL model is used, then gas absorbance database is read for the selected species number. Instead of determining the absorption coefficient, the absorbance value, column density, and temperature are recorded. This is repeated for each species type.

The database file is created next. For the ACAD model, a file is created for each region labeled "region1.opt", "region2.opt", etc. These files can be renamed. When the material entry is created in the material database for a plume region, the filenames need to be assigned to the extinction file variable. There are two database formats: single scattering and multiple scattering/gas absorption. In the first format, the optical coefficients (scattering, absorption, and extinction) are given for each frequency specified in the scene node file. In addition, the angular scattering coefficients are given for each frequency in 10° increments from 0° to 180° (a total of 19 entries). In the second format, the asymmetry parameter and the single scattering albedo are given instead of the angular scattering coefficients. For a gas plume these values default to zero. For the integrated JPL model, a file is produced for each species labeled "gas1.abs", "gas2.abs", etc. The first file should correspond to the species first listed in the "Plume_Input" file (see section 3.3.1), the second file to the second species, etc. This file lists the gas code, the column density and temperature from the gas database, and the absorbance values corresponding to the bandpasses listed in the scene node file.

3.5 DIRSIG

The equations described in section 2.4 are utilized by DIRSIG to construct a plume image for a scene as viewed by a particular sensor. A comprehensive discussion of DIRSIG can be found in the DIRSIG report (Schott, 1993). Only some highlights of DIRSIG will be covered here.

The following is a basic description of how DIRSIG works without plumes in the scene. The scene is constructed using ACAD to produce wire-frame objects. Faceted elements are assigned material attributes that contain optical and thermal properties. The ACAD scene is used with a ray tracer model. A sensor location is defined within the geometry. A ray is traced into the scene from each pixel in the sensor. In this way, the sensor-ground instantaneous field-of-view (GIFOV) is overlaid on the scene. When a facet is encountered within a pixel GIFOV, several calculations are made. The first determines the thermal self-emission from the facet that would be transmitted back to the sensor. Secondly, if the target is diffuse (Lambertian assumption), the radiance reflected from that facet due to downwelled skylight and atmospheric emission is determined. For specular facets, the ray is reflected to determine whether the sun, sky, or another background object is hit. Atmospheric transmission, self-emission, and scattered sunlight are determined through MODTRAN. A radiance database is generated before the DIRSIG run. The database is then accessed for each ray-trace to determine values like transmission and atmospheric path radiance along the sensor to facet path.

DIRSIG handles plumes in several ways. The first is to determine if the plume is represented in the geometric database (GDB) if created through ACAD, or if the integral JPL plume model is used. Depending on the plume constituent and model used, either the optical database (.OPT) or gas absorbance database (.ABS) is read. If the scattering is present, then either the single or multiple scattering model is selected. Currently, multiple plumes can be present only through the GDB file, and not the integrated JPL model. The following sections describe how DIRSIG is initialized, how it handles GDB plumes with distinct regions and their optical properties (single scattering, absorption, and emission), how it handles multiple scattering, the integrated JPL model, and other special cases.

3.5.1 Initializing DIRSIG

Before the actual ray tracing, DIRSIG must perform several preparatory actions (it is assumed that the user is familiar with running the DIRSIG program). The first is to create the batch file for executing DIRSIG. The following changes have been added to the original batch file. The directory of the optical or absorbance files must be specified. The environmental variable is called "DIRSIG_OPTICAL." Also several additional flags have been added. The "-j" flag indicates that the integrated JPL plume model will be run. The "-p" flag will disable the plume debug image creation. Once executed, DIRSIG first reads the scene node (SND) file. If the sensor location in the z (vertical) axis is zero, then a ground-based upward looking sensor is assumed and the appropriate flag is set. The GDB file is read next followed by the material file. In the material file a plume region is specified by designating the optical_description variable as "NON_UNIFORM_TRANSMISSION." The associated database filename is listed through the extinction_file variable. Note that this is done only for plumes specified in the GDB file.

Whenever a plume region is encountered in reading the material file, the associated optical database file for that region also is read. The type of file (multiple scattering/gas absorption or single scattering) is determined by the scattering type number (0 or 1). Each region will have its own scattering type, so that multiple plumes can have different scattering types. However, multiple regions within a single plume must all have the same scattering type. To determine if the region actually has scattering properties, the scattering coefficient is checked for each frequency. If all coefficients are zero, then a gas plume is present and no scattering routine is implemented. When reading in the optical database, the bandpasses are checked to ensure that they match those listed in the SND file. After all plume optical files are read, the number of plume regions is reported.

If the integrated JPL plume model is used (with the -j flag), then no plume regions are listed in the material file. It is assumed that the number and type of gases present in the "Plume_Input" file match the number of "gas#.abs" files in the "DIRSIG_OPTICAL" directory. If the first gas listed in "Plume_Input" is SF₆, then "gas1.abs" is the SF₆ database file created by the PMT. DIRSIG will automatically read in all the files with the name "gas#.abs" in the "DIRSIG_OPTICAL" directory. The number of gas files read in is then reported.

The plume values (transmission, radiance, etc.) are recorded for each ray trace. These values form a plume debug image (with the same image size as main DIRSIG radiance image). Plume debug images are automatically created unless the -p flag is set. The type of debug images created are dependent on the type of plume modeled. Table 3-3 lists the type of debug images for the ACAD plumes and Table 3-4 lists the debug images for the integrated JPL model.

Single scattering	Multiple scattering
Transmission for each region*	Transmission for entire plume*
Transmission for entire plume*	Total radiance from plume*
Path length traversed in each region	Emissivity of plume*
Scattered Radiance from each region*	Path length traversed in plume
Total radiance from plume*	Reflectivity of plume*
Emissivity of plume*	
Scattering angle	(* indicates image created for each bandpass)

Table 3-3. Plume Debug Images for ACAD Models

Column density
Temperature
Plume transmission *
Plume radaiance (self-emissive) *

Table 3-4. Plume Debug Images for Integrated JPL Model

These images are created in a directory with the DIRSIG base filename for the radiance image plus the appendix “_dir.” Thus if the DIRSIG image is called “plume_image,” then the directory name is “plume_image_dir.” This directory must be created by the user before DIRSIG is run. Since several debug images are created for each region for each bandpass, there may be quite a few large files produced if the plume debug image option is not turned off. The user needs to be aware of this, especially if disk space is scarce.

3.5.2 Ray-tracing through Plume Regions

For a sensor looking down on the plume a ray is cast out towards the ground. If a plume region is encountered the ray tracer determines how many regions it passes. If multiple regions exists, then several calculations are done as the ray enters each new region (or re-enters a region on the way out of the plume). In Figure 3-10, a simple three-region rectangular plume is encountered. The ray-tracer records a total of five distinct regions traversed by the ray.

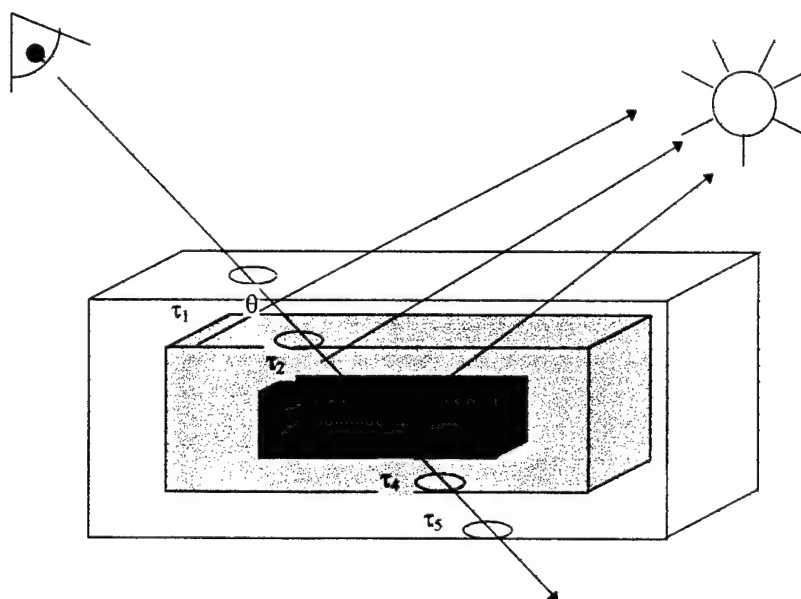


Figure 3-10. Ray Tracing Through Rectangular Plume Model

The distance the ray tracer traverses in each region is used to determine the transmission using eqn. 2-12 and the optical database for that region. The emissivity and self-emitted radiance are also calculated using the database and eqn. 2-35 and 2-33. If the single scattering model is being used for this plume, then a ray is traced from the mid-point of the region to the sun to determine the scattering angle θ as well as the transmission from that mid point to the exit point of the plume. Eqn. 2-46 is then used to determine the single scattered radiance from that region.

The set of calculations for transmission, emission, and single scattered radiance is repeated for each region. These calculations are also done spectrally for all the bandpasses. The total transmission through the entire plume is the product of the individual transmissions:

$$\tau_p = \tau_1 \tau_2 \tau_3 \tau_4 \tau_5, \quad (3-1)$$

where $\tau_{\#}$ is the transmission through each region (see Figure 3-10). The attenuation of self-emissive and scattered radiance by the intervening regions is also accounted for:

$$L_p = L_1 + L_2 \tau_1 + L_3 \tau_1 \tau_2 + L_4 \tau_1 \tau_2 \tau_3 + L_5 \tau_1 \tau_2^2 \tau_3 \quad [\text{W m}^{-2} \text{sr}^{-1}], \quad (3-2)$$

where $L_{\#}$ is the radiance from each region and L_p is the total radiance leaving the plume. Once the ray leaves the plume, it continues on through the rest of the DIRSIG interactions. This same process also takes place for secondary ray-traces from the ground to the sky. In this manner, the plume will cast a shadow on the ground. Notice that no diffuse radiation (i.e., skylight) is scattered in the single scattering model. There are two reasons for this: to keep the code computationally manageable and for small optical depths the amount scattered from diffuse sources is negligible compared to that from direct solar radiation.

3.5.3 Multiple Scattering

The multiple scattering model will be used when the plume optical file has a scattering type = 0 and the scattering coefficient > 0. While multiple region plumes can be used with this model, it is "cleaner" if the ray encounters only one region. The same process as described above is used with the exception that the single scattered radiance is not calculated. Once the ray exits the plume, the two-stream radiative transfer algorithm is used (see section 2.3.5 and Appendix D). The single scattering albedo and asymmetry parameter are determined from the weighted average in the individual regions based on their optical depths. The total optical depth is determined by the total plume transmission and inverting eqn. 2-12. The incident zenith solar angle is determined by the angle between the ray from the sun and that normal to the ground (+z direction). In this way, the radiative transfer layers are always perpendicular to the ground. This assumption may not hold for tilting plumes, large solar zenith angles (i.e., when the sun is near the horizon), or for side-looking plumes.

Once these input parameters are determined, then the two-stream algorithm is called for each wavelength. The resulting diffuse reflectivity for direct incident (solar) radiation r_{dir} and diffuse incident radiation r_{dif} are returned. The diffuse transmission through the plume is also calculated for direct and diffuse incident radiation, τ_{dir} and τ_{dif} , as well as the transmittance for a direct beam, τ_{DB} . For a downward-looking sensor, the scattered light from direct solar irradiance and the integrated atmospheric downwelled (both scattered and thermal) radiance is determined through eqn. 2-47 and 2-48, respectively. The downwelled radiance is integrated over the hemisphere above the plume. τ_{DB} is used as the transmission through the plume for radiance from the target background. The diffusely scattered radiation from beneath the plume (the earth background) is considered negligible and not calculated. Figure 3-11 shows how the reflectivities and transmissivities from the two-stream approximation are used for the downward looking sensor.

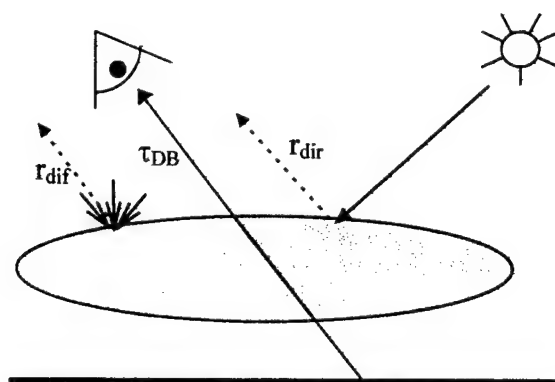


Figure 3-11. Multiple Scattering Sources for Downward Looking Sensor

For an upward-looking sensor, radiation will be scattered through the plume down to the sensor. τ_{dir} is used to determine the solar radiation that is diffusely scattered (eqn 2-50). τ_{DB} is used for the plume transmission to determine the attenuation of radiation directly behind the plume along the ray-trace. Recall scattered diffuse radiation (using τ_{dif}) is omitted due to unrealistic physical results. Scattering from any earth radiation sources is considered negligible. Figure 3-12 shows how the transmissivities from the two-stream approximation are used for an upward-looking sensor.

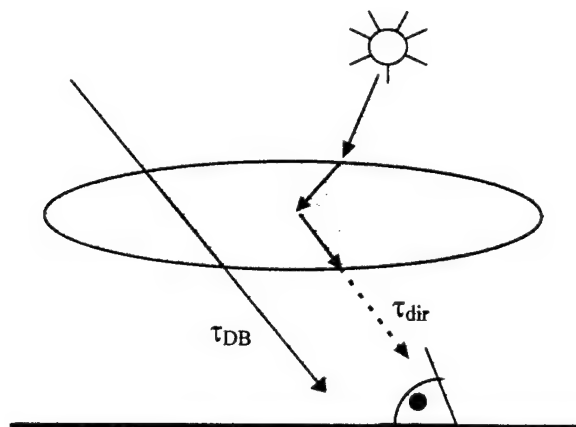


Figure 3-12. Multiple Scattering Sources for Upward Looking Sensor

3.5.4 Integrated JPL Plume Model

Running the integrated JPL plume model for gas plumes is less cumbersome than using the ACAD models. None of the Build_JPL routines need be done and the only ACAD scene required is that of the background. The "Plume_Input" described in section 3.3.1 needs to be prepared, as well as a meteorological file if time-varying conditions are desired. The PMT code is run to produce the necessary ABS files. The order of the ABS files (gas1.abs, gas2.abs, etc.) must be the same as the order of gases specified in the "Plume_Input" file. Once these steps are completed, DIRSIG can be run.

The integrated model is run with the -j flag. For every ray trace in the scene, the JPL model is called. The location of the sensor and the target hit point are recorded and passed to the JPL model. If the trace is to the sky, the target point is determined by the product of the direction vector and a large distance. The JPL model then determines if the plume is hit by the ray based on the parameters in the "Plume_Input" file. A bounding volume check for the plume is made for the ray to save compute time. If it is determined that the ray intersects the plumes, then the column density and temperature along that ray are calculated. The column density is found by integrating the VMR for each distance increment along the ray. The temperature is the average along the ray. The column density and temperature, along with the number of species present, are returned to DIRSIG.

DIRSIG checks to see if the returned temperature is greater than zero. If so, the plume is present for that ray trace. The ratio of the returned column density and temperature to the corresponding database values is used to determine the optical depth through eqn. 2-15. If there are more than one species, then the individual optical depths are summed together. The Beer-Lambert law is used to determine the transmission through the plume at that point. The emissivity is taken as one minus the transmission, and the plume self-emission is the emissivity times the Planck blackbody radiance at the plume temperature.

No scattering is assumed for gas plumes. The self-emitted radiance and plume transmission are then used to determine the radiance reaching the sensor.

The integrated model presents several benefits over the other methods. The most obvious is not having to construct the ACAD model. This makes running the plume scene quicker and less complicated. Also the effect of changes in the plume characteristics is studied more easily. The plume adjustment parameters (Table 3-2) can be varied to determine the appearance and shape of the plume. The main disadvantage is the inability to model scattering processes. Also, there is a limited ability to give the plume texture, other than to vary the meteorological conditions. Only one plume at a time can be modeled. The JPL code can be considerably streamlined to improve run times, as it is inefficient in its current form. For example, the "Plume_Input" file is unnecessarily re-read for every ray trace. The choice of the sampling step size parameter may cause aliasing effects in the plume image. This can usually be avoided by reducing the step size, but at a cost of increased run time.

3.5.5 Other Special Cases

A few other cases that DIRSIG can model should be mentioned. Multiple ACAD plumes are allowed as long as none overlap in either two or three dimensions (i.e., one plume is behind another). This limitation is due to the ray-tracer and should be corrected in the future. The plumes can be a combination of single scattering, multiple scattering, or absorption only. Thus plumes can contain both water droplets and water vapor. The ACAD plume and the integrated JPL plume can not be run simultaneously. Also there can not be two simultaneous integrated JPL DIRSIG runs in the same directory since they both will use the same "Plume_Input" file (unless that is desired).

4. Results

This chapter will present the results of this research. Different DIRSIG scenes of plumes are generated and the images and numerical results are displayed. There are many variables involved when creating a plume in DIRSIG, and thus only a few will be adjusted to illustrate their effects on the image. This research is intended to provide a tool for studying remote sensing of plumes. As such, the aim of these results is to demonstrate how sensitivity studies can be done, but is not meant to be comprehensive. It should also be remembered that any model can always be improved, and often evolves over time. Thus the results presented here are a snapshot of the DIRSIG plume code as it stands at the time of this writing. It is likely that errors (bugs) in the code will be found in the future and that improvements will be added to the model. The results presented here will have to be redone to either revalidate or invalidate them.

This chapter has two main sections. The first is on absorption/emission and gas plumes. The second is on scattering effects and cooling tower plumes. A comparison of the radiance from the plume and the background, as well as the interaction between the two is presented. The effects of change in the plume properties also are presented. Validation of the DIRSIG plumes are presented in the next chapter. The unit for radiance in all graphs is given in $\mu\text{Watts/cm}^2\text{-sr}^{-1}\text{-}\mu\text{m}^{-1}$ (or $\mu\text{Watts/cm}^2\text{-sr}^{-1}$ if integrated over a spectral band). The images presented are auto-scaled over 255 gray levels. If comparisons are made between different images, the same gain and bias will be used. The appearance of the image can be greatly affected by the type of gain and bias applied to it. Also, subtle features may be lost due to the limiting resolution of the printer.

4.1 Gas Plumes

4.1.1 JPL ACAD Model

The JPL plume model with three nested regions is used to create an image of a gas plume (see Figure 3-7). The gas concentrations for the three regions are artificially set to illustrate the differences between the regions. Region 3 has the highest concentration and temperature, and is embedded in the center of regions 1 and 2. Region 2 is in turn embedded in region 1. Methyl chloride (CH_3Cl) is selected as the constituent due to its strong absorption peaks at 3.5 and 10 μm , both of which lie within the atmospheric transmission windows. A hyperspectral sensor with 10 cm^{-1} resolution is used to image the plume from an airborne platform (1.2 km altitude) and also from a ground-based platform. The images are run at 3.33 μm (3000 cm^{-1}) and 10 μm (1000 cm^{-1}) at a 128x128 pixel resolution. Table 4-1 shows the properties of each region in the gas plume.

Region No.	Temperature (K)	VMR (ppm)	Extinction Coefficient (m^{-1}) MWIR (3.33 μm) / LWIR (10 μm)
1	293	100	$5.02 \times 10^{-2} / 2.42 \times 10^{-3}$
2	308	300	$1.51 \times 10^{-2} / 7.27 \times 10^{-3}$
3	323	500	$2.51 \times 10^{-3} / 1.21 \times 10^{-3}$

Table 4-1. Methyl Chloride Plume Properties

Note that the absorption of methyl chloride is twice as strong in the MWIR as in the LWIR. To simplify the runs, the background is composed of a grass background (emissivity ≈ 0.98) and a 18% reflectance gray card (both at 288 K°). The ambient air temperature is 280 K°. Figure 4-1 shows these four images. The length of the plume is approximately 85 m with the height varying from 50 to 80 m.

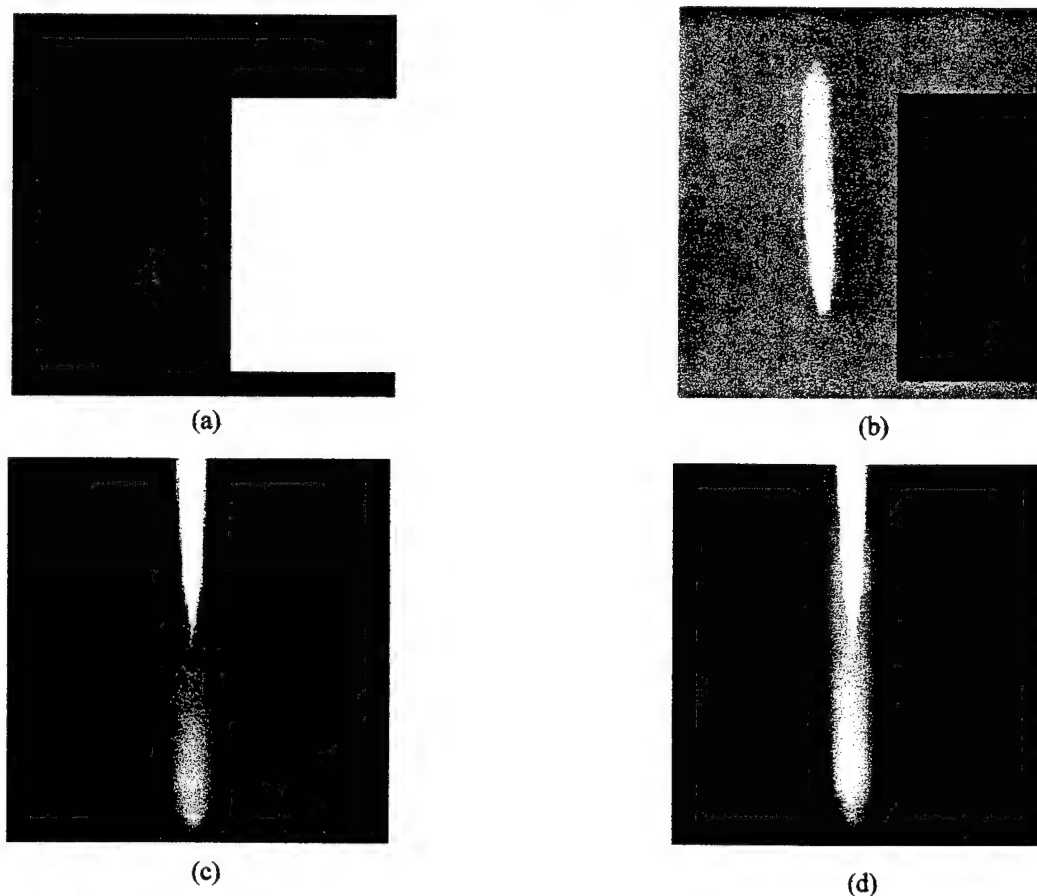


Figure 4-1. Hyperspectral images of CH_3Cl plume from an airborne sensor at 3.33 μm (a) and 10 μm (b) and a ground based sensor at 3.33 μm (c) and 10 μm (d)

The plume shadow is faintly visible on the gray card in the MWIR airborne image (Figure 4-1a). Due to its reflectivity, the card is the most radiant object and therefore appears white, while the plume and background

are darker due to their non-reflective nature. The contrast is very low between the outer region and the background, making that region almost invisible. However, the inner region with the higher temperature and concentration can be clearly seen. The same case occurs in the LWIR (Figure 4-1b). Now the reflective gray card is dark in the LWIR. This is because in this band thermal self-emission is the dominant process and the reflective card has a lower emissivity than the ground. The plume has similar contrasts in both bands in the upward-looking case (Figure 4-1 (c) and (d)). Table 4-2 compares the plume and total radiance values (integrated over the 10 cm^{-1} band) from the inner region pixel for the downward-looking plume image.

Band (μm)	Atmospheric transmission	Plume transmission	Plume radiance reaching sensor	Total observed radiance	Contrast
3.33 down	.421	.812	0.0307	0.127	0.198
10 down	.887	.888	12.7	83.8	0.063
3.33 up	n/a	.812	.058	0.139	0.43
10 up	n/a	.888	13	31.9	0.47

Table 4-2. Radiometric Values Plume Images

The total observed radiance in the downward-looking case includes the plume, background, and atmospheric upwelled radiance reaching the sensor (including atmospheric attenuation effects). The plume radiance reaching the sensor accounts for atmospheric transmission. The radiance in the LWIR band is larger due to the strong thermal self-emission from the plume and background. The contribution from solar irradiance in the MWIR is negligible since both the plume and background are poor reflectors. The last value is the contrast ratio as defined in eqn. 2-49. Despite the lower overall plume radiance at $3.33\text{ }\mu\text{m}$, the contrast is higher than at $10\text{ }\mu\text{m}$. This is not immediately apparent in the images due to the auto scaling applied in converting the radiance values to 8-bit gray levels. For the upward-looking case, the radiance is from the plume and atmospheric downwelled radiance. In the LWIR, this is primarily thermal self-emission, while there is a small amount of solar scattered light in the MWIR. Here the contrast ratios are reversed, where the LWIR is slightly higher than the MWIR. This is seen in the images where the LWIR outer region is visible, whereas in the MWIR the outer region is not.

The JPL "wander" plume model is illustrated next. This plume has a varying wind speed and atmospheric stability number (Pasquill-Gifford stability number). When this is done, shape and texture are given to the plume (see Figure 3-8). A plume model with four nested regions is created with the varying atmospheric conditions. A background scene is also used to illustrate a complete DIRSIG image. The scene is of the Kodak Hawkeye complex which contains a smokestack 53 m high and with a diameter of 5 m. Two images are produced with this model, one with the plume filled with water droplets and the other with methyl chloride. These images are shown in Figure 4-2. The visible color image is produced using the process described in Appendix F. The "wander" due to the change in wind speed is the attempt to

simulate the puffing of the plume. This is seen in the variation in brightness in the outer region of the cooling tower plume. The slight yellowish tint on the plume is the reflected color from the scattered sunlight. The scattered blue skylight from the plume may be underestimated since this would contribute to a more neutral plume color (white).



Figure 4-2. JPL "wander" plume filled with water droplets (left, visible band) and methyl chloride (right, 3.33 μm)

The DIRSIG plume model is used next to determine the effect of variations of certain plume properties. Several images of the methyl chloride plume are produced with different concentrations and temperatures. The JPL wander plume with only a single region is used. It is viewed using the airborne sensor with 128x128 pixels. In the first set of images, the plume temperature is set to 303 K° and the VMR varied from 100 to 500 ppm (see Figure 4-3 and Figure 4-5). In the second set the VMR is set to 300 ppm and the plume temperature varied from 288 to 323 K° (see Figure 4-4 and Figure 4-6). Images in the same set are all scaled to the same gain and bias to facilitate comparison.

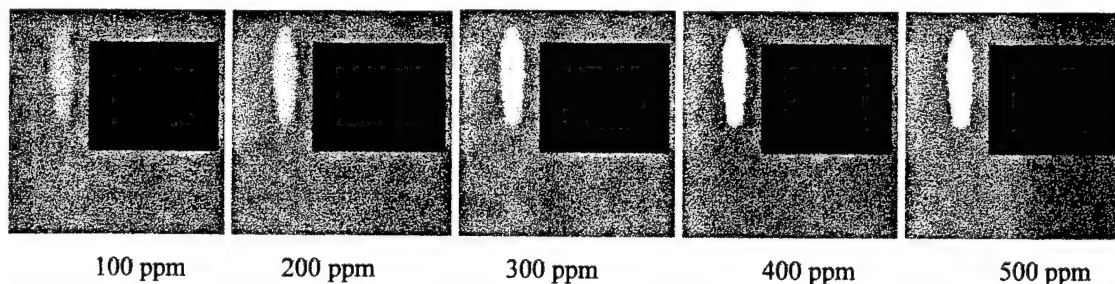


Figure 4-3. 10 μm Images of CH_3Cl with Variable Concentration

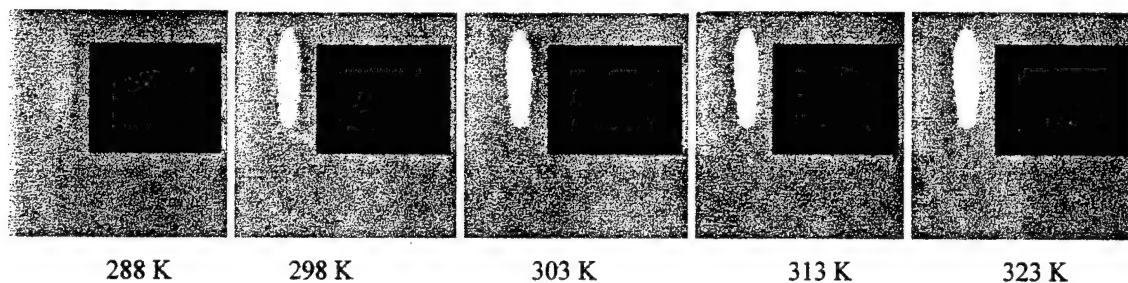


Figure 4-4. 10 μm Images of CH_3Cl with Variable Temperature

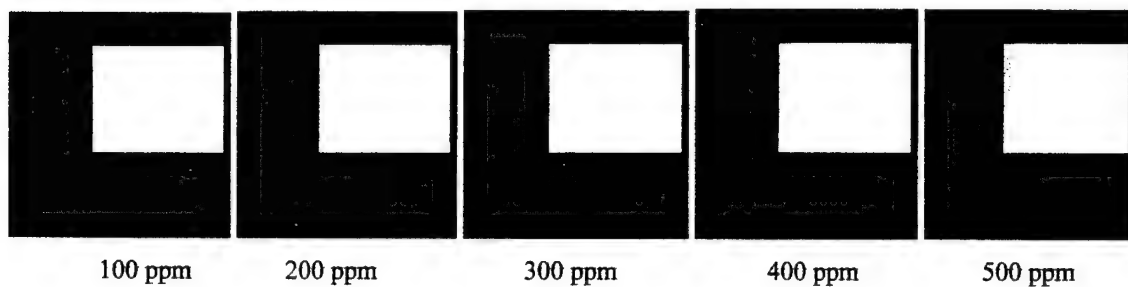


Figure 4-5. 3.33 μm Images of CH_3Cl with Variable Concentration

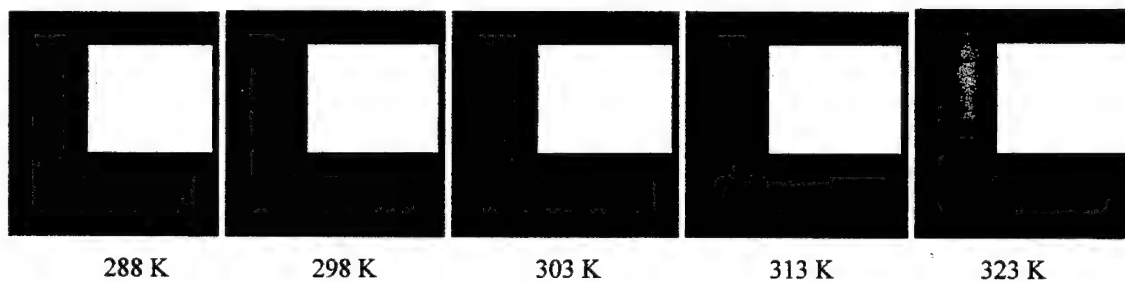


Figure 4-6. 3.33 μm Images of CH_3Cl with Variable Temperature

The change in contrast ratios with VMR and temperature is show in Figure 4-7.

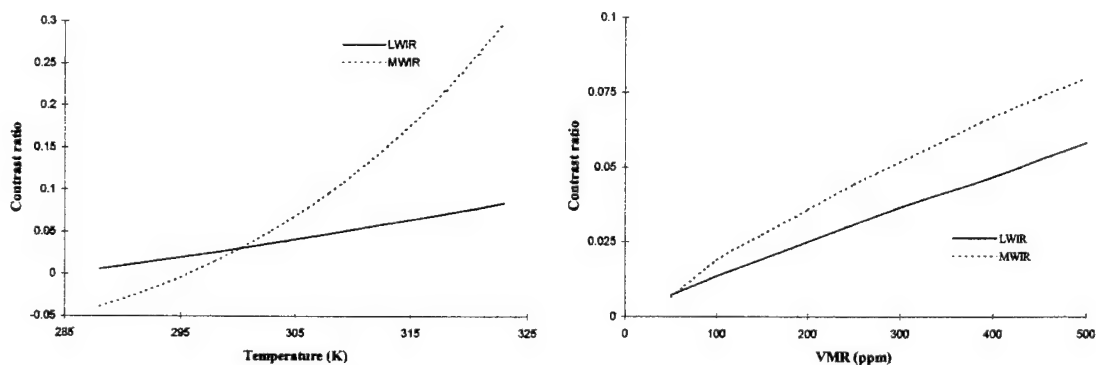


Figure 4-7. Contrast Ratios for Change in Plume Temperature and VMR

The plume contrast increases faster with changes in temperature than in concentration, which is especially apparent in the MWIR. This is evident in both the plots and images. This is due to the non linear nature of the Planck function. Also note the negative contrast in the MWIR when the plume is at the same temperature as the background (288 K°). This results from the plume absorbing more radiation than it is emitting. At 298 K° the amount absorbed and emitted are nearly equal and thus the plume is nearly invisible. From that point the plume has a positive contrast with increasing temperature. A variation in temperature changes the self-emission of the plume, not its absorbance. This is why the shadow of the temperature varying plume looks the same in the MWIR. On the other hand, a variation in concentration will vary both the absorbance (as seen in the darkening of the plume shadow) and self-emission (as seen in the plume brightness). This is why lowering the concentration will not necessarily cause a negative contrast since both the absorbance and self-emission are being lowered. From the contrast ratios, the MWIR is the better band for detection of plumes. However this is not evident in the images due to the different gain and bias applied for proper scaling. Again the examples shown here are not intended to be actual cases of plume detection, but rather to demonstrate the potential capabilities of using DIRSIG to study the remote sensing of plumes.

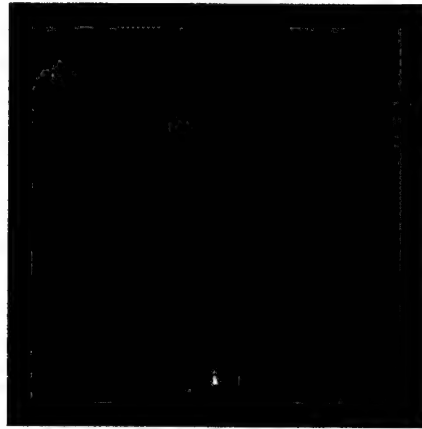
4.1.2 Integrated JPL Model

The results using integrated JPL model are shown next. The same downward and upward-looking scene geometries used for the ACAD model are also used here. Methyl Chloride is also used with the scene being run at 3.33 μm and 10 μm . The regions in the ACAD model were filled with an arbitrary VMR to illustrate the difference between the region. This can not be done with the integrated model since the column density downwind is based on the initial conditions in the "Plume_Input" file. Thus the ACAD and integrated model will have different gas concentrations. A more direct comparison between the two models is made in Chapter 5. The baseline plume characteristics defined in the Plume_Input file are shown in Table 4-3.

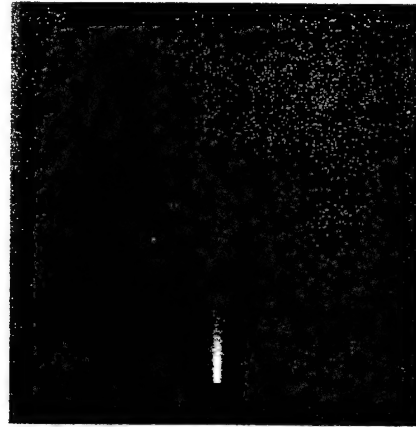
Release rate	300 lbs/hr
Gas temperature	394 K
Release velocity	15 m/s
Stack diameter	0.81 m
Wind speed	7 knots
Atmospheric stability number	40 (neutral)

Table 4-3. Initial Plume Characteristics

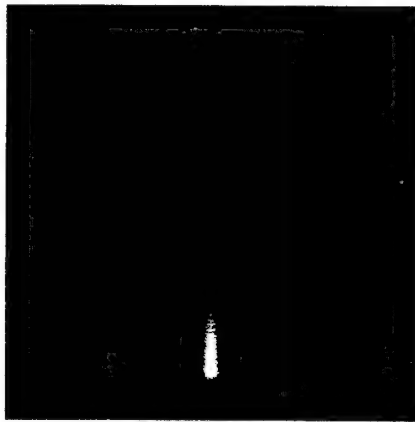
The release rate and temperature are made higher than normal to ensure the plume visibility. The images for the downward and upward looking cases in the MWIR and LWIR are show in Figure 4-8.



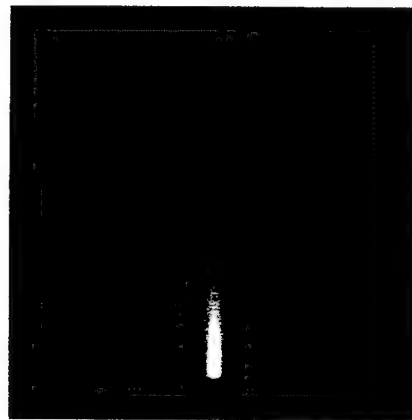
(a)



(b)



(c)



(d)

Figure 4-8. Integrated JPL model images from an airborne sensor at 3.33 μm (a) and 10 μm (b) and a ground based sensor at 3.33 μm (c) and 10 μm (d)

The most noticeable difference is the smaller size of the plume and the rapid drop-off in the plume visibility. The first effect is due to the smaller stack diameter used (0.81 vs. 5 m) in order to keep the plume concentration at a relatively high level. The second effect is due to the Gaussian nature of the plume where the concentration drops off at an exponential rate. Since the ACAD model had regions with constant VMR's, this effect is not seen. In the upward looking case the contrast in the LWIR is again slightly better than in the MWIR. The column density, temperature, transmission, and contrast ratio (for the downward looking case) as a function of downwind distance are shown in Figure 4-9.

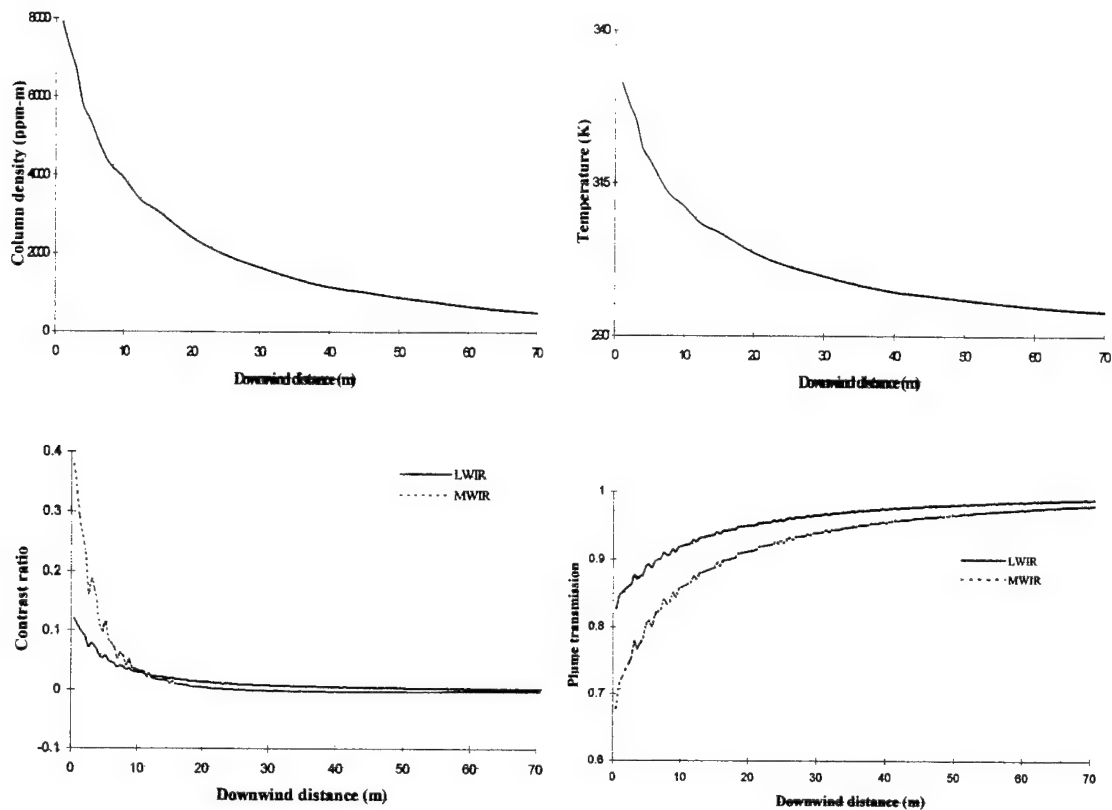


Figure 4-9. Downwind Characteristics of Integrated Plume Model

The top edge of the image is about 100 m downwind from the stack exit in the downward-looking case. The Gaussian nature of the plume is seen clearly. Both the column density and temperature have a similar shape since they are both based on the same dilution factor calculation. Even though the release temperature is 394 K°, by one meter downwind the temperature has dropped off below 340 K°. Whether this is realistic will be tested in Chapter 5. The contrast ratio is higher in the MWIR in the first 10 m, but then drops below the LWIR, and actually has a slightly negative contrast. Again this is not immediately apparent in the images due to the auto-scaling applied. The reason for this reversal is the higher absorbance in the MWIR band. When the plume is still hot near the stack exit, the MWIR has a higher radiance due to its higher emissivity. As the plume cools, the blackbody radiance decreases due to both the decrease in temperature and emissivity, causing both bands to lose contrast. However, due to the higher absorbance in the MWIR, its contrast ratio becomes negative. Absent from the MWIR image is the plume shadow. This is due to the lack of a gray card and the auto-scaling process.

Several plume parameters are varied to determine the effects on the image and properties of the plume. The first is to cut the release rate in half to 150 lbs/hr. The images and contrast ratio are shown in Figure 4-10.

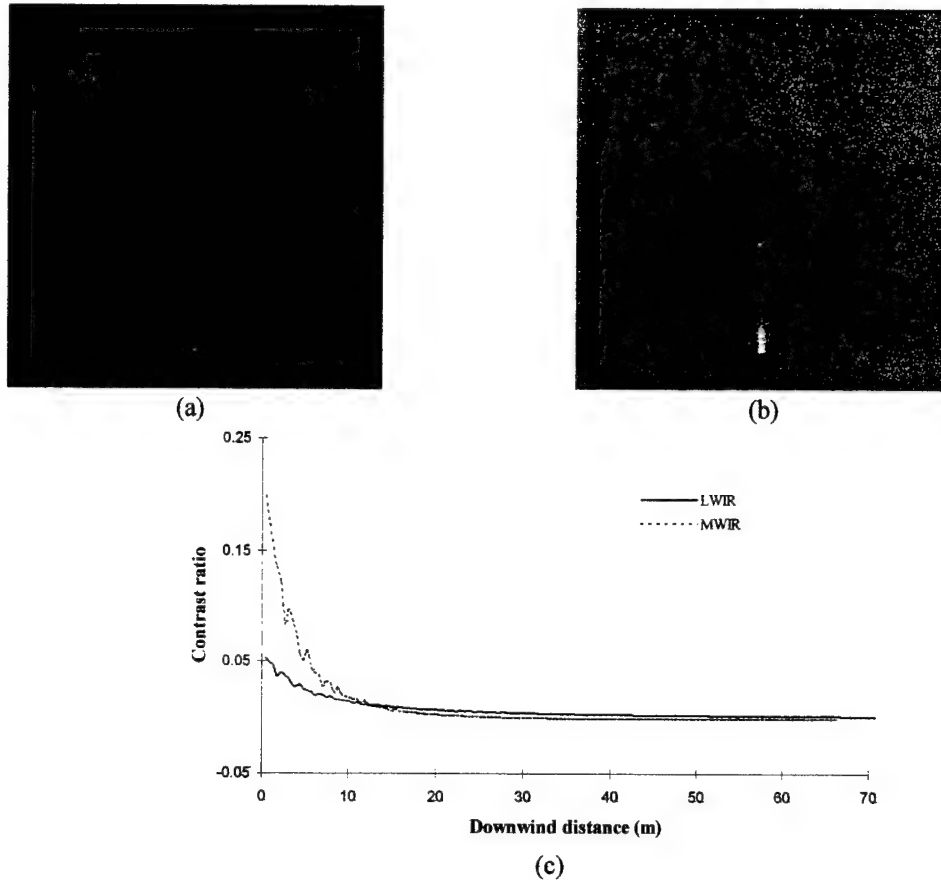


Figure 4-10. Reduced Gas Release Rate Images at 3.33 μm (a) and 10 μm (b) and Contrast Ratio (c)

Reducing the release rate will lower the column density and make the plume more transmissive. The emissivity will also decrease reducing the plume self-emission. As a result the plume contrast ratio drops off quicker than the baseline plume.

The next parameter changed (the release rate is reset to its original value) is to decrease the initial plume temperature from 394 to 366 K°. The images and contrast ratio are shown in Figure 4-11.

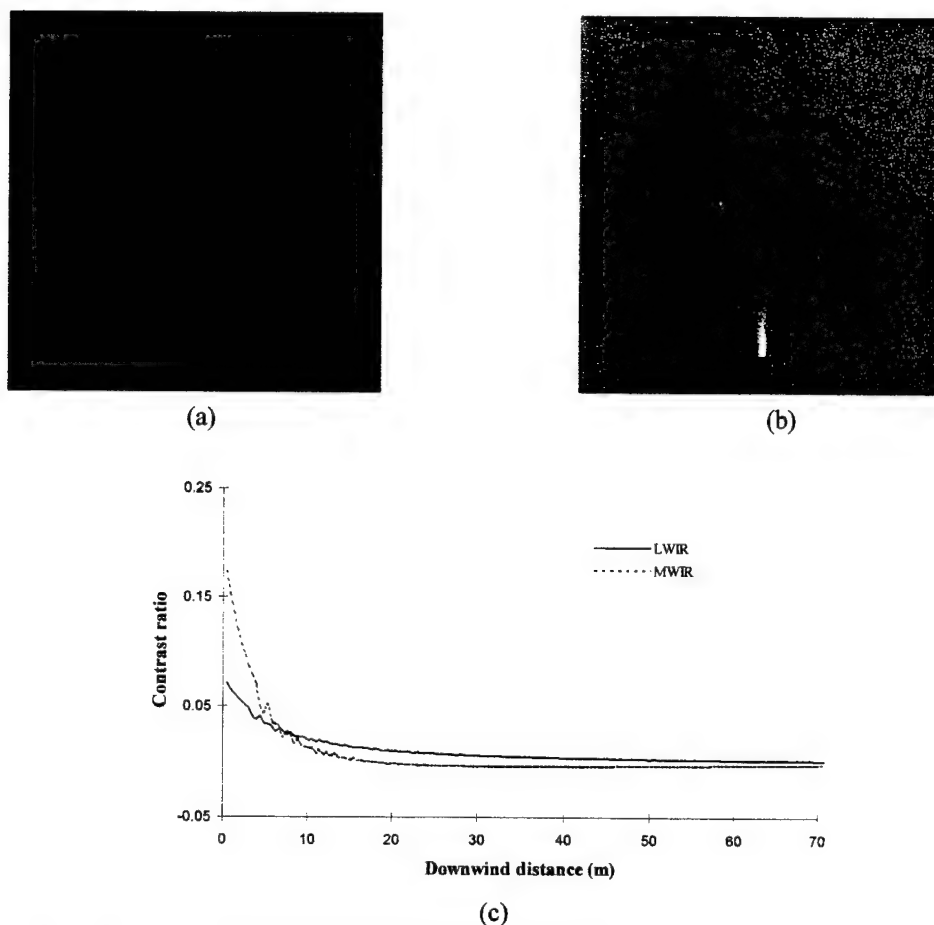
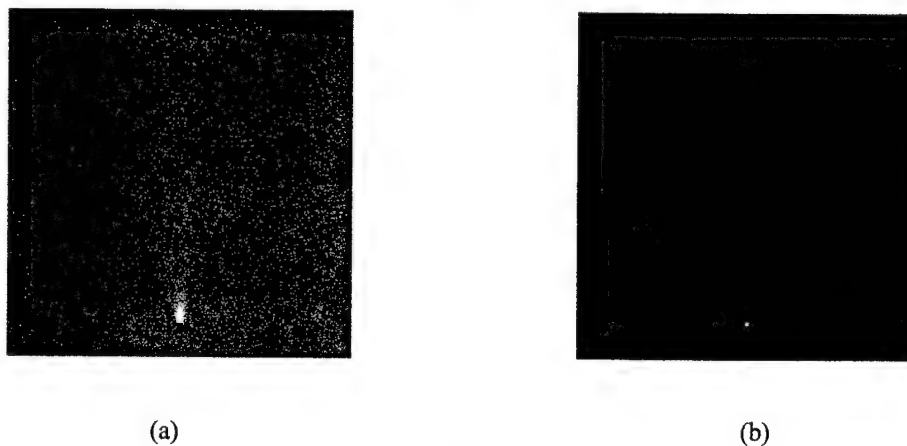


Figure 4-11. Decreased Plume Temperature Images at 3.33 μm (a) and 10 μm (b) and Contrast Ratio (c)

The results are similar to the reduced release rate. The lowered temperature reduces the plume self-emission, however the plume transmission remains the same. There is a quicker reversal in the contrast between the MWIR and LWIR than in the baseline or reduced release rate case.

The final parameter changed is the atmospheric stability number. This is lowered from 40 to 20 to produce a more unstable atmosphere. The images and contrast ratio are shown in Figure 4-12.



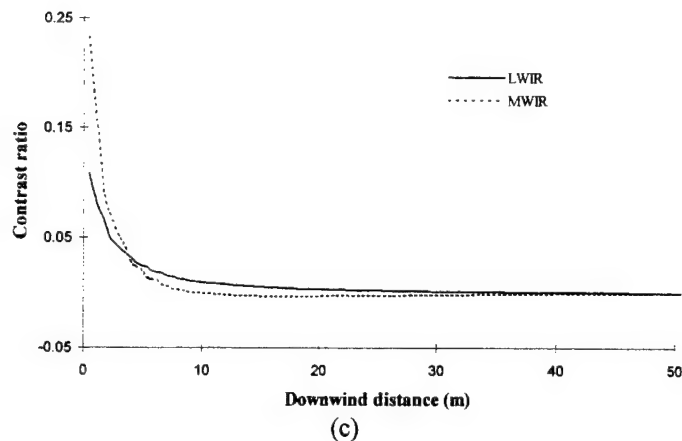


Figure 4-12. Lowered Atmospheric Stability Images at 3.33 μm (a) and 10 μm (b) and Contrast Ratio (c)

The unstable atmosphere forces the plume to dissipate quicker. This is evident in the images and the contrast ratio where the plume disappears after 10 m from the stack. Several other parameters can also be adjusted including stack release velocity, wind speed, and stack diameter. No results for these parameters are shown.

One of the main interests in remote sensing of gas plumes is to look at specific gas absorption lines. Using the same hyperspectral sensor as above with a 10 cm^{-1} spectral resolution, several side looking images of the CH_3Cl plume are taken. The images are taken at different absorption lines with varying absorbance strengths. Figure 4-13 shows the absorbance curves for CH_3Cl in the 3.33 and 10 μm bands, and the spectral location of where the images are taken.

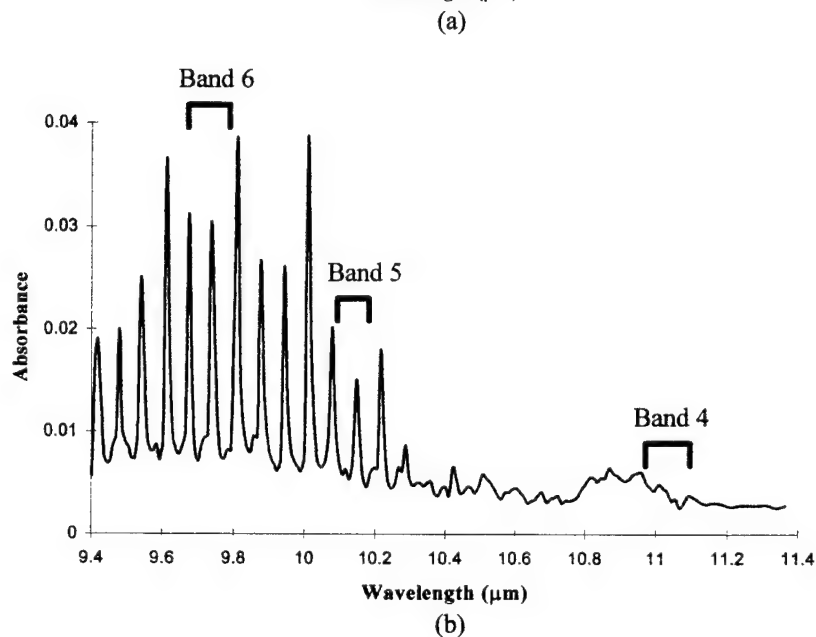
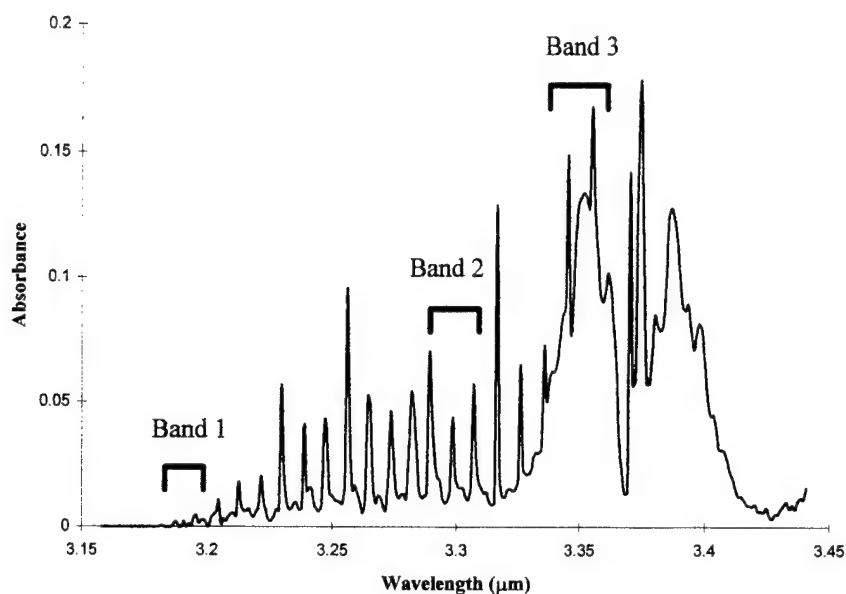


Figure 4-13. Absorbance Curves for Methyl Chloride (CH₃Cl) in MWIR (a) and LWIR (b)

Because of the finite spectral resolution, several absorbance peaks may be included in each 10 cm^{-1} spectral window. The absorbance is averaged over that band as described in section 3.4, even though the conditions for the smeared line model are not strictly met. The corresponding images for each of the bands are shown in Figure 4-14.

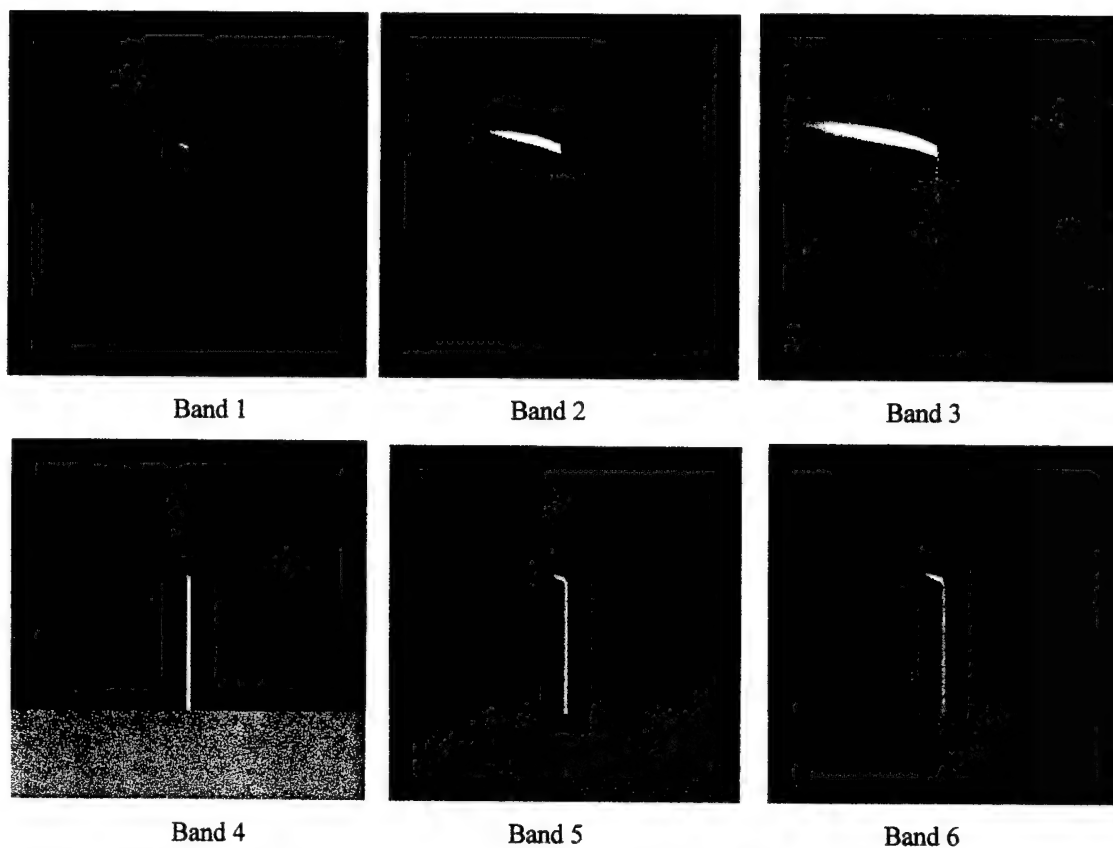


Figure 4-14. Plume Images at Designated Spectral Bands

In the MWIR there is a dramatic increase in plume visibility at the peak spectral absorbance. One reason for this is that the peak (band 3) has a continuous absorption band, as oppose to individual separated peaks. The absorbance in band 3 is approximately four times stronger than band 2, and ten times stronger than band 1. In the LWIR, there is a more gradual increase in plume visibility as the absorbance increases. The peak absorbance is five times smaller than in the MWIR. Also the peaks in bands 5 and 6 are discrete, resulting in a lower absorbance as a result of averaging of the spectral band.

The final image of the integrated JPL model is with time-varying meteorological conditions. The wind speed and atmospheric stability number are varied at three second intervals. Under these conditions the plume is given some shape and made more realistic looking. SF_6 is used as the plume constituent in order to make it more visible (the image is at $10.5 \mu\text{m}$).

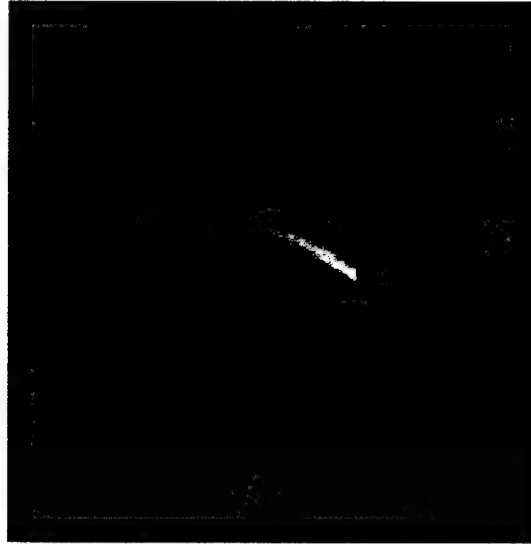


Figure 4-15. Integrated JPL Model with Time Varying Meteorological Conditions

4.2 Scattering Plumes

The generic scattering effects of plumes are illustrated using the JPL ACAD model containing water droplets. The plume is composed of a single region with homogenous properties. Both the single scattering and multiple scattering algorithms are used in creating plume images. The LANL plume model is used to simulate a cooling tower plume with varying properties downwind. Only the multiple scattering algorithm is used here due to the large optical depths present.

4.2.1 Homogenous (Water Droplet) Plume

A homogenous plume is used to show the results of the single and multiple scattering algorithms. The JPL ACAD model is used to produce this single region plume. Time-varying meteorological condition are used to give some shape and texture to the plume. The plume is approximately 80 m long, and has a maximum thickness of approximately 24 m. This plume is then filled with water droplets. The droplet size distribution is kept constant at a mean radius of 6 μm and a LANL modified Gamma size distribution with $\alpha = 25$ (see Appendix B). The number density is varied to produce plumes with varying optical depths. The densities (in cm^{-3}) are set to 100, 200, 600, and 1000. These are intended to represent typical densities found in a cooling tower plume. The properties of the plume are examined at five wavelengths in which scattering effects are dominant. Table 4-4 shows the properties of the plume at these five wavelengths.

Wavelength (μm)	Scattering Cross-section (μm^2)	Single Scattering Albedo	Asymmetry Parameter
0.4	246.03	1	0.85764
0.5	247.37	1	0.85747
0.667	251.66	1	0.84552
1.0	255.71	.99967	0.83759
2.0	262.63	.95951	0.81235

Table 4-4. Optical Properties of Homogenous Plume

Notice that the properties are fairly constant spectrally, with the most notable difference in the drop of the single scattering albedo at longer wavelengths. Figure 4-16 shows the maximum optical depths (based on the maximum plume thickness) of the 4 plume types as a function of wavelength.

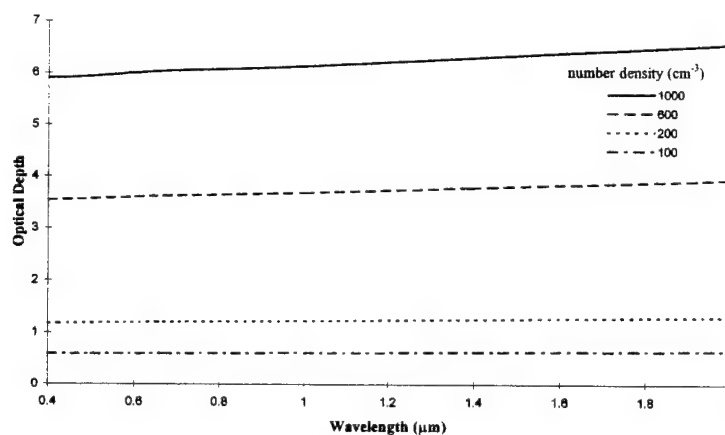
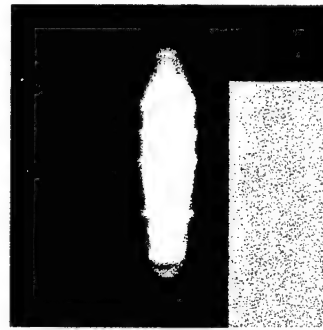
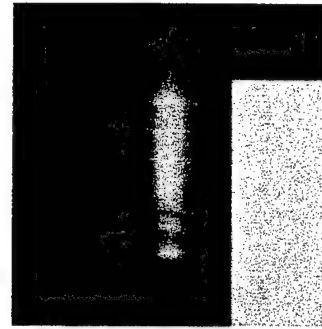


Figure 4-16. Maximum Optical Depth for Four Plume Number Densities

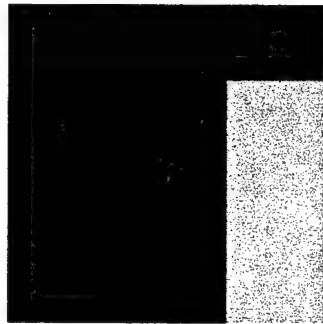
The multiple scattering algorithm is used for all four optical depths, while the single scattering algorithm is used only for the two lower optical depths. For the first case, a downward-looking sensor (at 750 m) is used. The plume is at a height of about 50 m over a grass background and a 18% reflecting card. The images were run for two different times of day in order to vary the scattering angle. The first is at 8:00 A.M. with a solar zenith angle of 60° and the second is at noon with a zenith angle of 0° . To produce the visual images (0.4- 0.714 μm) of the plumes, the technique described in Appendix F is used. Figure 4-17 shows the images from the multiple scattering algorithm, while the optical and radiometric properties are plotted in Figure 4-18.



1000 cm⁻³



600 cm⁻³



200 cm⁻³



100 cm⁻³

Figure 4-17. Visible Images of Plume at Noon with Varying Number Density

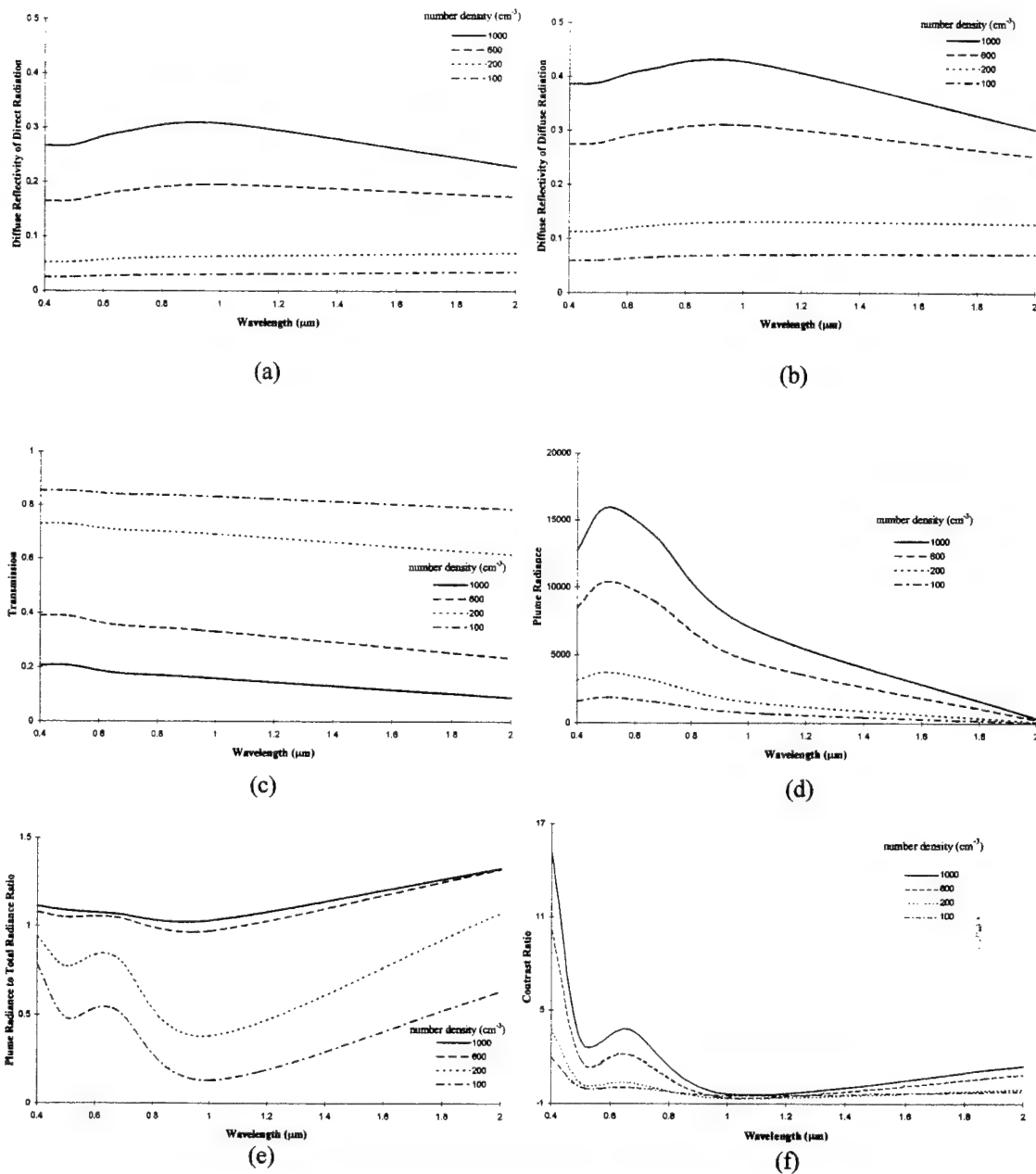


Figure 4-18. Optical and Radiometric Properties for Noon Plumes

The images are all scaled with the same gain and bias to preserve the relative plume brightness. The optical and radiometric values are all based on a sample pixel in the middle of the plume (~24 m thickness). Thus the sensor is looking straight down at this sample pixel. As expected the plumes with the larger number densities scatter more light back towards the sensor, thus appearing brighter. The plumes are also white, which is expected for water droplets which scatter light in a neutrally spectral manner (as seen

in clouds). This is evident in Figure 4-18 (a) and (b), where the reflectivity is spectrally flat. While the reflectivity for diffuse radiation is slightly higher than for direct radiation, the scattered sunlight is greater than the scattered skylight because of the higher direct solar radiation. The plume radiance peaks in the visible (Figure 4-18 (d)), which is the same region where the solar irradiance is at a maximum (see Figure 2-6). It then decreases towards the longer wavelengths due to the lower solar irradiance and reflectivity. The two plumes with the lower number densities do not scatter enough light back, and thus appear darker than the background because of their transmissive properties (Figure 4-18 (c)). The plume radiance to total radiance ratio reaching the sensor is shown in Figure 4-18 (e). The reason the ratio exceeds one is that the plume radiance is measured right at the plume, before it undergoes atmospheric attenuation to the sensor. Notice that this ratio is greater than one when the plume appears white. However the multiple scattering algorithm is suspect at these lower optical depths (see section 2.3.5). The contrast ratio is plotted in Figure 4-18 (f). This indicates the plume is most easily detected at the shorter wavelengths, and least visible in the $1.0 - 1.2 \mu\text{m}$ region, probably due to the atmospheric absorption bands. The sharp rise in contrast at $0.4 \mu\text{m}$ is due to the very low reflectivity of grass at that wavelength, thus making the background radiance extremely small. It should be remembered that all these curves are plotted with only 5 spectral points, and any in-depth analysis in this area requires a larger number of spectral points.

The single scattering algorithm is used on the two plumes with lower number densities. The optical depths are low enough (~ 1.2 and ~ 0.6) where the single scattering approximation may be used. Since the single scattering model only scatters direct solar irradiance, no scattering of skylight is accounted for. Figure 4-19 shows the images and Figure 4-20 shows the radiometric properties of the plume.

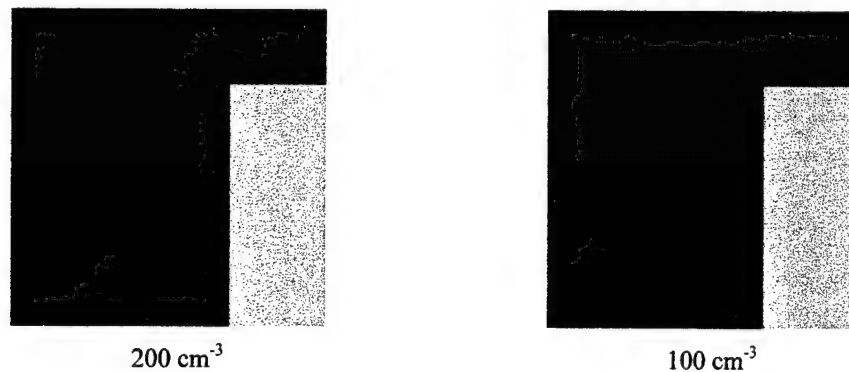


Figure 4-19. Visible Images of Plume at Noon Using Single Scattering Model

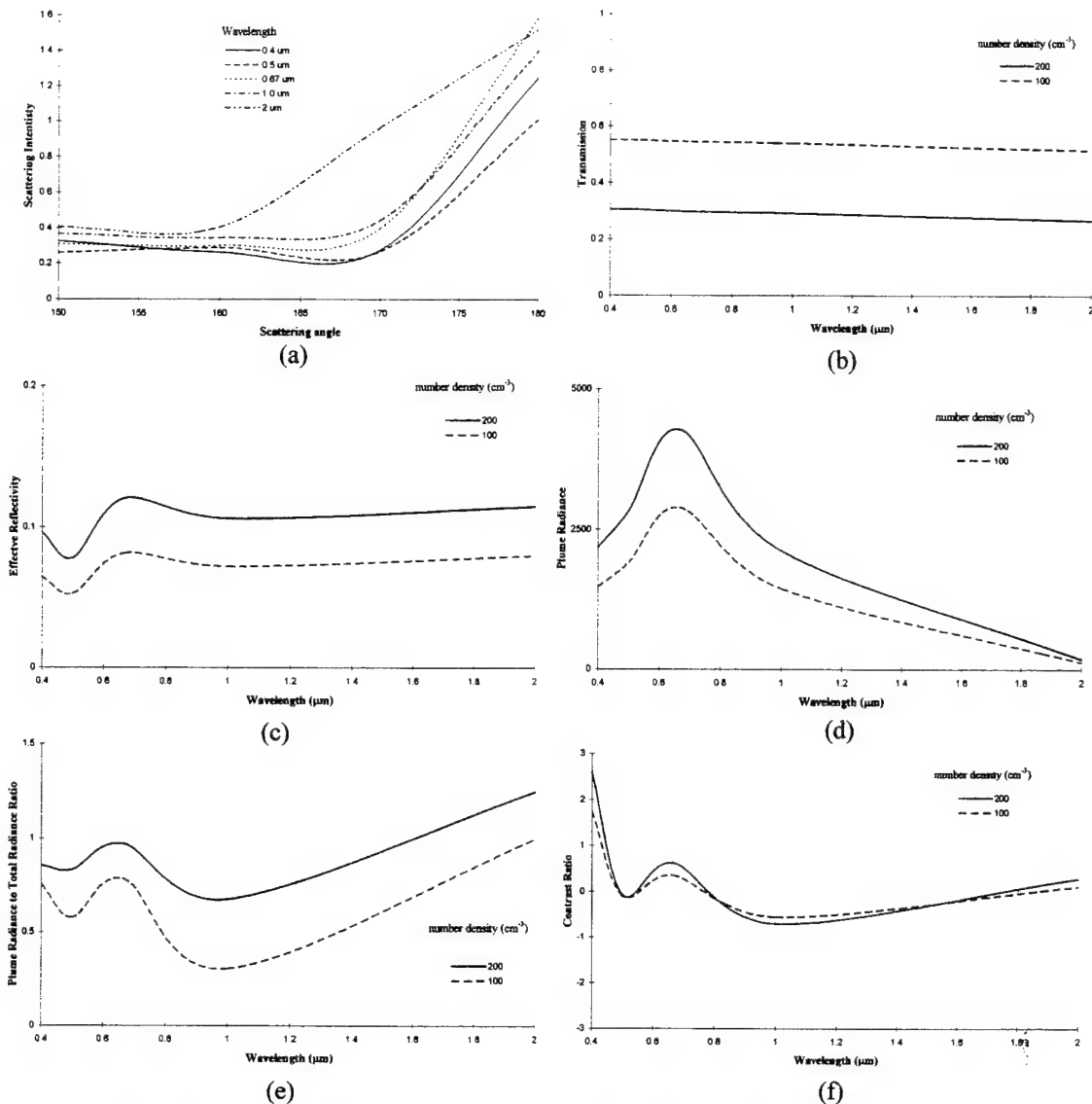


Figure 4-20. Optical and Radiometric Properties for Noon Plumes Using Single Scattering Model

In the single scattering model, attenuation is based on the Beer-Lambert law (eqn. 2-12), which results in a transmission about 50% lower than that based on eqn. 2-41 (Figure 4-20b). This effect, along with not accounting for scattered downwelled radiance, results in an 80% lower overall radiance from the plume than the multiple scattering model (Figure 4-20 (d)). This results in a darker plume and lower contrast ratio. In fact, there is little difference in appearance between the two plumes, as evident in the contrast ratios. However, the actual solar irradiance scattered is higher. The effective reflectivity is the ratio of the scattered radiance to the incident solar irradiance assuming the plume is a Lambertian reflector. This effective reflectivity is about twice as high as the diffuse reflectivity for direct radiation (Figure 4-20 (c)). The reason for this is the backscatter peak associated with the scattering phase function (Figure 4-20 (a)). This effect is seen in the images by the slightly brighter spot in the middle of the plume. Unlike the

multi-scattering model, where the solar incident angle is fixed throughout the plume, the scattering angle varies throughout the plume for the single scattering model. The validity of using the single scattering model is determined in Chapter 5.

The plume scene is next run at a different time (8:00 A.M.). This provides a different solar zenith incident angle of 60° . The visible images are shown in Figure 4-21 and the optical and radiometric properties in Figure 4-22.

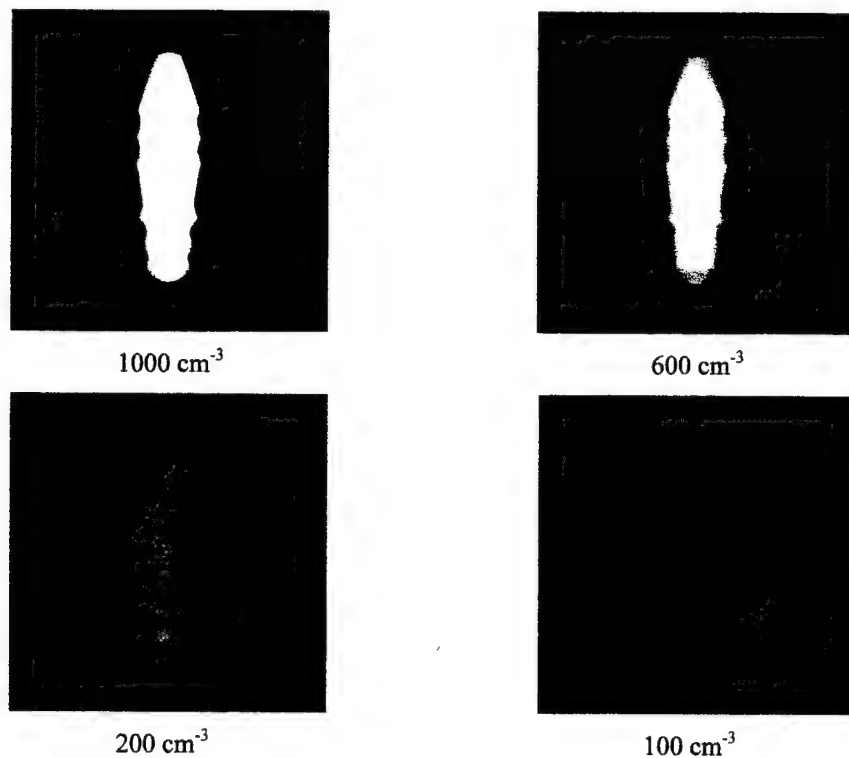


Figure 4-21. Visible Images of Plume at 8:00 A.M.

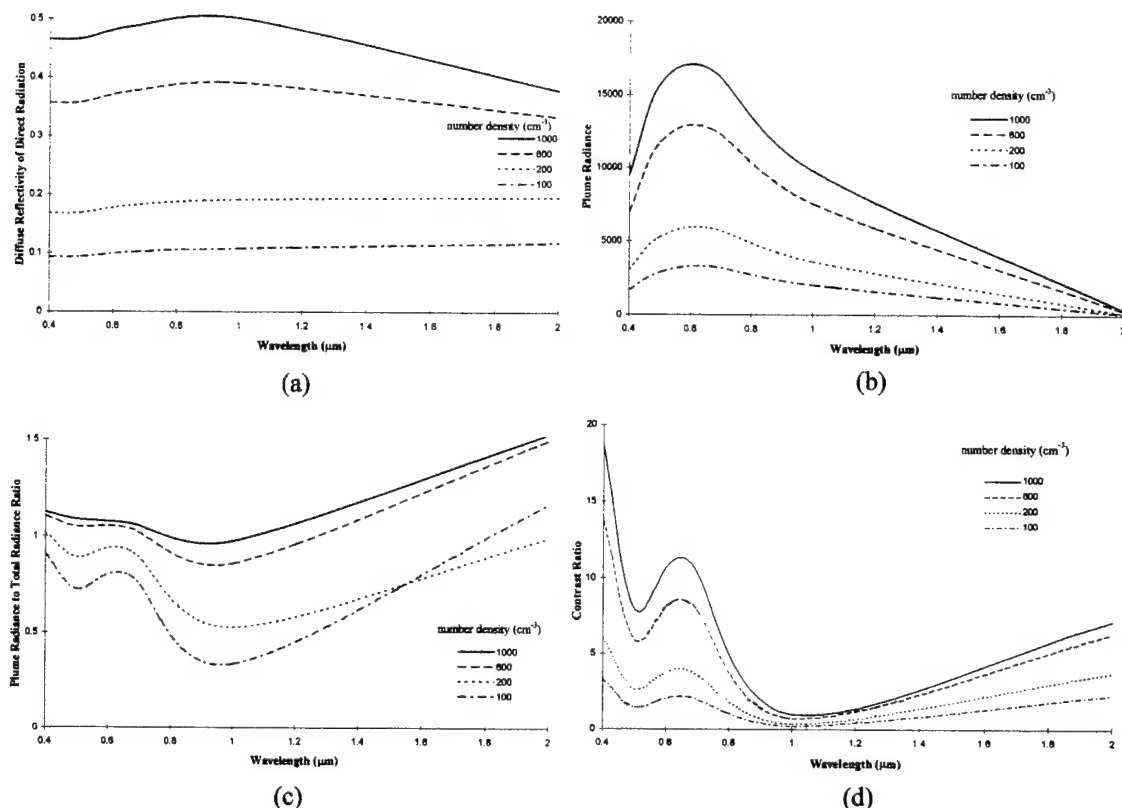


Figure 4-22. Optical and Radiometric Properties for 8:00 A.M. Plumes

At this solar incident angle, all four plumes have a positive contrast against the background, which appears darker due to the lower solar irradiance. This is due to the higher reflectivity of direct radiation at this incident angle than at noontime, which compensates for the lower solar irradiance at 8:00 A.M. (about 40% lower than at noon). A shadow also appears above the plume now that the sun is at a lower elevation angle. The reflectivity for diffuse radiation and transmission are the same at noon, since they are independent of solar angle. The yellowish appearance of the plume is due to the color of the sun, which is the source of the majority of the scattered radiance. This same effect is seen as redness of clouds at sunset (see Chapter 5). The two plumes with the lower number densities have the biggest change in appearance, both of which now have a positive contrast. In fact, the contrast ratios are 10-20 times higher for these two plumes, and only 2-3 times for the two denser plumes. However, the multiple scattering algorithm is suspect at these low optical depths. A reason for the increase in reflectivity is that for smaller scattering angles between the source and sun, multiply scattered light has a greater chance of emerging from the plume in the direction of the sensor. This is especially true when the light is highly forward scattered as in these cases ($g \geq 0.8$). This effect has been shown in studies of various two-stream algorithms (King, 1985). As discussed in section 2.3.5, the delta-Eddington approximation is not well suited for either larger incident

angles ($> 60^\circ$) or small optical depths (< 5), so the results for this 8:00 A.M. may have to be further investigated. However for remote sensing purposes, it may be more advantageous to observe cooling tower plumes in the morning or afternoon when the scattering angle relative to the sun is smaller. Of course this need must be balanced with the need for sufficient solar irradiance to reach the plume.

The single scattering model was again run for the two thinner plumes. These images and radiometric values are shown in Figure 4-23 and Figure 4-24.

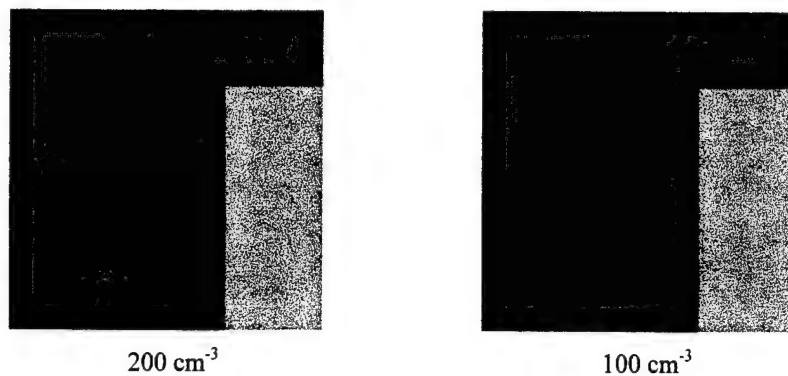


Figure 4-23. Visible Images of Plume at 8:00 A.M. Using Single Scattering Model

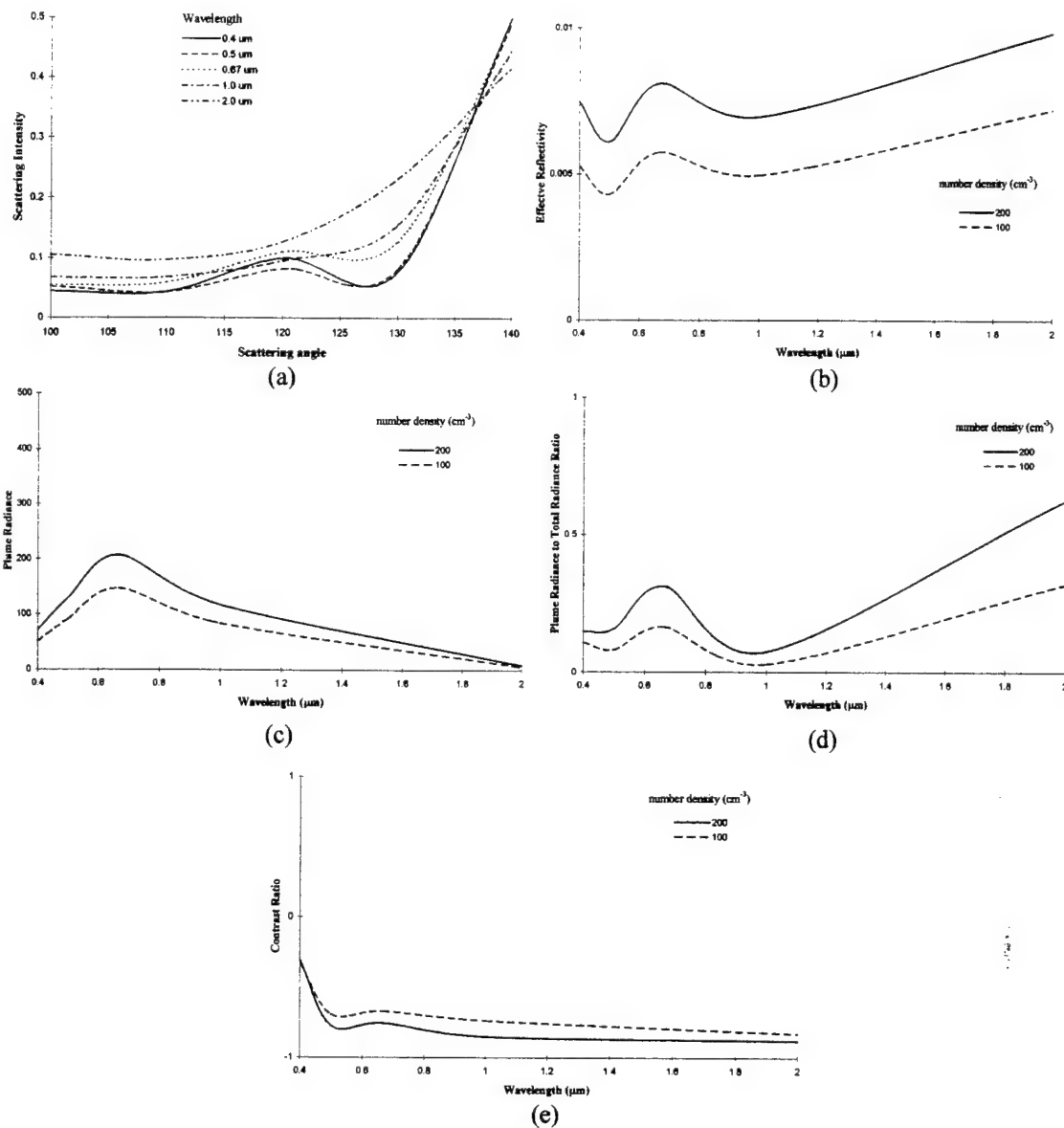


Figure 4-24. Optical and Radiometric Properties for 8:00 A.M. Plumes Using Single Scattering Model

The angular scattering intensity at 120° is about one-tenth of that at 180° (Figure 4-24a). This results in a smaller scattered radiance and a darker looking plume than at noon, though the transmission is the same. This is the opposite effect from the multiple scattering case, where diffuse scattering hides the large angular variations in the phase functions. The effective reflectivity (Figure 4-24b) is little less than half of that in the multi-scattering model. The contrast ratio for the thinner 100 cm^{-3} plume is slightly higher than for the 200 cm^{-3} plume (Figure 4-24e). This can be seen in the image with the slightly brighter 100 cm^{-3} plume.

This is the result of the higher transmission of the thinner plume, since scattered radiance is negligible from both plumes (as seen in the low plume to total radiance, Figure 4-24d).

A ground-based sensor looking straight up is modeled next to produce the plume scenes. The same parameters are used for the downward-looking case with the exception that the noontime scene is run at 11:00 A.M. instead. This is done to avoid forward scattering and looking straight into the sun, both of which are difficult situations to model. The solar zenith angle at 11:00 A.M. is 15.9° . The visible images using the multi-scattering algorithms are shown in Figure 4-25 and the optical and radiometric properties are shown in Figure 4-26. These properties are again taken at a pixel in the center of the plume directly above the upward-looking sensor.

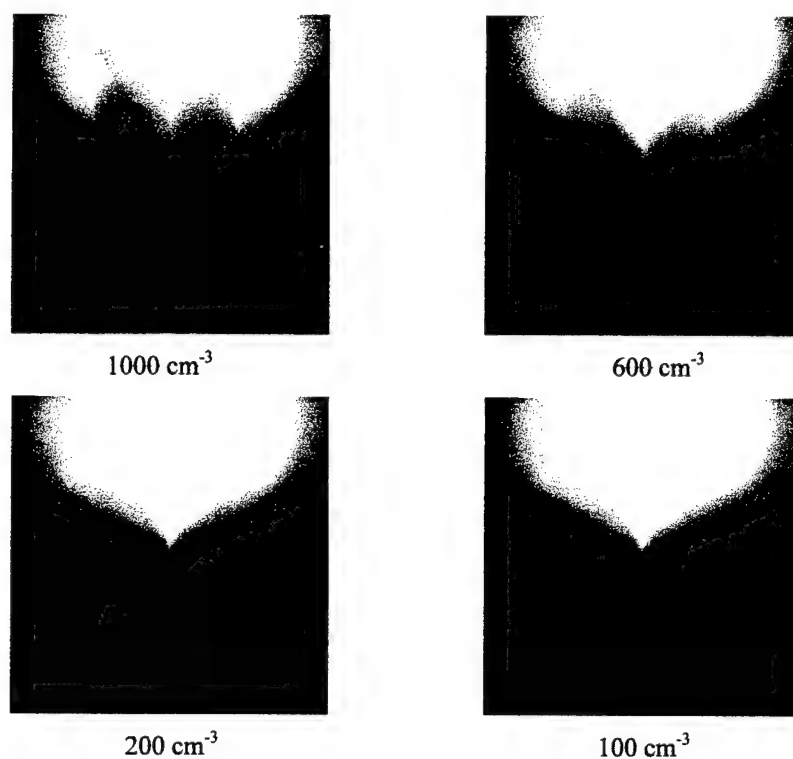


Figure 4-25. Visible Images of Plume at 11:00 A.M. for Upward Looking Sensor

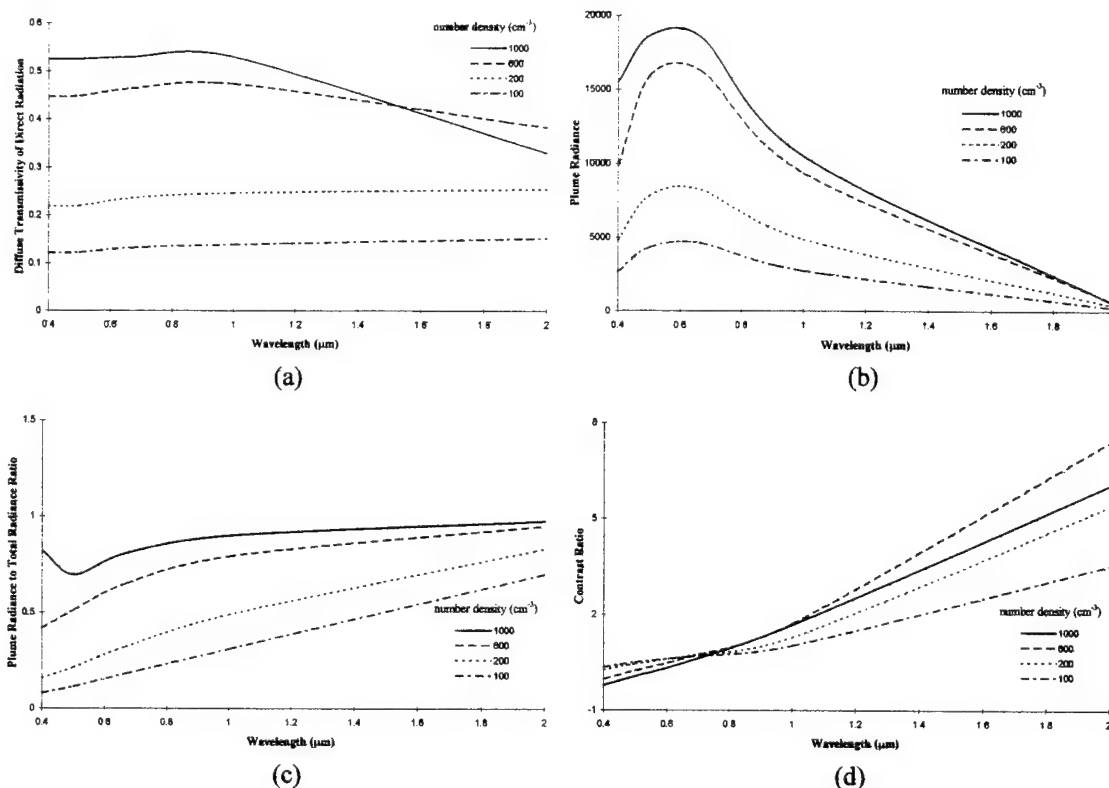
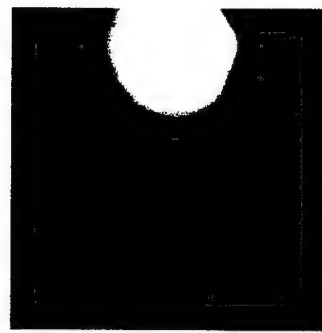


Figure 4-26. Optical and Radiometric Properties for 11:00 A.M. Plumes for Upward Looking Sensor

It is quite apparent that the images are saturated when the sun is in the field-of-view. The “rays” emerging from the plume are a result of the interpolation of the downwelled radiance, which is calculated in increments of 15° zenith and 30° azimuth. An increase in number density (and optical depth) produces a plume that is darker than the background. This is the result of two competing processes. A larger optical depth will produce more scattered radiance coming from the plume (see Figure 4-26a and b); however, it will also cause more attenuation of the radiance along the ray through the plume (see Figure 4-18c). The increased attenuation is the dominant process and causes a thicker plume to be darker. This is evident in Figure 4-26d where the thicker plume has the lower (and negative) contrast ratio in the visible region. At the longer wavelengths conservative scattering is no longer present ($\tau_o < 1$) and the thicker plume’s scattered radiation (Figure 4-26a) decreases rapidly due to self-absorption within the plume. The contrast ratio for all plumes increases past 1 μm due to the drop in scattered skylight in the NIR. In this case, the ratio for the thicker plume increases faster since the scattered radiance (sunlight) becomes the dominant process over the attenuation of decreasing skylight. Remember that the atmosphere below the plume is considered negligible (no attenuation). From Figure 4-26d it is evident the plume will be more visible in the NIR, and may be the preferred spectral region in which to observe the plume.

The single scattering model is again run for the two plumes with the lower number densities. These images and radiometric values are shown in Figure 4-27 and Figure 4-28.



200 cm⁻³



100 cm⁻³

Figure 4-27. Visible Images of Plume at 11:00 A.M. for Upward Looking Sensor Using Single Scattering Model

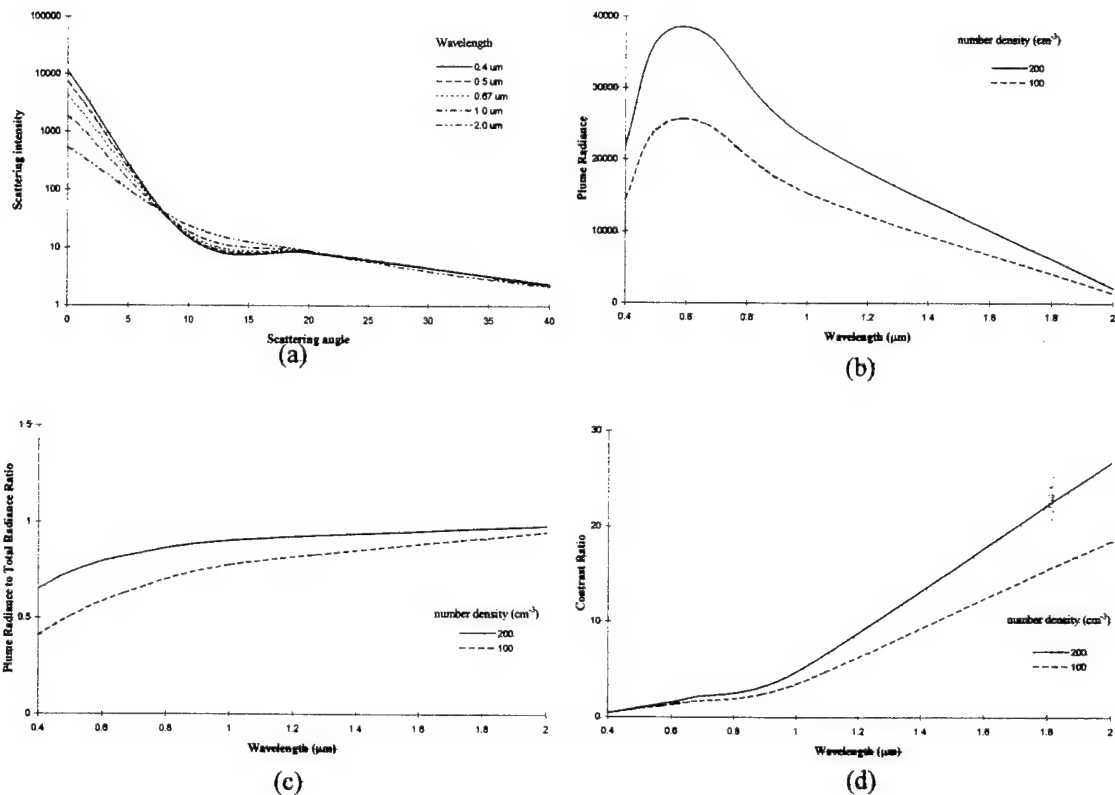


Figure 4-28. Optical and Radiometric Properties for 11:00 A.M. Plumes for Upward Looking Sensor Using Single Scattering Model

The forward scattering cone can be clearly seen, since the Mie phase function for water droplets in this regime is sharply peaked in the forward direction (Figure 4-28a). The scattering intensity in the first 10° differs by several orders of magnitude. This can be seen in the image where the scaling is linear. The point

where the scattering angle is 0° appears as the bright spot. In fact, scattering from the plume is so strong that the actual sun seen in Figure 4-25 (whose intensity is determined from MODTRAN) is too dim to be seen (as well as anything else in the scene). Figure 4-28 b, c, and d are for the center pixel which has a scattering angle of 15° . This is far enough from the forward scattering angle so that the results are comparable to the multi-scattering case, although the radiance is still five times higher. The same trend of increasing plume radiance to total radiance ratio and contrast ratio in the NIR is seen. The problem with handling strong forward scattering is one of the main drawbacks with the single scattering model, and thus looking towards the sun should be avoided

The next set of images Figure 4-29 and plots Figure 4-30 are for the upward looking case at 8:00 A.M.

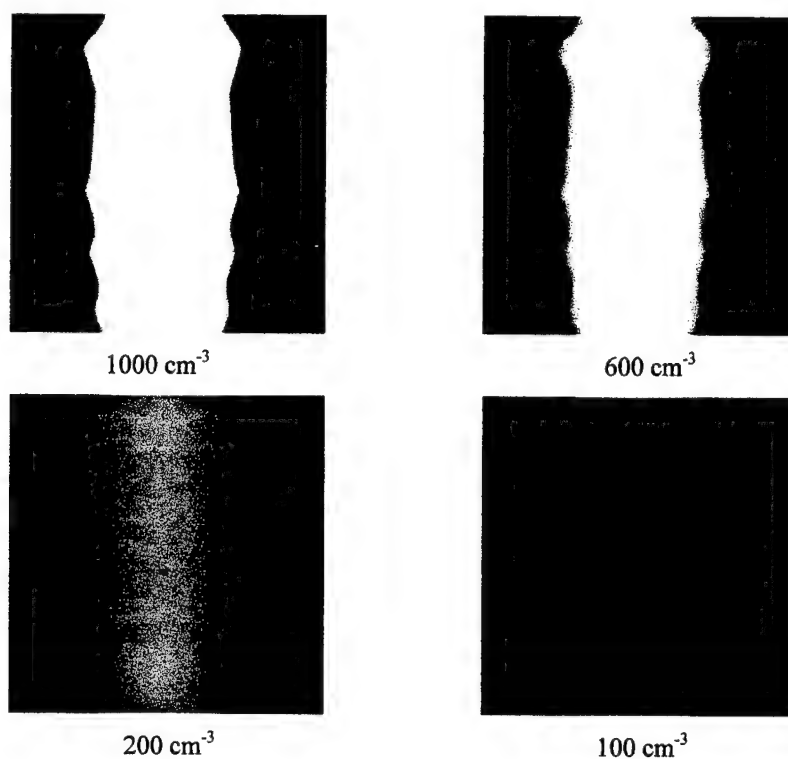


Figure 4-29. Visible Images of Plume at 8:00 A.M. for Upward Looking Sensor

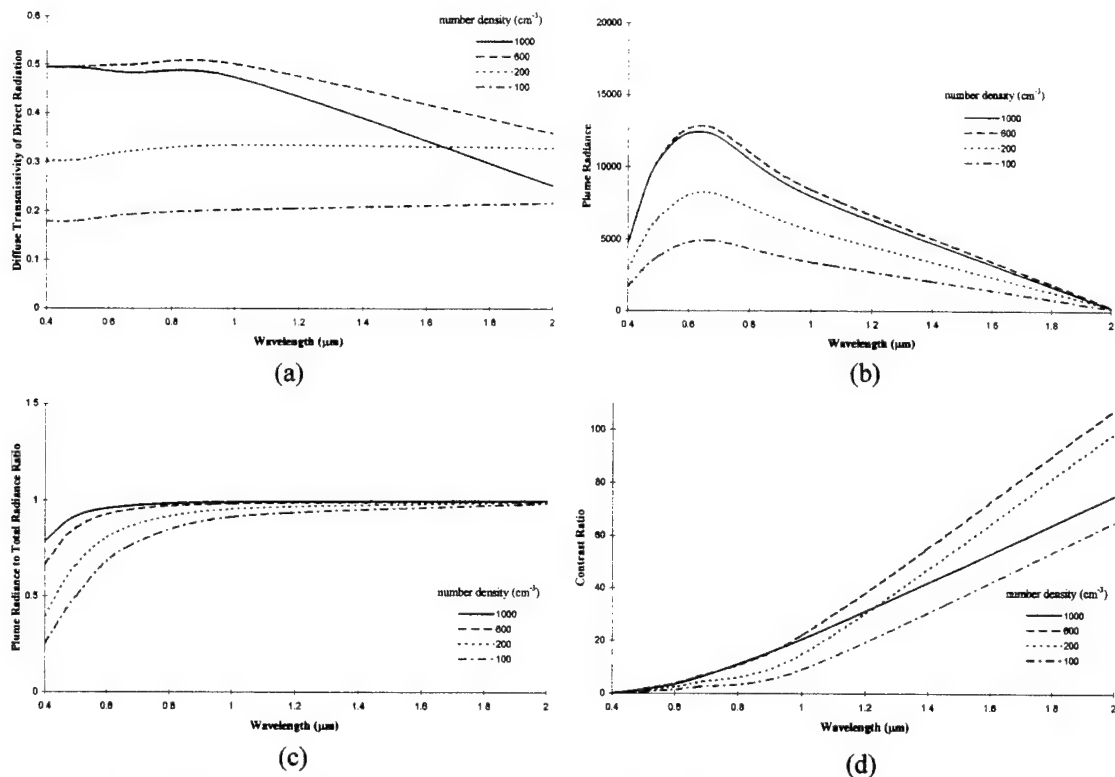
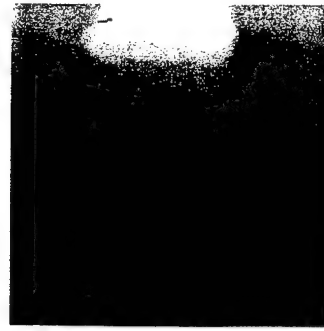


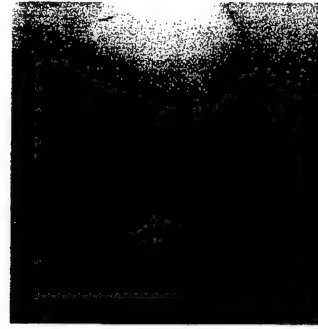
Figure 4-30. Optical and Radiometric Properties for 8:00 A.M. Plumes for Upward Looking Sensor

In this case, there is no direct sunlight in the background so the plumes are very visible. In fact, the background radiance is 5-10 times weaker than at 11:00 A.M., resulting in large contrast ratios. The color of the sun is seen in the scattered radiance. The color of the plume is somewhat artificial since scattered downwelled radiance is not considered. The 1000 cm^{-3} plume has a slightly lower transmissivity and plume radiance than the 600 cm^{-3} plume due to the increased attenuation. This effect can also be seen in the middle section of the 1000 cm^{-3} plume, which is darker than the optically thinner edge. The ratio of plume radiance to total radiance quickly approaches unity (Figure 4-30c), indicating that almost all plume radiance is due to scattered solar radiation, as opposed to transmitted background radiation. This also explains the increasing contrast ratio at longer wavelengths. Again, all caveats stated above for the delta-Eddington approximation apply here, with the added difficulty of modeling forward scattering.

The single scattering case (Figure 4-31 and Figure 4-32) is also handled better at this scattering angle away from the forward peak.



200 cm⁻³



100 cm⁻³

Figure 4-31. Visible Images of Plume at 11:00 A.M. for Upward Looking Sensor Using Single Scattering Model

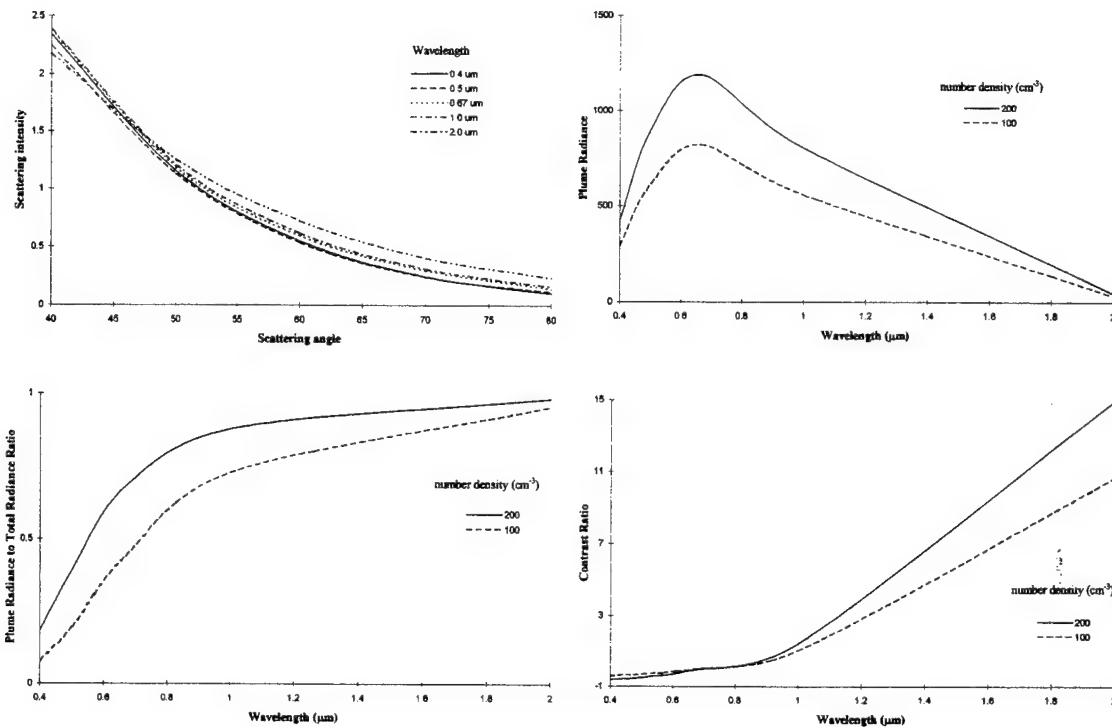


Figure 4-32. Optical and Radiometric Properties for 8:00 A.M. Plumes for Upward Looking Sensor Using Single Scattering Model

The scattering intensity at this angle (60°) is much lower than at 11:00 A.M. As a result, the plume scatters less radiance (about one-fifth) than the multi-scattering model, and thus the image has a lower contrast. The angular variation in the scattering function can be seen by the brightness of the plume towards the sun (top of the image). This differs from the uniform diffuse scattering of the multi-scattering model. The higher number density enhances the contrast (both negative and positive) in the plume.

These same scenes will be used for validation against MODTRAN in Chapter 5. Some conclusions about the applicability of the models will be given there.

4.2.2 LANL Cooling Tower Plume

The LANL plume model is illustrated next. As mentioned in Chapter 3, the code is still under development, so the results presented here are meant to illustrate the capabilities of DIRSIG, but not to model actual plume properties. The same Kodak Hawkeye complex is used as the background scene. It contains a stack of height 53 m and a diameter of 5 m. Actual cooling towers have diameters considerably larger. The LANL plume model is run with 12 regions each approximately 6.5 m long. The ACAD wire frame is shown in Figure 3-3. The initial plume parameters are shown in Table 4-5.

Plume exit temperature	300 K
Plume exit velocity	4 m/s
Initial water droplet density	1033 cm^{-3}
Initial droplet size	$6 \mu\text{m}$
Wind speed	5 m/s (11.25 mph)
Time of day	1400 (local)
Ambient air temperature	280 K

Table 4-5. Properties of LANL Plume

The LANL plume model is run to determine the plume characteristics for each region downwind. The only plume constituent is water droplets. Figure 4-33 shows the change in number density, temperature, and mean droplet size for each region.

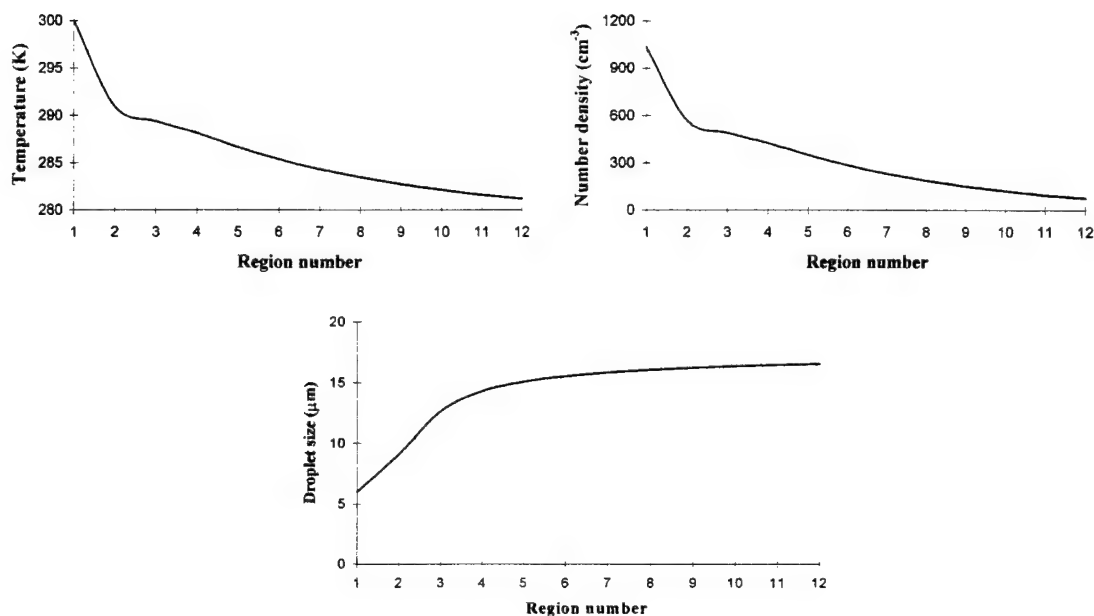


Figure 4-33. LANL Plume Properties

The droplet size increases due to additional condensation of water vapor onto the aerosol nuclei. The size levels out after region six due to evaporation effects. The temperature and number density both drop quickly due to dilution of the plume, as also seen in the JPL plume model. They are similar since the number density is proportional to the temperature contrast.

The image is run in three spectral bands. The first is the visible (0.4-0.714 μm), the second is the MWIR (3-5 -4 μm), and the third in LWIR (10 -11.5 μm). The droplets have a modified Gamma size distribution with $\alpha = 25$. The shape of the size distribution is constant throughout the plume. The optical properties of a 6 μm water droplet in the three bands are given in Table 4-6.

Band	$C_{\text{scattering}} (\mu\text{m}^2)$	$C_{\text{absorption}} (\mu\text{m}^2)$	ω_o	g
Visible	247	0	1.0	0.86
MWIR	243	18.4	0.93	0.70
LWIR	67.33	78.84	0.46	0.84

Table 4-6. Optical Properties of 6 μm Water Droplet

The absorption is largest in the LWIR, while scattering is strongest in the visible band. The multiple scattering algorithm is used. The images of the three bands are shown in Figure 4-34. The optical properties along the centerline of the plume for each region are plotted in Figure 4-35.

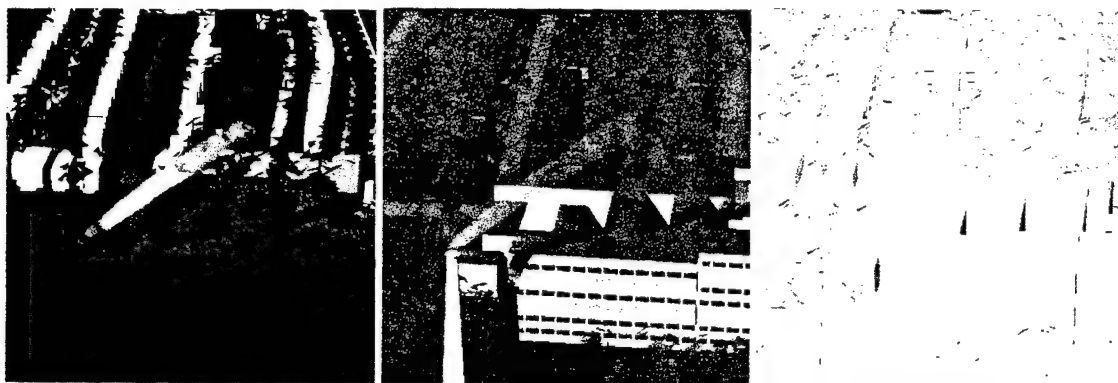


Figure 4-34. Visible, MWIR, and LWIR Images of the LANL plume model

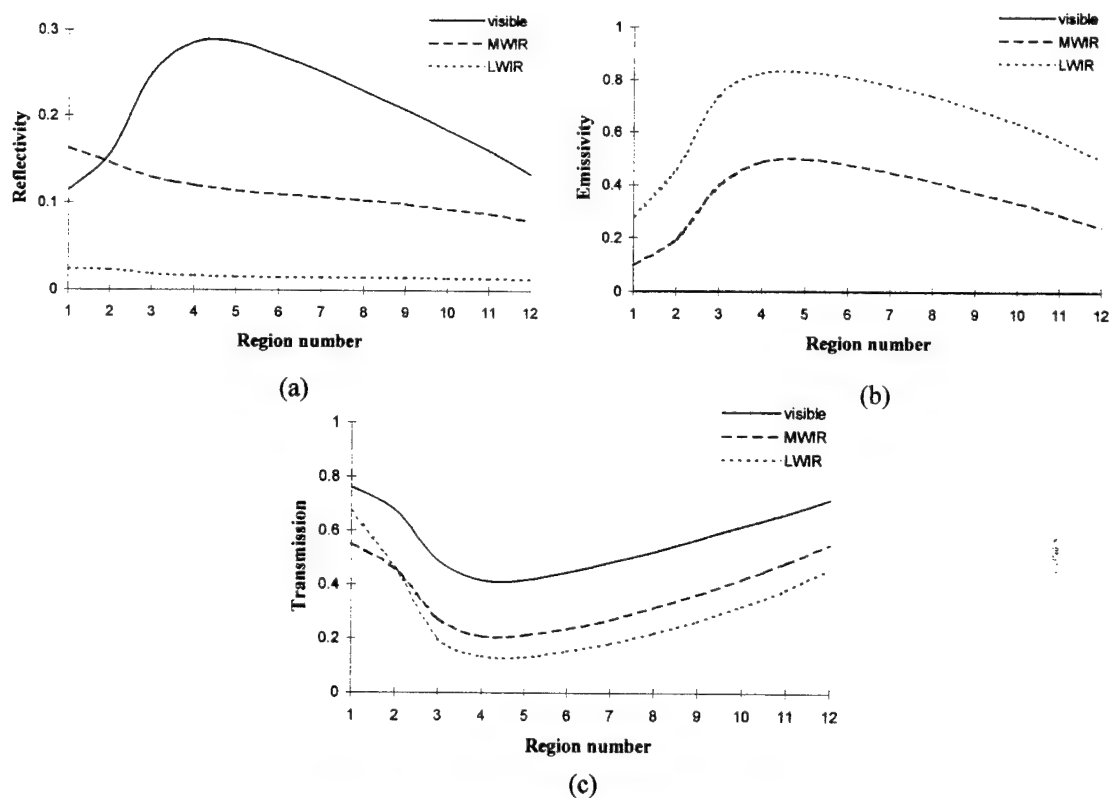


Figure 4-35. Optical Properties of LANL Plume

The reflectivity plotted represents the diffuse reflectivity for direct sunlight. The visible region has the highest reflectivity due to conservative scattering in that band. Notice that the reflectivity increases downwind until region five, then decreases. This can be seen in the image where the plume becomes more visible and then begins to dissipate. This is due to two competing effects. The first is the increase in droplet size resulting in a larger scattering cross-section. The second is the dilution of the plume and decrease in number density. As the plume exits the stack, the droplet size is still small, despite the large

number density. As the droplet size grows, the plume becomes more visible. However the decrease in number density causes the plume to disappear further downwind from the stack. The effect of scattering decreases in the MWIR, and is negligible in the LWIR where self-emission is the source of plume radiance. The emissivity undergoes the same behavior of increase followed by decrease except in the visible band where there is no absorption. The plume is most transparent in visible light, since the scattering is conservative and in the forward direction (see eqn 2-41). Because of the narrow radius of the plume, the optical depth is rather low for a cooling tower plume. The contrast of the plume in the LWIR is low due to the low temperature contrast of the plume ($< 5\text{ K}^\circ$ after region seven). Also the individual plume regions become visible in the MWIR and LWIR bands. This is an artifact when computing the self-emission due to the attenuation of intervening regions. The regions are not as apparent in the visible since the two-stream calculation is based on the total optical depth through the plume.

5. Validation

To validate the DIRSIG plume model requires experimental data. Unfortunately, little is available, especially on the scattering aspect. Data are available on the release of a gas (SF_6) plume in the LWIR. This will be used to validate the gas plume model. No data was found for a cooling tower plume. The scattering model will require validation based on other models or qualitative observed phenomena. To accomplish this, MODTRAN will be used to simulate a "plume" layer and the results compared with DIRSIG. Also, the scattering models will be tested by simulating two different atmospheric scattering phenomena in nature.

5.1 Validation of Gas Plume Model

This section describes the validation of the gas plume model with actual collected data. Because the validation is in the LWIR region, only absorption and self-emission effects are taken into account. The data is that of a SF_6 plume released at the Nevada Test Site (NTS) and collected by a multi-spectral imager. The DIRSIG gas plume model will be validated using both the ACAD JPL model and the integrated JPL model. A comparison of the plume characteristics, radiance values, and plume-background contrast is made at two different spectral bands. Note that all radiance values here are integrated over the appropriate spectral band and given in $\mu\text{Watts-cm}^{-2}\text{-sr}^{-1}$.

5.1.1 Experimental Description

In February and March of 1994 the Effluent Tracking Experiment was conducted at the NTS. A variety of chemicals were released to simulate a chemical manufacturing site. A particular data set from 25 February was chosen for use in validating the DIRSIG plume model. Vaporized SF_6 was mixed with hot air from a jet start cart and released from a 71-foot tall stack with a 0.41275 m diameter. SF_6 is an inert gas with a strong absorption and emission band from 10.5 to 10.75 μm . Figure 5-1 shows the spectral absorbance curve for SF_6 .

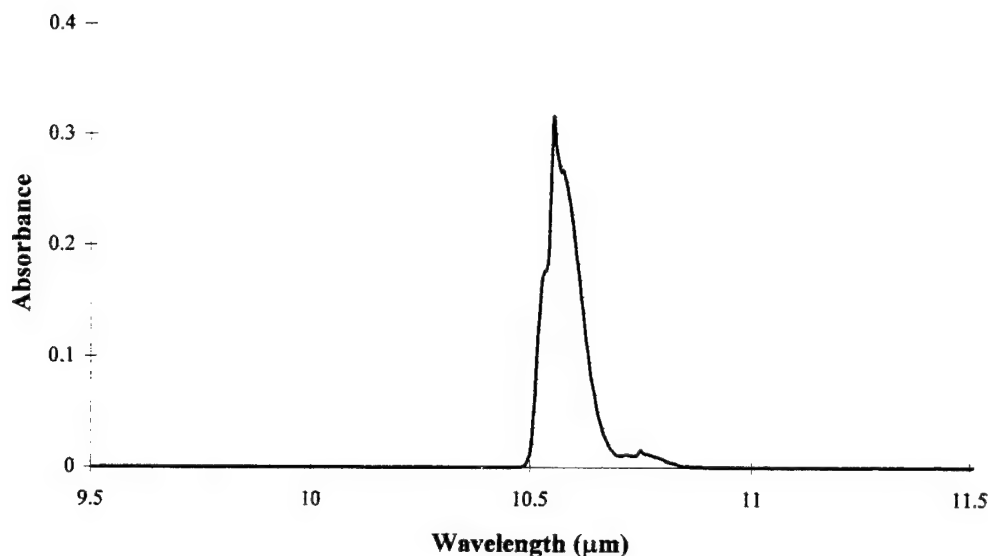


Figure 5-1. Absorbance Curve for SF₆ at 10 ppm-m

A description of the chemical release parameters can be found in a report by Westerberg, et al., 1994.

The sensor used for the data collection was a Texas Instrument IRLS-RS18c multi-spectrometer. There were 6 bands ranging from 7.75 to 11.75 μm . The two bands chosen as the validation data were from 10.4 to 11 μm and 9.8 to 11 μm . Figure 5-2 shows the spectral response of the sensor at these two bands.

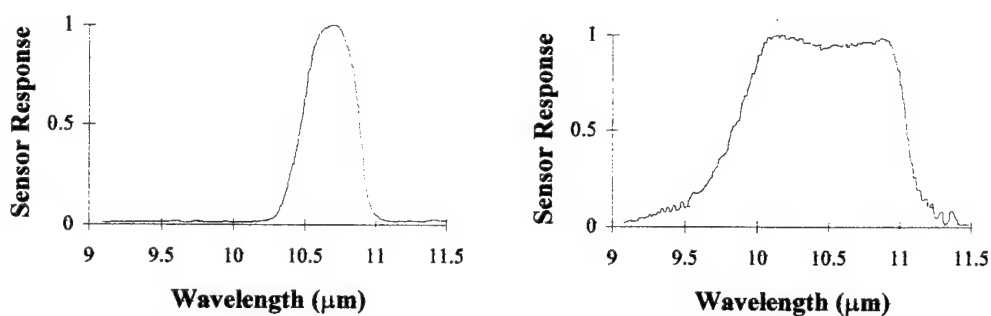


Figure 5-2. Sensor Response of Band 1 (left) and Band 2 (right) of the TI IRLS-RS18c Sensor

At these two bands a 400 by 400 pixel image of the plume was collected and the calibrated radiance values were assigned to each pixel. The images in these two bands are shown in Figure 5-3.

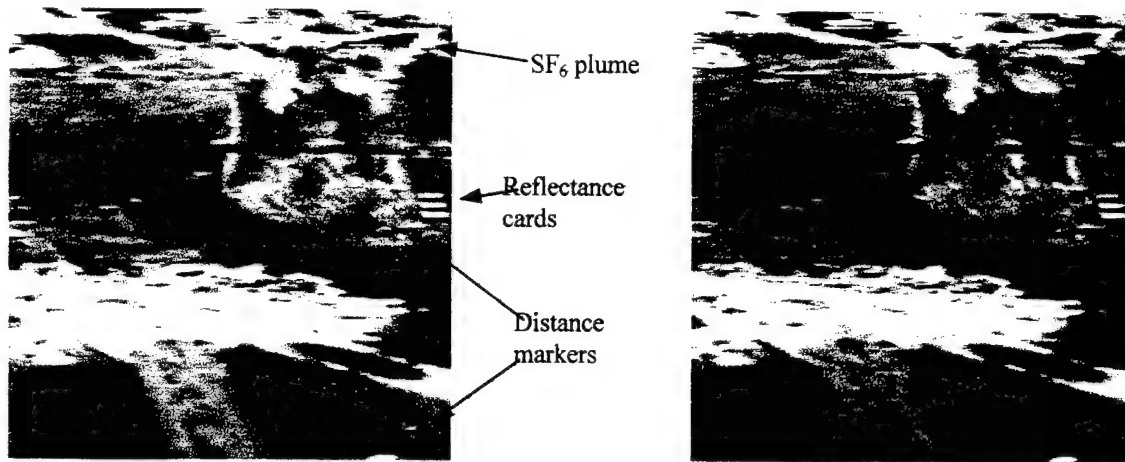


Figure 5-3. SF₆ Plume Images from Band 1 (left) and 2 (right) of TI ILRS-RS18c

The scene contains reflectance cards as well as a string of distance markers. These markers are spaced 25, 50, 100, and 200 meters apart. The plume is seen distinctly the first 25 m from the release point, and then fades away quickly. The plume passes over a bright patch of ground and “disappears” due to the lack of contrast. The bright patch is most likely due to a change in emissivity from the surrounding ground. It then reappears for a short distance before passing over an ever brighter patch of ground. The plume is also more visible in band 1 since its response is designed to match that of the SF₆ absorbance curve.

The images were taken at 4:18 P.M.. The ambient air temperature is at 18.5 C° with an average ground temperature of 9 C° and a wind speed of 3.4 m/s (~7 knots). This data was collected later in the afternoon at 5:20 P.M.. The sensor is at an altitude of 152 m with a ground speed of 100 knots. The release rate of SF₆ is 50 lbs/hr at a temperature of 363 K°. The stack release velocity is 15 m/s.

5.1.2 Creation of the DIRSIG Background Scene

The first step in creating the DIRSIG scene is to create the background. The main objects in the scene are the background, the first bright patch the plume passes over (labeled dirt patch 2), the second brighter patch (labeled dirt patch 1), the distance markers, and 4 reflectance panels. The temperature of all these objects are set to the average measured temperature of 9 C°. No experimental information was provided on the emissivities of the dirt and the patches. The emissivities of these objects in DIRSIG (except for the reflectance panels) are calibrated so as to match the radiance measured at the sensor in band 1. The background and dirt patches are intended to represent the average radiance in that area (based on the measured radiance). The reflectance panels have reflectances of 90%, 60%, 30%, and 0%. The markers have a 70% reflectance. The emissivities, DIRSIG radiance, and actual radiance values (in $\mu\text{Watts-cm}^{-2}\text{-sr}^{-1}$) for these objects are listed in Table 5-1.

Object	DIRSIG emissivity	DIRSIG radiance Band 1 / Band 2	Measured radiance Band 1 / Band 2
Background	0.65	196 / 511	195 / 550
Dirt patch 1	0.875	259 / 678	260 / 800
Dirt patch 2	0.73	218 / 568	215 / 710
Reflectance Panel 1	0.10	40 / 101	-174 / -1088
Reflectance Panel 2	0.40	125 / 324	233 / 718
Reflectance Panel 3	0.70	210 / 548	250 / 812
Reflectance Panel 4	1.0	295 / 771	261 / 837
Distance Markers	0.30	96 / 247	180 / 630

Table 5-1. Emissivity and Radiance Values for NTS Scene

The emissivity for the background is lower than what dirt normally is the LWIR (around 0.8). The reason why it is set this low is to match the calibrated radiance values from band 1. This indicates that there is some discrepancy between the calibration method done on the NTS experimental data and the radiance values calculated in DIRSIG. Also note the negative measured radiance value for reflectance panel 1. Since the interest in this research is plume modeling, the contrast between the plume and background is more important than absolute radiometric values. The lower emissivity value does cause the DIRSIG radiance to be lower in band 2. If realistic emissivity values were used then the backgrounds in band 2 would match more closely. This indicates the calibration problem is probably in band 1. An overhead scene is shown in Figure 5-4.

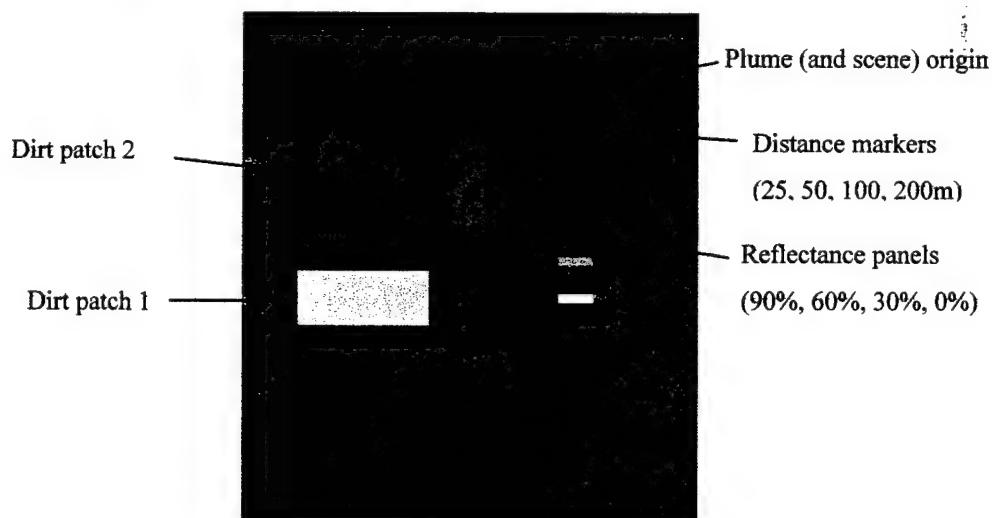


Figure 5-4. DIRSIG Scene of NTS Background

Since the exact coordinates of where the sensor was is unknown, the view angles for the scene are set-up to best recreate the scale and angle of the actual scene. The plume release point is set to an absolute coordinate value of $(x,y,z) = (0, 0, 0)$. The scene center is located at $(-80, -40, 0)$, with units in meters, and the sensor is located at $(-80, -354, 350)$. The sensor has a 50mm focal length and is looking down 30° below the horizon. Note that the reported sensor altitude is lower (~ 152 m), but the correct look angles could not be reproduced using that altitude.

The same two frequency bands and their appropriate sensor response are recreated in DIRISG. The first band has a frequency from 910 to 960 cm^{-1} at a 5 cm^{-1} interval (10.4167 - $10.989\text{ }\mu\text{m}$). The second band has a frequency from 910 to 1020 cm^{-1} at a 10 cm^{-1} interval (9.804 - $10.989\text{ }\mu\text{m}$). MODTRAN is used to calculate the appropriate atmospheric transmission and upwelled radiance for those two bands. The sensor responses are taken from Figure 5-2.

5.1.3 Validation of ACAD JPL Model

Common to both models is the JPL plume code. The "Plume_Input" file is setup to match the meteorological and plume release conditions described above. A listing of this file is shown in Appendix I. This input file is used in generating the ACAD plume model as well as the integrated JPL model. The ACAD model is generated by sampling the plume every 20 m to a distance of 180 m downwind. Four regions are created with each region differing in dilution by approximately an order of magnitude. Table 5-2 describes each region's characteristics.

Region #	Maximum Length (m)	Temperature (C°)	VMR (ppm)
1	180	18.47	2.7
2	100	18.85	36.55
3	40	20.77	261
4	18	26.68	939.9

Table 5-2. Region Description of ACAD Plume Model

The difference in dilution (and VMR) between each region is about an order of magnitude except for the last two regions. The inner region (#4) has a high VMR that is an overestimation by the plume model (this same effect occurs with the integrated model). However, the effects are minimized since the region is very thin (less than a 1 m radius). The PMT generates the appropriate GDB file and optical tables (include in Appendix I). The GDB has over 650 facets for the plume. A 400×400 pixel image is generated for an overhead view (sensor altitude of 350 m) and a ground view looking up. The plume is oriented along the distance markers to give an indication of its dimension. Figure 5-5 shows these images in band 1.

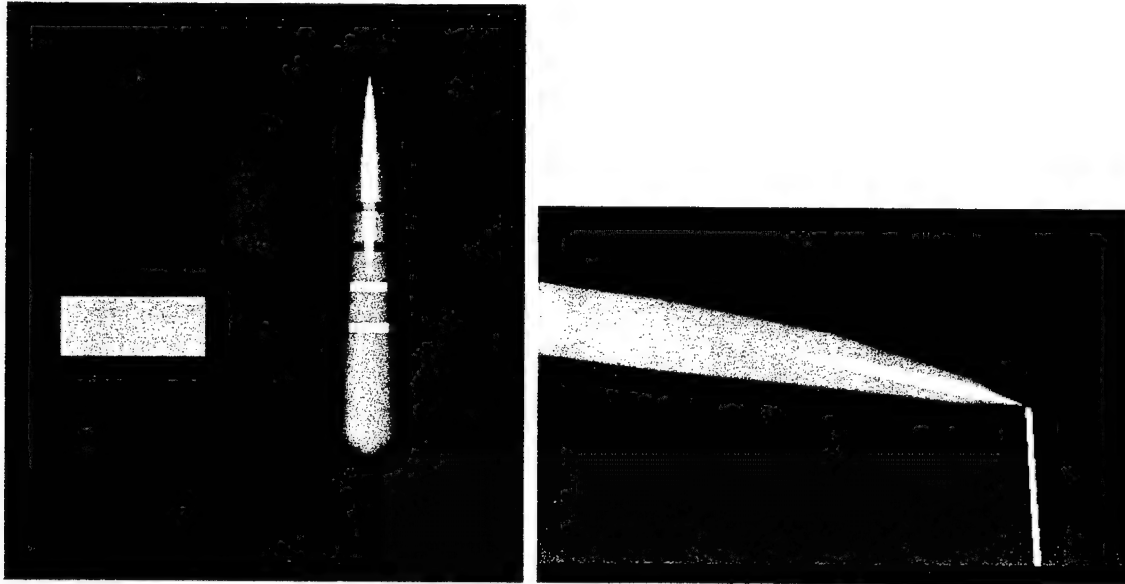


Figure 5-5. Overhead and Side View of ACAD Plume Model (Band 1)

The plume extends out to 180 m. The plume appears blocky because of the constant characteristics of each region. Region's one and two can be seen quite distinctly in the overhead view, while the inner two regions are harder to make out due to the shorter length. Region three is seen more distinctly from the side view, and region 4 is barely seen as a thin line extending from the stack. The stack is slanted due to the wide field-of-view. The total computer run time for this size image is about fifty minutes. The scene is next run using the NTS look angles described above. Figure 5-6 shows the images for band 1 and 2.

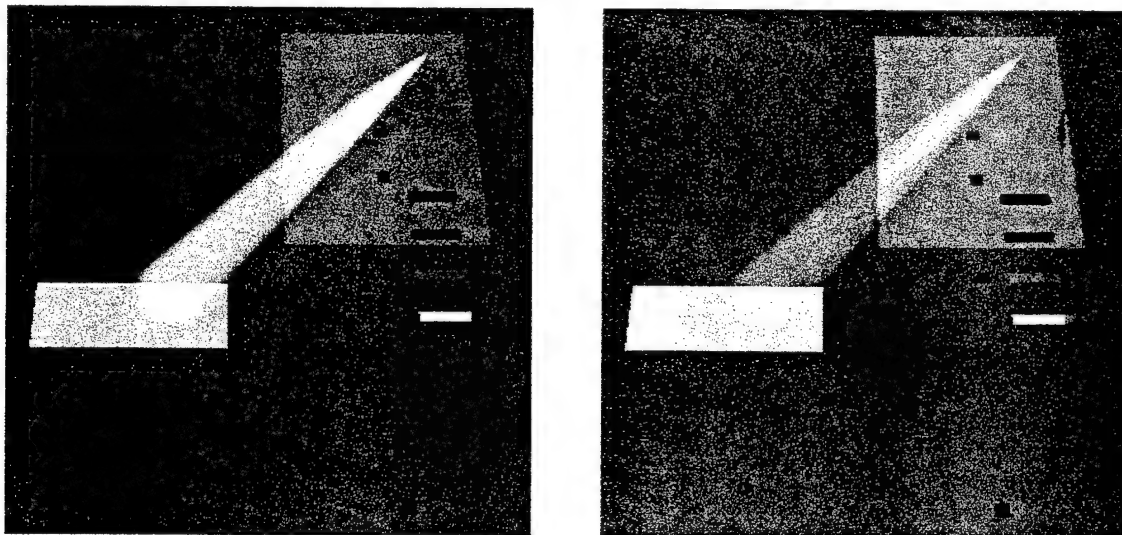


Figure 5-6. ACAD Plume Model in Band 1 (left) and Band 2 (right) using NTS Look Angles

Each image is auto-scaled independently. The plume is less apparent in band 2 since it is had a broader spectral band. The radiance profile along the centerline of the plume is taken from both the NTS image and

the DIRSIG image for the first 35 m. It is up to this distance where the plume is most visible and the background is fairly constant. The profiles are shown in Figure 5-7 and Figure 5-8.

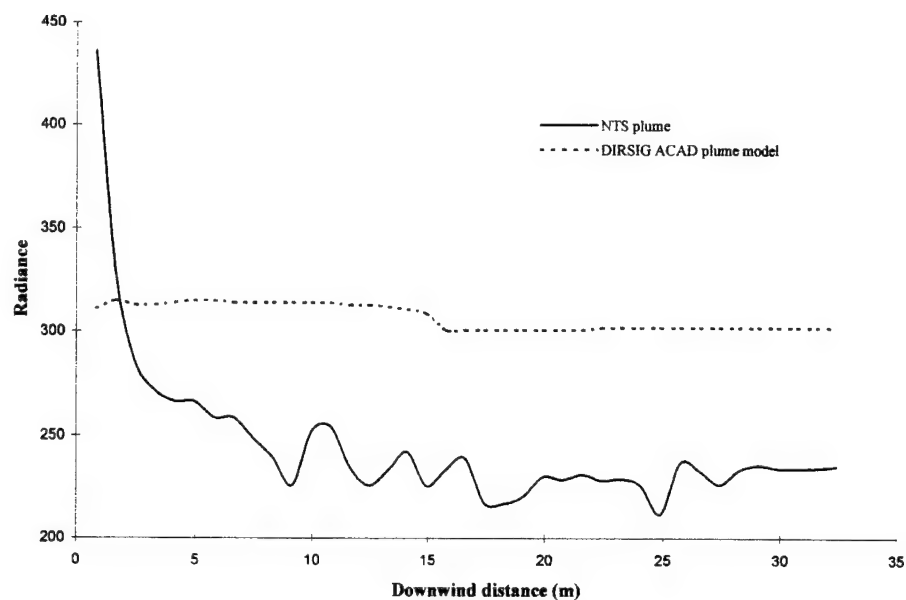


Figure 5-7. Downwind Radiance Profile in Band 1

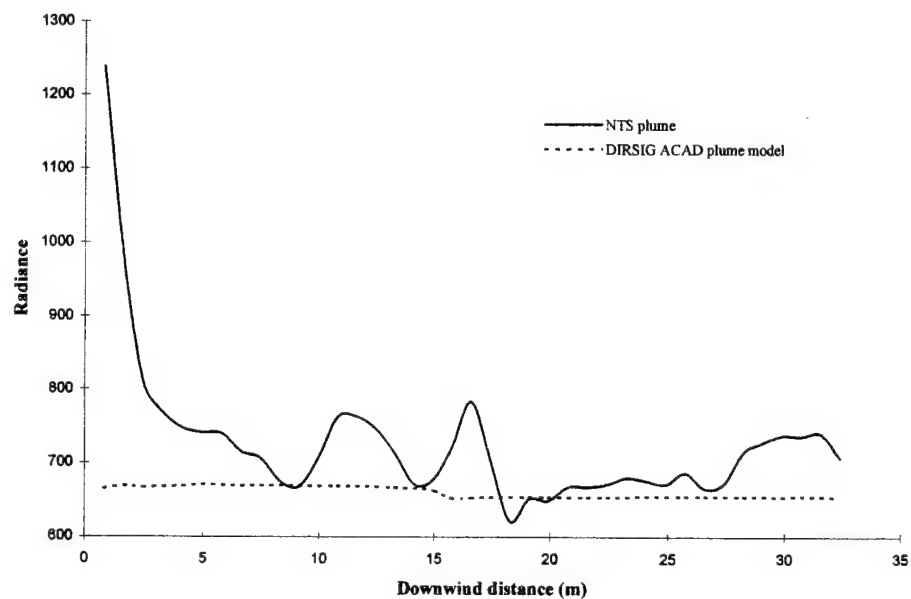


Figure 5-8. Downwind Radiance Profile in Band 2

There is little variation in the DIRSIG ACAD model, with a slight drop at 15 m where the plume transitions from region 4 to region 3. In band 1 DIRSIG overestimates the actual plume by over 30%

(except for the first 5 m). This is evident in the DIRSIG image where the plume is more visible than in the NTS image. In band 2 the DIRSIG radiance matches more closely the average real plume radiance. The better results for band 2 are unexpected, since the background matching is done for band 1. The cross-sectional radiance profile across the plume is taken at 7 m and 100 m downwind. These profiles are taken where there is minimal background variation behind the plume. The profiles at 7 m are shown in Figure 5-9 and Figure 5-10.

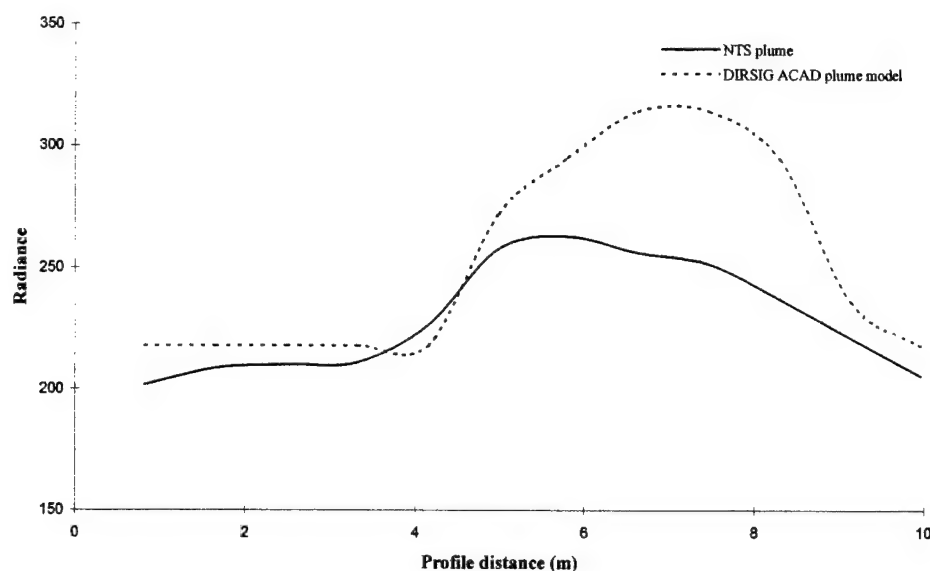


Figure 5-9. Cross-sectional Radiance Profile of Plume 7 Meters Downwind in Band 1

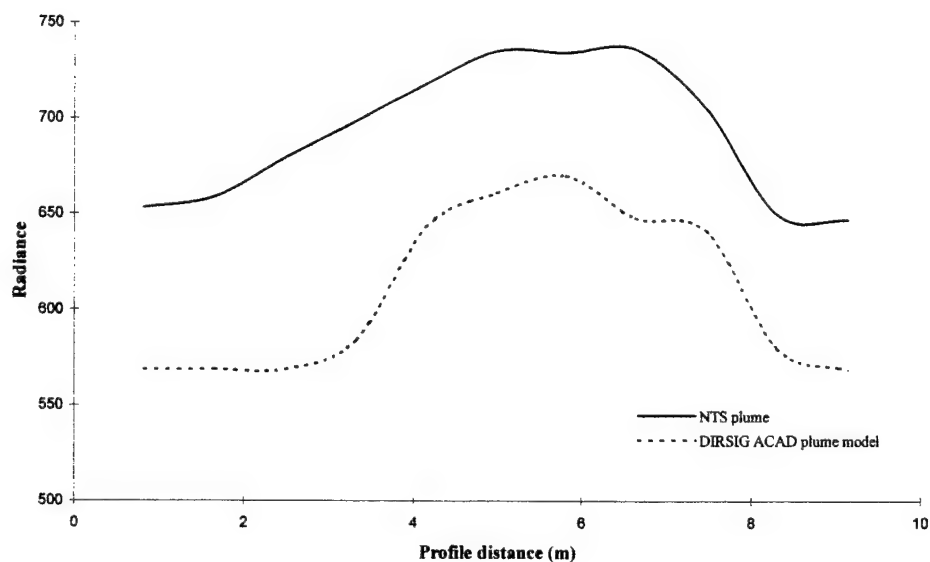


Figure 5-10. Cross-sectional Radiance Profile of Plume 7 Meters Downwind in Band 2

As evident in the downwind profiles, DIRSIG overestimates the radiance by 30% in band 1, while it underestimates it by 9% in band 2. However the profile shape of the DIRSIG plume is in good agreement with the actual plume. The background matching in band 1 can clearly be seen. The profiles at 100 m down wind are shown in Figure 5-11 and Figure 5-12.

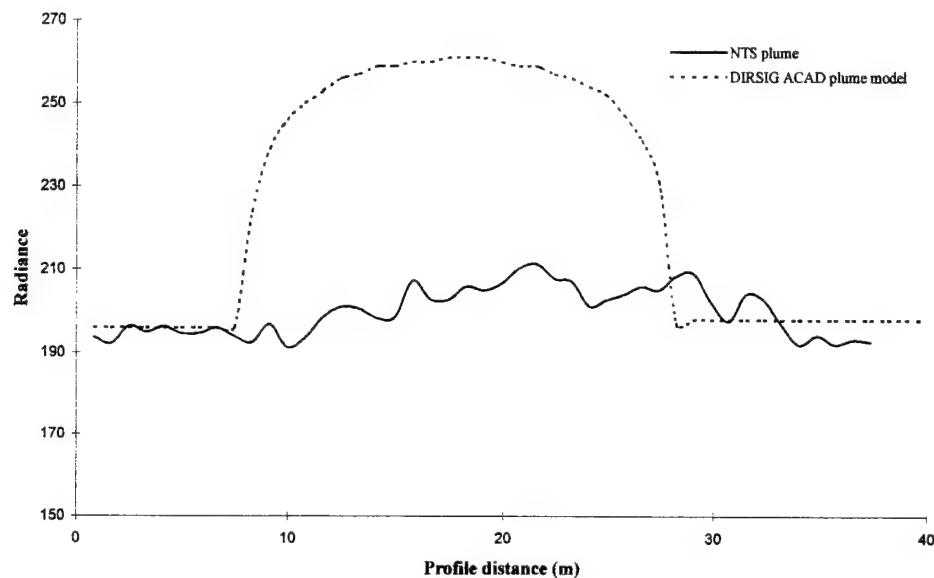


Figure 5-11. Cross-sectional Radiance Profile of Plume 100 Meters Downwind in Band 1

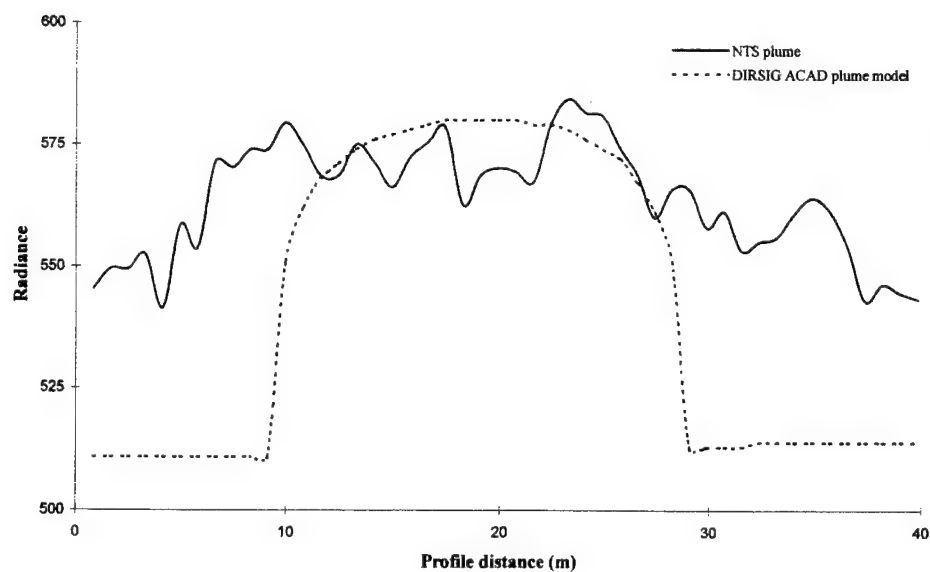


Figure 5-12. Cross-sectional Radiance Profile of Plume 100 Meters Downwind in Band 2

DIRSIG continues to overestimate the radiance (by 20%) in band 1. It would also overestimate it in band 2 if the backgrounds were matched. The profile of the DIRSIG plume is much more distinctive, while in the NTS image the background noise hides the plume. This is seen when comparing the DIRSIG and NTS images.

The ACAD model produces a discrete plume, and thus all its properties are discrete. As a result it does not follow the trend of the real plume downwind. Also the ACAD model considerably overestimates the plume radiance downwind. This is clearly evident in the DIRSIG image where the plume is quite visible for an extended distance compared to the NTS plume. One reason for this is that the DIRSIG plume is a "solid" object, while in reality the plume puffs and has gaps within its boundary. Another problem with the ACAD model is the considerable amount of work that needs to be done before actually running DIRSIG. This means re-running certain parameters (wind speed, stack release rate) involves a considerable effort.

5.1.4 Validation of Integrated JPL Model

The integrated JPL plume model is validated next using the same JPL input file. The PMT is used to generate the SF₆ absorbance table which is included in Appendix I. The overhead and side views for band 1 are shown in Figure 5-13.

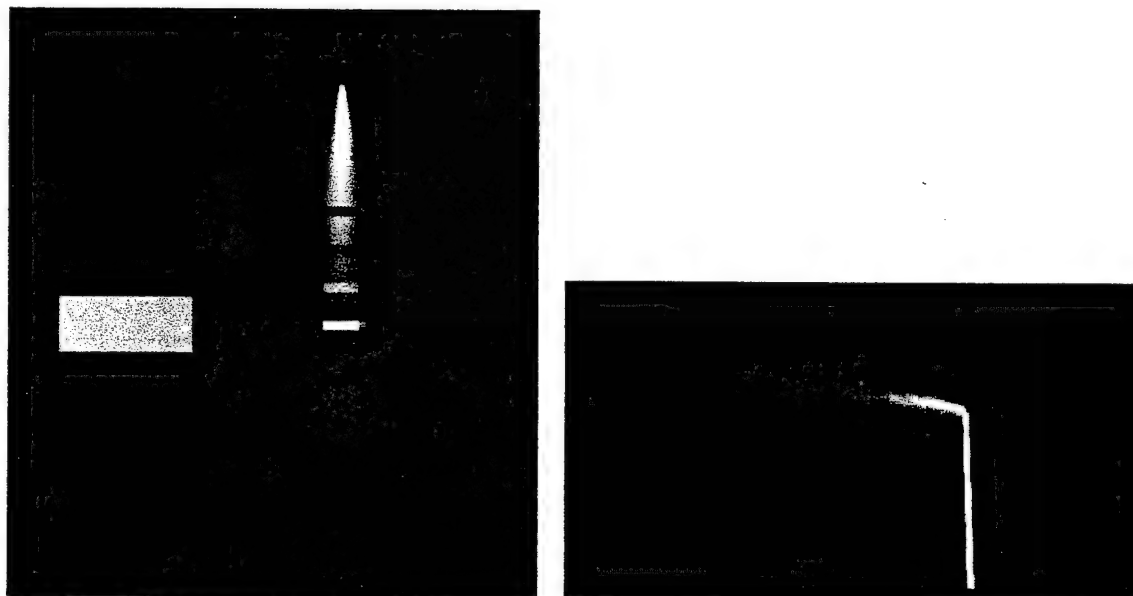


Figure 5-13. Overhead and Side View of Integrated JPL Plume Model

The total computer run time for this image is also approximately fifty minutes. The plume extends out to approximately 225 m, however it is only visible for the first 100 m. The plume has a Gaussian shape out to about 100 m, and beyond that remains constant. This is because the plume code is set to register the presence of a plume only when the column density is greater than 1 ppm-m. Thus the plume actually

shrinks further downwind because of this condition. The image from the integrated plume model has a more continuous and smooth looking plume than the ACAD model. The four distinctive regions in the ACAD model can be vaguely seen in the integrated model. The temperature profile along the centerline of the plume is derived using the plume debug images. This can be compared with the actual measured plume temperature during the experiment (although the temperature was not measured at the same time as the image was taken). This temperature was derived using a blackbody fit based on measurements from a spectrometer. These two graphs are plotted in Figure 5-14 and Figure 5-15.

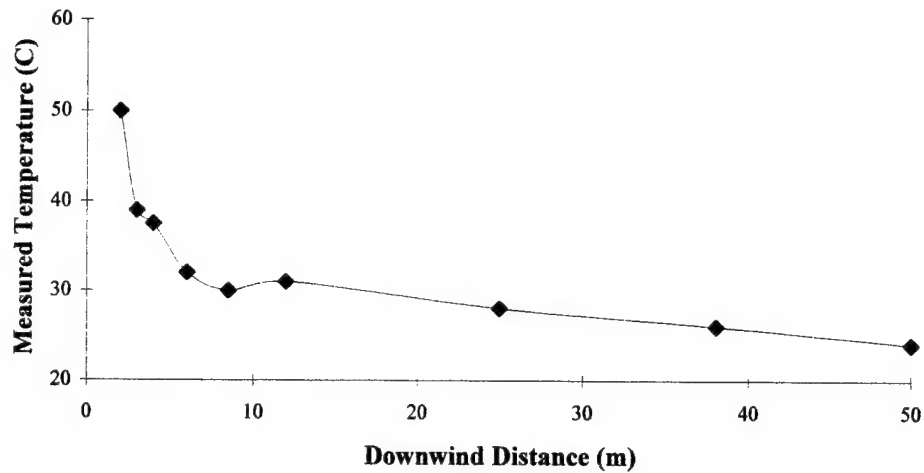


Figure 5-14. Measured Plume Temperature Downwind from Stack

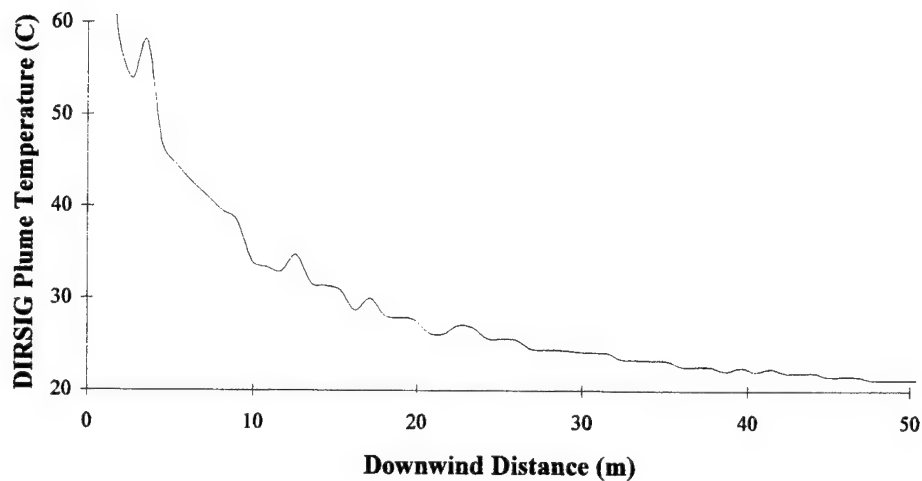


Figure 5-15. DIRSIG Plume Temperature

DIRSIG over predicts the plume temperature for the first 15 m. At 10 m the DIRSIG temperature is approximately 10% higher than the measured temperature. This error may be expected since entrainment of ambient air is not modeled and thus the plume does not cool off as quickly. However further downwind the model and experimental data match quite closely (less than 10%) when the difference in ambient temperature is accounted for. The column density profile along the centerline can also be plotted using the debug images. This is shown in Figure 5-16.

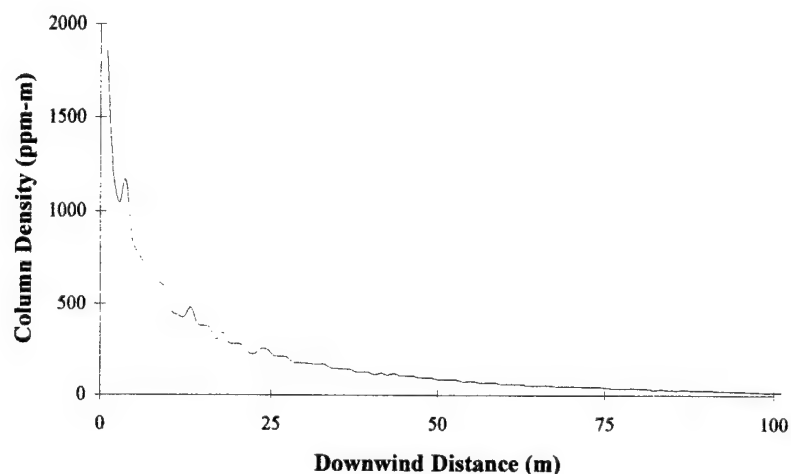


Figure 5-16. DIRSIG Column Density Downwind from Stack

The same trend as the plume temperature is evident with a rapid drop-off in value in the first 25-30 m and then a gradual leveling out. This is because in the model both the temperature and VMR are based on a common dilution factor. No experimental data was available showing the column density as a function of downwind distance. However, the AEROSPACE Ram Van spectrometer did take profile measurements of the column density across the plume at certain downwind distances. One particular measurement was taken 100 m downwind. The Ram Van and DIRSIG profiles are shown in Figure 5-17.

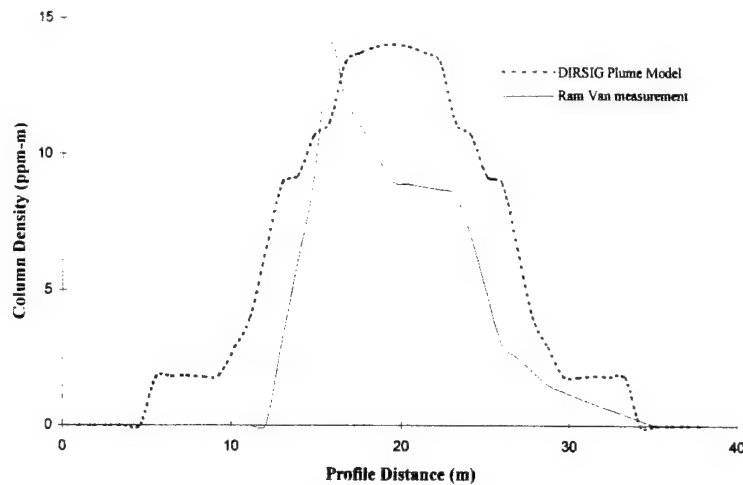


Figure 5-17. Column Density Profile at 100 Meters Downwind of Stack

The peak column density of both measurements are in good agreement with an error of less than 5%. The profile of the DIRSIG plume is wider by about 5 m, or 20%, than the measured profile. This is caused by a variety of conditions, most notably the difference in the instantaneous atmospheric conditions that set in the plume model. The only other column density profile available is at 500 M, which is beyond the downwind distance of the DIRSIG plume model.

The scene is then run using the NTS look angles. Figure 5-18 shows the images for band 1 and 2.

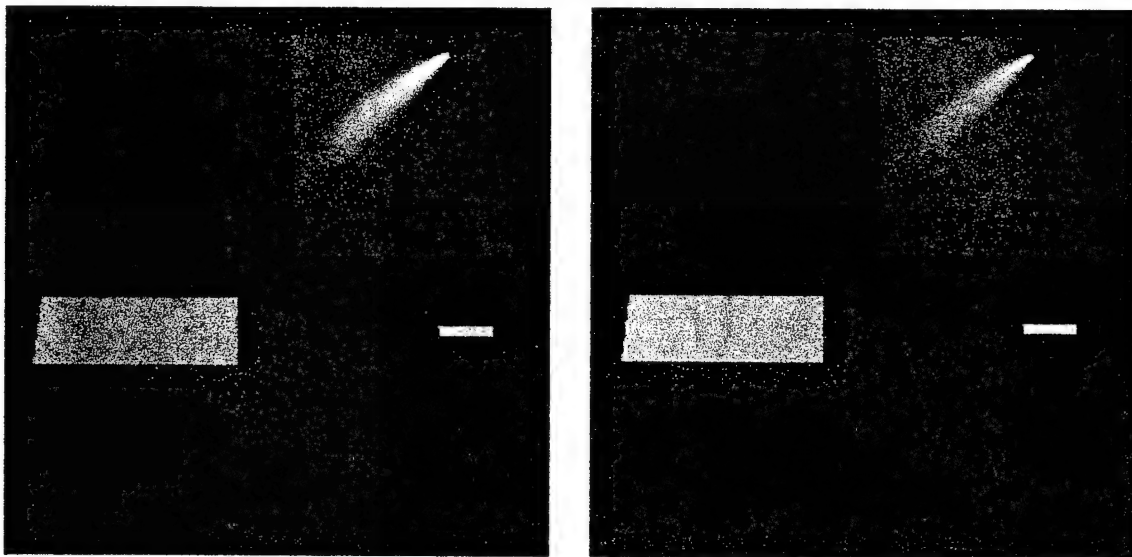


Figure 5-18. Integrated Plume Model in Band 1 (left) and Band 2 (right) using NTS Look Angles

The plume looks smoother and more realistic than the ACAD model. It is easily visible for the first 30 m, and then starts to fade rapidly. The plume is barely visible over the background, and loses contrast over dirt patch 1. The plume is also more visible in band 1, which is tuned to the SF_6 absorption band. The

radiance profile along the centerline of the plume is taken for the first 35 m. The two profiles for band 1 and 2 are shown in Figure 5-19 and Figure 5-20.

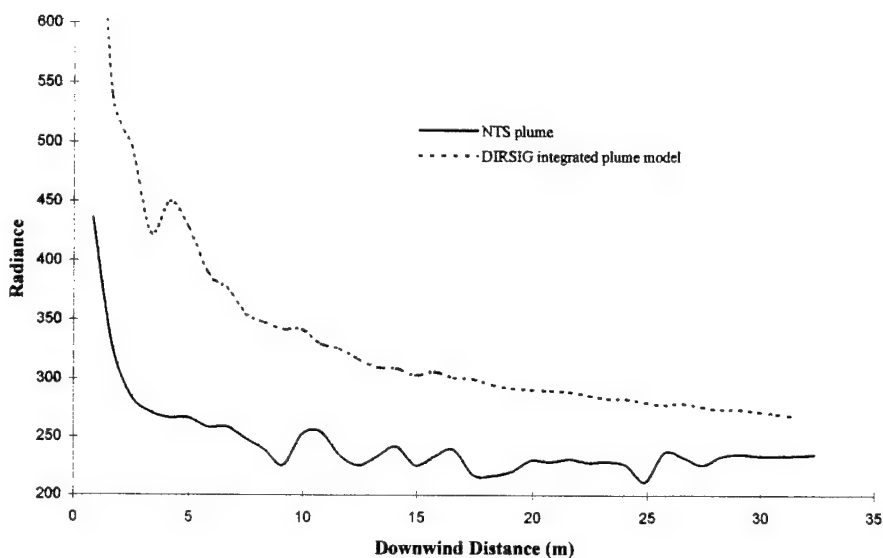


Figure 5-19. Downwind Radiance Profile in Band 1

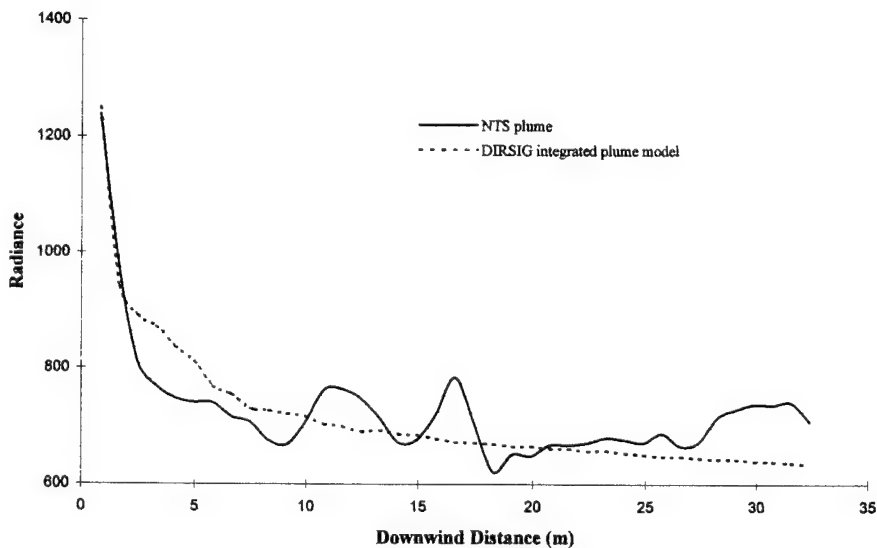


Figure 5-20. Downwind Radiance Profile in Band 2

In band 1 there is significant overestimation by DIRSIG in the first 5 m. This is the same case as with the plume temperature (possibly due to inaccurate entrainment modeling). After that, the gap between the two profiles narrows to where DIRSIG overestimates the radiance by about 20%. The bumps in the NTS images are from the variation in the background, which is uniform in the DIRSIG image. Remember the

radiance value from the DIRSIG background is set to match that from the NTS images, thus effectively eliminating any bias in the plume radiance value. The profiles in band 2 match more closely, practically overlapping each other. Again the better results for band 2 are unexpected, since the background matching is done for band 1. The cross-sectional radiance profile across the plume is taken at 7 m and 100 m downwind. The results for both bands at 7 m are shown in Figure 5-21 and Figure 5-22.

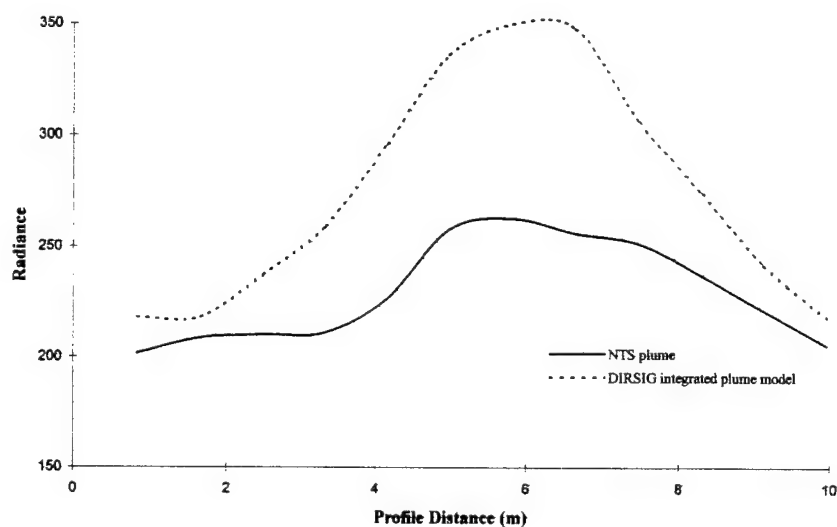


Figure 5-21. Cross-sectional Radiance Profile of Plume 7 Meters Downwind in Band 1

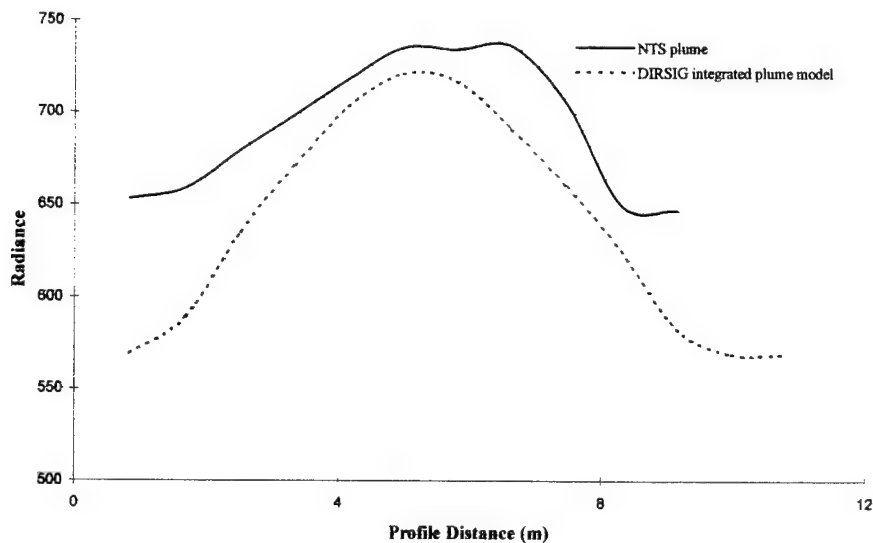


Figure 5-22. Cross-sectional Radiance Profile of Plume 7 Meters Downwind in Band 2

As expected the peak radiance of the DIRSIG model in band 1 is 40% higher than in the NTS data. However, the profile width matches fairly close, indicating the spatial extent of the DIRSIG model is correct. In band 2 the peak error is even less, however the mismatch in the background radiance is evident in the wings. The DIRSIG value for the background (dirt patch 2) is smaller by 15%. This is due to the artificially lowered emissivity values assigned in DIRSIG in order to match band 1. The profiles 100 m downwind are shown in Figure 5-23 and Figure 5-24.

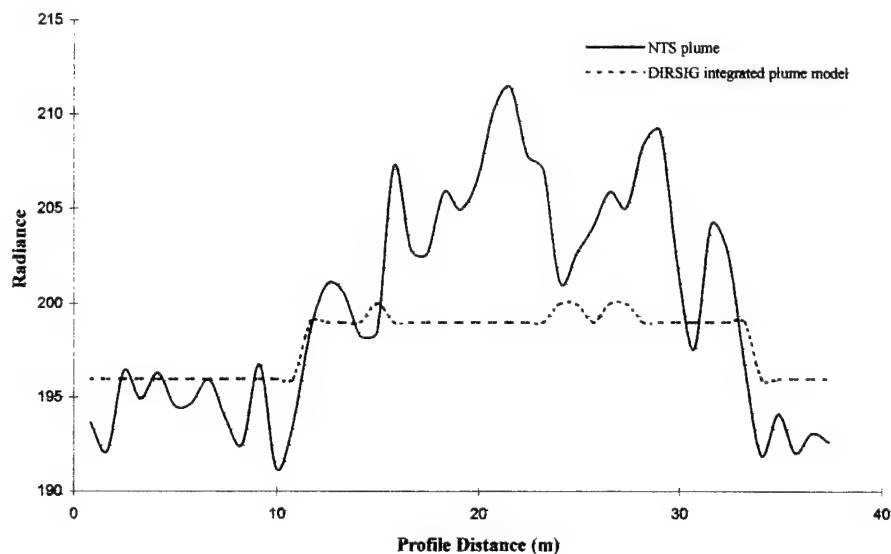


Figure 5-23. Cross-sectional Radiance Profile of Plume 100 Meters Downwind in Band 1

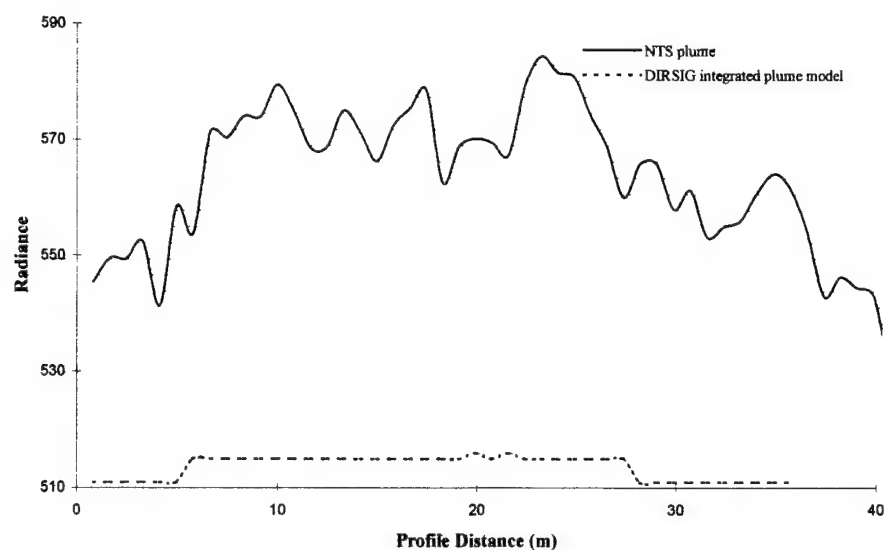


Figure 5-24. Cross-sectional Radiance Profile of Plume 100 Meters Downwind in Band 2

At 100 m downwind the DIRSIG values are now lower than the NTS plume in band 1 and 2. In band 1 the error in the peak values is now less than 15%. This corresponds to the good agreement in the column density measurements at 100 m (see Figure 5-17). In band 2 the lower DIRSIG value is primarily due to the mismatch in background values (as opposed to the matched backgrounds in band 1). This error should disappear when the calibration problem is resolved and the DIRSIG emissivity values are raised.

As it is clearly evident the integrated DIRSIG model is superior to using the ACAD model. The profiles in all the cases match more closely than the ACAD model, and the images of the plume look more natural. The temperature and column density are in good agreement to experimental measurements. The issue of the artificially low emissivity used in DIRSIG, due to possible calibration problems in band 1, still need to be resolved. However some observations about the plume radiance contrast can still be made. In the first 5 m the DIRSIG plume significantly overestimates the radiance value. This may be associated with the difficulty in modeling the turbulent jet-like flow coming right out of the stack. It seems entrainment of the ambient air is not quick enough, and the dilution factor remains too high in the model. After this point the model and data come into fairly good agreement. The profile at 100 m shows an error less than 10%. However, after 100 m the DIRSIG plume starts to dissipate faster than the NTS plume, as evident in the image. This is in part due to the model, which has a cutoff at 1 ppm-m. Also at these distances from the stack, the variability in meteorological conditions has had more time to impact the formation of the plume. The DIRSIG plume is run with constant meteorological conditions. It can be summarized from these validation results that the integrated DIRSIG plume model overestimates the plume radiance under 5 m from the stack, is in agreement to within 20% from 5 to 100 m, and then underestimates the radiance beyond 100 m due to limitations in the model.

The actual DIRSIG run times between the two models are the same. However the integrated version had very little preparation time associated with it. Changing certain parameters such as wind speed and release rate can be done quickly by changing the Plume_Input file and rerunning DIRSIG. Considering the better performance, ease of use, and shorter overall run time, the integrated JPL model should generally be used over the ACAD JPL model for gas plumes.

5.2 Scattering Validation with MODTRAN

There were no readily available experimental data on cooling tower plumes to validate the scattering algorithms. Also, it would be difficult to validate any sort of scattering data from plumes since the number of variables involved would make it hard to exactly model the same scene. Another possible source of data is from cloud observations. This is a common way to validate radiative transfer codes, such as the one adopted for DIRSIG (Slingo, 1985).

To radiometrically validate plume scattering, a MODTRAN "plume" is created that approximates the DIRSIG plume. The different cases run in section 4.2.1 are recreated in MODTRAN. While this method can not be really considered a validation (comparing one computer model with another), it will

determine whether the DIRSIG results are reasonable. To phenomenologically validate the scattering models, two occurrences in nature that result from scattering are used. For single scattering this is the rainbow, while for multiple scattering it is the red clouds seen at sunset.

5.2.1 MODTRAN

MODTRAN is a radiative transfer code developed by the Air Force Philips Lab that is widely used in the atmospheric modeling community (Anderson, 1995). It allows a user to define the atmosphere, scene geometry, and meteorological conditions. The outputs include atmospheric transmittance, self-emitted radiance, and scattered radiance. MODTRAN is used in DIRSIG to determine many of the atmospheric parameters in a scene. The MODTRAN multiple scattering model used for validation is based on a two-stream "flux-adding" method (Isaacs, 1987).

To create a "plume" in MODTRAN requires a special card deck to be built. A specific layer is defined as a plume layer, and the optical constants of the plume are used in that layer. This approach is similar to the one in Appendix B when comparing multiple to single scattering effects. The same optical constants used to create the DIRSIG plumes in section 4.2.1 are used in MODTRAN (from the Mie scattering code). The same variation in number density (1000, 600, 200, and 100 cm^{-3}) is also used. The layer is set at ground level and has a height of 25 m. For the downward-looking case the sensor is at 26 m, since a comparison is made of the scattered radiance right at the plume. For the upward-looking case the sensor is at ground level. In both cases the sensor look angle is normal to the plume layer (straight up or down). The same five wavelengths (0.4, 0.5, 0.67, 1.0, and 2.0 μm) are used. For the downward-looking case the noontime and 8:00 A.M. cases are used (solar zenith incident angles of 0° and 60° , respectively), while for the upward case the 11:00 A.M and 8:00 A.M. times are used (15° and 60° respectively). Figure 5-25 shows the geometries for these four cases.

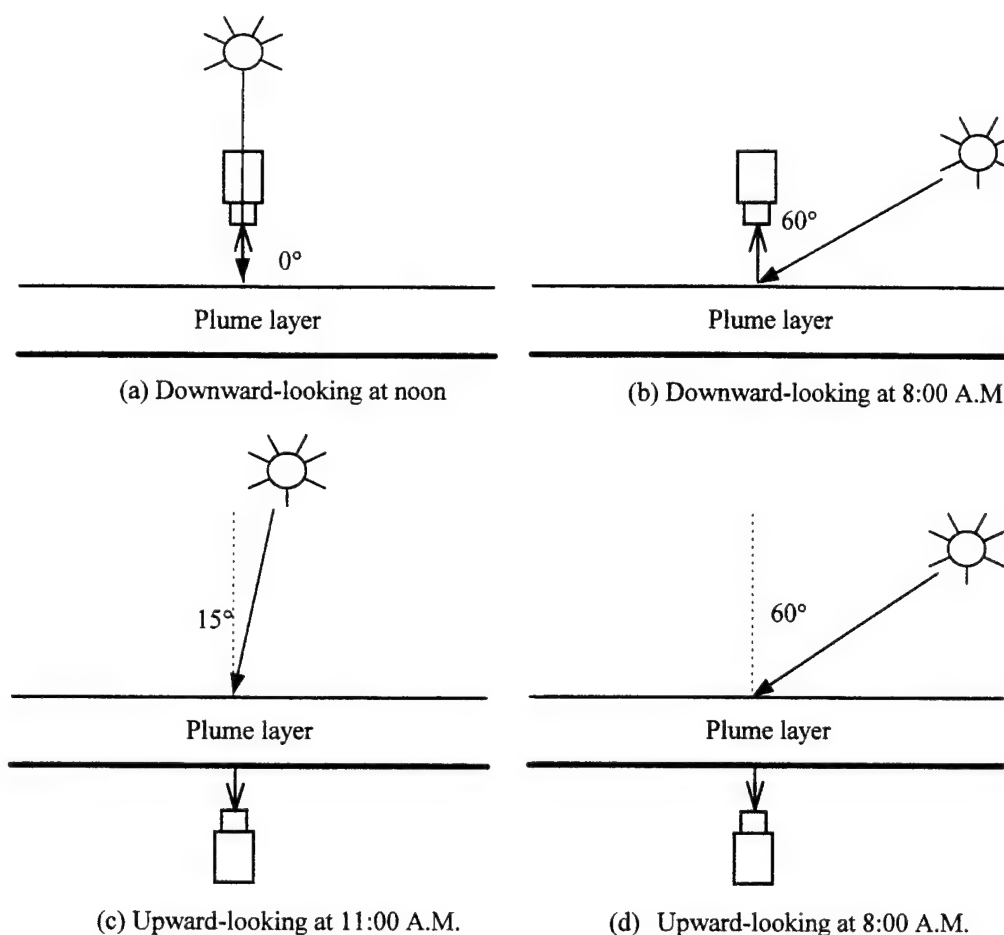


Figure 5-25. Geometries used for Scattering Validation

5.2.2 Results

A MODTRAN run is made for each of the four number densities. The radiance reaching the sensor from the plume layer for each run is recorded. Since the sensor is right at the edge of the plume layer, there are no intervening transmission losses. For the downward-looking case the radiance is solely from the scattered sunlight. There is no scattering of downwelled radiance. For the upward-looking case the radiance is from scattered sunlight and the transmitted downwelled radiance directly above the sensor.

The DIRSIG runs made in section 4.1.1 are used for the validation. There are four different number densities (1000 , 600 , 200 , and 100 cm^{-3}) for the multiple scattering algorithm, and two (200 and 100 cm^{-3}) for the single scattering algorithm. The center pixel radiance value in the plume is recorded. For the downward-looking case, the radiance comes only from the diffuse reflection of sunlight so as to correspond to the same radiance value represented in MODTRAN. For the upward-looking case the radiance comes from the diffusely transmitted (i.e., scattered) sunlight and the directional downwelled

radiance for the sensor look angle (straight up) accounting for the attenuation from the plume. The difference between the DIRSIG and MODTRAN radiance value is divided by the MODTRAN radiance value, which is assumed to be the "truth" value. This gives a contrast value between the two models. Figure 5-26 and Figure 5-27 show this contrast value for the downward-looking noon and 8:00 A.M. case. The M or S following the number density stands for the multiple or single scattering case.

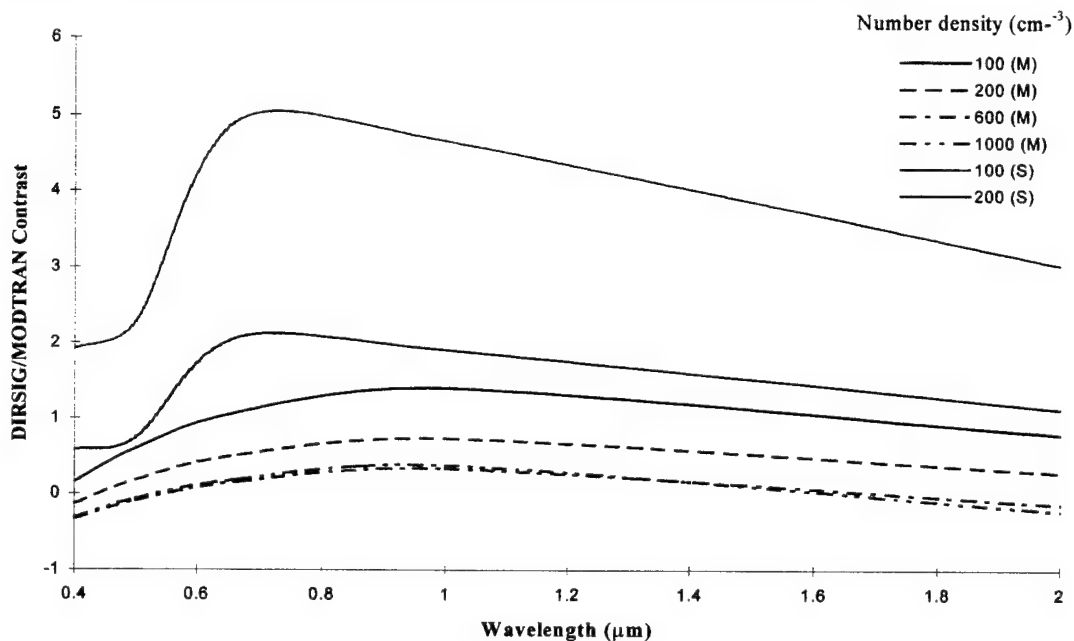


Figure 5-26. DIRSIG-MODTRAN Contrast for Downward-looking Noon Case

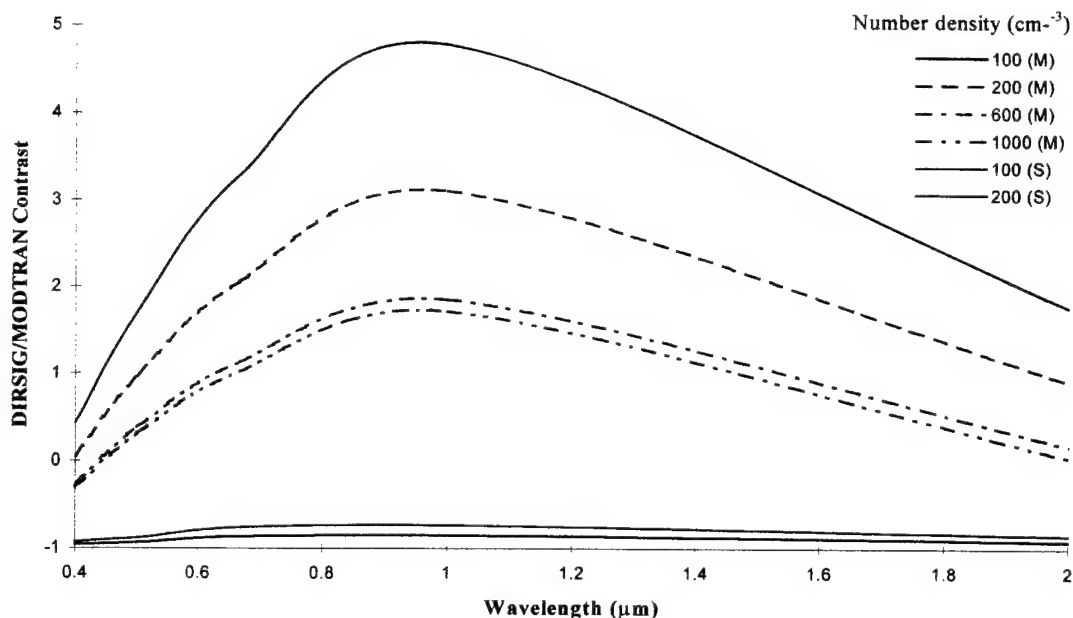


Figure 5-27. DIRSIG-MODTRAN Contrast for Downward-looking 8:00 A.M. Case

For the multiple scattering case the contrast decreases as the number density increases. This is to be expected since the delta-Eddington algorithm used in DIRSIG is best suited for optically thick cases. For the noontime case the two thickest plumes (optical depths of 3.5 and 6) have similar results with a contrast under 0.5. The error is greater at 8:00 A.M., with the larger solar zenith angle. Again this is expected since the delta-Eddington algorithm is not well suited for large zenith angles ($> 60^\circ$). DIRSIG overestimates the scattered radiance by up to a factor of two for the two thicker plumes. There is also a spectral variation, with the most error coming from the $1\mu\text{m}$ band. The cause for this is unknown. It is interesting to note that at $2\mu\text{m}$ where the scattering is non-conservative ($\omega_0 = .95$), the contrast decreases. For the single scattering case the results are highly dependent on the solar angle, which is to be expected. For the noontime case there is a strong backscatter peak (Figure 4-20a), which causes an overestimation of the scattered radiance. The opposite case occurs at 8:00 A.M., where there is a significant underestimation of the radiance. This is a result of the weaker scattering intensity at this angle (about 10 times lower than at noon).

The contrast between DIRSIG and MODTRAN for the upward-looking case is shown in Figure 5-28 and Figure 5-29.

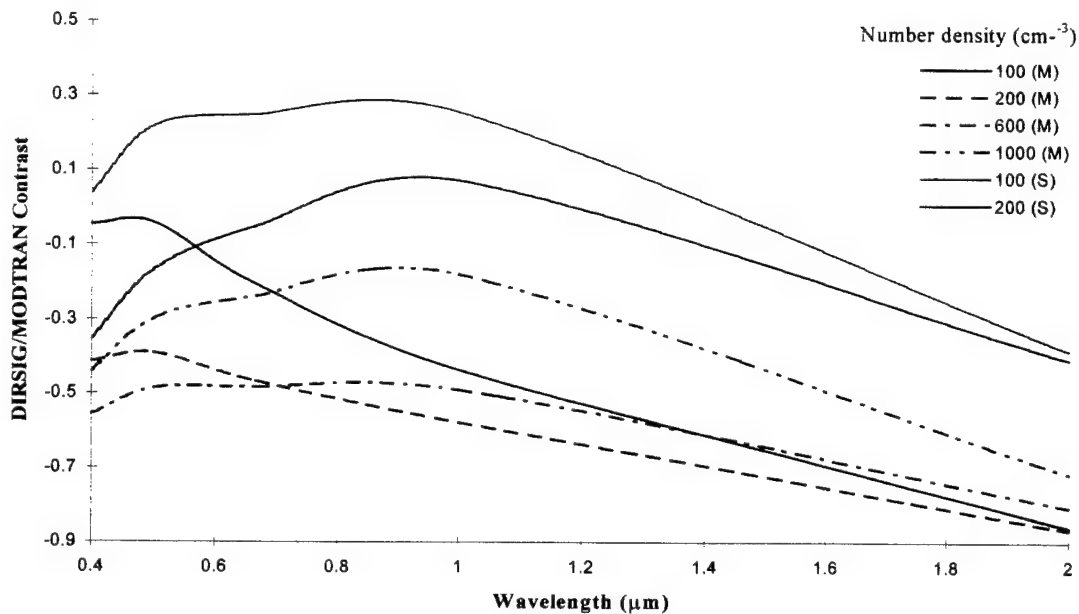


Figure 5-28. DIRSIG-MODTRAN Contrast for Upward-looking Noon Case

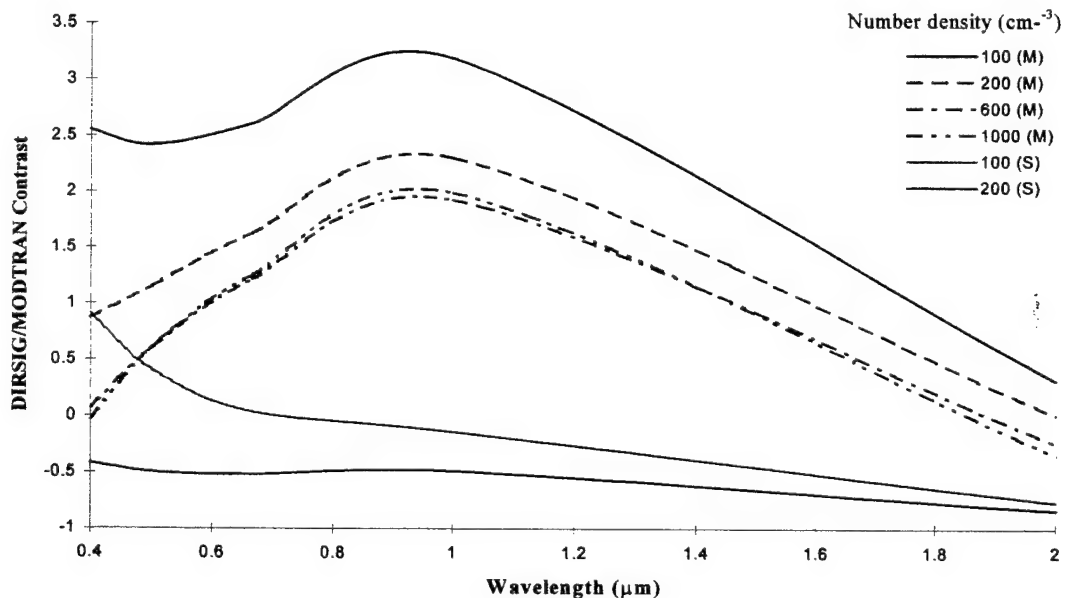


Figure 5-29. DIRSIG-MODTRAN Contrast for Upward-looking 8:00 A.M. Case

Again the same trend is seen in the multiple scattering case. The thicker the plume and the smaller the solar zenith angle, the better the results. The contrast for the 8:00 A.M. case is particularly poor, with an overestimation by a factor of two. The single scattering case does remarkably well, especially for the

11:00 A.M. case where the scattering angle is small. At both times the single scattering model has a better contrast value than the multiple scattering model.

Some conclusions can be drawn from the results presented in section 4.2.1 and the validation presented here. The multiple scattering model works best for optical depths greater than two, and at small solar incident angles. Both upward and downward-looking cases follow those two guidelines. There does not seem to be a difference when the scattering is non-conservative, however there probably is a lower limit to what the single scattering albedo can be before the model is no longer valid. Because the scattering is diffuse, there is very little variation spatially in the plume images. This is observed in real life in thick cooling tower plumes as well as clouds. The single scattering model should be used for optical depths less than one. It should not be used when the scattering angle is less than 10° if strong forward scattering is present. For these small angles the scattered radiance may be stronger than the source, which is physically unrealistic. Also there are strong spatial variations in the plume image because of the direct dependence on the scattering phase function. For most cooling tower plumes the optical depth is great enough that only the multiple scattering model will be used. Note no comparisons were done for Rayleigh scattering, where the scattering is more isotropic. In this case the single scattering model may perform better since the optical depths are smaller (due to a smaller scattering cross-section) and there is no strong forward scattering peak. There are no modifications needed in DIRSIG to model Rayleigh scattering since this is already covered in the Mie scattering code.

5.3 The Rainbow

The rainbow is one of nature's most beautiful creations. Though the principles of geometrical optics are often used to explain the colors, these can also be explained by applying Mie scattering theory to water droplets. This section demonstrates how a rainbow is reproduced when using the single scattering model described in Chapters two and three. The same color matching functions used to produce the visible Hawkeye images are also used to here to recreate the colors of the rainbow. The effects of water droplet size and size distribution on the appearance of rainbows are also studied using the DIRSIG single scattering model.

5.3.1 Theory

A rainbow occurs when sunlight scatters off water droplets and the variation in the index of refraction causes the white light to be split out into distinct spectra. A rainbow can be seen from a water cloud if looking at the correct scattering angles and if the water droplets are sufficiently large. Conventional ray-tracing optics can be used to describe the rainbow since the droplet size is large compared to the wavelengths in the visible region. However using Mie scattering theory covered in Appendix A the theory of the rainbow can also be explained. In this case geometrical optics is really just an approximation of Mie theory for a large size parameter.

As a light ray enters the water droplet it undergoes refraction and reflection. If the ray is internally reflected, then the outgoing rays can be concentrated in particular directions, much like the focus of a lens. Thus for certain scattering angles the scattering intensities will be infinite. Single and multiple internal reflections will produce different scattering angles. The formula for the scattering angle as given by geometrical optics is

$$\theta = 2\Theta_i - 2(n + 1)\Theta_t - \pi \quad \text{for } n \text{ odd} \quad (5-1)$$

$$\theta = 2(n + 1)\Theta_t - 2\Theta_i \quad \text{for } n \text{ even} \quad (5-2)$$

where

$$\cos \Theta_t = \sqrt{\frac{m^2 - 1}{n(n + 2)}} \quad (5-3)$$

$$\Theta_i = \sin^{-1}\left(\frac{\sin \Theta_t}{m}\right) \quad (5-4)$$

where m is the index of refraction and n is the number of internal reflections the ray undergoes. In nature the primary ($n = 1$) and secondary ($n=2$) rainbows are seen. Since the index of refraction varies with wavelength, the angle will be different for each color, and thus the appearance of the rainbow. The angles for several wavelengths are give in Table 5-3.

wavelength (nm)	primary rainbow angle	secondary rainbow angle
350	139.35°	126.52°
450	138.5°	128.07°
550	137.92°	129.11°
650	137.63°	129.64°

Table 5-3. Primary and Secondary Rainbow Angles Using Geometrical Optics

The Mie angular scattering coefficient is defined in Chapter two as the intensity of light scattered into a unit solid angle about a particular scattering angle for a particular particle density. This term is calculated for light at 450 nm incident on a 0.1 mm water droplet and plotted against the scattering angle (with 0° indicating forward scattering) in Figure 5-30.

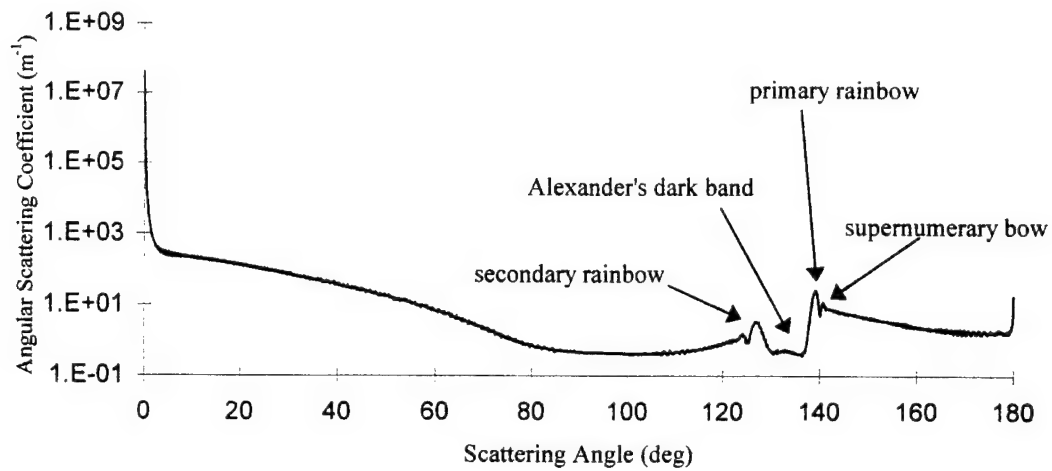


Figure 5-30. Angular Scattering Coefficient for a Water Droplet at 450 nm

The large forward scattered intensity is characteristic of Mie scattering. The main rainbow peak can be seen at $\sim 138^\circ$. Also evident is the weaker secondary rainbow, Alexander's dark band, and the supernumerary bow. For the different wavelengths in the visible band the angle of peak scattering will shift. Table 5-4 shows the primary and secondary rainbow angles using Mie theory.

wavelength (nm)	primary rainbow angle	secondary rainbow angle
350	139.88°	125.6°
450	139.16°	126.87°
550	138.80°	127.41°
650	138.61°	129.17°

Table 5-4. Primary and Secondary Rainbow Angles Using Mie Scattering Theory

The size distribution of the water droplets is another factor involved in the appearance of rainbows. Typically water droplets in clouds are characterized by a modified Gamma distribution (Liou, 1992,). Narrow distributions causes overlap of the different color peaks. This results in a rainbow with little color. As the distribution is broadened the peaks at each wavelength separate out bringing color to the rainbow. By changing the parameters in this distribution the colors in the rainbow are made more vivid. This effect will be demonstrated through the different rainbow images.

5.3.2 Procedure

A scene is constructed in which the observer is looking at a "wall" of water droplets. The size and size distribution of the water cloud are varied to produce different rainbow images. The first cloud is modeled after a fog bank with a mean water droplet size of $10 \mu\text{m}$ and particle density of 20 cm^{-3} . The

second cloud band is modeled with raindrops with a mean size of $100\text{ }\mu\text{m}$ and density of 5 cm^{-3} . The final cloud bank has a mean size of $200\text{ }\mu\text{m}$ and density of 3 cm^{-3} . The size distribution is also increased. For each cloud bank, a Mie scattering table is created. The visible region from 400 nm to 714 nm is split into 23 bands. The angular resolution is set to 0.1° for 100 radius bins. Over 4 million Mie scattering calculations are required for each cloud. The number of terms in the series expansion of the Bessel function needed for convergence is proportional to the size of the particle. This leads to lengthy computer run times for the $200\text{ }\mu\text{m}$ droplets. It took over 60 hours to generate the Mie scattering database on a dedicated DEC Alpha workstation (400 MHz clock speed).

DIRSIG uses a ray-tracing model that constructs a ray from each sensor pixel out into the scene. The ray-tracer determines the scattering angle between the outgoing ray and the sun vector. The appropriate angular scattering coefficient is obtained from the scattering database for this angle and the incident wavelength. This value is multiplied by the solar irradiance onto the wall of water (accounting for atmospheric transmission) and the depth of the wall as determined by the ray trace. This determines the solar radiance scattered towards the sensor. In addition, DIRSIG uses MODTRAN to determine the scattered atmospheric radiance reaching the sensor. The cloud will attenuate this skylight on its way to the sensor. This calculation is done for each pixel in the sensor and for each of the 23 wavebands.

The geometry of the scene is that a ground observer (the sensor) is looking up at a cloud in the west. The sun is rising from the east and is thus over the shoulder of the observer. This results in the correct scattering angles so that the rainbow may be seen (Figure 5-31).

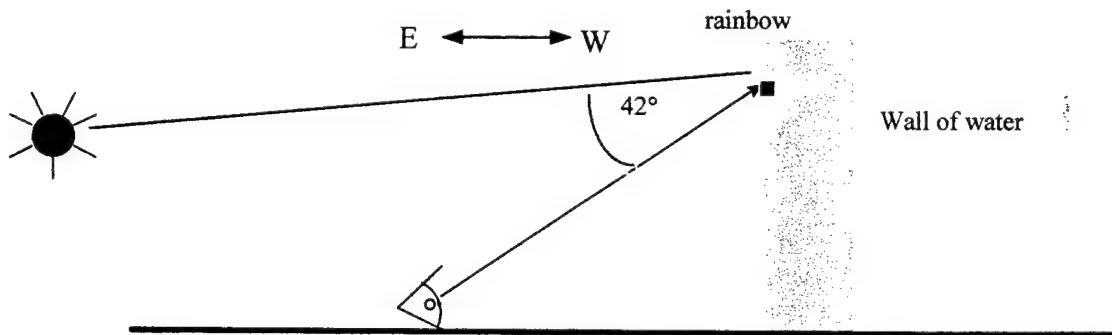


Figure 5-31. Geometry Used to Create Rainbow Scene

The field of view is 40° (square). The sensor is composed of 1024×1024 pixels. This permits a quarter rainbow to be seen. The wall of water is 3.75 km high by 3 km wide. For the smaller droplet size the wall is 8 m thick, while the two larger sizes have a thickness of 0.35 m . The reason for the larger thickness is to ensure that sufficient light is scattered off the smaller droplets so that the rainbow could be seen. A DIRSIG run is made for each type of cloud. The production of a color image is done through the procedure described in Appendix F.

5.3.3 Results

Figure 5-32, Figure 5-33, and Figure 5-34 are images for the three types of clouds. The images have been cropped for a better view of the rainbow. Beneath each are the angular scattering coefficients and droplet size distribution. In Figure 5-32 the droplet size is small and the angular separation between the different wavelengths is negligible. This results in a bow with all the colors evenly mixed. This is commonly referred to as a white rainbow, cloud bow, or fog bow and can be seen in fog banks with water droplet sizes $\sim 10\text{ }\mu\text{m}$. The yellowish band towards the bottom is an artifact of the MODTRAN code when looking towards the horizon. The auto-scaling causes this effect to be magnified due to the weak intensity of the fog bow.

The more familiar looking rainbow appears for droplet sizes of $100\text{ }\mu\text{m}$ (Figure 5-33). The three peaks at each wavelength begin to separate causing the appearance of the rainbow. However the narrow size distribution causes some overlap among the three curves, and thus the rainbow colors are still "dull." The second, smaller peak to the right causes the supernumerary bow. Since the three curves overlap, this bow appears as a faint white arc inside the primary bow. The secondary rainbow hump also appears around the 128° scattering angle. However the secondary rainbow is barely visible in the image since its intensity is about nine times smaller than the main peak and the curves all overlap.

The $200\text{ }\mu\text{m}$ droplet size produces a very vivid rainbow (Figure 5-34). The larger droplet size causes a higher scattered radiance reaching the sensor and thus a brighter rainbow. The wider size distribution clearly separates the three curves resulting in the distinctive colors of the rainbow. The secondary rainbow colors are also more visible due to the separation of the curves. Alexander's dark band is also seen since the sky inside the primary rainbow is brighter ($\sim 5\text{-}7$ times) than the sky between the primary and secondary bow. The supernumerary bow has a blue-greenish color to it. This is a result of more scattering towards that end of the spectrum as seen in the angular scattering curves. Finally a full rainbow is shown in Figure 5-35. The field of view was increased to 70° in order to observe the entire rainbow.

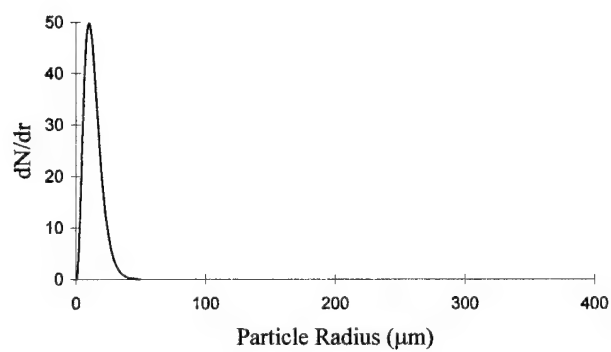
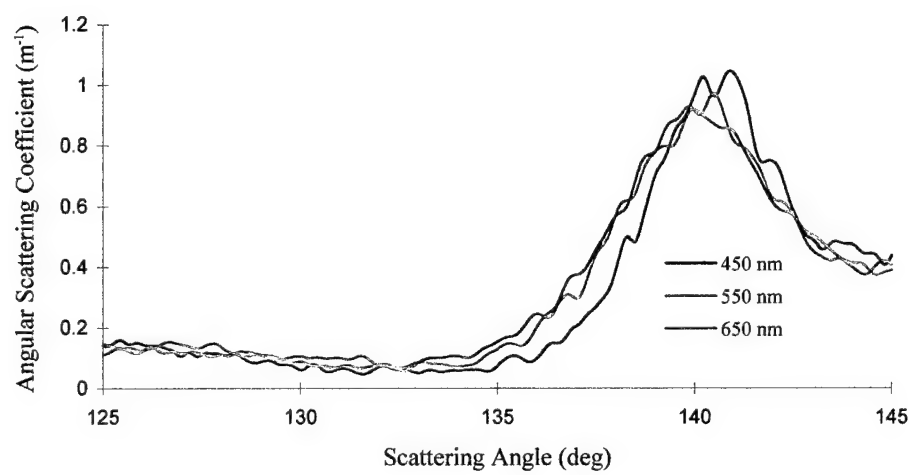
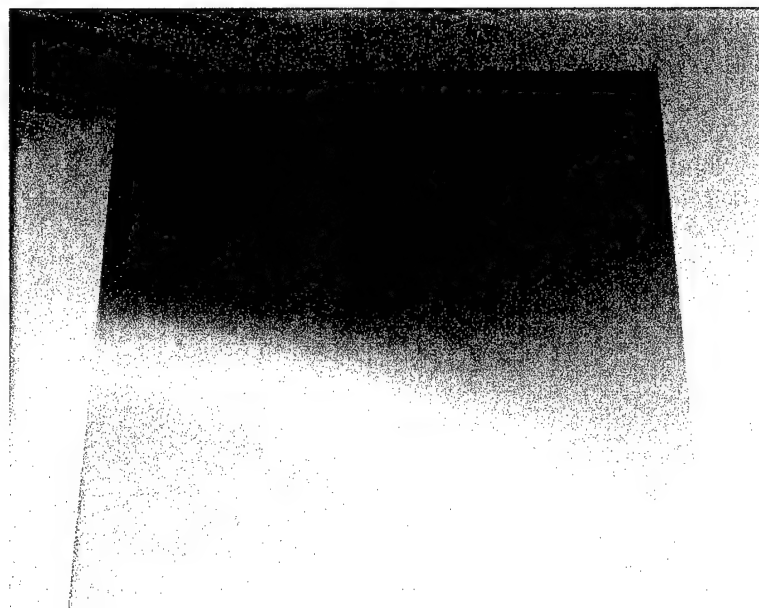


Figure 5-32. Rainbow with 20 μm mean droplet size and associated size distribution and angular scattering coefficient charts

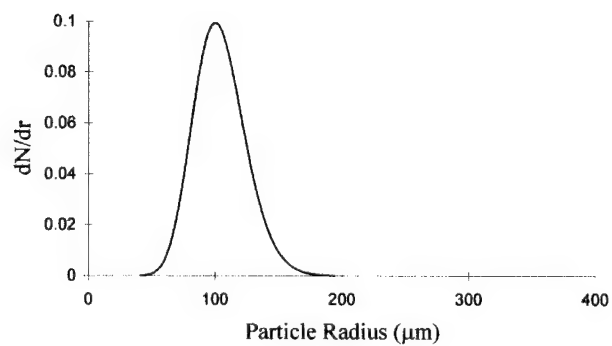
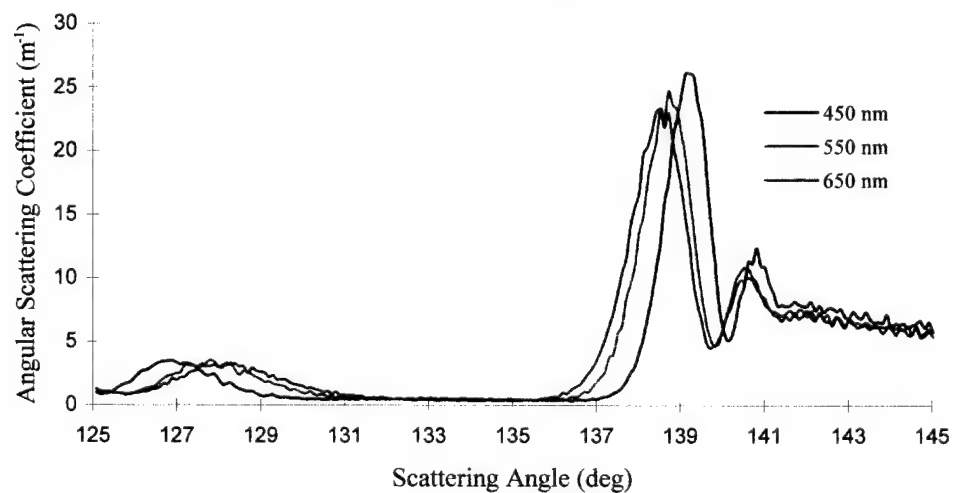


Figure 5-33. Rainbow with 100 μm mean droplet size and associated size distribution and angular scattering coefficient charts

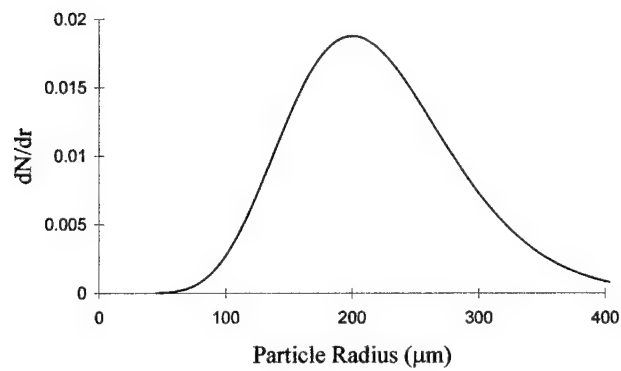
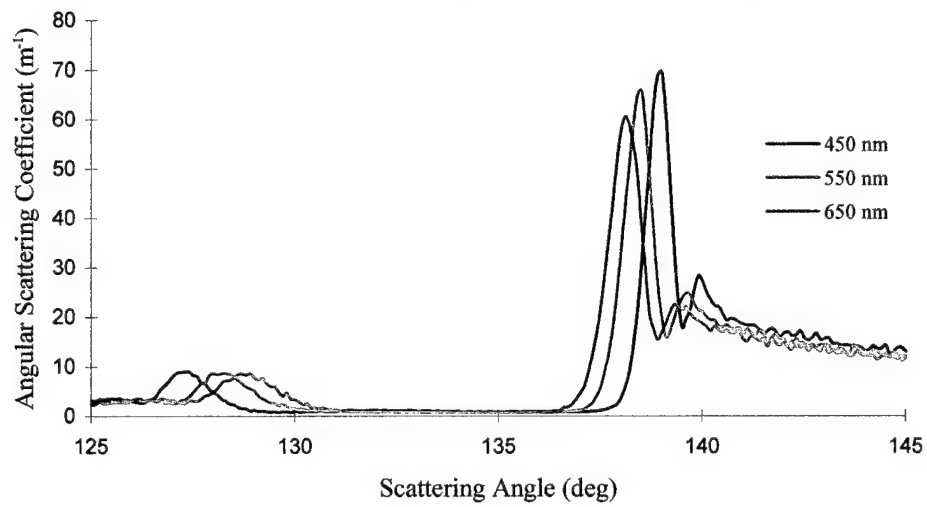
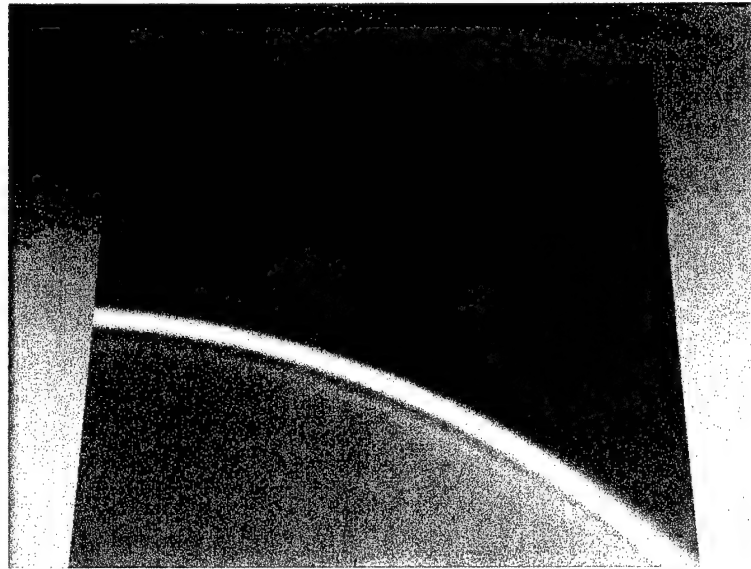


Figure 5-34. Rainbow with 200 μm mean droplet size and associated size distribution and angular scattering coefficient charts

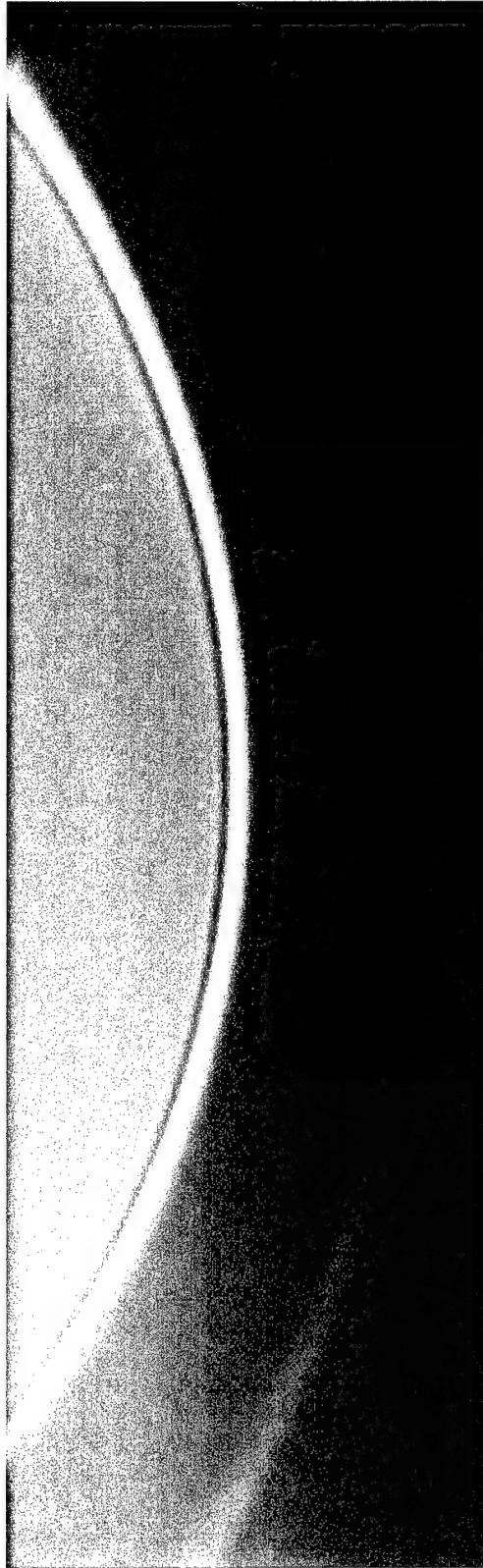


Figure 5-35. Full DIRSIG Rainbow

5.4 Sunset with Red Clouds

The sunset with red clouds is another excellent example of the scattering process in our atmosphere. This phenomena is used to qualitatively demonstrate the multiple scattering model. The actual red fringes in clouds at sunset are caused by two processes. The first is that the incident solar light has very little of the blue component left in it due to Rayleigh scattering by the atmosphere. The long slant path at sunset causes almost total extinction in the blue, resulting in reddish sunlight. This red light is scattered by clouds, thus making them appear red. The red fringes are a result of the smaller optical depths at the edges, which allow more of the scattered radiance to be transmitted.

Like the rainbow, the DIRSIG sunset images shown are designed for aesthetic purposes. Only the multiple scattering model is used. However to be physically realistic, the single scattering model should be used at the fringes where the cloud is optically thin. The clouds are modeled using the JPL ACAD plume with a single region filled with water droplets that are representative of low maritime clouds (Liou, 1992). Three separate clouds are present with different optical depths. Table 5-5 shows the properties of each cloud.

Cloud #	Mean droplet size (μm)	Number density (cm^{-3})	Max optical depth
1	2	100	2.8
2	2	150	2.1
3	2	200	1.67

Table 5-5. Cloud Characteristics

The top cloud in the scene is cloud 1, the middle is cloud 2, and lowest cloud is cloud 3. The location of the scene is Maui, Hawaii looking west. MODTRAN is run using a tropical atmosphere model. A special high resolution map of the sky radiance is used with a resolution of 2° in both azimuth and elevation. The ocean is simulated by a reflective surface with high specularly. No texture of the ocean surface is included. Three different times are run to simulate a setting sun. The DIRSIG images for the three times are shown in Figure 5-36, Figure 5-37, and Figure 5-38. Two actual pictures of the Maui sunset are also included for comparison.

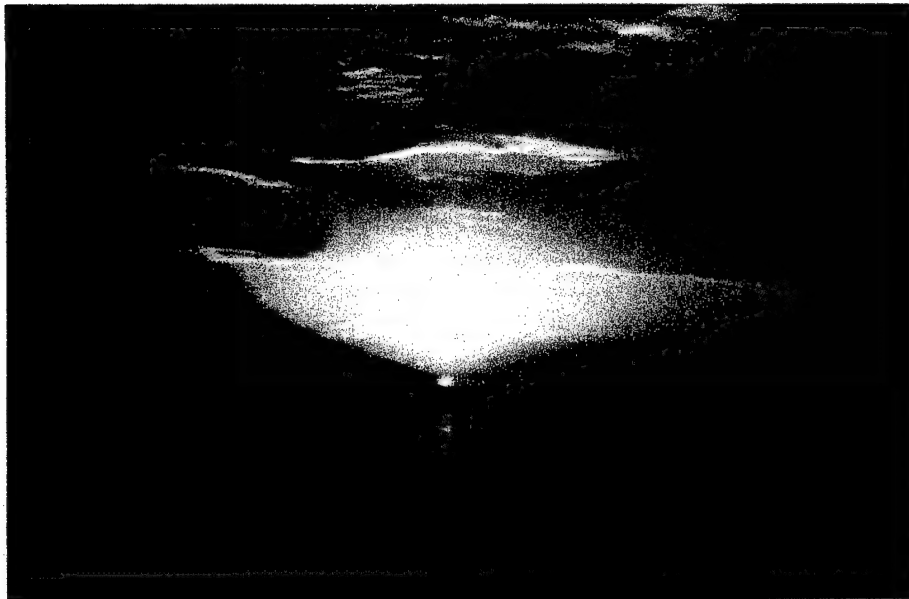


Figure 5-36. Actual and DIRSIG (1815) Sunset Images



Figure 5-37. Actual and DIRSIG (1830) Sunset Images



Figure 5-38. DIRSIG (1840) Sunset Image

The sun is a result of the high resolution sky radiance map. The scaling of the image is done on a logarithmic basis so the sun does not saturate the image. The color of the sunset transitions from orange to red, as in the real images. The cloud with the largest optical depth (#1) appears the darkest, while the cloud #3 has the most contrast. The red fringe is seen at the edge of the clouds due to the thinner optical depths at that location. The solar irradiance incident on the clouds from the three times is shown in Figure 5-39.

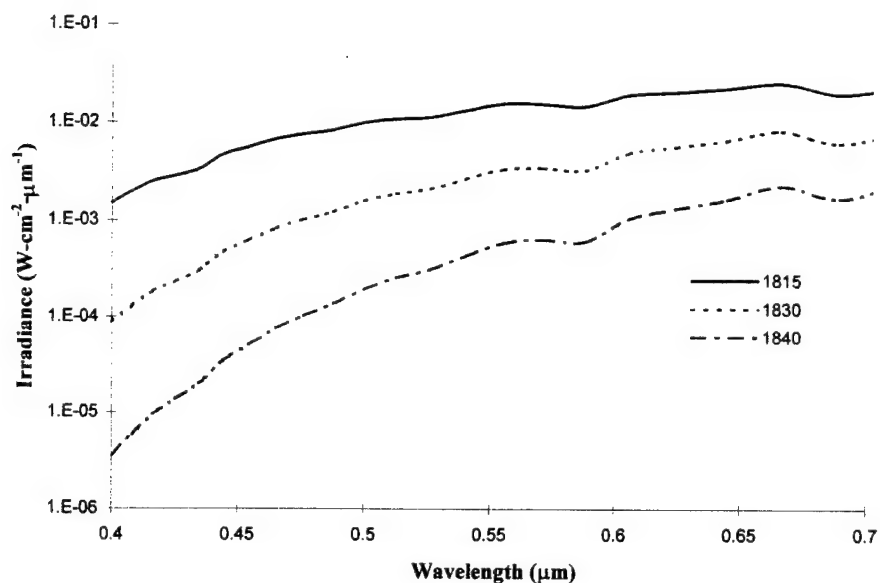


Figure 5-39. Solar Irradiance on Clouds at Three Sunset Times

The irradiance decreases as the sun sets. In addition, the ratio of the red end to the blue end of the spectrum increases as the sun gets lower on the horizon. This results in the orange to red color as the sunsets. The radiance from the top cloud at 1830 is shown at a location in the center of the cloud and at the fringe of the cloud.

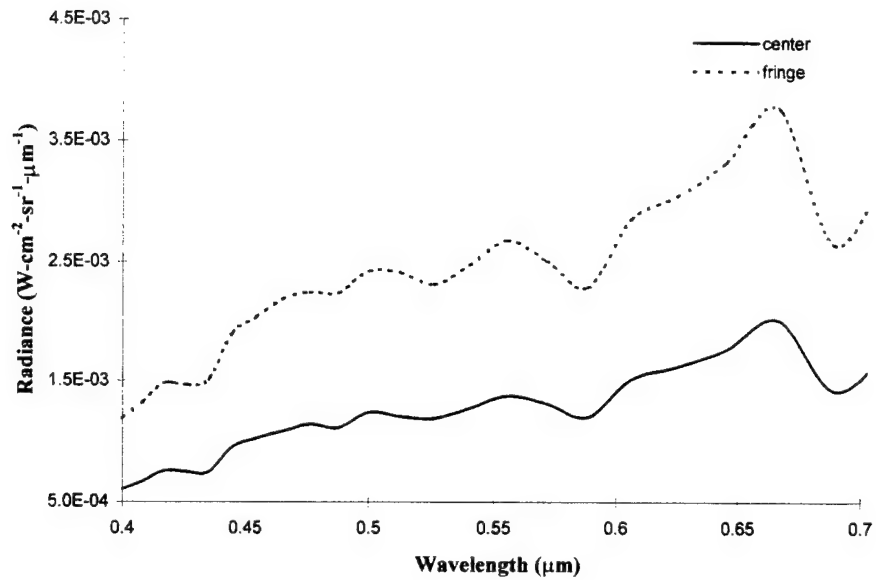


Figure 5-40. Radiance from Center and Fringe of Cloud

The fringe has a higher radiance due to more scattered sunlight as well as a higher transmission. It also has a slightly higher red to blue ratio, resulting in the red fringe effect.

The sunsets presented here should be considered a first order estimate of the actual thing. Both multiple scattering and single scattering effects occur in the cloud. The sky radiance calculated by MODTRAN is also suspect due to the long horizontal paths. More realistic looking clouds should be shaped after fractal models (Nishita, 1996) instead of using a plume model.

6. Conclusions and Recommendations

6.1 Summary

A method of generating synthetic images of plumes using DIRSIG has been presented in this dissertation. Existing models of plumes are used to determine the shape and characteristics of the plume in the image. Mie scattering and gas absorption theory are used to determine the optical properties of the plume. DIRSIG computes the radiometric signal from both the plume and background by performing a ray-trace on a pixel by pixel basis. Currently two plume models are available. The first is developed by LANL and is used to simulate cooling tower plumes. The second model was originally developed by JPL and used for gaseous plumes. ACAD is used to represent the plume in DIRSIG. With the JPL model, the plume model can be directly called within DIRSIG to produce an integrated plume in the scene. In addition to producing the radiometric image, several other images of plume characteristics (transmission, temperature, etc.) are generated.

Several examples are given on how DIRSIG plumes are used to aid in the investigation of remote sensing of plumes. Various images are generated with different plume characteristics. Both the ACAD LANL and JPL models are shown, as well as the integrated JPL model. Different wavelengths and sensor platforms are also used to observe the plume. The plume contrast ratio is used as a benchmark to determine how visible the plume is under changing conditions. Hyperspectral sensor models are used to image gas plumes with unique spectral absorbance curves. Inverse algorithms that attempt to determine plume concentrations are tested on DIRSIG plumes.

The JPL plume model is validated against experimental data collected on a SF_6 plume. The actual plume and environmental conditions are simulated as close as possible in the plume input files. The sensor response of the multi-spectral instrument used is also modeled. Two spectral bands tuned to the peak SF_6 absorbance curve are used. A crude background scene is generated and emissivity values are set to produce the same radiance signal as the actual background. Both the ACAD and integrated models are tested. The DIRSIG plume characteristics and contrast ratio are compared with the available experimental data. No experimental data were available for cooling tower plumes. Instead the scattering algorithms are tested against MODTRAN. A simulated water droplet plume is set up in MODTRAN and the results are compared with the DIRSIG plume. Both the single and multiple scattering algorithms are tested this way against plumes with varying optical depths.

6.2 Conclusions

Attempting to account for all the physical interactions that occur between the plume and its environment is an ambitious task. The work done here is a first-cut attempt at trying to simulate the main

interactions. One of the limitations to the accuracy and validity of the DIRSIG plumes is the model of the plume itself. If the JPL or LANL models do not accurately predict the plume characteristics, then the plume images will not be accurate. The adage of "garbage in garbage out" applies here. Both models are still under development so future refinements should improve the validity of DIRSIG.

Modeling the scattering aspect is perhaps the most difficult task. While single scattering properties can be derived in a straightforward manner from Mie scattering, it is rarely applicable to plumes. In addition the strong forward scattering present in water droplets is hard to model, as seen in the case of looking up through the plume towards the sun. For scattering angles less than 10° unphysical results can occur. Simulation of multiple scattering is usually accomplished through Monte Carlo methods. However radiative transfer techniques are used in this research. The multiple scattering model should be used when the optical depth is greater than 0.7, however the delta-Eddington approximation used here works best for optical depths greater than 2. Also the solar incident zenith angle should be less than 60° . The scattering process is generally limited to the visible region for two reasons. The first is the rapid decrease in solar irradiance in the IR. Secondly the single scattering albedo also decreases in the IR due to the presence of absorption.

The DIRSIG image of LANL cooling tower plume has several problems with it. The uniform cross-sectional property makes the plume look blocky and discrete. Also in the LWIR the distinct regions are seen. The plume radius is also small for a cooling tower plume, resulting in a lack of visibility, especially in the visible region. While no attempts are made to apply inverse algorithms to cooling tower plumes, it is likely that the LWIR will provide the most information. The scattering in the visible will probably not be able to provide any useful information due to the many variables involved in that process.

Gas absorption is easier to model than scattering. The number of parameters involved are fewer, and there is no angular dependence involved. The biggest assumption made is using the smeared line model over several discrete absorbance peaks. The JPL model provides a more realistic Gaussian distribution to the shape of the plume than the LANL model. When comparing the two methods of running the JPL model, clearly the integrated method is superior to the ACAD method. The integrated method has no lengthy pre-processing operations involved, and changes in the plume parameters can more easily be investigated. The computer run times are about equal between the two methods. The plume itself also looks smoother and more natural. The ability to vary the meteorological conditions provides for an even more realistic looking plume. The JPL model is quite sensitive to the plume adjustment parameters. Changing these values will alter the appearance of the plume, especially in the integrated model.

The sensitivity studies investigated the changes in several plume parameters. The biggest impact on the plume image is a change in temperature and concentration. The variation in the plume concentration affects both the self-emitted radiance (via emissivity) and the transmission. The inverse algorithms

generally work well on gas plumes under ideal conditions. However when the plume temperature is estimated to be ambient, then algorithm performs poorly.

The validation of the JPL model is done against data collected for a SF_6 plume. The emissivity of the background needed to be lowered in order to match the calibrated radiance values in band 1. The ACAD model overestimates the radiance in this band by over 30% throughout the length of the plume. This is due to the plume being modeled as a "solid" gas with a constant VMR. The integrated model overestimates the radiance by a factor of two within the first five meters of the stack. It is then within 20% of the actual values to 100 m downwind. The downwind radiance and column density cross-sectional profiles at 100 m have errors less than 15%. For distances greater than 100 m downwind, the model underestimates the radiance. This is due to the difficulties in accurately modeling a plume at far distances from the stack.

The research done in this dissertation presents a new tool to visualize plumes under a variety of conditions. All three research objectives were satisfied. A radiometrically accurate method of representing plumes in images was developed using DIRSIG. A new method of combining a ray-tracer with radiative transfer calculations was developed to simulate multiple scattering. An existing plume model was integrated into the DIRSIG code resulting in a more realistic and accurate plume image. The second objective was satisfied by giving several examples demonstrating how the plume-background interaction can be easily studied using the work done in this research. Several types of SIG plumes were shown to illustrate how plume sensitivity studies can be made. The final objective of validating the code was done through experimental data and other computer models. Several limitations to the scattering model became apparent, as discussed above. The results of the integrated gas plume model matched the experimental data well. This is somewhat remarkable considering how unpredictable plumes really are. Finally a synthetic rainbow was made based on Mie scattering theory. This illustrated some aspects of the rainbow not explainable through geometrical optics.

6.3 Recommendations

There are several areas in this research that can undergo further improvements. Since this is a first-cut effort at generating plume images, further refinements will improve the quality of the image. The recommendations are grouped under four general categories: Cooling tower plumes, scattering, gas plumes, and applications.

As mentioned previously the main drawback to the LANL model is the discrete regions and uniform properties. This results in some unattractive plumes. It may be desirable to rerun the LANL using the radius from an actual cooling tower. There are two other potential cooling tower models available. The first is the RAMS code developed by DOE (O'Steen, 1995). The plumes produced have realistic shape and texture. However the time to run this code is on the order of days. Also it would have to be integrated into

DIRSIG since it would be too difficult to facetize under ACAD. The second model is developed by Hanna (1989), and similar to the LANL model giving plume characteristics as a function of downwind distance. One improvement to the LANL model is tracking the change in size distribution downwind. Also validation with actual data collected on a cooling tower plume should be done.

There are two additional cases of scattering that can be modeled. A water droplet formed around an aerosol nuclei can be represented by a coated sphere. An ice crystal can be represented by a cylinder. There are Mie solutions for both of these cases and exist in the form of FORTRAN (Bohren, 1983). The index of refraction for ice can be found in Hobbs (1974). Scattering from hexagonal ice structures may also be modeled through geometrical optics. Plumes that involve Rayleigh scattering should also be investigated using the single scattering model. These cases involve optically thin plumes, and isotropic scattering, both conditions that favor the single scattering model. Improvements to the multiple scattering model include reorienting the plane parallel layers at different angles (i.e., the sunset scene). This would mean determining the angle between the ray trace vector and sun vector. There are also other radiative transfer models that can be used. A comparison between them is made by King (1986). For truly accurate multiple scattering modeling, either the independent pixel approximation (Marshak, 1995), or volume element scattering (Nishita, 1996) should be used.

The effects of scattering of gas plumes also need to be investigated. The index of refraction of soot and flyash has been measured (Twitty, 1971 and Volz, 1973) and can be added to the database. Rayleigh scattering will predominate due to the smaller particle sizes ($< 0.5 \mu\text{m}$). There are numerous sensitivity studies that can be done. One that was not covered in this paper is the effect of sensor spectral resolution on plume contrast. Also the variation in background and sensor altitude are two other studies that can be done. In addition to spatial contrast, spectral contrast can also be used as a benchmark in the sensitivity studies. This involves making comparisons in the signal at different spectral bands for gases. It can be determined whether the gas spectral signature can be detected at the sensor after accounting for the atmospheric and background noise.

The main improvement to the JPL model is cleaning up the code. It is quite inefficient as it stands now. The "Plume_Input" is re-read for every ray-trace. It also contains information that is not needed. It is doubtful that the ACAD version will be used much, since the integrated version is faster and more accurate. However the integrated model can not simulate scattering plumes, while the ACAD model can. Additional texture can be given to the plume by adding a small variation to the plume concentration value for each ray trace. This variation can be determined randomly within some normal distribution.

There are several possible applications for DIRSIG from this research, all of which involve the scattering model. The first is cloud modeling, which was done to some extent with the sunset scenes. Fractal models will give the most realistic looking clouds. The clouds may be either be represented with ACAD, or internally in DIRSIG with some sort of algorithm. Common cloud properties are given in Liou

(1992). Cirrus clouds will have ice crystals so the Mie scattering for cylinders will have to be implemented. The multiple scattering code was originally designed for clouds, so no modifications should be needed.

Aircraft contrails can also be modeled in DIRSIG, since they are essentially water droplets condensed onto jet exhaust. Several interesting studies can be made from synthetically generated scenes of contrails. The contrast of contrails against different backgrounds from satellite sensors under a variety of weather conditions can be looked at. Also the thermal images of contrails may yield information on the their sources. Models of contrails from different aircraft can be built and then scenes can be generated by DIRSIG.

The second area of application is simulating battlefield obscuration. The modern battlefield will be filled with both natural (dust) and artificial (smoke) particulates. These will interfere with target acquisition systems. DIRSIG may be able to model the scattering of a source behind a cloud of dust and smoke. The current multiple scattering model will not be applicable since the optical depths are not large enough and the geometry of the plane parallel layers would not work with horizontal paths. The single scattering model may work if the particulates are small enough to be in the Rayleigh regime, and if the cloud is not too optically thick. Otherwise strong forward scattering will be problem. The range for which the single scattering model will hold under these conditions will need to be investigated. A good discussion on scattering of dust particles is given in Chapter 6 of Iqbal (1983), in which the extinction coefficient is proportional to $\lambda^{-0.75}$. DIRSIG will have to be modified to handle multiple non-solar sources. Texture can be applied to the dust or smoke cloud in the same manner as described above to render a more realistic looking image.

Appendix A : Mie Scattering Theory

The general formulation is to start with Maxwell's equations and solve for free space using spherical coordinates. A sphere with a different index of refraction from the medium is introduced. An electromagnetic field is induced inside the sphere and a scattered field is generated outside the sphere. Boundary conditions are imposed so that the tangential components of the electric and magnetic fields are continuous across the medium interface. The solution to the field inside the particle the scattered field depends on the geometry of the particle. Figure A-1 show the geometry of the incident and scattered fields.

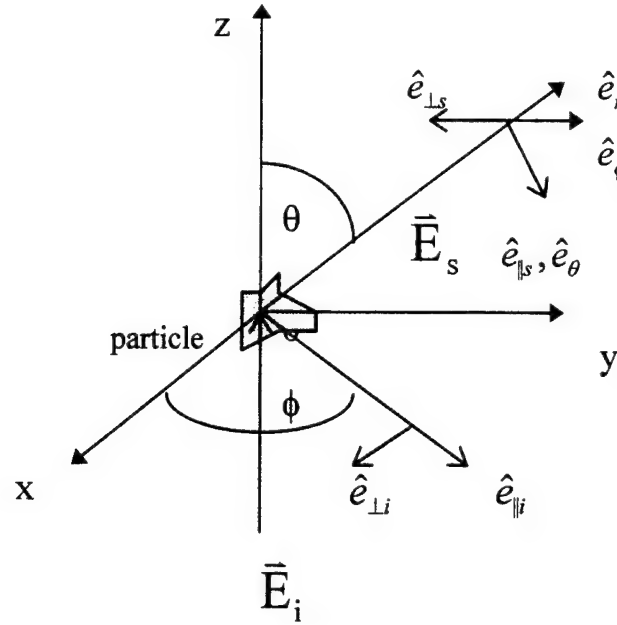


Figure A-1. Geometry of Incident and Scattered Fields

The incident and scattered fields can be defined in terms of their two principal components:

$$\vec{E}_i = \vec{E}_{\parallel i} \hat{e}_{\parallel i} + \vec{E}_{\perp i} \hat{e}_{\perp i} \quad (\text{A-1})$$

$$\vec{E}_s = \vec{E}_{\parallel s} \hat{e}_{\parallel s} + \vec{E}_{\perp s} \hat{e}_{\perp s}.$$

In the far field ($kr \gg 1$) the amplitude of the scattered and incident wave can be related as:

$$\begin{pmatrix} \vec{E}_{\parallel s} \\ \vec{E}_{\perp s} \end{pmatrix} = \frac{e^{ik(r-z)}}{-ikr} \begin{pmatrix} S_2 & S_3 \\ S_4 & S_1 \end{pmatrix} \begin{pmatrix} \vec{E}_{\parallel i} \\ \vec{E}_{\perp i} \end{pmatrix}, \quad (\text{A-2})$$

where $\mathbf{E}_{\parallel i, s}$ and $\mathbf{E}_{\perp i, s}$ are the parallel and perpendicular incident and scattered electric fields, \mathbf{k} is the wavevector, r is the distance to the detector, and z is the direction of propagation of the incident field. The elements of the amplitude scattering are angularly dependent. An alternative way to express this relationship is using the Stokes parameters I , Q , U , and V :

$$\begin{pmatrix} I_s \\ Q_s \\ U_s \\ V_s \end{pmatrix} = \frac{1}{k^2 r^2} \begin{pmatrix} S_{11} & S_{12} & S_{13} & S_{14} \\ S_{21} & S_{22} & S_{23} & S_{24} \\ S_{31} & S_{32} & S_{33} & S_{34} \\ S_{41} & S_{42} & S_{43} & S_{44} \end{pmatrix} \begin{pmatrix} I_i \\ Q_i \\ U_i \\ V_i \end{pmatrix}. \quad (\text{A-3})$$

The elements of this scattering matrix (also known as a Mueller matrix) can all be related to the elements of the amplitude scattering matrix. Since the Stokes parameter's of light scattered by a collection of randomly separated particles is the sum of the Stokes parameters of the individual particles, then the scattering matrix for a collection of these particles is the sum of the individual scattering matrices. This assumes the scattering is independent among the particles with no phase relationship between them. For a spherical particle, the wave equation is put in terms of spherical coordinates. The even and odd solutions for the scalar wave equation are expressed as:

$$\begin{aligned} \Psi_{emn} &= \cos m\phi P_n^m(\cos\theta) z_n(kr) \\ \Psi_{omn} &= \sin m\phi P_n^m(\cos\theta) z_n(kr) \end{aligned} \quad (\text{A-4})$$

where $P_n^m(\cos\theta)$ is the associated Legendre functions of the first kind and $z_n(kr)$ is the spherical Bessel functions. The solution to the vector wave equation is found by decomposing Ψ_{emn} and Ψ_{omn} into spherical harmonics. The scattered field is then found by expanding the scattered plane wave in terms of the vector spherical harmonics and applying the appropriate boundary conditions. The series can be approximated and transformed so that the scattered field may be related to the incident field in the form of eqn. A-2 as:

$$\begin{pmatrix} \mathbf{E}_{\parallel s} \\ \mathbf{E}_{\perp s} \end{pmatrix} = \frac{e^{ik(r-z)}}{-ikr} \begin{pmatrix} S_2 & 0 \\ 0 & S_1 \end{pmatrix} \begin{pmatrix} \mathbf{E}_{\parallel i} \\ \mathbf{E}_{\perp i} \end{pmatrix}. \quad (\text{A-5})$$

The elements of the scattering matrix are expressed as:

$$\begin{aligned} S_1 &= \sum_n \frac{2n+1}{n(n+1)} (a_n \pi_n + b_n \tau_n) \\ S_2 &= \sum_n \frac{2n+1}{n(n+1)} (a_n \tau_n + b_n \pi_n), \end{aligned} \quad (\text{A-6})$$

where π_n and τ_n are defined as:

$$\pi_n = \frac{P_n^1}{\sin \theta} \quad (\text{A-7})$$

$$\tau_n = \frac{dP_n^1}{d\theta}.$$

The scattering coefficients a_n and b_n are:

$$a_n = \frac{m\psi_n(mx)\psi'_n(x) - \psi_n(x)\psi'_n(mx)}{m\psi_n(mx)\xi'_n(x) - \xi_n(x)\psi'_n(mx)} \quad (\text{A-8})$$

$$b_n = \frac{\psi_n(mx)\psi'_n(x) - m\psi_n(x)\psi'_n(mx)}{\psi_n(mx)\xi'_n(x) - m\xi_n(x)\psi'_n(mx)},$$

where m is the relative index of refraction, ψ_n and ξ_n are the Riccati-Bessel and Hankel functions and x is the particle size parameter:

$$x = ka = \frac{2\pi m_o a}{\lambda}, \quad (\text{A-9})$$

where a is the radius of the particle and n_o is the medium index of refraction. In terms of the Stokes parameters eqn. A-3 for a spherical particle becomes

$$\begin{pmatrix} I_s \\ Q_s \\ U_s \\ V_s \end{pmatrix} = \frac{1}{k^2 r^2} \begin{pmatrix} S_{11} & S_{12} & 0 & 0 \\ S_{12} & S_{22} & 0 & 0 \\ 0 & 0 & S_{33} & S_{34} \\ 0 & 0 & -S_{34} & S_{33} \end{pmatrix} \begin{pmatrix} I_i \\ Q_i \\ U_i \\ V_i \end{pmatrix}, \quad (\text{A-10})$$

where

$$\begin{aligned} S_{11} &= \frac{1}{2}(|S_2|^2 + |S_1|^2) \\ S_{12} &= \frac{1}{2}(|S_2|^2 - |S_1|^2) \\ S_{33} &= \frac{1}{2}(S_2^* S_1 + S_2 S_1^*) \\ S_{34} &= \frac{i}{2}(S_1 S_2^* - S_2 S_1^*). \end{aligned} \quad (\text{A-11})$$

For sunlight, (which is unpolarized light), the relationships for the Stokes parameters reduce to

$$E_s = \frac{1}{k^2 r^2} S_{11} E_i \quad Q_s = \frac{1}{k^2 r^2} S_{12} E_i \quad U_s = V_s = 0. \quad (\text{A-12})$$

Note the notation for irradiance has been changed from I to E [W/m^2] for consistency with the DIRSIG notation. The previously unpolarized incident light will be polarized upon scattering and degree of polarization is given by

$$P = -\frac{S_{12}}{S_{11}}, \quad (\text{A-13})$$

such that $|P| < 1$. If P is positive, the scattered light is partially polarized perpendicular to the scattering plane, and parallel to the scattering plane for negative P . For 0° and 180° , forward scatter and backscatter, the light will always be unpolarized ($P=0$).

A few more terms that are encountered in scattering theory are relevant to scattering in a plume. The first is the scattering cross section, C_{sca} which can be defined as the amount of energy scattered across the surface area of the particle by the incident irradiance. For a sphere, this becomes

$$C_{\text{sca}} = \frac{2\pi}{k^2} \sum_{n=1}^{\infty} (2n+1) (|a_n|^2 + |b_n|^2) \quad [\text{m}^2]. \quad (\text{A-14})$$

The differential scattering cross section $dC_{\text{sca}}/d\Omega$ is the energy scattered per unit time into a unit solid angle about the scattering angle θ and azimuthal angle ϕ . The irradiance of the scattered light can be related to the incident irradiance through the differential scattering cross section:

$$E_s = \frac{dC_{\text{sca}}}{d\Omega r^2} E_i \quad [\text{W}/\text{m}^2]. \quad (\text{A-15})$$

where r is the distance to the detector. For unpolarized light, the differential scattering cross section can be expressed as:

$$\frac{dC_{\text{sca}}}{d\Omega} = \frac{S_{11}}{k^2} \quad [\text{m}^2/\text{sr}]. \quad (\text{A-16})$$

The phase function is often used to describe the angular distribution of the scattered energy:

$$p = \frac{1}{C_{\text{sca}}} \frac{dC_{\text{sca}}}{d\Omega}. \quad (\text{A-17})$$

The integral of p over all solid angles is usually set equal to 4π . The angular scattering coefficient $\beta(\lambda, \theta)$ is the amount of light scattered into the direction θ per unit solid angle per unit length of the scattering medium. It is defined as:

$$\beta = N \frac{dC_{\text{sca}}}{d\Omega} \quad [\text{m}^{-1}\text{sr}^{-1}]. \quad (\text{A-18})$$

where N is the number density of the medium. The scattering efficiency is the scattering cross section divided by the particle cross-sectional area. For a sphere this is

$$Q_{sca} = \frac{C_{sca}}{\pi a^2}. \quad (A-19)$$

The absorption and extinction efficiencies have similar definitions. Another term encountered is the backscatter cross-section. This is the differential cross section in the backward direction multiplied by 4π sr.

$$C_b = 4\pi \frac{dC_{sca}(180^\circ)}{d\Omega} \quad [m^2] \quad (A-20)$$

The scattering coefficients a_n and b_n of eqn. A-8 can be simplified if $|m|x \ll 1$, i.e. the size is small compared to the wavelength of light. For this case, the higher-order terms are negligible and $|b_1| \ll |a_1|$, so that the only significant term is a_1 ,

$$a_1 = -\frac{i2x^3}{3} \frac{m^2 - 1}{m^2 + 2}. \quad (A-21)$$

The terms in the amplitude scattering matrix become:

$$S_1 = \frac{3}{2} a_1 \quad S_2 = \frac{3}{2} a_1 \cos \theta. \quad (A-22)$$

The corresponding scattering matrix is:

$$\frac{9|a_1|^2}{4k^2 r^2} \begin{pmatrix} \frac{1}{2}(1 + \cos^2 \theta) & \frac{1}{2}(\cos^2 \theta - 1) & 0 & 0 \\ \frac{1}{2}(\cos^2 \theta - 1) & \frac{1}{2}(1 + \cos^2 \theta) & 0 & 0 \\ 0 & 0 & \cos \theta & 0 \\ 0 & 0 & 0 & \cos \theta \end{pmatrix}. \quad (A-23)$$

For unpolarized light, the scattered irradiance is related to the incident irradiance through the matrix element S_{11} :

$$E_s = \frac{8\pi^4 n_o^4 a^6}{\lambda^4 r^2} \left| \frac{m^2 - 1}{m^2 + 2} \right|^2 (1 + \cos^2 \theta) E_i \quad [W/m^2]. \quad (A-24)$$

This is the well known equation for Rayleigh scattering and exhibits the $1/\lambda^4$ dependency (assuming the index of refraction is weakly dependent on wavelength). The scattering and backscattering efficiencies are

$$Q_{sca} = \frac{8}{3}x^4 \left| \frac{m^2 - 1}{m^2 + 2} \right|^2$$

$$Q_b = 4x^4 \left| \frac{m^2 - 1}{m^2 + 2} \right|^2. \quad (\text{A-25})$$

Appendix B : Importance of Multiple Scattering in Plumes

There is clearly no doubt that multiple scattering (m.s.) is an effect that needs to be accounted for when modeling plumes in the visible. However it is desirable to see how big an effect m.s. has on solar scattered radiance. To do this it is necessary to investigate how much an increase there is in scattered radiance when using m.s. models instead of single scattering models. Also of interest is how this factor varies with wavelength and optical depth of the plume.

To do this study MODTRAN3 is used. It uses the Discrete Ordinate Method (DOM) developed by Chandrasekar (1960) and described in detail by Goody (1989). DOM expands the phase function in the radiative transfer equation (eqn. 2-39) using spherical harmonics and then solves the equation using Gaussian quadrature. The DOM can be run with 2, 4, 8, or 16 streams, each corresponding with an increase in run time and supposedly accuracy (though not guaranteed according to MODTRAN3 documentation). The 8 stream option is chosen for all the runs.

MODTRAN3 is normally used to model a layered atmosphere. When run with the m.s. option, the solar scattered radiance from the atmosphere is reported, as well as the total radiance (scattered plume self-emissive) and transmission. Also reported is the scattered radiance if only single scattering effects are considered. This presents a convenient way to compare the effects of m.s. against single scattering. To simulate the effects of a plume, a user defined atmosphere is built using the properties of a plume. Four layers are defined, each 10 m in altitude and having infinite horizontal extent (see Figure B-1).

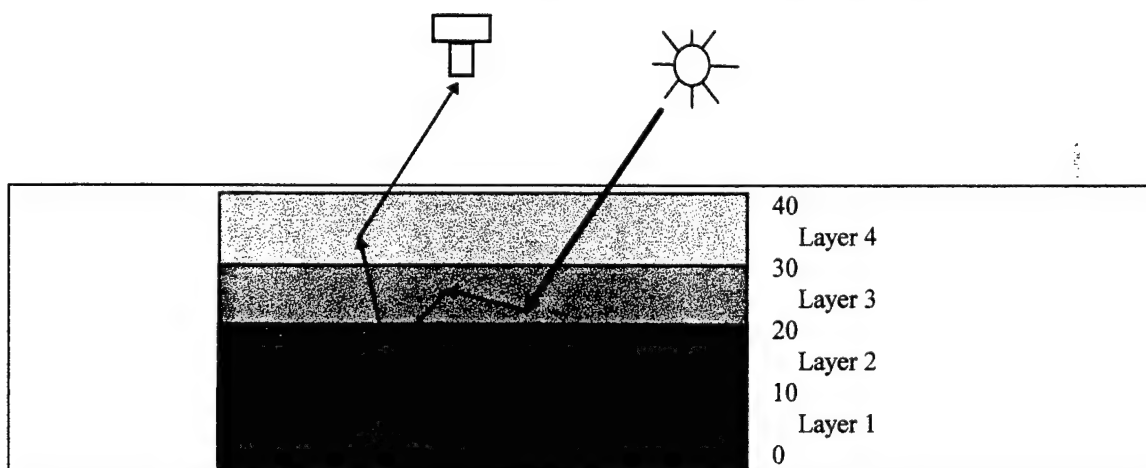


Figure B-1. Plume Layer Model Constructed for MODTRAN3

For each layer the Mie scattering code is run to generate the optical properties of water droplets characteristic from that of LANL cooling tower plume model. Table B-1 show the properties of each plume layer.

Plume Layer	Mean water droplet size (μm)	Number density (cm^{-3})	Extinction coefficient at $0.55 \mu\text{m}$ (km^{-1})	Temperature (K°)
1	6	600	150	310
2	9	200	110	300
3	12	70	69	295
4	18	20	43	290

Table B-1. Characteristics of Each Plume Layer

The upper layers are supposed to represent the downwind portions of the plume after it has undergone dilution (the droplet size has also increased due to condensation). A modified gamma size distribution with $\alpha=25$ was used (see Appendix C). The Mie scattering code generated the extinction and absorption cross-sections for the different wavelength intervals required by MODTRAN3. These values are multiplied by the appropriate number density at each layer to generate the extinction and absorption coefficients for each layer. These four layers are then put into the appropriate format and inserted as card 2d2 in the MODTRAN3 card deck. The single scattering albedo averaged over the four layers is shown in Figure B-2.

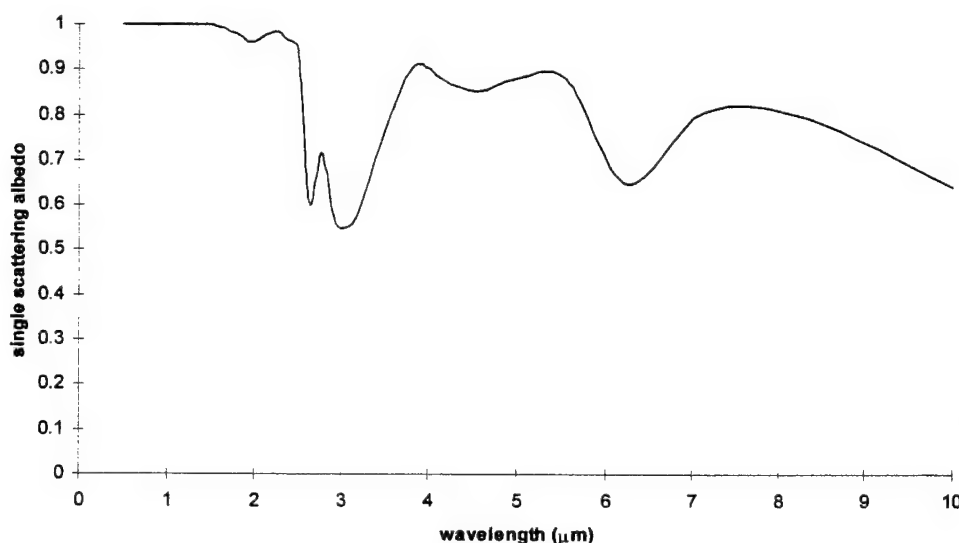


Figure B-2. Average Spectral Single Scattering Albedo of Plume

The dips at 3 and $6.5 \mu\text{m}$ correspond to the increase in the water droplet's imaginary index of refraction and thus also the absorption coefficient.

To examine the importance of m.s. for different plume optical depths, the number density of the original plume model is divided by 2, 3, and 4. This way four different types of plume models with varying degrees of optical depths are generated from the original model. Thus model 1 has the original characteristics listed in Table B-1, model 2 has half the number density in each layer (and thus the extinction coefficient is also half), model 3 had one-third the original number density, and model 4 has one-

quarter the original number density. An imaginary sensor was placed at 50 m (10 m above the plume) looking straight down. The location is Rochester NY at 10 AM in August. This results in a solar zenith angle of 32°, or a scattering angle of 148°. The overall spectral transmission for each plume model is plotted in Figure B-3.

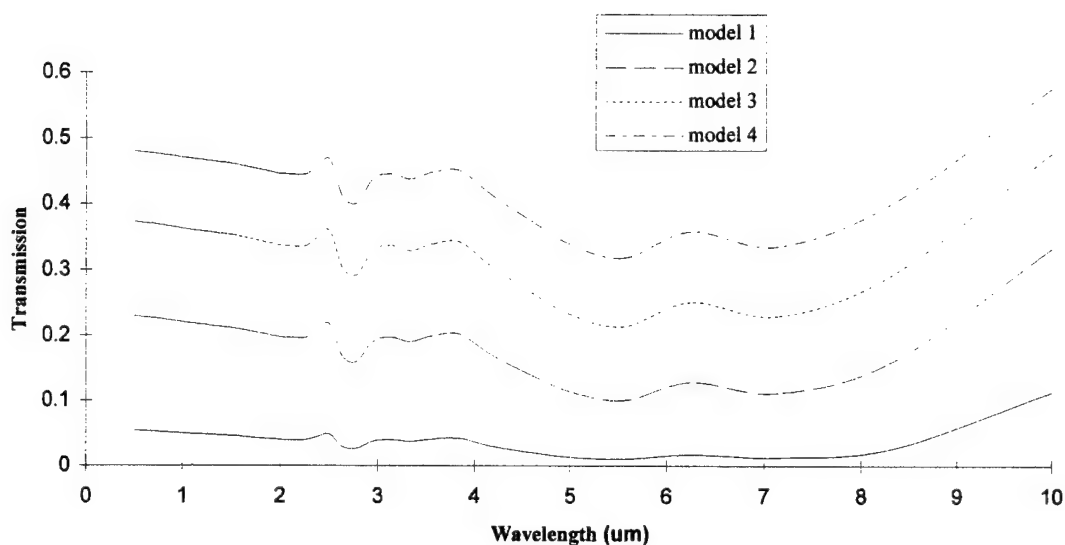


Figure B-3. Spectral Transmission for Different Plume Models

As can be seen the plume models varied from 0.05 to 0.5 transmission in the visible. As expected model 1, with the highest number density, is a very optically thick plume. For each model the increase in scattered radiance due to multiple scattering is calculated as

$$\frac{(\text{scattered radiance with multiple scattering}) - (\text{scattered radiance from single scattering})}{(\text{scattered radiance from single scattering})}$$

This ratio will be a function of wavelength since both the optical properties of water, as well as the Mie scattering process itself, varies over wavelength. The spectral result for this ratio for each model is plotted in Figure B-4.

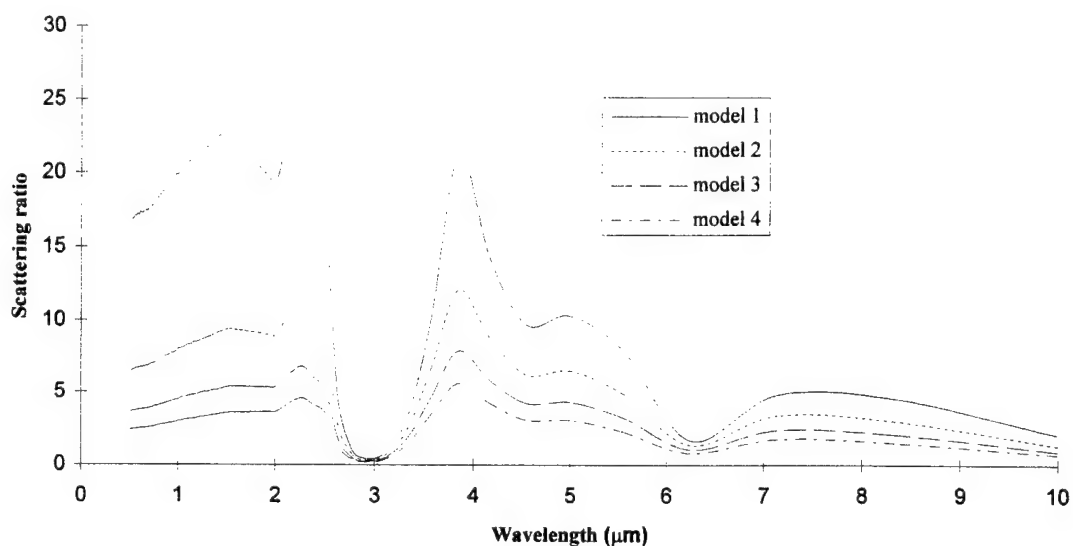


Figure B-4. Spectral Ratio of Multiple to Single Scattering for Plume Models

The ratio of total scattered radiance (with m.s.) to total plume radiance (scattered plus self-emitted) is plotted in Figure B-5.

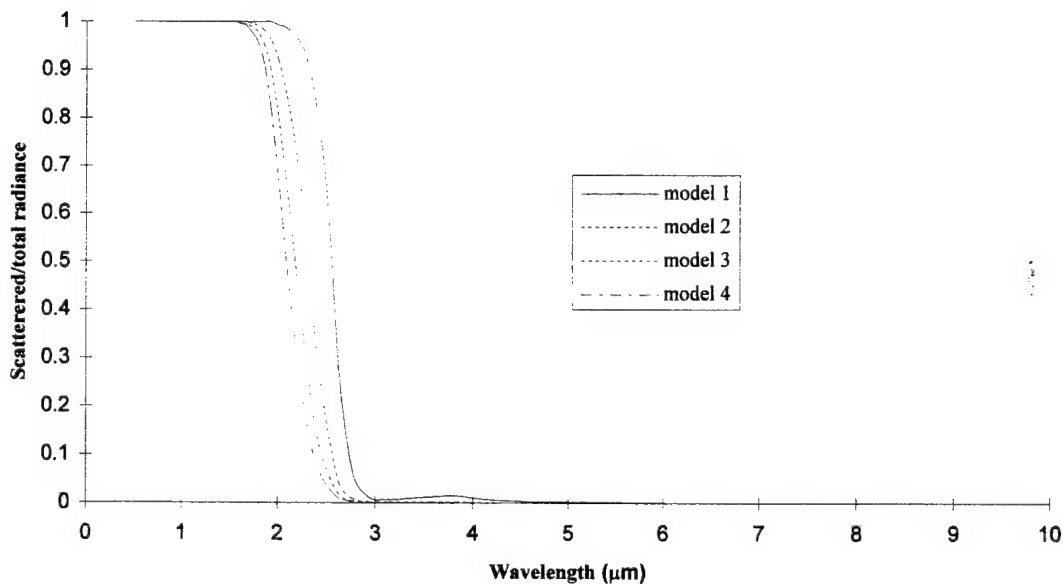


Figure B-5. Spectral Ratio of Scattered to Total Radiance for Plume Models

As expected the inclusion of m.s. increases the amount of scattered radiance dramatically. This can be an increase from 4 to 24 times in the visible and NIR depending on the optical thickness of the plume. The dips in Figure B-4 correspond to the increase in the absorption coefficient for water droplets (as can be seen correspondingly in the single scattering albedo). Even in the MWIR multiple scattering is a large contributor to scattered radiance. However the scattered radiance drops dramatically compared to the overall radiance at around $2.5\text{ }\mu\text{m}$. Thus overall contribution due to m.s. past $3\text{ }\mu\text{m}$ is negligible. It is interesting to note for the thicker plume (model 1) the ratio drop occurs at longer wavelengths.

The plume model is really a series of infinite plane parallel layers and not a closed volume. This will result in an overestimated multiple scattering effect. How much the overestimation is unknown unless calculations are done for a closed volume such as an ellipsoid. Monte Carlo methods may help give an estimate but is beyond the scope of this work (see Adams (1978)). However it seems clear that for cooling tower plumes in the visible and NIR with a transmission less than 0.5, m.s. needs to be accounted for to accurately calculate scattered radiance.

Appendix C : Particle Size Distribution

In any plume, the particles, (whether water droplets or other aerosols), will have a range of sizes (polydispersion) that is characterized by the size distribution function $n(a)$. The distribution within the plume depends on the distribution function exiting the stack or tower. This distribution will then change due to coagulation with dust particles or other atmospheric aerosols, and gravitational sedimentation. The distribution for water droplets from cooling towers can be modeled after those in clouds (Deirmendjian, 1964), while factory stack effluents can be characterized atmospheric aerosol distributions (Shettle, 1979 and Parameswaran, 1991).

Radar measurements done on cooling towers (Sauvageot, 1989) show that droplet size distribution is bimodal with the small particles ranging in radius from 1 to 10 μm while large particles have radius larger than 50 μm . The number of large particles is about 1/10 that of small size particles, and thus can be ignored for modeling purposes. The size distribution used in the LANL model is a modified gamma distribution and is based on research done on cloud water droplet distributions (Liou, 1992). It is given as:

$$n(a) = \frac{\alpha^{\alpha+1}}{\Gamma(\alpha+1)} \frac{1}{a_m} \left(\frac{a}{a_m} \right)^{\alpha} e^{-\alpha \frac{a}{a_m}}, \quad (\text{C-1})$$

where a_m is the mode radius, Γ is the gamma function, and α describes the half-width of the distribution. This distribution is normalized so the number density is 1 particle/ cm^3 . While the maximum value of the radius is at a_m , the mean radius is given as:

$$\bar{a} = \frac{\alpha+1}{\alpha} a_m, \quad (\text{C-2})$$

As α decreases the distribution becomes wider and also more skewed. Figure C-1 shows the distribution produced by the LANL plume code.

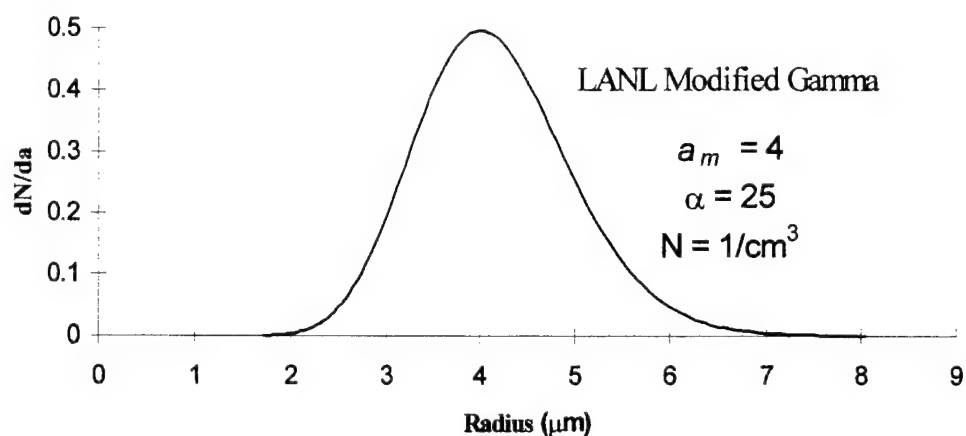


Figure C-1. LANL Modified Gamma Size Distribution

A modified gamma distribution is used for the fog and cloud models in MODTRAN and is given as:

$$n(a) = K a^\alpha e^{-ba}, \quad (\text{C-3})$$

where the constants K , α , and b determine the number density and the mode radius. The distribution shown in Figure C-2 uses parameters for a heavy fog normalized to 42 particles/cm³.

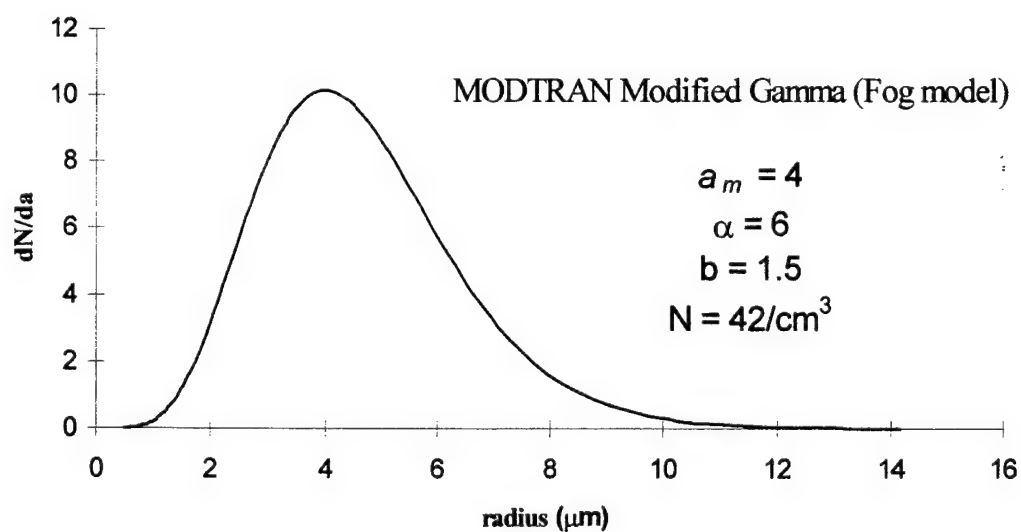


Figure C-2. MODTRAN Modified Gamma Size Distribution

The size distributions for aerosols are often represented by one or the sum of two lognormal distributions:

$$n(a) = \sum_{j=1}^m \frac{N_j}{\ln(10)a\sigma_j\sqrt{2\pi}} \exp\left[\frac{-(\log a - \log a_j)^2}{2\sigma_j^2}\right], \quad (C-4)$$

where the summation is over the number of radii modes, a_j is the mode radius, σ_j is the standard deviation, and N_j is the total number of particles having a_j as the mode radius. Usually there are two modes, one for larger particles and one for smaller particles. A single mode distribution with parameters taken from the MODTRAN urban aerosol model is shown in Figure C-3.

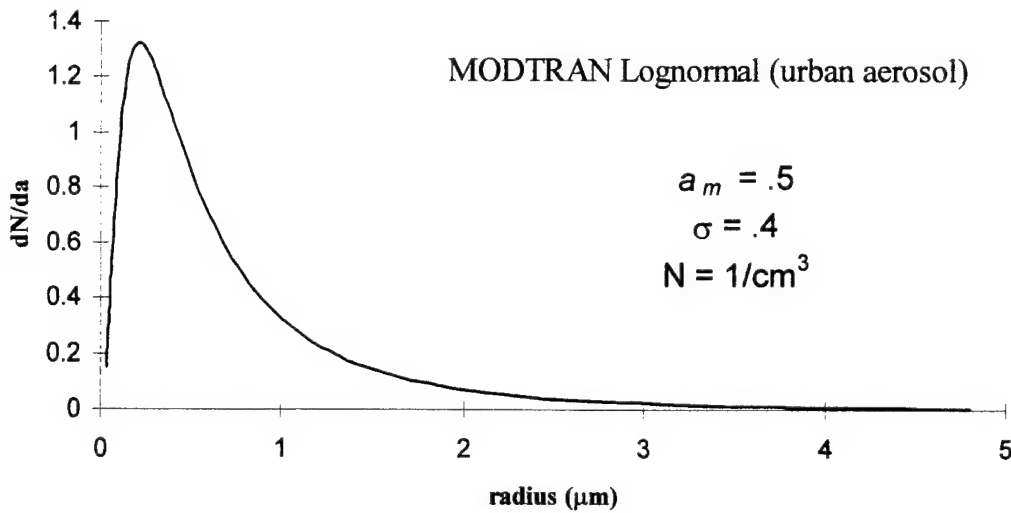


Figure C-3. MODTRAN Lognormal Size Distribution

An approximation to the lognormal is the power or Junge distribution. Since the scattering from smaller particles in the distribution is negligible, the particles from the front-end of the distribution can be given the in the simplified form

$$n(a) = Da^{-v} \quad r_2 < a < r_3 \quad (C-5)$$

where r_2 is normally at the peak value of the lognormal distribution.

The effect of implementing size distributions in the plume code is to suppress the interference and ripple structure seen for single particles as calculated from Mie scattering. This is demonstrated in Figure C-4 where the extinction efficiency (which is equal to the scattering efficiency in this case) is plotted against the size parameter for increasing variance in a lognormal size distribution. The particle type is water droplets illuminated by light at $0.55 \mu\text{m}$. For a narrow distribution both the interference and ripple structure can be clearly seen. As the particle size becomes more disperse the ripple structure disappears. As the distribution is further widened the interference structure fades away.

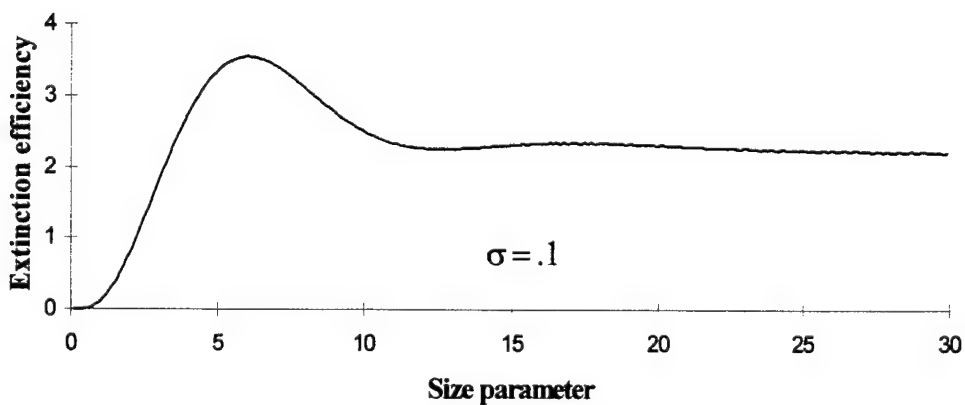
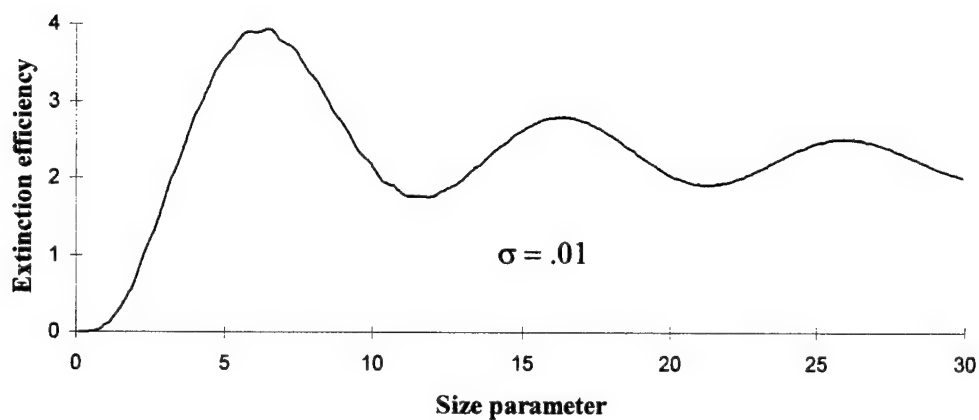
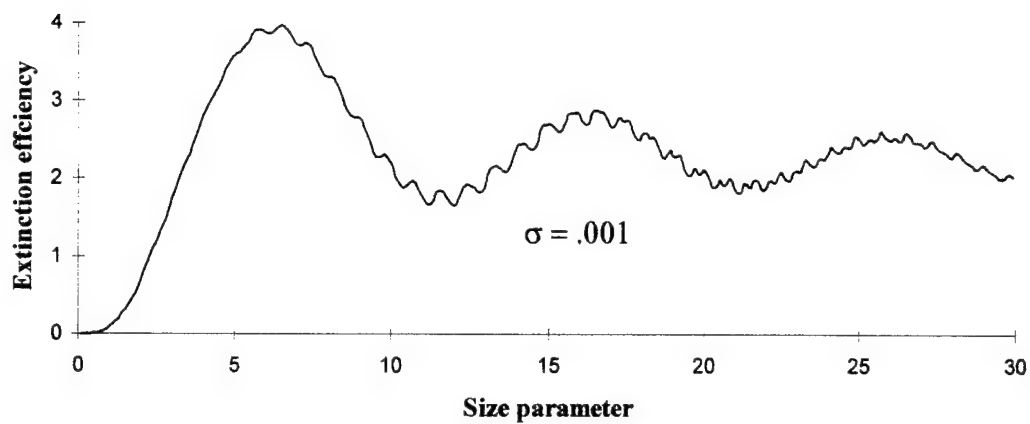


Figure C-4. Effects of Variance in Size Distribution on Extinction Efficiency

By considering the particle size distribution the scattering effects in the plume will be modeled more realistically. The “noise” from a single size particle distribution (Dirac delta function) will be

eliminated, which is especially important when looking at narrowband imagery. A particle size distribution will also increase the extinction and scattering coefficients compared to the delta distribution since the larger particles (compared to the mode radius) will carry more weight than the smaller particles. As described in Chapter 3 the user will have the option from choosing among the MODTRAN fog model, the LANL modified gamma, and the MODTRAN lognormal size distributions. He will also specify what the specific parameters are for the size distribution.

Appendix D : Two-Stream Approximation for Radiative Transfer in Water Clouds

The theory of radiative transfer has been used to determine cloud albedo and transmission. Parameterized models using the two-stream approximation have been applied to general circulation models in determining atmospheric radiation budgets. These models need to be sufficiently fast, accurate, and simple to be used in practical computational applications. There have been numerous books and articles written on the two-stream approximation including comparison and validation between different models and observed data (Coakley, 1975, Stephens, 1978, Zdunkowski, 1980, and Liou, 1992). The two-stream approximation in a multiple scattering atmosphere uses the optical depth (τ'), single scattering albedo (ϖ_0), asymmetry parameter (g) and the cosine of the incident angle of solar radiation (μ_0) as input parameters. This appendix describes the theory behind the multiple scattering code used in DIRSIG for cooling tower plumes. It is based on the delta-Eddington approximation and designed for water clouds. Validation of the model has been carried out by Slingo (1989).

For a plane parallel layer consider a system composed of diffuse upward (F_1) and downward (F_2) fluxes, and direct incident solar radiation (S) as shown in Figure D-1.

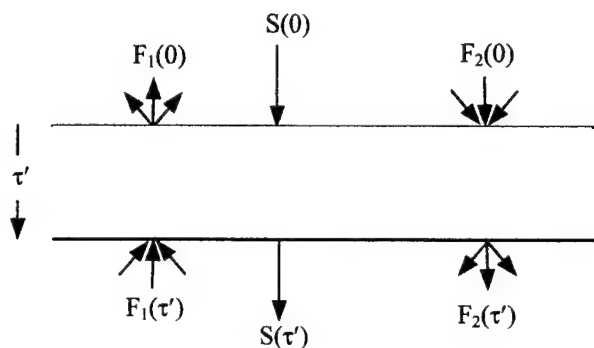


Figure D-1. Two-Stream Approximation using Plane Parallel Layer

It can be shown (Zdunkowski, 1980) that from the radiative transfer equations (2-38 and 2-39) a set of three coupled differential equations can be formed from these fluxes:

$$\begin{aligned} \frac{dF_1}{d\tau'} &= \alpha_1 F_1 - \alpha_2 F_2 - \alpha_3 \frac{S}{\mu_0} \\ \frac{dF_2}{d\tau'} &= \alpha_2 F_1 - \alpha_1 F_2 - \alpha_4 \frac{S}{\mu_0} \\ \frac{dS}{d\tau'} &= -(1 - \varpi_0 f) \frac{S}{\mu_0} \end{aligned} \tag{D-1}$$

f is the fraction of the scattered direct flux which emerges at angles close to the incident beam. This fraction of flux can be added back to the original direct flux since it emerges from the layer at essentially the same angle. The coefficients in the differential equations are expressed as:

$$\begin{aligned}\alpha_1 &= U_1[1 - \varpi_o(1 - \beta_o)] \\ \alpha_2 &= U_2\beta_o\varpi_o \\ \alpha_3 &= (1 - f)\varpi_o\beta(\mu_o) \\ \alpha_4 &= (1 - f)\varpi_o[1 - \beta(\mu_o)].\end{aligned}\tag{D-2}$$

U_1 and U_2 are the reciprocals of the effective cosines for the diffuse upward and downward radiation, β_o is the fraction of diffuse radiation scattered in the backward hemisphere, and $\beta(\mu_o)$ is the same for direct radiation.

The main difference between the variations in the various two-stream approximations are how f , U_1 , U_2 , β_o , and $\beta(\mu_o)$ are defined. These parameters are dependent on the scattering properties of the layer. The delta-Eddington method is used for strong forward scattering phase functions such as those found in water clouds for visible radiation (see Figure 2-2 and 2-3). In this case the Dirac delta function is used as an approximation for the scattering phase function. Under this approximation the scattering parameters are defined as:

$$\begin{aligned}f &= g^2 \\ \beta &= \frac{3}{7}(1 - g) \\ \beta(\mu_o) &= \frac{1}{2} - \frac{3\mu_o g}{4(1 + g)} \\ U_1 &= \frac{7}{4} \\ U_2 &= \frac{7}{4} \left[1 - \frac{(1 - \varpi_o)}{7\varpi_o\beta_o} \right],\end{aligned}\tag{D-3}$$

where ϖ_o is the single scattering albedo and g is the asymmetry parameter.

The reflectivity and transmission of the layer are defined in terms of the original fluxes as:

$$\begin{aligned}
 T_{DB} &= \frac{S(\tau')}{S(0)} \quad (\text{transmission of direct solar beam}) \\
 T_{Dif} &= \frac{F_2(\tau')}{F_2(0)} \quad (\text{diffuse transmission of diffuse incident radiation}) \\
 R_{Dif} &= \frac{F_1(0)}{F_2(0)} \quad (\text{diffuse reflectivity of diffuse incident radiation}) \\
 T_{Dir} &= \frac{F_2(\tau')}{S(0)} \quad (\text{diffuse transmission of direct solar beam}) \\
 R_{Dir} &= \frac{F_1(0)}{S(0)} \quad (\text{diffuse reflectivity of direct solar beam}).
 \end{aligned} \tag{D-4}$$

When the set of coupled differential equations in eqn. D-3 are solved these reflectivity and transmission values are expressed as:

$$\begin{aligned}
 T_{DB} &= \exp \left[- (1 - \varpi_o f) \frac{\tau'}{\mu_o} \right] \\
 T_{Dif} &= \frac{E(1 - M^2)}{(1 - E^2 M^2)} \\
 R_{Dif} &= \frac{M(1 - E^2)}{(1 - E^2 M^2)} \\
 T_{Dir} &= -\gamma_2 T_{Dif} - \gamma_1 T_{DB} R_{Dif} + \gamma_2 T_{DB} \\
 R_{Dir} &= -\gamma_2 R_{Dif} - \gamma_1 T_{DB} T_{Dif} + \gamma_1.
 \end{aligned} \tag{D-5}$$

where

$$\begin{aligned}
 \varepsilon &= \sqrt{\alpha_1^2 - \alpha_2^2} \\
 M &= \frac{\alpha_2}{\alpha_1 + \varepsilon} \\
 E &= \exp(-\varepsilon \tau') \\
 \gamma_1 &= \frac{(1 - \varpi_o f) \alpha_3 - \mu_o (\alpha_1 \alpha_3 + \alpha_2 \alpha_4)}{(1 - \varpi_o f)^2 - \varepsilon^2 \mu_o^2} \\
 \gamma_2 &= \frac{-(1 - \varpi_o f) \alpha_4 - \mu_o (\alpha_1 \alpha_4 + \alpha_2 \alpha_3)}{(1 - \varpi_o f)^2 - \varepsilon^2 \mu_o^2}.
 \end{aligned} \tag{D-6}$$

As can be seen the input parameters for solving the reflection and transmission for the layer simply depends on τ' , ϖ_o , g , and μ_o . For a cooling tower plume the first three parameters are derived from the water droplet

characteristics, number density, and plume thickness. The last parameter depends on the sun-plume-sensor angle, and is only needed for direct incident radiation (R_{Dir} and T_{Dir}). The resulting reflectivities and transmissivities can then be applied to either the direct solar radiation or to diffuse radiation (skylight, earthshine, self-emission) to determine the multiple scattering effects of the plume.

Appendix E : Testing Inverse Algorithms on Plume Images

There is a strong interest in trying to determine plume characteristics from a remote sensing perspective. This is known as the inverse problem. The current techniques use the new generation of hyper-spectral sensors to both qualify and quantify gas plumes. There are various techniques to determine the type of gas based on the absorption spectra, which is beyond the scope of this research. Once the gas is identified through its "fingerprint," then there are some quantitative techniques to determine the concentration of the plume. The purpose of this appendix is to demonstrate how DIRSIG plumes can be used to test these algorithms. It is not intended to evaluate the accuracy and robustness of these algorithms.

One possible way to determine the signature of the plume is to do a simple background subtraction. While this will show the spectral regions where species within the plume are absorbing, the bandshape will be distorted. This is because the plume both absorbs and emits radiation. In addition background subtraction leaves the signal in sensor digital counts, and does not provide a direct way to calculate the plume density. Aerspace Corp. (Polack, 1995) has developed a way to overcome these shortcomings through a special ratio technique. This is done by determining the plume transmission by inverting the radiance equation given in Chapter 2. Since scattering is negligible in gases, and the spectral bands of interest are in the IR, the radiance reaching a ground based sensor is (from eqn. 2-50)

$$L = (1 - \tau_P)L_{PBB} + L_{D\epsilon}\tau_P. \quad (E-1)$$

The assumptions are that the atmosphere below the plume is negligible and that Kirchoff's Law is used to relate the plume emissivity and transmission. The downwelled radiance is determined by measuring a background pixel that does not contain the plume. L_{PBB} is obtained from an ambient black plate spectrum (the plume and the black plate are assumed to be at the same temperature). This assumes that the plume temperature and is the same as the ambient temperature, an assumption that certainly does not hold near the stack exit. The transmission of the plume can be expressed as this special ratio:

$$\tau_P = \frac{L - L_{PBB}}{L_{D\epsilon} - L_{PBB}}. \quad (E-2)$$

For an optically thick plume, the radiance reaching the sensor will be close to the blackbody radiance at the plume temperature.

For an airborne sensor the same method is applied, with a few added terms. Again neglecting scattering in the IR and solar effects, the radiance reaching the sensor is (from eqn. 2-53)

$$L = (1 - r_E)L_{EE}\tau_P\tau_{atm} + \epsilon_P L_{PBB}\tau_{atm} + \epsilon_P L_{PBB}r_E\tau_P\tau_{atm} + L_{UE}. \quad (E-3)$$

The first term is the earth's thermal self emission, the second is the plume's self-emission, the third is the reflection of the plume off the earth, and the last term is the upwelled radiance from the atmosphere. Again the atmosphere under the plume has been ignored, as well any reflection of the downwelled radiance. If the earth is considered a perfect blackbody, then the plume transmission is

$$\tau_p = \frac{L - L_{UE} - L_{PBB}\tau_{atm}}{L_{EE}\tau_{atm} - L_{PBB}\tau_{atm}} \quad (E-4)$$

L_{UE} and τ_{atm} can be derived either through MODTRAN or in-scene techniques, and L_{EE} is obtained from a background (earth) pixel.

Once τ_p is calculated then the species concentration can be determined. τ_p is first converted into absorbance through eqn. 2-12:

$$A = -\log_{10} \tau_p \quad (E-5)$$

After the absorbance is known for that particular pixel, the plume depth needs to be estimated. This is where the spatial information of a hyperspectral sensor is useful. A first-cut assumption is the plume is rotationally symmetric around the plume axis. Thus the width of the plume is same as the depth, assuming the sensor LOS through the plume is perpendicular to the plume axis. If the LOS is at an angle, then the plume depth can be estimated as $z = \frac{w}{\sin \theta}$ where w is the plume width perpendicular to the plume axis, and θ . Figure E-1 illustrates the geometry.

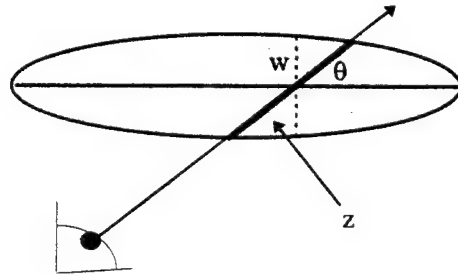


Figure E-1. Estimating Plume Depth

Once the plume depth is estimated, then the VMR is found by:

$$VMR = \frac{1}{0.434 A_{database}} \cdot \frac{column_density_{database}}{plume_depth} [ppm]. \quad (E-6)$$

$A_{database}$ is the spectral absorbance for the particular gas taken from the database. $Column_density_{database}$ is the column density at which the gas was measured. This process can be done for each plume pixel in the image. This way the VMR can be estimated spatially over the entire plume based on the radiance values.

A computer program was developed to implement the algorithm described above. It can be used for either the upward or downward looking case. The radiance values for the plume pixel and background pixel are taken directly from the DIRISG radiance image. The atmospheric radiance and transmission values are taken from the MODTRAN calculations. The actual temperature of the plume can be entered, or the plume temperature can be set equal to the ambient temperature. The user defines the bounding area of the plume. Currently the plume needs to be oriented in either a horizontal or vertical position. The program then scans the area for the plume based on a change in radiance value and determines its width along each row (or column). In the pixels where the plume is detected the plume transmission is determined as described above. The plume depth along that row is then used to determine the VMR through eqn. E-6. The type of gas is assumed known, so that the appropriate absorbance and column density from database are used. A VMR image of the plume is then constructed.

A single region JPL ACAD plume is used to test this algorithm. The wind conditions are varied to give the plume some texture. The single region contains Methyl Chloride with a VMR of 500 ppm. The two spectral bands selected are at $3.33\ \mu\text{m}$ (MWIR) and $10\ \mu\text{m}$ (LWIR) with a spectral resolution of $10\ \text{cm}^{-1}$. The first case run is for a ground based sensor looking up at the plume 50 m above the ground. A single background pixel is selected to obtain the downwelled radiance. The actual plume temperature ($303\ \text{K}^\circ$) is used to obtain the blackbody radiance. Figure E-2 shows the radiance images and Figure E-3 shows the VMR images and a sample of the estimated VMR values for the center of the plume.

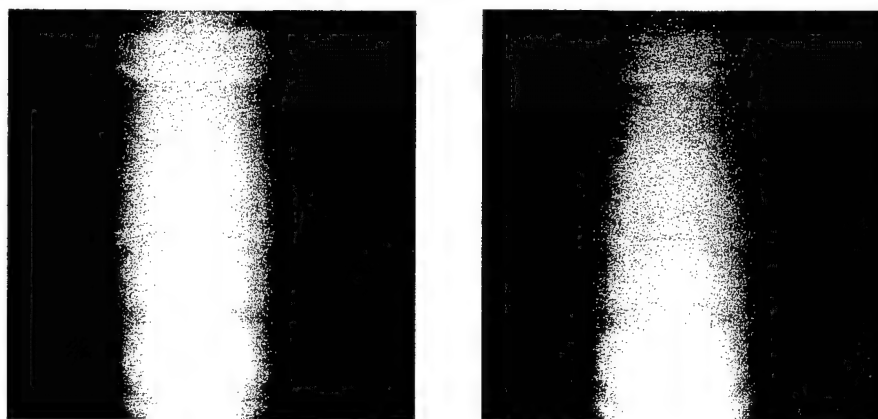
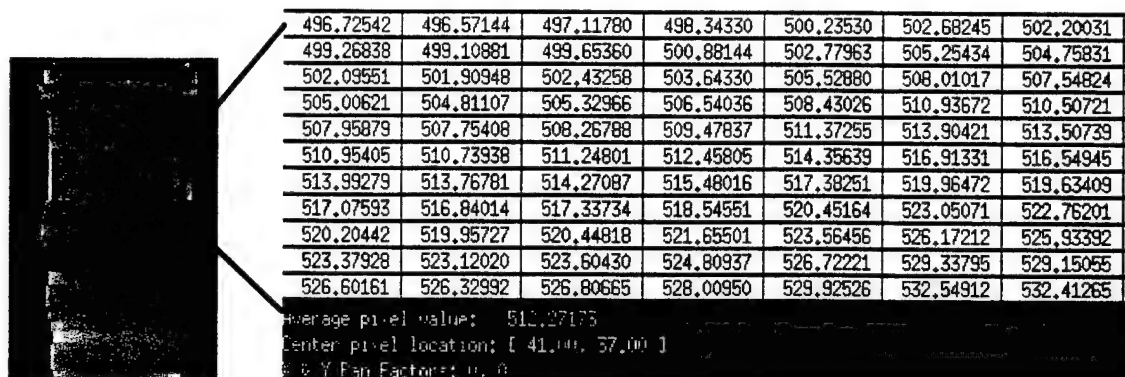
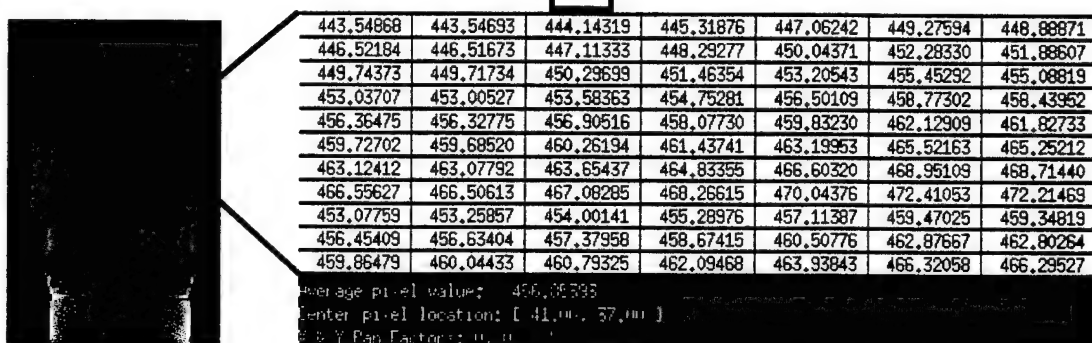


Figure E-2. LWIR and MWIR Images of Single Region JPL ACAD Plume



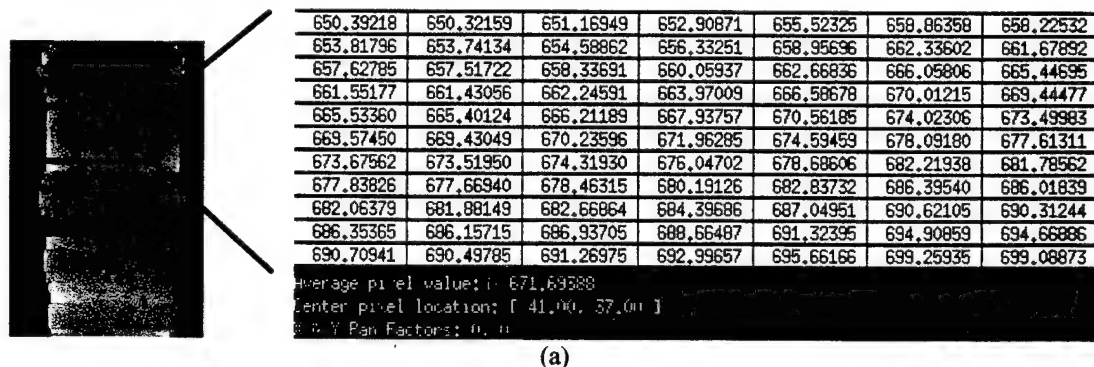
(a)



(b)

Figure E-3. Estimated VMR Image and Values of Plume in LWIR (a) and MWIR (b)

In the MWIR image the lower right hand corner appears slightly brighter due to the solar scattering from the sun (it is 8:00 A.M.). The VMR estimate in the LWIR is very good since all the assumptions are true. The DIRSIG image neglects the atmosphere below the plume which is one of the assumption in the inverse algorithm. The variation in the VMR from the actual value comes primarily from estimate of the plume depth. In the MWIR there is more solar scattering, causing a poorer estimate of the VMR than in the LWIR. The algorithm is rerun setting the plume temperature equal to the ambient temperature (293 K°). The VMR images are shown in Figure E-4.



(a)

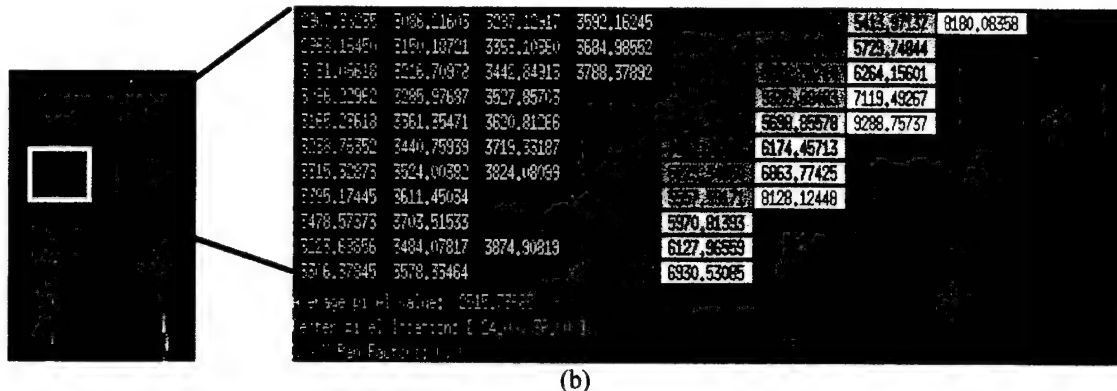


Figure E-4. Estimated VMR Image and Values of Plume in LWIR (a) and MWIR (b) for Plume at Ambient Temperature

The lower estimate of the plume temperature causes an overestimation of the VMR in the LWIR. Since the blackbody radiance has gone down, the emissivity of the plume must increase to keep the same plume radiance. A higher emissivity can only be achieved by a denser plume, and hence the increase in VMR. In the MWIR, the algorithm breaks down. The exact cause for this needs further investigation, but is probably due to the increased solar scattering at this wavelength.

The downward looking case is run next. An airborne sensor at 1.2 km is used with the same spectral bands and resolution as stated above. The background is grass, a near-perfect blackbody ($\epsilon \approx 0.98$) in the MWIR and LWIR. The images and VMR estimates (using the actual plume temperature) are shown in Figure E-5 and Figure E-6.

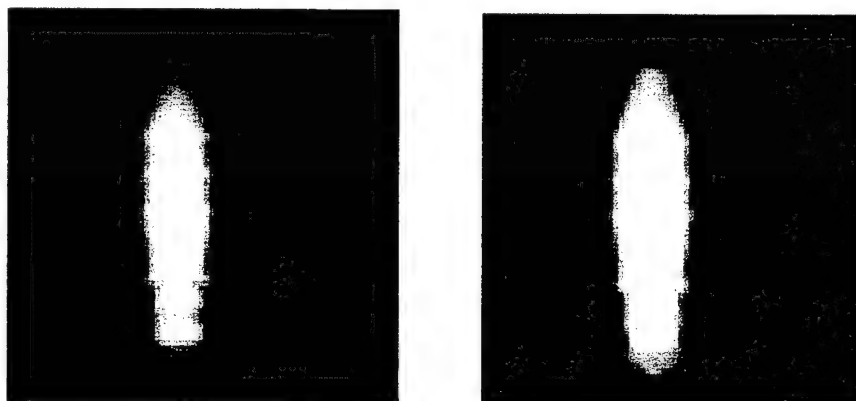


Figure E-5. LWIR and MWIR Images of Single Region JPL ACAD Plume

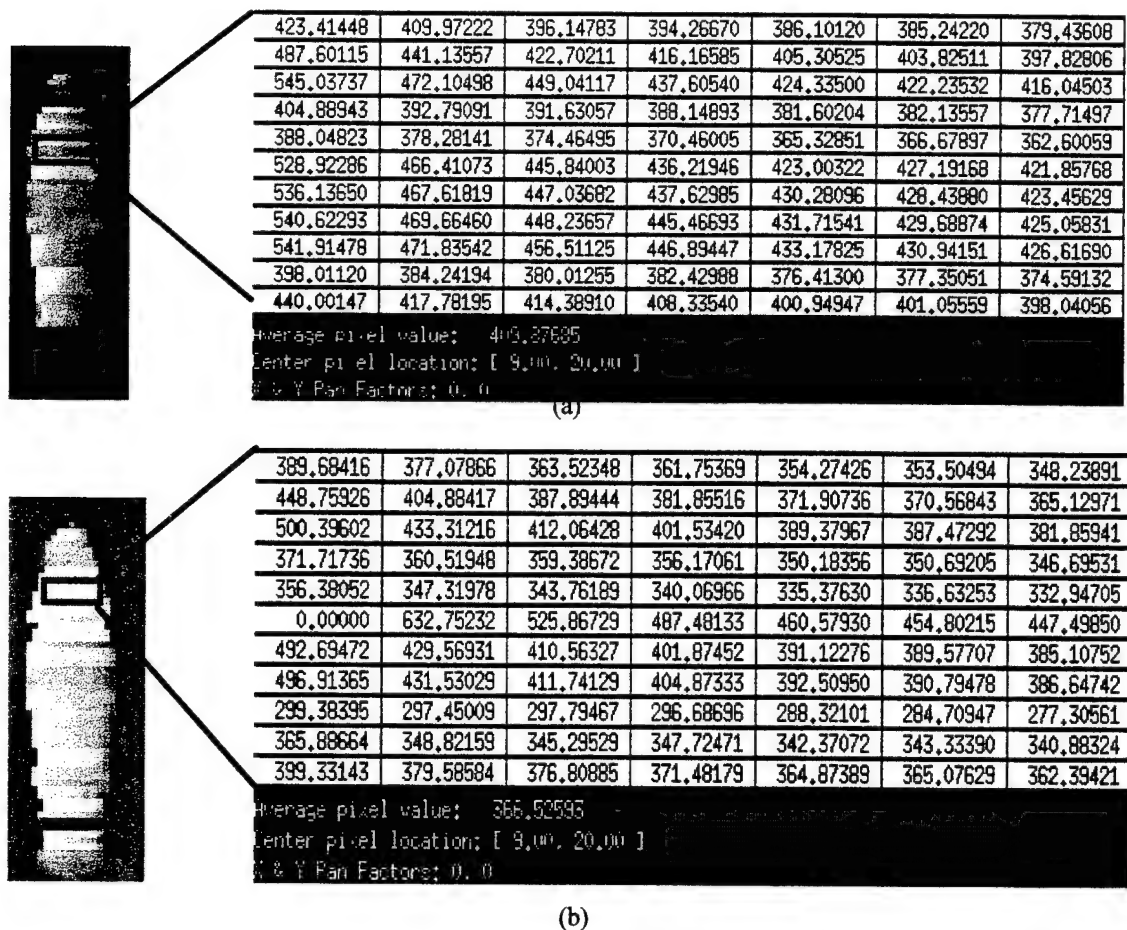


Figure E-6. Estimated VMR Image and Values of Plume in LWIR (a) and MWIR (b) from an Airborne Sensor

Again the VMR estimate is better in the LWIR than the MWIR, although both underestimate the actual value. This is due to the intervening atmosphere that adds “noise” to the actual plume signal, thus making harder to make an accurate estimate. In the LWIR parts of the plume are missing since the change in radiance from the background is not above the set threshold. In the MWIR parts of the plume shadow appear in the VMR images. The VMR estimate is rerun with the plume temperature set equal to the ambient temperature. In this case the algorithm breaks down in both bands indicating that for an airborne sensor the plume needs to be examined far enough downwind. Of course dilution of the plume will be significant at this point.

This appendix is intended only to give a demonstration of how DIRSIG can be used to test and develop the inverse algorithms for plume VMR estimation. There are several investigations that can be done to see how various parameters affect these algorithms. Also the spectral bands and resolution to use for optimal performance can be investigated.

Appendix F : Creating A Color Image in DIRSIG

The color images displayed in this research are created in a special process that involve techniques borrowed from color science. Normally DIRSIG images are 8-bit gray scale based on the radiance value for that particular spectral band. However color images can be produced based on the human visual system.

The first step is to run DIRSIG in the visible band. This is done by taking the spectral band from 25000 cm^{-1} (400 nm) to 15000 cm^{-1} (714 nm) and dividing it into 500 cm^{-1} increments. This results in 23 points in the visible. Radiance calculations are done for each of these points in DIRSIG (and the associated MODTRAN radiance file). The radiance values from this visible band are then independently multiplied by three different color matching functions. These three functions are based on the XYZ color matching functions used in color science, multiplied by a RGB transformation matrix for a typical monitor. The resulting color matching function curves are shown in Figure F-1.

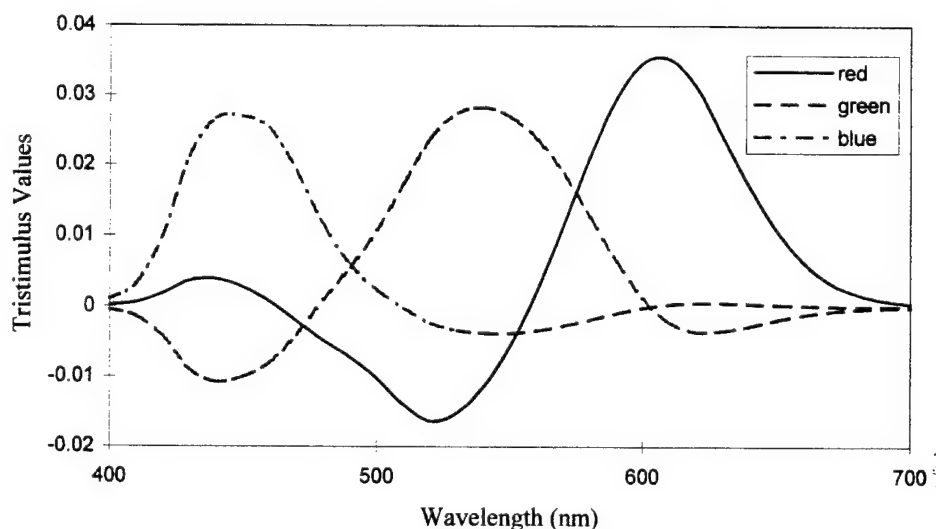


Figure F-1. RGB Color Matching Functions

Each color channel is based on the response of the human visual system. Notice the functions have negative values. This is needed to reproduce the full color spectrum with proper color mixing of the three functions. Each curve has an integrated value of one. At this point the DIRSIG image is represented by three color channels (red, green, and blue). Note that when this process is done, the absolute radiometric values are lost. If gray cards are available in the image, then each channel is independently auto-scaled to produce an 8-bit tiff image for each color. If there are no gray cards in the image, then all three channels should be scaled to the same gain and bias to produce the 8-bit images. The three channels are then combined through UNIX PBM utilities to produce a 24 bit color tiff image. The rainbow and sunset in Chapter 5 demonstrate the faithful reproduction of color when using this technique.

Appendix G : Adding Additional Gases to the Gas Database

Currently there are a limited number of gases that can be used in DIRSIG. However this is easily expandable. The source of gas absorbance databases is from the combined USAF/EPA internet web site. This site contains both experimentally measured databases as well as HITRAN generated databases. The address for this site is "<http://info.arnold.af.mil>" The desired gases can be downloaded via FTP. The files are in ASCII (do not chose the .spc format unless the showspc.exe program on a P.C. is available to view the file).

Once the files are download they need to be converted into a format that the PMT can read. This is done using the "convert_gas.C" program. This program creates a file called "*gas.dat*" where *gas* is the user defined name. The file has a header containing the gas temperature, column density, and number of spectral points. The frequency and absorbance are then listed. The program also prints out the minimum and maximum frequency.

The PMT code needs to be modified next. The gas filename, minimum and maximum frequency, are added in the code. The gas also needs to be assigned a code number. The gases present in the code should serve as an example format of how to add the additional gas. After the changes are made the PMT code needs to be recompiled. The new *gas.dat* file has to be in the same directory as the PMT program. A future improvement is to have the PMT read in the gas filename directly instead of the gas code. In this way the PMT code itself should never have to be altered.

Appendix H : DIRSIG Plume File Formats

The following are the files associated with the DIRSIG plume model. These include both files used in the pre-processing stage (i.e. PMT), as well as in the actual DIRSIG run itself. The files described in the DIRSIG User's Tutorial (1995), are not covered here. There is a short description for each file stating where it was produced, and which program uses it, as well as any additional comments. Text in *italics* are not part of the actual file, but rather used to describe the file entry.

LANL plume model output file (anl.out):

This file is produced by the LANL plume model and used in the build_lanl program. It describes the plume's x,z location, temperature, plume radius, mean droplet radius, and number density for each region.

Number of regions:

12					
x (cm)	z (cm)	tp (K)	rplume (cm)	mean_radius (μm)	num_den (cm ⁻³)
0.00000	0	300.000	196.330	6.00000	1033.66
678.417	381.190	290.994	244.695	9.09898	570.148
1278.42	689.083	289.413	275.650	12.6483	489.947
1878.42	980.083	288.159	303.760	14.3075	426.610
2478.42	1257.68	286.661	329.726	15.0706	350.580
3078.42	1522.72	285.373	354.060	15.5273	285.361
3678.42	1775.58	284.316	376.899	15.8371	232.021
4278.42	2016.57	283.448	398.316	16.0604	188.374
4878.42	2245.99	282.729	418.369	16.2277	152.396
5478.42	2464.11	282.130	437.113	16.3570	122.491
6078.42	2671.16	281.625	454.602	16.4593	97.4368
6678.42	2867.39	281.196	470.882	16.5417	76.2940

JPL plume model input file (Plume_Input):

This file is used as input for the JPL plume code. There are three versions. The first is for the stand-alone version (jpl_model), the second for the ACAD version (jpl_acad_model), and the third for integrated DIRSIG version. The file shown below is the condensed version, with superfluous items excluded

```

/* SignificantChangeInPlumeDilution = */ 0.1
/* SignificantPlumeDilutionMinimum = */ 0.001 /*(this needs to be <= 0.001) */
/* Fraction of stack diameter to use
   as minimum plume sampling step = */ 1 /* (down plume this is not too sensitive <= 1.) */
/* Fraction of maximum plume
   contrast contribution that is
   considered significant = */ 0.01 /* (this can be ~0.01 - 0.1) i think */
/*

```

Format for each chemical is:

1. Chemical name.
2. Molecular weight of the chemical
3. Quantity of chemical. Meaning depends on plume model
 - a. If plume model is simple slab model (S, or s), then the quantity is:
volume mixing ratio (VMR) in parts per million.
 - b. Otherwise, the quantity is:
Pounds per hour released at the top of the stack.

*/

SF6 146.0 50.

/* Name of the data set from which time sampled meteorology and release rates can be obtained. This input, if present takes precedence over the average values for similar quantities. If it is not used (when name = "None"), then average rates read in are operable.

*/

None

/* Number of plume planes modeled. Plume planes are separated by distances = windspeed * sample interval = */ 100

/* Units used to measure distances and speeds in the input data, and the average data below. Possible are "Feet" or "Meters". = */ Meters

/* Height of met instruments = */ 21.64

/* Height of stack release point. = */ 21.64

/* Stack diameter (set negative to avoid plume modeling completely) = */ .4127

/* X, Y, Z location of the stack in the coordinate system of the scene (stack base) = */ 0. 0. 0.

/* Direction in scene coordinate system from which mean wind direction is coming from (degrees) with north = 0 degrees, and west = 90 degrees = */ 310

/* Average wind speed in knots. = */ 7.

/* Atmospheric stability number (Pasquill-Gifford stability number) = */ 40

/* Average stack release temperature in degrees Fahrenheit = */ 194.

/* Average stack release velocity in Units (Feet or Meters) per sec = */ 15.

/* Average sample interval in seconds = */ 1.

/* Number of sigma (float number) beyond which plume is negligible = */ 5.

The following is for the stand-alone version:

/* The following set of three dimensional points are the starting (sensor) and ending (target) points for a ray path. Units are meters. Termination of this list is via an EOF. */

1 0 1000 1 0 0

2 0 1000 2 0 0

3 0 1000 3 0 0

4 0 1000 4 0 0

5 0 1000 5 0 0

The following is for the ACAD version:

/ This is a new a method for building the plume model for DIRSIG. The sensor and ray starting point are moved along the direction of the plume (the y-axis in this case) so that a vertical slice is taken through the plume */*

/ The number of slices to take through the plume = */ 10*

/ Increment (in meters) between each slice = */ 20*

The integrated DIRSIG version does not have sensor/target geometry data (DIRSIG determines this)

Meteorological file for Plume_Input (met_file):

This file gives the time varying meteorological conditions to be read in by JPL plume model (as indicated in the Plume_Input file). The format is very hard to read due to the exact format requirements. All values for a particular time are on a single line with no spaces in between. The number in parentheses is the number of spaces allocated for that value. If applicable, the units are also given.

Format:

month(2)

date(2)

year(2)

24hour(2)

min(2)

sec(2)

wind direction(3, deg)

wind velocity(3, kts)

ambient air temp (3, F°)

atmospheric stability number (2)

stack temperature (4, F°)

stack velocity (3, m/s)

release rate (5, lbs/hr) repeated for each species present

102596150000270.3.765.40294.15.40

102596150003270.3.665.30294.14.40

102596150005270.3.665.40294.15.40

Plume input file for build_jpl (jpl.dat):

This file is created by the JPL ACAD plume model and used by build_jpl to make the .dxf and .pdt file. It gives the cross-sectional plume properties at certain intervals down wind.

1 *number of species*

7

species ID number

0.2 *stack radius (m)*

363.15 *stack temperature (K°)*

290.00 *ambient temperature (K°)*

10	<i>number of plume slices</i>			
20.0	<i>interval of slices (m)</i>			
<i>distance downwind (m)</i>	<i>vertical distance (m)</i>	<i>dilution</i>	<i>temp contrast (K)</i>	<i>VMR (parts per part)</i>
0.000000	20.838510	0.002122	0.155211	1.783480e-05
•	•	•	•	•
•	•	•	•	•
•	•	•	•	•

Input file for build_jpl (input.dat):

This file describes how to build the ACAD model (i.e. number of regions) for the JPL plume.

3	<i>number of regions</i>
.06212	<i>max dilution</i>
.005	<i>step size of first region (as fraction of max dilution)</i>
1	<i>material of first region</i>
.07	<i>step size of second region (as fraction of max dilution)</i>
2	<i>material of second region</i>
.5	<i>step size of third region (as fraction of max dilution)</i>
3	<i>material of third region</i>

Plume description file for plume model translator (*.pdt)

This file is generated by either build_jpl or build_lanl and describes each region of the plume.

1	<i>number of regions</i>
region1	<i>name of region</i>
1	<i>region number</i>
300.000	<i>temperature of region (K)</i>
2	<i>number of constituents in region</i>
4	<i>constituent number (4 = CH₃Cl)</i>
-1	<i>particle radius (-1 for gases)</i>
50	<i>VMR (ppm) or number density (cm⁻³)</i>
1	<i>constituent number (1 = water droplet)</i>
1	<i>particle radius (μm)</i>
100	<i>VMR (ppm) or number density (cm⁻³)</i>

Index of refraction database file (H2O.dat)

This file gives the index of refraction for a scattering particle and read in by the PMT. Currently only water droplets are in the database.

0.200	<i>starting wavelength (mm)</i>
29.0	<i>ending wavelength</i>
0.025	<i>wavelength increment</i>
<i>real</i>	<i>imaginary index of refraction</i>
1.39600	1.10000e-07
1.37300	1.32257e-14
•	•
•	•

EPA gas absorbcency database (*.dat)

This is gas database read in by the PMT. It is modified from the original EPA format.

33179	<i>number of spectral points</i>
1503	<i>column density (ppm-m) of gas measured for database</i>
298	<i>temperature (K°) of gas measured for database</i>
<i>frequency (cm⁻¹)</i>	<i>absorbance</i>
4399.918	0.002061
4399.797	0.0010314
4399.677	0.00073737
4399.557	0
4399.436	0.00039278
4399.315	0.001001

Optical database file for DIRSIG (*.opt)

This is the optical input file for DIRSIG when using the ACAD plume model. Each region will have its own optical file. There are two formats, one for single scattering and one for multiple scattering. The bandpasses need to match that of the scene node file. The filename is specified in the region's material entry in the material database under the extinction filename.

(single scattering format):

1	<i>format type (1 = single scattering)</i>
1	<i>number of spectral bands</i>
18180	<i>starting frequency for band 1 (cm⁻¹)</i>
18200	<i>ending frequency (cm⁻¹)</i>
20	<i>frequency increment (cm⁻¹)</i>
<i>frequency (cm⁻¹)</i>	<i>extinction coefficient (km⁻¹) scattering coefficient (km⁻¹)</i>
18200 22.501 22.501	
18180 22.348 22.348	
18180	<i>starting frequency for band 1(cm⁻¹)</i>
18200	<i>ending frequency (cm⁻¹)</i>
20	<i>frequency increment (cm⁻¹)</i>
0.00	<i>starting angle (deg)</i>
180.0	<i>ending angle (deg)</i>
10	<i>angular increment (deg)</i>
<i>frequency (cm⁻¹)</i>	<i>angle (deg) angular scattering coefficient (km⁻¹)</i>
1.82e+04 0 4196.2	
18200 10 6.8958	
18200 20 9.5427	
18200 30 2.4291	

(multiple scattering format):

0	<i>format type (0 = multiple scattering)</i>
1	<i>number of spectral bands</i>
14000	<i>starting frequency (cm⁻¹)</i>

25000 *ending frequency (cm⁻¹)*
 500 *frequency increment (cm⁻¹)*
frequency (cm⁻¹) extinction coefficient (km⁻¹) scattering coefficient (km⁻¹)
 25000 2.8722 2.8722
 24500 2.8782 2.8782
 24000 2.8733 2.8733
frequency (cm⁻¹) single scattering albedo asymmetry parameter
 25000 1 0.82685
 24500 1 0.82611
 24000 1 0.82905

Absorbance database file for DIRSIG (*.abs)

This file is used by the DIRSIG integrated JPL model. It is based on the EPA absorbance database.

7 *gas ID number*
 298 *database temperature (K^o)*
 10 *database column density (ppm-m)*
 2 *number of spectral bands*

 910 *starting frequency for band 1 (cm⁻¹)*
 960 *ending frequency (cm⁻¹)*
 5 *frequency increment (cm⁻¹)*
frequency (cm⁻¹) absorbance
 960 0
 955 0.00088119
 950 0.150294

Appendix I : NTS Validation Files

The following are a few files used in the JPL plume model validation. These are the ACAD view file, the scene node file, the SF6 absorbance database, and the Plume_Input file. Other files used were too long to be included (i.e. geometric and radiometry databases).

NTS.adv:

-9200 5000 0 (*target location (x, y, z) in mm*)
-53455 5000 52691 (*sensor location*)
49.9733 180. 0.0 (*sensor elevation, azimuth, and twist*)
50 (*sensor focal length (mm)*)
400 400 (*image size (pixels)*)

NTS.snd

0.527 (*sensor height for MODTRAN input (km)*)
2 (*number of spectral bands*)
910. 960. 5. (*band 1 start, stop, and increment frequency (cm⁻¹)*)
910. 1020. 10. (*band 2 " " " " " "*)
20.0 86.0 2.0 (*MODTRAN view angle elevation*)
2 25 94 (*date*)
23.3 (*GMT*)
7.0 (*Difference between local time and GMT*)
36.8 115.95 (*Latitude and Longitude*)

SF6.abs

7 (*gas number*)
298 (*database temperature (K)*)
10 (*database column density (ppm-m)*)
2 (*number of spectral bands*)
910 (*starting frequency for band 1 (cm⁻¹)*)
960 (*stopping frequency*)
5 (*frequency increment*)
960 0 (*frequency and absorbance*)
955 0.00088119
950 0.150294
945 0.242627
940 0.0880151
935 0.0149287
930 0.0120917
925 0.00547446
920 0.000461799
915 3.89e-07
910 0

910 (*starting frequency for band 2*)
1020
10

1020 0
 1010 0
 1000 0
 990 0
 980 0
 970 0
 960 0
 950 0.14367
 940 0.0981114
 930 0.0108173
 920 0.00117568
 910 0

Plume_Input file (*condensed*)

```
/* SignificantChangeInPlumeDilution = */ 0.1
/* SignificantPlumeDilutionMinimum = */ 0.001 /*(this needs to be <= 0.001) */
/* Fraction of stack diameter to use
   as minimum plume sampling step = */ 1 /* (down plume this is not too sensitive <= 1.) */
/* Fraction of maximum plume
   contrast contribution that is
   considered significant = */ 0.01 /* (this can be ~0.01 - 0.1) i think */
/*
```

Format for each chemical is:

1. Chemical name.
2. Molecular weight of the chemical
3. Quantity of chemical. Meaning depends on plume model
 - a. If plume model is simple slab model (S, or s), then the quantity is:
 volume mixing ratio (VMR) in parts per million.
 - b. Otherwise, the quantity is:
 Pounds per hour released at the top of the stack.

*/

SF6 146.0 50.

```
/* Name of the data set from which time sampled meteorology and release rates can
   be obtained. This input, if present takes precedence over the average values
   for similar quantites. If it is not use (when name = "None"), then average
   rates read in are operable.
```

*/

None

```
/* Number of plume planes modeled. Plume planes are separated by
   distances = windspeed * sample interval = */ 100
/* Units used to measure distances and speeds in the input data, and
   the average data below. Possible are "Feet" or "Meters". = */ Meters

/* Height of met instruments = */ 21.64
/* Height of stack release point. = */ 21.64
/* Stack diameter (set negative to avoid plume modeling completely)= */ .4127
/* X, Y, Z location of the stack in the coordinate system of the
```

```

scene (stack base)                = */ 0. 0. 0.
/* Direction in scene coordinate system from which mean wind
   direction is coming from (degrees) with north = 0 degrees,
   and west = 90 degrees            = */ 310
/* Average wind speed in knots.     = */ 7.
/* Atmospheric stability number (Pasquill-Gifford stability number)
   */ 40
/* Average stack release temperature in degrees Farenheight = */ 194.
/* Average stack release velocity in
   Units (Feet or Meters) per sec   = */ 15.
/* Average sample interval in seconds = */ 1.
/* Number of sigma (float number) beyond which plume is negligible = */ 5.

```

References

- Anderson, G. P., et. al., FASCOD/TRAN/LOWTRAN: Past/Present/Future, *18th Annual Review Conference on Atmospheric Transmission Models*, 1995.
- Barrett, J., The Optical Properties of Water Droplets in the Infrared, *Journal of Physics D: Applied Physics*, **18**, 753-764, 1985.
- Bennet, M., A Lidar Study of the Limits to Buoyant Plume Rise in a Well Mixed Boundary Layer, *Atmospheric Environment*, **29**, 2275-2288, 1995.
- Blumenthal, D. L., et. al., Effects of a Coal Fired Power Plant and Other Sources on Southwest Visibility, *Atmospheric Environment*, **15**, 1955-1969, 1981.
- Bohren, C., and Huffman, D., *Absorption and Scattering of Light by Small Particles*, Wiley and Sons, 1983.
- Brown, S. D., et. al., *DIRSIG User's Tutorial*, Center for Imaging Science, Rochester Institute of Technology, 1994.
- Cahalan, R. F., et. al., Independent Pixel and Monte Carlo Estimates of Stratocumulus Albedo, *Journal of the Atmospheric Sciences*, **51**, 3776-3790, 1994.
- Carhart, R. A., et. al., *Studies on Mathematical Models for Characterizing Plume and Drift Behavior from Cooling Towers*, Electric Power Research Institute Report CS-1683, 1981.
- Carhart, R., and Policastro, A., A Second-Generation Model for Cooling Tower Plume Rise and Dispersion, *Atmospheric Environment*, **25**, 1559-1576, 1991.
- Carlson, H., et. al., Infrared Extinction Spectra of Some Common Liquid Aerosols, *Applied Optics*, **16**, 1598-1604, 1977.
- Carrascal, M. et. al., Sensitivity of Gaussian Plume Model to Dispersion Specifications, *Theoretical and Applied Climatology*, **48**, 147-157, 1993.
- Chandrasekhar, S., *Radiative Transfer*, Dover Publications, 1960.
- Chylek, P., Grams, G., and Pinnick, R., Light Scattering by Irregularly Randomly Oriented Particles, *Science*, **193**, 480-482, 1976.
- Coakley, J., and Chylek, P., The Two Stream Approximation in Radiative Transfer, *Journal of the Atmospheric Sciences*, **32**, 409-418, 1975.
- Cox, S., Observations of Cloud Infrared Effective Emissivity, *Journal of the Atmospheric Sciences*, **33**, 287-289, 1976.
- Deirmendjian, D., Scattering and Polarization Properties of Water Clouds and Hazes in the Visible and Infrared, *Applied Optics*, **3**, 187-196, 1964.
- Downing, H., and Williams, D., Optical Constants of Water in the Infrared, *Journal of Geophysical Research*, **80**, 1656-1661, 1975.

- Erbrink, H., Plume Rise in Different Atmospheres, *Atmospheric Environment*, **28**, 3625-3636, 1994.
- Fenn, R. W., et. al., *Handbook of Geophysics and the Space Environment*, Chapter 18, Air Force Geophysics Lab, 1985.
- Fraser, R., and Kaufman, Y., The Relative Importance of Aerosol Scattering and Absorption in Remote Sensing, *IEEE Transactions on Geoscience and Remote Sensing*, **5**, 625-633, 1985.
- Gat, N., et. al., Chemical Detection Using the Airborne Thermal Infrared Imaging Spectrometer (TIRIS), SPIE Proceedings 3082, 1997.
- Goody, R. M., and Yung, Y.L., *Atmospheric Radiation*, Oxford University Press, 1989.
- Haman, K., and Malinowski, S., Observations of Cooling Tower and Stack Plumes and Their Comparisons with Plume Model Alina, *Atmospheric Environment*, **23**, 1223-1234, 1989.
- Hänel, G., Computation of the Extinction of Visible Radiation by Atmospheric Aerosol Particles as a Function of the Relative Humidity, *Aerosol Science*, **3**, 377-386, 1972.
- Hanna, S., and Paine, R., Hybrid Plume Dispersion Model Development and Evaluation, *Journal of Applied Meteorology*, **28**, 206-224, 1989.
- Haus, R., et. al., FTIS Remote Sensing of Smoke Stack and Test Flare Emissions, *SPIE Vol 1506 Air Pollution and Visibility Measurements*, 45-53, 1994.
- Higleman, T., Advanced Plume Analysis Software for Gas Measurement, *SPIE Aerosense Conference*, 1996.
- Hobbs, P.V., *Ice Physics*, Oxford Press, 1974.
- Iqbal, M., *An Introduction to Solar Radiation*, Academic Press, 1983.
- Isaacs, R. G., et. al., Multiple Scattering LOWTRAN and FASCODE Models, *Applied Optics*, 1272-1281, **26**, 1987.
- Joseph, J. H., Wiscombe, W. J., and Weinman, J. A., The Delta-Eddington Approximation for Radiative Transfer Flux, *Journal of the Atmospheric Sciences*, **33**, 2452-2459, 1976.
- King, M. D., and Harshvardhan, Comparative Accuracy of Selected Multiple Scattering Approximations, *Journal of the Atmospheric Sciences*, **43**, 784-801, 1986.
- King, M. et. al., Aerosol Size Distributions Obtained by Inversion of Spectral Optical Depth Measurements, *Journal of the Atmospheric Sciences*, **35**, 2153-2167, 1978.
- Kocifaj, M., Spectral Angular Function of Scattered Radiation in Cloudless Molecular-Aerosol Atmosphere, *Physics of the Atmosphere*, **65**, 107-116, 1992.
- Leonard, E., Visual Simulation of Power Plant Emissions, *LASL Mini-Review*, 79-21, 1979.

- Liou, K., *An Introduction to Atmospheric Radiation*, Academic Press, 1980.
- Liou, K., *Radiation and Cloud Processes in the Atmosphere*, Oxford Press, 1992.
- Marshak, A., et. al., The Verisimilitude of the Independent Pixel Approximation Used in Clouds Remote Sensing, *Remote Sensing Environment*, **52**, 71-78, 1995.
- McKee, T. B., and Cox, S. K., Scattering of Visible Radiation by Finite Clouds, *Journal of the Atmospheric Sciences*, **31**, 1885-1892, 1974.
- Nishita, T., Dobashi Y., and Nakamae E., Display of Clouds Taking into Account Multiple Anisotropic Scattering and Sky Light, Proceedings of SIGGRAPH 96, **18**, 379-386, 1996.
- O'Steen, L., Cooling Tower Simulation with a Mesoscale Atmospheric Model, 1995.
- Parameswaran, K., Rose, K., and Murthy, B., Relationship between Backscattering and Extinction Coefficients of Aerosols with Application to Turbid Atmosphere, *Applied Optics*, **30**, 3059-3071, 1991.
- Penner, S. S., *Quantitative Molecular Spectroscopy and Gas Emissivities*, Addison Wesley, 1959.
- Pinnick, R. et. al., Backscatter and Extinction in Water Clouds, *Journal of Geophysical Research*, **88**, 6787-6797, 1983.
- Polak, M. L., Hall, J. L., and Herr, K.C., Passive Fourier-Transform Infrared Spectroscopy of Chemical Plumes: An Algorithm for Quantitative Interpretation and Real-Time Background Removal, *Applied Optics*, 5406-5412, **34**, 1995.
- Powers, B., *Cooling Tower and Plume Modeling for Satellite Remote Sensing Applications*, Los Alamos Tech Report LA-UR-95-1417, 1995.
- Sauvageot, H., Radar Measurement of Cooling Tower Drift, *Journal of Applied Meteorology*, **28**, 925-935, 1989.
- Schott, J., *Remote Sensing: The Image Chain Approach*, Oxford University Press, 1996.
- Schott, J. et. al., DIRSIG: Description, Enhancements, and Validation, *RIT/DIRS Report 92/93-51-146*, 1993.
- Seigneur, C. et. al., *Temporal and Spatial Variability of the Visual Effects of Stack Plumes*, EPA Report 600/3-85/039, 1985.
- Seigneur, C., Bergstrom, R. W., et. al., Measurements and Simulations of the Visual Effects of Particulate Plumes, *Atmospheric Environment*, **18**, 2231-2244, 1984.
- Selby, J., and Reed, R., Atmospheric Background and Smoke Stack Measurements, *SPIE Vol. 142 Optical Properties of the Atmosphere*, 9-15, 1978.

Shettle, E. P., and Fenn, R. W., *Models for the Aerosols of the Lower Atmosphere and the Effects of Humidity Variations on Their Optical Properties*, AFGL-TR-79-0214, 1979.

Smith, F., An Analysis of a Wet Stack Plume, *The Meteorological Magazine*, **120**, 97-106, 1991.

Stephens, G. L., Radiation Profiles in Extended Water Clouds II, *Journal of the Atmospheric Sciences*, **35**, 2123-2132, 1978.

Stephens, G. L., *Remote Sensing of the Lower Atmosphere*, Oxford Press, 1994.

Twitty, J. T., and Weinman, J.A., Radiative Properties of Carbonaceous Aerosols, *Journal of Applied Meteorology*, 725-731, **10**, 1971.

Twomey, S., and Seton, K. J., Inferences of Gross Microphysical Properties of Clouds from Spectral Reflectance Measurements, *Journal of the Atmospheric Sciences*, **37**, 1065-1069, 1980.

Van de Hulst, H., *Light Scattering by Small Particles*, Wiley and Sons, 1957.

Volz, F. E., Infrared Optical Constants of Ammonium Sulfate, Sahara Dessert, Volcanic Pumice, and Flyash, *Applied Optics*, **12**, 564-567, 1973.

Westberg, K. R., et. al., *Chemical Release Rates During the First Effluent Tracking Experiments at NTS*, Aerospace Report No. ATR-95(9975)-5, 1996.

White, W., and Patterson, D., On the Relative Contributions of NO₂ and Particles to the Color of Smoke Plumes, *Atmospheric Environment*, **15**, 2097-2104, 1981.

Zdunkowski, W. G., Welch, R. M., and Korb, G., An Investigation of the Structure of Typical Two-stream-methods for the Calculation of Solar Flux and Heating Rates in Clouds, *Atmospheric Physics*, 147-167, **53**, 1980.